IMPERIAL

Department of Life Sciences

PhD Thesis

Label retaining haematopoietic stem cells preserve their stemness during *Plasmodium berghei* infection and maintain low metabolic statuses

Christiana Georgiou

A thesis submitted for the degree of Doctor of Philosophy

2023

For Panayiotis, Stavros, mum, dad and
my brothers too

Declaration of Originality

All of the work presented in this thesis is my own, generated in Prof. Cristina Lo Celso's laboratory at Imperial College London, except where clearly stated otherwise. When data was generated by or in collaboration with others, I acknowledge it within the thesis.

Christiana Georgiou

Copyright Declaration

The copyright of this thesis rests with the author. Unless otherwise indicated, its contents are licensed under a Creative Commons Attribution-Non Commercial 4.0 International Licence (CC BY-NC).

Under this licence, you may copy and redistribute the material in any medium or format. You may also create and distribute modified versions of the work. This is on the condition that: you credit the author and do not use it, or any derivative works, for a commercial purpose.

When reusing or sharing this work, ensure you make the licence terms clear to others by naming the licence and linking to the licence text. Where a work has been adapted, you should indicate that the work has been changed and describe those changes.

Please seek permission from the copyright holder for uses of this work that are not included in this licence or permitted under UK Copyright Law.'

Abstract

Blood production is attributed to a rare haematopoietic population of cells called haematopoietic stem cells (HSCs). HSCs reside in specialised BM microenvironments, that secrete factors essential for HSC maintenance, quiescence, and survival. In health, HSCs occasionally proliferate to self-renew or differentiate, however during severe infection they are forced out of quiescence and into the cell cycle to replenish downstream haematopoieteic cells consumed during the immune response. Studies showed that due to proliferation-induced stress, the few HSCs that remain become deprived of their functional properties. However, in my opinion, it's impossible for an organism to lose almost completely its functional HSCs. Using the rodent malaria parasite *P. berghei*, I study HSCs' heterogeneous responses by identifying HSC subsets based on the NHS-ester-Biotin labelling system. A short pulse-chase during infection development allowed the identification of cells with limited, Biotin^{Hi}, or faster, Biotin^{Lo}, proliferation kinetics in both SLAM CD48^{neg} and E-SLAM HSC compartments. Chronic EdU administration confirmed that DNA replication correlated with biotin dilution. When functional properties of E-SLAM -Biotin subsets in both control and infected animals were studied, I found that E-SLAM Biotin^{Hi} HSCs purified from infected animals were highly functional, leading to engraftment similar to that of HSCs purified from healthy controls. In contrast, Biotin^{Lo} HSCs engrafted poorly. This was evident in the transcriptional profiles of Biotin^{Hi} "infected" and control HSCs, which carried molecular signatures associated with stemness, unlike that of Biotin^{Lo} HSCs from infected animals. Furthermore, I show that Biotin^{Hi} maintained low reactive oxygen species (ROS), mitochondria membrane potential (MMP) and mitochondrial mass compared to Biotin^{Lo} HSCs purified from infected animals. Relevant to understanding possible niche-dependent regulation of Biotin^{Hi} HSCs I investigated their localisation as well as infection-induced changes in the bone marrow microenvironment. In conclusion, I identified a "reserve" pool of HSCs that maintain stemness even after strong infection.

Acknowledgements

This wonderful journey would not have been possible without my supervisor's trust in me, Prof. Cristina Lo Celso, who allowed me the flexibility to create something that I loved, to fail, to repeat and succeed. Thank you for always keeping an open door for us. I will never forget the late night sort three days before I went in labour. You came and sat next to me while I sorted for sc-RNA experiments. Thank you again for your generosity and wonderful life discussions which I will always carry in my heart.

Secondly, I would like to thank my second supervisor, Dr Tiago Cunha Luis, who introduced me to NHS-Ester Biotin that played a pivotal role to bring my hypothesis to life. You shared tons of knowledge including Flow cytometry, sorting and transplantation and for that, I thank you too.

I would also like to thank Dr Andrew Blackborough, our malaria-savvy collaborator who provided the facility, mosquitos and reagents to create my *P. berghei* P0 stocks. Of course, this would not have been possible without the help of Kasia Sala, who drove the whole process, from phenyhydrazine animal injections to the last drop of P0 blood we collected together. It was fun working with both of you. Thank you!

I would like to thank our collaborators at Cambridge university too. Massive thanks to Professor Bertie Göttgens, Dr Nicola Wilson and Dr Qi Liu for the scientific discussions, brainstorms, sample processing and of course single cell and minibulk RNA sequencing analysis. It was an absolute pleasure to work with you.

A big fat Greek thank you to all passed, Sara Gonzalez Anton, Flora Birch, Myriam Haltalli, Chiara Pirillo and current Lo Celso group members, Cera Mai, Dina Pospori, George Adams, Germaine Chia, Floriane Tissot, Federica Bruno, Marine Secchi, Richard Burt and Samantha Atkinson, some of which I became good friends with. Thank you for gathering around our little coffee machine corner, for the chats and for your positive support during COVID-19 pandemic. Floriane, thank you for holding my hand in those difficult days when I felt hopeless with motherhood and work. Thank you for welcoming me/us in your family, I enjoyed every minute

of our outings with the boys. Federica, I couldn't ask for a better "malaria" successor. You have been a great friend and help too, thank you for all the laughs. Special thanks to Dr Dina Pospori, with whom I share some adventures with, one being Palermo, along with our science discussions. Thank you for everything Dina it was a great pleasure working with you and being your friend. Sara thank you for all the landscape photos you shared with me, art and general topic discussions, for the encouragement and kind words of motivation during Thesis writing. Thank you for the IVM training and microscopy training too.

I would like to thank my students who worked on BM stroma and especially Amaia Ochandorenasaa who helped me analyse all the BM stroma data from afar and during lockdown.

A special thanks to all the facility staff who helped me with various experiments and with whom I interacted on a daily basis. Thank you to Tess Boreham and Dennis Harnett for your support and animal orders and to Edgar, Julian, Andrew, Bruna and George for looking after my animals and ensuring that they are happy. I would like to thank the flow facility staff, Jess Rowley and Larissa Zarate Garcia for all the help with the sorts and FACS. Thank you to Francis Crick BRF staff who looked after my transplanted animals and Flow facility STP for their support.

Big massive thank you to my parents, μαμά και μπαμπά, ευχαριστώ από καρδιάς για τις θυσίες που κάνατε. Μου δώσατε φτερά για να πετάξω έτσι ώστε να εξερευνήσω τον κόσμο χωρίς φόβο, καλούπια, και πρέπει. Έφτασα εδώ με τη δική σας βοήθεια λοιπόν και γι' αυτό αξίζετε ένα τεράστιο ευχαριστώ. Thank you to my wonderful brothers, Panayiotis and Constantinos, with whom I have a BLAST every time I go back to Cyprus. I am the luckiest to have you as my brothers.

Finally, I would like to thank my husband Panayiotis. You have been there throughout this journey encountering my frustration, sadness but lots of happiness and ecstatic moments too. You have been the harbour to return to, the tree that provided me shade, the sea that calmed me down and the sun that gave me the energy to carry on. Thank you for being my life's best

friend and partner. Thank you for helping me (us) raise Stavros without the village, it has been hard and challenging but also sweet and wonderful. Σ'αγαπώ αφάνταστα!

My little angel Stavros, you have felt my stresses, the adrenaline rushes with experiments even before you were born. You came in my life and brought light and happiness. Thank you for waiting for mummy patiently to return home from work. You taught me that life is so beautiful in the simplest of things. Your smile, hugs and laughs filled a tiring day with so much joy and love. Σ'ευχαριστώ καρδία μου!

Contents

Declaration of Originality 5
Copyright Declaration 6
Abstract 7
Contents 11
List of Figures 13
List of Tables 16
Abbreviations 17

Chapter 1 - *Introduction* 23
1.0 – Haematopoiesis 23
1.1 – Heterogeneity in HSC self-renewal 27
1.2 – Heterogeneity in lineage output 28
1.3 – HSC heterogeneity associated with clonal haematopoiesis 29
1.4 – Infection and inflammation-driven changes in HSCs 32
1.5 – Metabolic and epigenetic signatures in HSCs in steady state and disease 37
1.6 – The HSC niche in homeostasis 42

1.6.1 – Different BM stroma cells shape HSC niche 43
1.6.2 – Bone marrow niche changes during stress 47

1.7 – Malaria, a life-threatening disease 51
1.8 – *Plasmodium berghei* parasite as a stressor of haematopoietic compartment 53
1.9 – Project hypothesis and research questions 54

Chapter 2 – *Materials and methods…* 55
2.1 – Animals 55

2.2 – *Plasmodium berghei* experimental model 56
2.2.1 – Counting infected parasites (parasitaemia) 58

2.3 – Flow cytometry 58

2.3.1 – EdU Click-iT 59
2.3.2 – Mitochondrial mass, membrane potential and ROS 59
2.3.3 – Cell cycle analysis 60
2.3.4 – Biotin localisation within BM 60

2.4 – BM stroma staining 61
2.5 – Transplantation assays 63

2.5.1 – Primary transplants 63

2.5.2 – Secondary transplants 65
2.5.3 – Multilineage reconstitution assessment..... 65

2.6 – Single-cell and minibulk RNA sequencing..... 65
2.7 – Bone processing, cryosectioning and immunofluorescence..... 66
2.8 – Microscopy 67

2.8.1 – Confocal microscopy of sections..... 67
2.8.2 – Intravital microscopy..... 67

2.9 – Image processing and quantification..... 68
2.10 – Statistical analysis and reproducibility..... 68
2.11 – Illustrated Figures..... 69

Chapter 3 – *Haematopoietic perturbations during P.berghei infection*..... 73
3.1 – Introduction 73
3.2 – *P. berghei* as a natural infection model to study stress haematopoiesis haematopoiesis 75
3.3 – PTH treatment does not rescue HSC function..... 77
3.4 – Malaria infection severely affects HSC self-renewal..... 81
3.5 – Discussion..... 84

Chapter 4 – *A subset of primitive HSCs maintain their stemness despite IFNγ*..... 86

4.1 – Introduction 86
4.2 – Defining primitive E-SLAM HSCs and MPP subpopulations..... 89
4.3 – Failure in establishing a tetracycline-regulated histone H2B GFP system to mark LRCs during *Plasmodium berghei* infection..... 91
4.4 – NHS- ester biotin as a pulse-chase labelling system to study HSC heterogeneity..... 93
4.5 – Biotin dilution correlates with the proliferation of HSPCs..... 98
4.6 – A. proportion of biotoin E-SLAM HSCs retain their functional properties..... 102
4.7 – Discussion 107

Chapter 5 – The *Biotin^{Hi} HSCs are transcriptionally and metabolically distinct from the Biotin^{Lo}*..... 111

5.1– Introduction 111
5.2 – Deciphering the molecular signatures of CD48^{neg} Biotin HSC subsets during steady state and stress..... 112
5.3 – CD48^{neg} Biotin^{hi} are metabolically less active compared to CD48^{neg} Biotin^{Lo} HSCs during infection..... 122
5.4 – CD48^{neg} and ESLAM Biotin^{Lo} cells exhibit higher ROS during infection 127

5.5 – Discussion..... 129

Chapter 6 – *Searching for biotin HSCs in the BM microenvironment*..... 133

6.1 – Introduction..... 133
6.2 – No preferential bone location for E-SLAM Biotin^{Hi} HSCs during malaria infection..... 135
6.3 – Endogenous α-catulin GFP HSC reporter enables the identification of E-SLAM Biotin^{high} HSCs..... 137
6.4 – *P. berghei* infection causes alternation in the BM stroma 140
6.5 – Severe infection remodels vasculature in central bone marrow areas..... 145
6.6 – Stromal ROS as a possible mechanism of HSC damage 150
6.7 – Discussion..... 153

Chapter 7 – *Summary, conclusions and future directions*..... 156

Bibliography 167
Appendix A – Collaborator methods 187
Appendix B – Bulk RNA sequencing analysis 190
Appendix C – HSC recovery..... 193

List of figures

Chapter 1– Introduction

Figure 1.1 Classical revised HSC differentiation hierarchy..... 26
Figure 1.2 Clonal haematopoiesis..... 30
Figure 1.3 Severe infection induced changes in HSCs..... 34
Figure 1.4 Mitochondria support HSC maintenance and proliferation 41
Figure 1.5 Bone marrow microenvironment and interactions with HSCs..... 50
Figure 1.6 *Plasmodium* life cycle in humans..... 52

Chapter 2– Materials and Methods

Figure 2.1 Experimental model..... 57
Figure 2.2 Gating strategy to define Biotin high and low HSCs..... 59
Figure 2.3 Gating strategy associated with mitochondria health..... 60
Figure 2.4 Gating strategy for BLC and CBM 62
Figure 2.5 Sort gates of E-SLAM Biotin high and low cells..... 64

Chapter 3 – Haematopoietic perturbations during P.berghei infection

Figure 3.1 Malaria infection induction through injection of *P.berghei* infected RBCs..... 76
Figure 3.2 PTH treatment did not rescue HSC function..... 78
Figure 3.3 HSC self-renewal is severely affected during *P. berghei* infection..... 80
Figure 3.4 HSCs display reduced engraftment after severe infection..... 82
Figure 3.5 Lineage^{neg}c-kit^{+} transplant shows reduced HSC self-renewal..... 83

Chapter 4 – *A subset of primitive HSCs maintain their stemness despite INFγ*

Figure 4.1 Phenotypic characterisation of E-SLAM CD48^{neg} HSCs and MPPs..... 90
Figure 4.2 Doxycycline effectively clears the parasite..... 93
Figure 4.3 Biotin labels all haematopoietic cells..... 95
Figure 4.4 NHS-biotin labelling system enables measurement of proliferation kinetics in cells..... 96
Figure 4.5 Biotin^{Hi} and Biotin^{Lo} identified as a result of malaria infection..... 98
Figure 4.6 Proliferation of biotin correlates with DNA replication..... 100
Figure 4.7 Biotin^{Hi} cells are quiescent..... 102
Figure 4.8 Experimental set-up to test reconstitution potential of biotin high and low HSCs..... 103

Figure 4.9 E-SLAM Biotin^{Hi} HSCs display the highest repopulation ability..... 105
Figure 4.10 E-SLAM Biotin^{Hi} maintain their stemness during secondary transplantation..... 107

Chapter 5 – *The Biotin^{Hi} HSCs are transcriptionally and metabolically distinct from the Biotin^{Lo}A subset of primitive HSCs maintain their stemness despite INFγ*

Figure 5.1 Indexed sort values of LKS SLAM CD48^{neg} HSCs..... 114
Figure 5.2 Differentially expressed genes between Biotin^{Hi} control and infected HSCs..... 116
Figure 5.3 Differentially expressed genes between Biotin$^{Hi/Lo}$ in infection..... 118
Figure 5.4 CD48^{neg} Biotin^{Hi} cells have high HSC score regardless of condition..... 121
Figure 5.5 MitoSox as a superoxide ROS indicator..... 123
Figure 5.6 MitoTracker Green as an indicator of mitochondrial mass..... 124
Figure 5.7 TMRM studies MMP in CD48^{neg} , E-SLAM and MPPs..... 126
Figure 5.8 Biotin^{Lo} HSCs have increased ROS compared to Biotin^{Hi} 127
Figure 5.9 NAC treatment abolishes ROS in HSCs..... 128

Chapter 6 –*Searching for Biotin HSCs in the BM microenvironment*

Figure 6.1 Dormant or proliferating HSCs evenly distributed in the BM..... 136
Figure 6.2 Localisation of α-catulin GFP E-SLAM Biotin..... 138
Figure 6.3 α-catulin GFP BM analysis..... 139
Figure 6.4 Loss of osteoblast in infected Col2.3 GFP animals..... 141
Figure 6.5 Osteoblast loss uncovered in bone sections..... 142
Figure 6.6 Endosteal vessel remodelling in severe infection..... 144
Figure 6.7 *P. berghei* impacts CBM ECs and PCs..... 146
Figure 6.8 IVM of LepR$^{+/-}$Cre; Rosa26YFP transgenic reporter mice to confirms the loss of LepR^{+} PCs in malaria..... 147
Figure 6.9 BM stroma cells are lost during severe infection..... 149
Figure 6.10 Assessing ROS in Flk2 GFP calvaria..... 151
Figure 6.11 Quantification of CELLROX signal in the calvaria of mice..... 152

Chapter 7- Summary, Conclusions and future directions

Figure 7.1 Outlined summary of thesis and open questions..... 166

List of tables

TABLE 1| Commonly used phenotypic markers to define HSPC populations and MPPs based on (Pietras *et al.,* 2015; Wilson *et al.,* 2015)…… 24

TABLE 2| Summary of studies describing the contribution of different stresses to HSC biology…… 36

TABLE 3| List of antibodies, chemicals, drugs, reagents, equipment, analysis, software used for the project…… 70

Abbreviations

·OH	hydroxyl radical
1CM	one carbon metabolism
AECS	Arteriolar Endothelial cells
ATP	Adenocine Triphospahte
ATRA	all-*trans* retinoic acid agonist
BM	Bone Marrow
BMD	Bone marrow density
BrDu	5-bromo-2-deoxyuridine
CAR	CXCL12 abundant reticular cells
CBM	Central Bone Marrow
CFU	Colony forming units
cGAMP	Cyclic guanosine adenosine monophosphate
cGAS	cyclic Guanosine adenosine synthase
CH	Clonal Haematopoiesis
CHIP	Clonal Haematopoiesis of Indeterminate potential
CXCL12	CXC-chemokine ligand 12
DAMPs	Damage associated molecular patterns
DC	Dendritic cells
DEG	Differentially expressed genes
dHSCs	Dormant HSCs
DOX	Doxycyclin
Drp1	Dynamin related protein 1
ECS	Error corrected sequencing
ECS	Endothelial Cells
EGFP	Enhanced Green Fluorescent protein

Emcn	Endomucin
EPCR	Endothelial Protein C
ER	endoplasmic reticulum
ETC	Electron Transport Chain
FA	Fanconi Anaemia
FACS	Fluorescent Activated Cell Sorting
FOXO	forkhead box protein O
G-CSF	Granulocyte colony stimulating factor
GPRC5C	G protein-coupled receptor 5
H2B-GFP	histone 2 Green fluorescent protein
H_2O_2	hydrogen peroxide
HSC	Haematopoietic Stem Cell
HSPCs	Haematopoietic Stem and Progenitor Cells
IFN	interferon
IFNα	Interferon α
IFNβ	Interferon β
IFNγ	Interferon γ
IL-1	Interleukin-1
IRGs	Interferon related genes
ISG	IFN stimulated genes
Jag1	Jagged 1
JAK-1	Janus kinase 1
JAK-2	Janus kinase 2
LKS	$Lin^-Sca\text{-}1^+c\text{-}Kit^+$
LPS	Lipolysaccharide
LT-HSCs	Long term HSCs
LTC-IC	Long-term culture-initiating cell assay
MHC II	Major histocompatibility Complex II

mitoDendra 2	Mitochondrion targeted Dendra 2
MkPs	Megakaryocyte progenitor population
MPP	Mitochondrial membrane potential
MPP1	Multipotent progenitor 1
MPP2	Multipotent progenitor 2
MPP3	Multipotent progenitor 3
MPP4	Multipotent progenitor 4
MPPs	Multipotent Progenitors
MSC	Mesenchymal stem cells
Mtb	Mycobacterium Tuberculosis
mtDNA	mitochondrial DNA
MTG	Mito Tracker Green
MTG	Mitotracker Green
MyRP	myeloid-restricted repopulation progenitors
NADH	Nicotinamide adenine dinucleotide (NAD) + hydrogen (H)
NF κB	Nuclear factor-κB
NG2	Neural glial antigen 2
NK	Natural killer cells
NOX	NADPH oxidases
O_2^-	superoxide anion radical
OBPs	Osteoblast precursors
OCPs	Osteoblast progenitors
OXPHOS	Oxidative Phosphorylation
PAMPs	Pathogen-associated molecular patterns
PB	Peripheral Blood
pbi	Post blood injection
PDGFRβ	platelet-derived growth factor receptor-β

PDPN	Podoplanin
pI:pC	polyinosinic:polycytidylic
PINK1	PTEN induced kinase 1
PKA	Pyruvate kinase activity
PRRs	pathogen-recognition receptors
PTH	Parathyroid hormone
Ptn	Pleiotrophin
qHSC	quiescent HSC
RBC	Red Blood Cell
RIG-1	Retinoic-acid-inducible gene 1 (RIG-1)
RLRs	Retinoic acid like receptors (RLRs)
RO	Alkoxyl radical
ROO·	Proxyl radical
ROS	Reactive oxygen Species
sc-RNA	Single cell RNA
sc-RNA sequencing	Sngle cell RNA sequencing
SCF	Stem cell factor
SECS	Sinusoidal endothelial cells
shRNA	Small hairpin RNA
SODs	Superoxide dismutases
ST-HSCs	Short Term HSCs
TCA	Tricarboxylic cycle
TF	Transcription factor
TGF-β	Transforming growth factor β
THPO	Thrombopoietin
TLRs	Toll like receptors
TMRM	Tetramethylrhodamine, methyl ester
TNFα	Tumor necrosis factor

VAF	variant allele fraction
VEGF	Vascular endothelial growth factor
VP	Verapamil
vWf	von Willebrand factor
WGS	Whole Genome Studies
WT	Wild-type

Chapter 1

Introduction

1. Haematopoiesis

The human body consists of multiple systems that are vital to maintain life. Each system encompasses tiny microscopic participants that function in such sophistication and synchrony that reminds me of Mozart's requiem masterpiece. An example of such orchestration is the process of haematopoiesis which takes place in the bone marrow, encased within the skeletal system. Haematopoiesis derives from the Greek word "αίμα"("hema"), blood, and "ποιείν"("peen"), to make, and means exactly as it reads, to make blood (Mpampiniotis, 2012). An important cellular component of this process are haematopoietic stem cells or HSCs. HSCs reside in the bone marrow (BM) as rare cells that sit at the top of the haematopoietic tree, occasionally proliferating to replenish downstream multipotent progenitors (MPPs) and their precursors. Self-renewal and multipotency lay at the heart of HSCs which translated to their ability to proliferate into a daughter cell or differentiate into downstream progenitors committed to generating terminally differentiated blood cells like red blood cells (RBCs), lymphoid (T and B cells) or myeloid cells respectively (Orkin and Zon, 2008; Laurenti and Göttgens, 2018). HSCs need to maintain a fine balance between self-renewal and tuning of cell lineage output programs to preserve normal haematopoiesis and maintain HSC compartment integrity. Multipotent progenitors on the other hand, MPPs, have reduced self-renewal and are highly biased towards cells of certain lineage (Cheng, Zheng and Cheng, 2020).

During unperturbed haematopoiesis, HSC descendants within the multipotent progenitor population will produce differentiated progeny according to the work carried out by both Camargo and Rodewald groups. Using a genetic fate-mapping system based on Cre-loxP-induced recombination of a transgenic barcode cassette, the Rodewald group showed that when barcoded single progenitor clones were labelled at fetal liver stage, their descendants could give rise to myeloid-erythroid and common lymphocyte cell lineages in the adult mouse

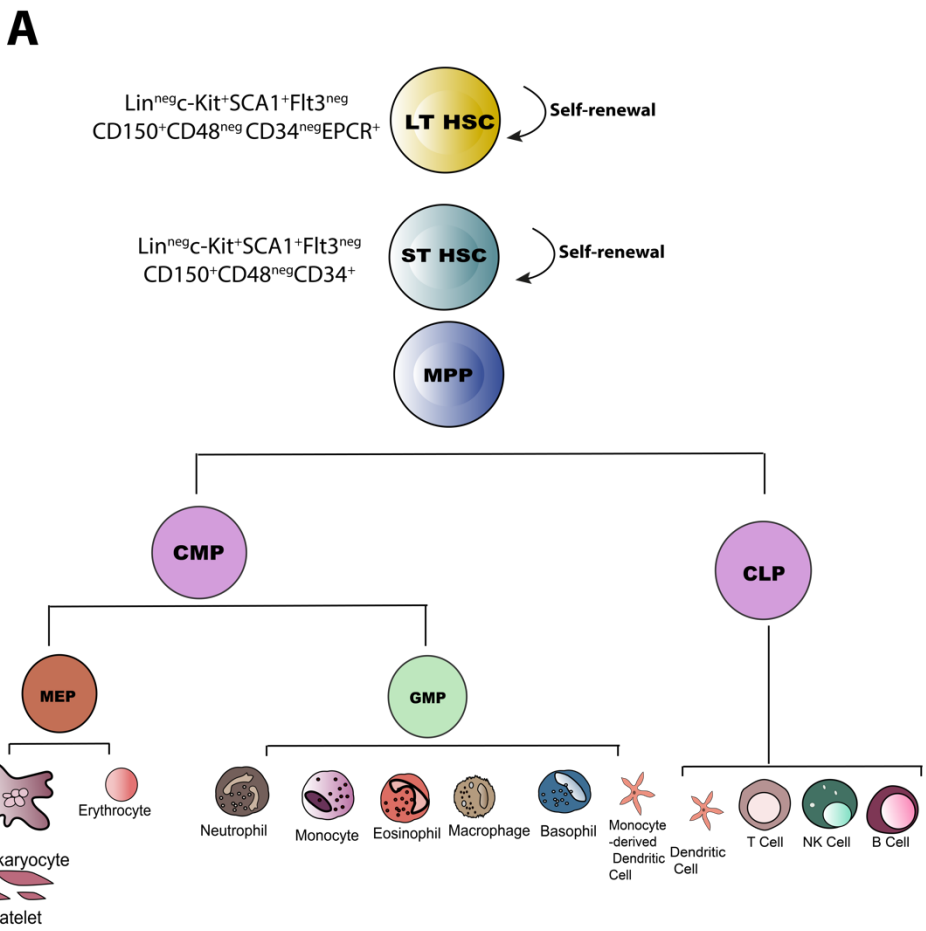
(Pei *et al.*, 2017). Similarly, using the sleeping beauty lineage-tracing model in mice Alejo Fraticelli and colleagues reported that within the multipotent progenitors, lineage-committed MPPs clones produced progeny of erythroid, myeloid, granulocyte and megakaryocyte progenitor cell origin (Rodriguez-Fraticelli *et al.*, 2018).

To gain insights into the world of HSCs at the cellular and molecular level, fluorescence-activated cell sorting (FACS) facilitates the immune-phenotypic enrichment and subsequent purification of transplantable HSCs (Spangrude, Heimfeld and Weissman, 1988). Markers like c-kit, or CD117, Stem cell antigen 1 (Sca1), SLAM (CD150 and CD48), CD34, Flt3 and Endothelial protein C receptor (EPCR) are used to discriminate long (LT-) and short (ST-) term HSCs. LT-HSCs give rise to ST-HSCs and can be immuno-phenotypically distinguished by the lack of CD34 antigen expression. Additionally, LT-HSCs have the capacity to reconstitute the BM of conditioned or lethally irradiated recipient mice for a longer period (>3-4 months) compared to ST-HSCs which are more transient (>1 month but <3-4 months) (Cheng, Zheng and Cheng, 2020). Hence, transplantable LT-HSCs are identified as Lin^{neg} $c\text{-}Kit^{+}$ $SCA1^{+}$ $CD150^{+}$ $Flt3^{neg}$ $CD48^{neg}$ $CD34^{neg}$ $EPCR^{+}$(Table 1) and ST-HSCs as Lin^{neg} $c\text{-}Kit^{+}$ $SCA1^{+}$ $CD150^{+}$ $CD48^{neg}$ $Flt3^{neg}$ $CD34^{+}$. ST-HSCs differentiate into multipotent progenitor cells (MPPs) and published work demonstrated that lineage specification not only occurs higher in the hierarchy but at the MPP level too. For example, MPP2 and MPP3 are myeloid-biased MPP subsets that work together with MPP4, a lymphoid-primed MPP, to control haematopoiesis (Pietras *et al.*, 2015).

Table 1| Commonly used phenotypic markers to define HSPC populations and MPPs based on (Pietras *et al.*, 2015; Wilson *et al.*, 2015)

Species	Name	Cell-surface Phenotype
Mouse	LT-HSC	$Lin^{neg}c\text{-}Kit^{+}SCA1^{+}Flt3^{neg}CD150^{+}CD48^{neg}CD34^{neg}EPCR^{+}$
	ST-HSC	$Lin^{neg}c\text{-}Kit^{+}SCA1^{+}Flt3^{neg}CD150^{+}CD48^{neg}CD34^{+}$
	MPP2	$Lin^{neg}c\text{-}Kit^{+}SCA1^{+}Flt3^{neg}CD150^{+}CD48^{neg}$
	MPP3	$Lin^{neg}c\text{-}Kit^{+}SCA1^{+}Flt3^{neg}CD150^{neg}CD48^{neg}$
	MPP4	$Lin^{neg}c\text{-}Kit^{+}SCA1^{+}Flt3^{+}CD150^{neg}CD48+$

The MPP subset is defined through the expression of Flt3 (also known as Flk2 or CD135) and SLAM markers as indicated in Table 1. Through *in vitro* expansion of transplanted cells (spleen-colony forming units S-CFUs), Pietras E. *et al* demonstrated that while MPP2 contributed to megakaryopoiesis (megakaryocyte production), MPP3 and MPP4 were found biased towards myeloid and lymphoid cell lineages respectively (Pietras *et al.*, 2015). Aside phenotypic characterisation of HSCs and MPPs, endogenous HSC fluorescent reporters (i.e *HOXb5-tri*-mCherry; *α-catulin* GFP(Acar et al., 2015; Chen et al., 2016)), shed light on the HSC heterogeneous behaviour and interactions with other haematopoietic cells and/or the BM niche. A quiescent HSC resides in a glycolytic, autophagy-dependent low metabolic activity state and occasionally self-renews during homeostasis (Ho *et al.*, 2017; Liang *et al.*, 2020; Stergiou and Kapsogeorgou, 2021). As discussed later, when HSCs respond to infection, they flip from “zen” to a proliferative/active mode (Laurenti and Göttgens, 2018; Cheng, Zheng and Cheng, 2020). This mode switch enables them to replenish haematopoiesis where needed.


A
Lin^neg c-Kit^+ SCA1^+ Flt3^neg
CD150^+ CD48^neg CD34^neg EPCR^+
LT HSC
Self-renewal
Lin^neg c-Kit^+ SCA1^+ Flt3^neg
CD150^+ CD48^neg CD34^+
ST HSC
Self-renewal
MPP
CMP
CLP
MEP
GMP
Erythrocyte
Megakaryocyte
Platelet
Neutrophil
Monocyte
Eosinophil
Macrophage
Basophil
Monocyte -derived Dendritic Cell
Dendritic Cell
T Cell
NK Cell
B Cell

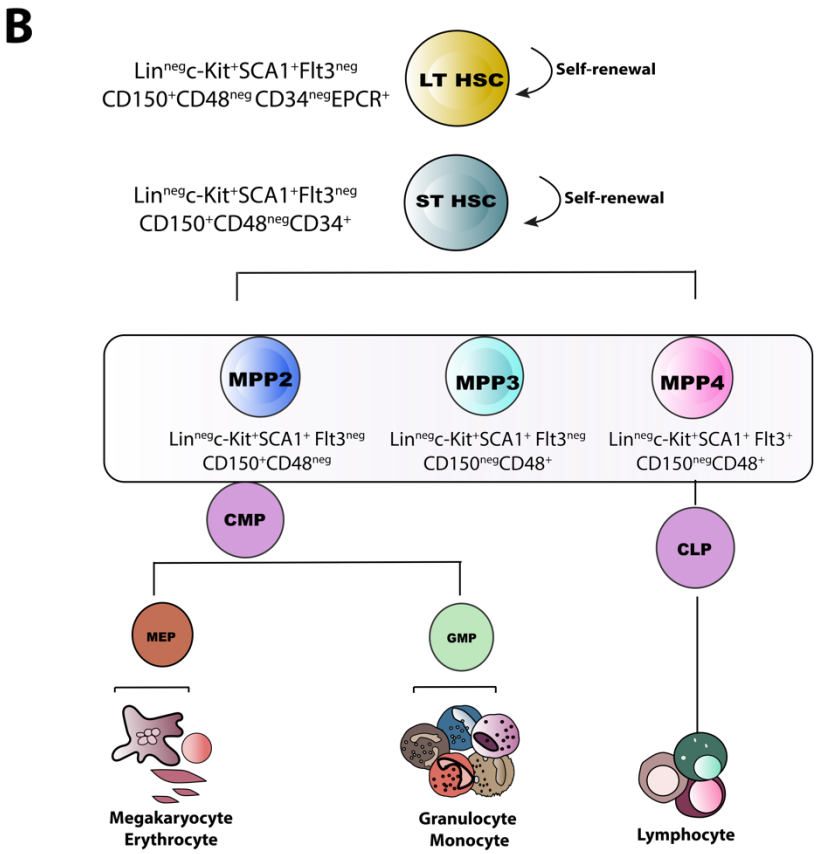

B
Lin^neg c-Kit^+ SCA1^+ Flt3^neg
CD150^+ CD48^neg CD34^neg EPCR^+
LT HSC
Self-renewal
Lin^neg c-Kit^+ SCA1^+ Flt3^neg
CD150^+ CD48^neg CD34^+
ST HSC
Self-renewal
MPP2
Lin^neg c-Kit^+ SCA1^+ Flt3^neg
CD150^+ CD48^neg
MPP3
Lin^neg c-Kit^+ SCA1^+ Flt3^neg
CD150^neg CD48^+
MPP4
Lin^neg c-Kit^+ SCA1^+ Flt3^+
CD150^neg CD48^+
CMP
CLP
MEP
GMP
Megakaryocyte
Erythrocyte
Granulocyte
Monocyte
Lymphocyte

Figure 1. 1. Classical and revised HSC differentiation hierarchy: A) In the classical haematopoeitic tree LT-HSCs sit at the appex of haematopoietic hierarchy where they occasionally proliferate and differentiate into ST-HSCs. ST-HSCs differentiate into MPPs which generate common lymphoid progenitors (CLP) and common myeloid progenitors (CMP). CMP can generate progenitors of megakaryocyte/erythroid (MEP) or Granucolcyte/monocyte (GMP) lineage. In turn MEPs give rise to megakaryocytes, and erythrocytes while GMPs differentiate into myeloid cells such as neutrophils, macrophages, monocytes etc. Lymphoid cells are the progeny of CLPs. The lineage outcome is controlled by cytokines and it varies depending on the disease or stress condition. B) Revised haematopoietic roadmap depicting that haematopoiesis is not a stepwise process and that LT-HSCs, ST-HSCs are all multipotent but differ in their self-renewal ability. HSCs differentiate into MPPs consisting of MMP2, MPP3 and MPP4. MPP2 and MPP3 give rise to CMPs that generate MEP and GMP respectively. MPP4 generates CLP. Inspired from (Zhang *et al.*, 2018)

1.1 Heterogeneity in HSC self-renewal

Historically, HSCs have been conceptualised to be a homogeneous population that undergo lineage commitment in a stepwise manner (Figure 1.1 A). The introduction of cell surface markers in combination with single-cell functional assays and transcriptomic analysis highlighted HSC differentiation as a continuum. In the past decade, a plethora of studies revealed that the HSC pool is more heterogeneous both in terms of self-renewal and multipotency. As a result, a combination of different factors possibly shapes HSC heterogeneity. Whether the underlying causes are attributed to stochastic, random distribution of molecules after mitosis, or deriving from cell-intrinsic or cell-extrinsic signals from BM environmental niche has been a subject of debate(Laurenti and Göttgens, 2018; Cheng, Zheng and Cheng, 2020). Genomic advances coupled with transgenic mouse models and single-cell transplantations shed light on HSC heterogeneity (Laurenti and Göttgens, 2018; Cheng, Zheng and Cheng, 2020). To put things in perspective, the field has accepted that for a LT-HSC, dormant (dHSC), or quiescent (qHSC) HSC to be considered a true HSC, both in mouse and humans, it needs to repopulate conditioned recipients' BM and sustain haematopoiesis for more than 16 weeks in a primary transplant and then secondary (at least) or tertiary set ups (Laurenti and Göttgens, 2018). When such multipotency occurs long-term, it is usually interpreted as the original HSC having the capacity to self-renew. Other studies showed variability in HSC reconstitution and progenitor kinetics (Dykstra *et al.*, 2007; Yamamoto *et al.*, 2013; Lauridsen *et al.*, 2018). Similarly, single-cell RNA (sc-RNA) sequencing of different HSC populations provided a dynamic range of genes involved in either cell cycle status or proliferation (Wilson *et al.*, 2015; Lauridsen *et al.*, 2018). It is apparent that HSC fate decisions have been correlated with the time that LT-HSCs spend in cell cycle stages. Label-

retaining studies using either 5-bromo-2-deoxyuridine (BrdU)-labelled cells or transgenic mice that expressed the doxy-regulated fusion protein histone 2B - green fluorescent protein (H2B-GFP), revealed that dormant HSCs (dHSCs) retained the label over multiple months displaying the longest repopulation capacity (Wilson et al., 2008; Bernitz et al., 2016). This indicated that heterogeneity is caused by the ability of HSCs to variably engage between cellular processes (Cheng, Zheng and Cheng, 2020). Furthermore, regulation of cycling within the HSC pool differs based on the CDK6 levels between ST-HSCs and qHSCs (the lower levels of CDK6 the higher dormancy) thus determining the kinetics of quiescence exit (Laurenti et al., 2015). Dormancy is also associated with low levels of protein synthesis (Ito *et al.*, 2016; Vannini *et al.*, 2016), MYC activity, an increase in transcriptional (Liu *et al.*, 2009; Bondar and Medzhitov, 2010; Insinga *et al.*, 2013), translation and biosynthetic activity (Norddahl et al., 2011; Reid, Dai and Locasale, 2017; Haas, Trumpp and Milsom, 2018; Papa, Djedaini and Hoffman, 2019; Hinge et al., 2020; Lu et al., 2022; Mortensen et al., 2022). Regulation of dormancy depends on hyaluronic acid, a BM extracellular matrix (ECM) component, which activates GPRC5C signalling (Zhang *et al.*, 2022). Cabezas and colleagues reported that retinoic acid signalling (RA) was highly enriched in dHSCs compared to active HSCs (aHSCs) (Cabezas-Wallscheid *et al.*, 2017). Gprc5c-EGFP mice, which express EGFP under the control of the orphan G protein-coupled receptor expressing *Gprc5c* gene promoter, were enriched in dHSCs. Furthermore, treatment of Gprc5c-EGFP HSPCs *ex vivo* with the RA agonist (all-*trans* retinoic acid (ATRA)) showed higher retention of GFP suggesting that the RA agonist induced cell cycle arrest and inhibited HSPC proliferation after being exposed to inflammatory stress (Cabezas-Wallscheid *et al.*, 2017).

1.2 Heterogeneity in lineage output

Combined approaches robustly showed that within the cellular pool, HSCs and MPPs display distinct differentiation behaviours. By using limiting-dilution analysis and single-cell transplantations, multiple groups have shown that HSCs display certain “biases” towards the dynamic production of myeloid, lymphoid, megakaryocytic outputs (Figure 1.1 B). Müller-Sieburg described HSCs (My-bi HSCs) to differentiate restrictively towards myeloid progenitors hence having a myeloid bias (My-HSCs) (Muller-Sieburg *et al.*, 2004). The Jacobsen group provided evidence that a proportion of LT-HSCs express von Willebrand factor (vWf^{+}) and had

a platelet-restricted fate (Carrelha *et al.*, 2018). The existence of lineage-biases in HSCs has also been reported in barcoding lineage tracing analysis and mRNA profiling by the Camargo group, where HSCs behaved as a potent source of MPP2, primed to a megakaryocyte output (Rodriguez-Fraticelli *et al.*, 2018; Rodriguez-Fraticelli *et al.,* 2020). Large-scale clonal analysis undertaken by Yamamoto *et al.* reported that not only HSC composition changes with age, but also single cell transplants of HSC clones revealed myeloid-restricted repopulation progenitors (MyRPs) from myeloid-biased LT-HSCs (Yamamoto *et al.*, 2018). Similarly, the dynamic changes in the haematopoietic output of single HSCs were studied in serial a transplantation setting discerning four patterns of long-term repopulation; the behaviour of two cell types showed a strong propensity of myeloid and lymphoid cell outputs and robust self-renewal-activity proposing that these patterns were intrinsically predefined in the cells before transplantation (Dykstra *et al.*, 2007).

Taken together, these and other studies have transformed our perception of how HSCs commit to certain lineages and sustain blood production to meet haematopoietic demand (Haas, Trumpp and Milsom, 2018).

1.3 HSC Heterogeneity associated with Clonal Haematopoiesis

Hundreds of millions of cells are produced daily for haematopoiesis to be maintained. Even though HSCs occasionally switch on their cellular machinery to proliferate and maintain blood production; they will naturally acquire a somatic mutation as a function of time (Lee-Six *et al.*, 2018; Jaiswal and Ebert, 2019; Beneyto-Calabuig *et al.*, 2023). Because of this, somatic mutations, particularly observed in aged individuals, enable a fitness advantage to the cell, referred to as the "clone", and its progeny to expand. This is known as "clonal haematopoiesis" (CH). The somatic mutations are caused by the inability of DNA machinery to repair insertion or deletion errors during homologous recombination or more specifically 5-methylcytosine residue deamination to thymine (Jan, Ebert and Jaiswal, 2017; Jaiswal and Ebert, 2019; Alagpulinsa *et al.*, 2022). Lee-Six *et al*. estimated that about 50,000-200,000 HSCs contribute to unperturbed human haematopoiesis (Lee-Six *et al.*, 2018). Given this number, if each HSC acquires one exonic mutation every decade of life, by the age of 70, an average person will

carry 1.4 million protein-coding variants relating to 70 mutations per gene per clone (Jaiswal and Ebert, 2019). Somatic mutations were first uncovered in whole genome studies (WGS) using peripheral blood (PB) DNA from humans, in which haematopoietic cells were shown to derive from a small number of expanded clones in the absence of haematological implications (Steensma, 2018; Florez *et al.*, 2022). To expand our understanding of CH, Steensma D. *et.al.,* utilised a highly sensitive error-corrected sequencing (ECS) approach that enabled the detection of rare variant allele fractions (VAF) at a much lower rate (<2%) than previously reported (>2%)(Young *et al.*, 2016; Steensma, 2018; Jaiswal and Ebert, 2019; Florez *et al.*, 2022).

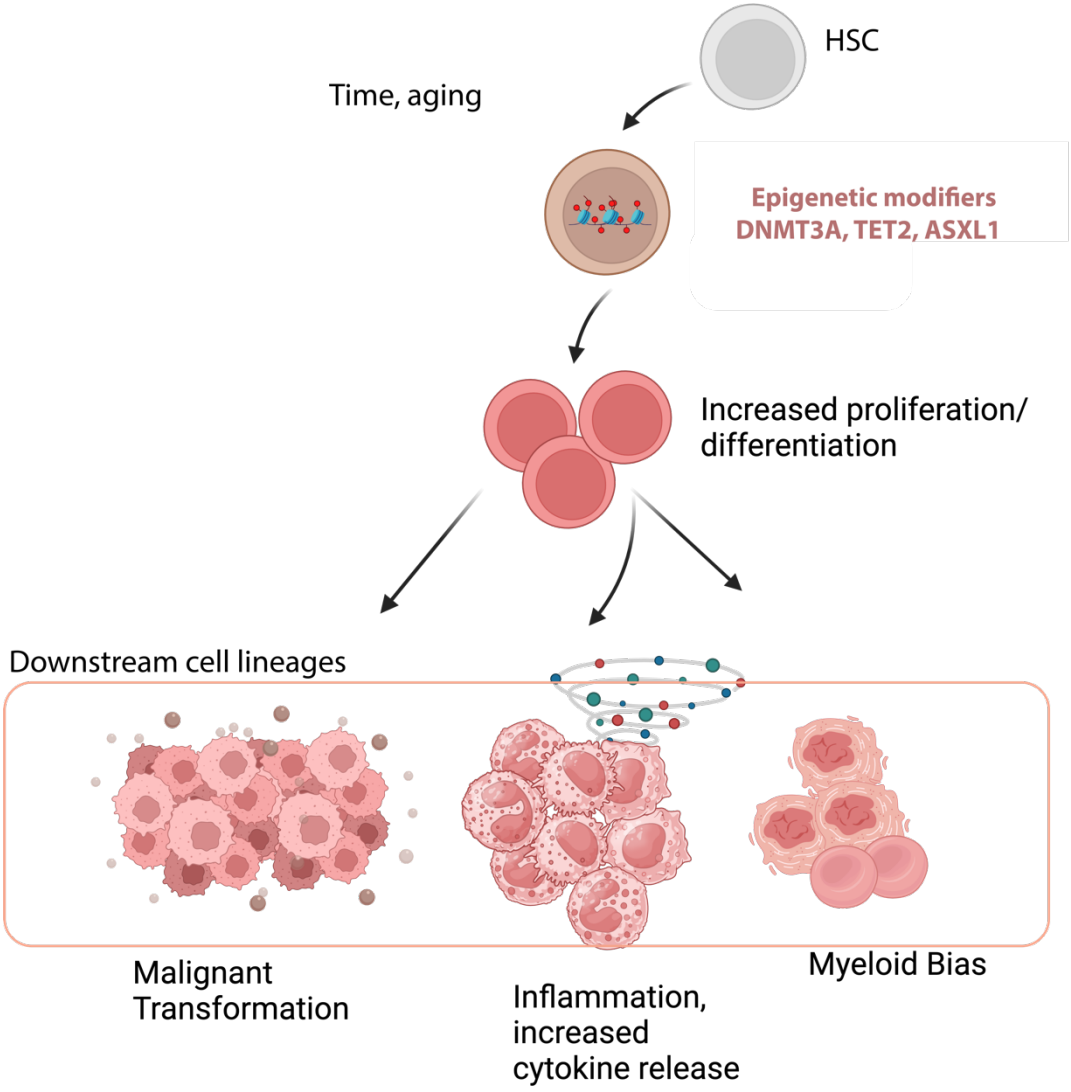


Figure 1. 2 Clonal Haematopoiesis During our life HSCs will acquire somatic mutations that will facilitate expansion of a single HSC clone due to its fitness advantage over other HSC clones. This process termed clonal haematopoiesis is different from malignant clonal haematopoiesis known as Clonal haematopoiesis of Indeterminate potential (CHIP). Ageing, severe infection drive mutations in HSCs and haematopoietic cells associated with epigenetic modifiers such as *Dnmt3a, Tet2* and *ASXL1* genes.

HSCs exhibit transcriptional oscillations that drive lineage commitment, a process known as transcriptional priming (Izzo *et al.*, 2020), leading to HSC transcriptional heterogeneity possibly determined, at a clonal level, epigenetically (Yu *et al.*, 2016). Mutations commonly identified in individuals with haematological malignancies and CH are associated with mutations in genes involved in DNA methylation such as *TET2, DNMT3A, ASXL1* (Figure 1.2). Druley and colleagues reported that in unperturbed haematopoiesis, mutations in *DNMT3A and TET2* genes occur in both myeloid and lymphoid progenitors and that longitudinally these mutations were stable (Young *et al.,* 2016). Deletion of *DNMT3A*, a *de novo* CpG methyltransferase, and *TET2*, essential of CpG demethylation, led to methylation changes subsequently impacting HSC expansion and skewing of certain lineages concordant with transcriptional priming (Izzo *et al.*, 2020). Ostrander E. and colleagues showed that loss of Dnmt3a or Tet2 in conditional knockout mice led to unlimited self-renewal and exhaustion of HSCs, respectively (Ostrander *et al.*, 2020). Furthermore, a human germline mosaic DNMT3A, evolved polyclonally and dominated PB maintaining a conserved methylation pattern (Tovy *et al.*, 2020). The selective clonal advantage of mutated HSC clones was shown in animals carrying an inducible mutant allele found in humans, *Dnmt3a*^{R878H}. Upon exposure to pI:pC, Dnmt3a$^{R878H/1}$ HSCs showed resistance to cytokine stimulation consequently preserving their molecular self-renewal programs thus conferring a sustained functional competitive advantage in transplantations (Tovy *et al.*, 2020; SanMiguel *et al.*, 2022). Interestingly, in patients with Fanconi anaemia (DNA-instability disorder caused by biallelic germline mutations in one of the 22 FANC genes), CH has been solely caused by chromosomal rearrangements, rather than TET2 or DNMT3A mutations, and still led to a pre-leukemic haematopoiesis (Sebert *et al.*, 2023). Lastly, HSC Dnmt3a mutant clones outcompeted wild-type (WT) murine cells in response to INFγ after *Mycobacterium avium* infection; an observation supported by DNA methylation silencing of differentiation programs in Dnmt3a mutant HSCs (Hormaechea-Agulla *et al*., 2021).

1.4 Infection and inflammation-driven changes in HSCs

So far, I have outlined the heterogeneity within the HSC compartment during health and the clonal evolution of certain HSCs acquiring mutations. Somatic mutations occurring in these clones promote their fitness enabling them to self-renew or acquire a bias towards a certain lineage. Considering the above, several questions arise: what are the effects of infection upon HSCs, what are the changes associated with their cellular, molecular and metabolic properties and how HSCs recover from stress?

Humans, like any other mammal, have the urge to protect themselves from danger. Similarly, LT-HSCs, have a stress response machinery expressing a variety of cytokines and pathogen-recognition receptors (PRRs). PRRs include Toll-like receptors (TLRs), retinoic-acid-inducible gene 1 (RIG-1) like receptors (RLRs), cyclic guanosine adenosine monophosphate (cGAMP) and cyclic guanosine adenosine synthase (cGAS) (Pascutti, Erkelens and Nolte, 2016). PRRs detect damage- and pathogen-associated molecular patterns (DAMPs, PAMPs). HSC activation is triggered via a cascade of downstream signalling events due to the inflammatory *milieú* released by immune cells. HSCs respond to signals associated with interferons (INFs)(Essers et al., 2009; Baldridge et al., 2010; Haas et al., 2015; Haltalli et al., 2020), tumor necrosis factor-alpha (TNFα) (Yamashita and Passegué, 2019; Willemsen *et al.*, 2021), G-CSF(Wilson *et al.*, 2008b; Hérault *et al.*, 2017), TLR ligands(Choi *et al.*, 2011a), and transforming growth factor β (TGF-β) (Challen et al., 2010; Zhang et al., 2016). According to their type, Type I INFs (IFNα, IFNβ) or Type II INF (IFNγ) (Naik *et al.*, 2018; Demerdash *et al.*, 2021; Yang and de Haan, 2021), can impact a variety of cellular processes. Once produced and secreted by immune cells, IFNs bind their receptor (type I IFN receptor- IFNAR) initiating upregulation of IFN-stimulated genes (ISGs). Several ISGs were previously found to contribute towards host immunity by inducing antiviral response whereas other ISGs were found to trigger inflammation, transcription and signalling (Lee and Ashkar, 2018). Wu and colleagues reported that stem cells can protect themselves from viral infection as they are hardwired to express antiviral ISGs (Wu *et al.*, 2018). Interferon tolerance and subsequent maintenance of HSC quiescence was shown by Xia P. *et al* through a circular RNA antagonist for cGAS (cia-cGAS) expressed in the nucleus of LT-HSCs, cia-cGAS bound to cGAS with high affinity protecting LT-HSCs from exhaustion (Xia *et al.*, 2018). Animals deficient in cia-cGAS displayed elevated expression of type I IFNs in BM

leading to reduced LT-HSCs numbers (Xia *et al.*, 2018). Chronic activation of HSCs with IFNα led to their exhaustion and functional impairment (Essers *et al.*, 2009). Type I IFNs instruct quiescent stem-like megakaryocyte committed progenitor population (SL-MkPs), into cell cycle to regenerate the lost platelet pool (Haas et al., 2015). In contrast, type II IFN is predominantly produced by NK cells during infection. IFNγ signals through IFNγ receptor (IFNGR) ligation, leading to JAK1 and JAK2 activation which results in STAT1 homodimerisation and phosphorylation(Lee and Ashkar, 2018). As a response to 5-fluorouracil (5-FU), HSCs deficient in JAK1 were shown to have decreased competitiveness, a failure to enter cell cycle and a reduction in cytokine sensing marking their incapability to equilibrate haematopoiesis (Kleppe *et al.*, 2017). *Mycobacterium avium,* a bacterial infection known to produce a chronic systemic IFNγ-mediated immune response, promoted HSC proliferation affecting their cycling and function (Baldridge et al., 2010). A possible mechanism by which HSCs are depleted due to IFNγ signalling is through *Batf2,* an IFNγ responsive transcription factor (TF) that acts upon HSCs limiting their differentiation towards myeloid cells (Matatall et al., 2016). Also, IFNγ was shown to affect HSC stromal surroundings. Haltalli M. and colleagues revealed that during malaria infection with *Plasmodium berghei* parasite, IFNγ not only caused HSC proliferation that subsequently led to HSC exhaustion and functional decline, but it also affected components of the HSC niche (Haltalli *et al.*, 2020). Osteolineage cells loss and leaky vessels were the hallmark consequences of high INFγ levels due to malaria infection (Haltalli *et al.*, 2020). Similarly, Florez M. *et al.* reported that upon IFNγ stimulation, HSCs were displaced from the niche, and that this was mediated by BST2, an IFNγ-induced protein found on HSCs (Florez et al., 2020). Inhibition of IFNγ activity led to improved HSC transplantation (Lobo de Figueiredo-Pontes *et al.*, 2021) (Figure 1.3, Table 3).

As mentioned, different types of endogenous and exogenous factors, ranging from pathogens to ageing, activate host innate immunity to respond to either local or systemic inflammation. HSCs respond to the insult by tuning on their metabolism and cell-cycle machinery, mobilising into the circulation and differentiating to replenish blood lineages. For example, a model of polymicrobial sepsis, the cecal content from an animal is intraperitoneally injected to other animals, induced a repertoire of inflammatory cytokines and factors (IL-1, IL-6, IL-23, IL-27, myeloid growth factors (GM-CSF), TNF-α and IFNs) that associated with enhanced myelopoiesis without increasing HSC input, pinpointing MPPs as a key source for myeloid cell

replenishment (Fanti *et al.*, 2023). Yamashita *et al.* showed that during chronic inflammation, TNF-α acted directly on HSCs to maintain NFκB activity, protecting HSCs from necroptosis and driving myeloid priming (Yamashita and Passegué, 2019; Belenguer *et al.*, 2021). TNF signalling genes were enriched in granulocyte-monocyte progenitors (GNPs) of patients with multiple sclerosis (MS), which was linked to increased priming of HSCs towards the myeloid lineage (Shi *et al.*, 2022). Moreover, work from Choi *et al.* demonstrated that during *Mycobacterium tuberculosis* (Mtb), secretion of TNF-α and IL-6 leads to haematopoietic progenitor cell expansion suggesting that their association with TLR signalling may contribute to HSC proliferation during Mtb (Choi *et al.*, 2011).

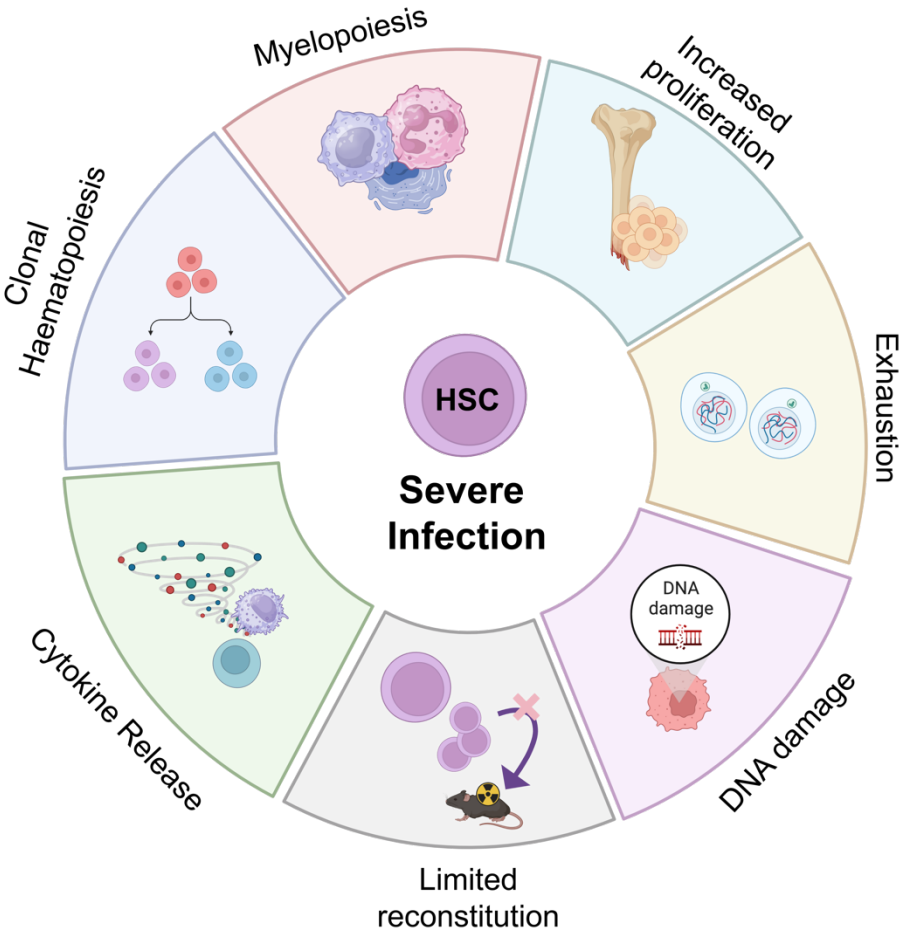


Figure 1. 3 Severe infection induced changes in HSCs Severe infection and ageing models have shown to be associated with a cytokine storm driving increased HSC proliferation for the replenishment of terminally differentiated myeloid cells. Excess proliferation leads to HSC exhaustion. Exhausted HSCs tend to engraft and reconstitute haematopoiesis poorly in lethally irradiated recipients.

Haojian Zhang and colleagues through small hairpin RNA (shRNA) identified a hyperactive TGF-β signalling in HSPCs mediating BM failure in Fanconi anaemia (FA) that, when inhibited, rescued HSPCs from stress-induced DNA damage (Zhang et al., 2016). During continuous inflammatory stress with *pI:pC*, a toll-like receptor 3 agonist, LT-HSCs were shown to progressively compromise their functional potency, leading to accelerated haematologic aging (Bogeska *et al.*, 2022). It is prominent that chronic exposure to cytokine insults impairs HSC self-renewal leading to differentiation of HSCs to promote myelopoiesis (Yang and de Haan, 2021).

All these data point towards a myriad of proinflammatory mediators that have an impact on HSC biology. Without inflammation, our bodies are unable to initiate the healing processes and defence mechanisms. Extremes like chronic inflammation lead to detrimental effects on both HSCs and the BM niche (Pascutti, Erkelens and Nolte, 2016; Lee and Ashkar, 2018; Hormaechea-Agulla, Le and King, 2020; Wilkinson, Igarashi and Nakauchi, 2020; Demerdash *et al.*, 2021; Colom Díaz, Mistry and Trowbridge, 2023).

Table 3| Summary of studies describing the contribution of different stresses to HSC biology.

Insult	Effect on HSCs	Molecular Mechanism	Reference
Plasmodium Berghei	Reduced repopulation potential of HSPCs	PTH and NAC combined to rescue osteoblasts and scavenge ROS achieve partial rescue of HSC	(Haltalli *et al.*, 2020) *Nature Cell Biology*
pI:pC	HSC attrition and phenotype associated with ageing	Assessment of polar distribution of H4K16ac and DNA methylome clock to predict biological age of purified LT-HSCs	(Bogeska *et al*., 2022) Cell Stem Cell
TNF-α induction	TNF-α exposure limited HSCs' engraftment potential.	p65-NF-kB protects HSCs from TNF-α chronic exposure, prevents necroptosis and pushes HSCs towards myeloid differentiation. Cycling HSCs with deactivated NF-kB display the lowest regeneration potential	(Yamashita and Passegué, 2019)*Cell Stem Cell*
Vesicular stomatitis virus (VSV) and murine cytomegalovirus (MCMV)	System virus infection impairs HSC function and reconstitution ability	Inflammatory *milieu* present during non acute MCMV infection contributes to changes in gene expression profiles in HSCs, i.e interferon stimulated genes (ISGs)	(Hirche *et al*., 2017)*Cell Reports*
Chronic IL-1 exposure	IL1 impairs HSC function	IL-1 exposure triggers acceleration in HSC differentiation towards myeloid lineages through PU.1 activation	(Pietras *et al.*, 2016)*Nature Cell Bioloy*
Mycobacterium Avium	HSC self-renewal defect	Myeloid differentiation driven by INFγ transcription factor Batf2 as a mechanism of HSC loss	(Matatall *et al.*, 2016)*Cell Reports*
pI:pC	HSC attrition after repeated activation of HSCs	Inactivation of Fanconi anaemia DNA repair pathway leads to compromised HSC genomic integrity	(Walter *et al.*, 2015) *Nature*
Mycobacterium Avium	HSC functional reconstitution impairment	IFNγ as a regulator of HSC proliferation	(Baldridge *et al.*, 2010) *Nature*
pI:pC	INFα treatment leads to increase HSC proliferation. INFα compromises HSC function	IFNα binds to and activates IFNR leading to STAT1 and PKB phosphorylation	(Essers *et al.*, 2009) *Nature*

1.5 Metabolic and epigenetic signatures in HSCs in steady state and disease

Cell intrinsic damage accumulated during inflammation as well as cell-extrinsic changes in the BM niche lead to HSC attrition (Haltalli *et al*., 2020; Hinge *et al*., 2020; Filippi, 2021). To conquer stress-induced damage, HSCs rely on their metabolic cues to secure their quiescent status and to facilitate activation and entry into cell cycle to replenish blood cells (Sommerkamp and Trumpp, 2016). Mitochondria are biosynthetic and signalling organelles crucial to HSC cellular metabolism. Generally, mitochondria serve as the "power hubs" in cells by generating adenosine triphosphate (ATP) via oxidative phosphorylation (OXPHOS) and sustained electron transport chain (ETC) (Chakrabarty and Chandel, 2021; Fernández-Vizarra *et al.*, 2022). Their functions are not strictly limited to ATP production but rather participate in several metabolic pathways such as tricarboxylic (TCA) cycle, fatty acid oxidation (FAO) and the one-carbon metabolism (1CM) to generate metabolites that will potentially act as signals for post-translational modifications (Zhang, Menzies and Auwerx, 2018). Glucose, fatty acids and glutamine feed into the TCA cycle to generate metabolites such as citrate and oxaloacetate and reducing equivalents of NADH and $FADH_2$ (Zhang, Menzies and Auwerx, 2018; Chakrabarty and Chandel, 2021). Metabolites are utilised for the synthesis of macromolecules like lipids, nucleotides and products for histone acetylation (Figure 1.4). Aside their importance in cellular metabolism, mitochondria are involved in calcium homeostasis, inflammation, cell death and regulation of intracellular signalling (Papa, Djedaini and Hoffman, 2019).

Recent studies brought to light the ability of mitochondria to shape and dynamically determine HSC fate decisions and function. Changes in mitochondrial function lead to alterations in transcription that are deterministic for HSC fate. Reactive oxygen species (ROS), a by-product of OxPHOS, impact mitochondrial functions in HSCs. Elevated levels of ROS lead to oxidative stress (Sies and Jones, 2020). Before reviewing the latest studies about how ROS impact mitochondrial changes in HSCs due to oxidative stress it is worthwhile defining ROS. As the name implies, ROS refer to an array of derivatives of molecular oxygen formed by reduction-oxidation (redox) reactions or by electron excitation (Murphy, 2009). ROS can be divided into non-radical and free radical. Well-known examples of non-radical ROS are hydrogen peroxide (H_2O_2) and organic hydroperoxides (ROOH). In contrast, free radical ROS

include superoxide anion radical (O_2^-), hydroxyl radical ($^{\cdot}OH$), peroxyl radical ($ROO^{\cdot}$) and alkoxyl radical (RO) (Sies and Jones, 2020). Transmembrane NADPH oxidases (NOXs) are the major endogenous enzymatic sources of O_2^- and H_2O_2. In the ETC, O_2^- /H_2O_2 are released by complex I and part complex II toward the mitochondria matrix, whereas complex III releases O_2^- /H_2O_2 towards the *cristae* lumen and intermediate space of mitochondrion (Figure 1.4). H_2O_2 is also generated by several oxidases localised in the endoplasmic reticulum (ER), peroxisomes as well as superoxide dismutases (SOD1-SOD3) (Wong *et al.*, 2017; Sies and Jones, 2020). Other studies highlighted mitochondrial plasticity and its importance in controlling the maintenance and self-renewal of HSCs. ROS are by-products of mitochondrial respiration and while they are critical for activation of signal transduction (Picard and Shirihai, 2022), excess production of ROS can lead to detrimental effects on the HSCs and their mitochondria. Impairment of mitochondrial activity due to oxidative stress leads to limited differentiation capacity and HSC exhaustion (Papa, Djedaini and Hoffman, 2019). Increased levels of ROS not only limited HSC lifespan but also inhibited their repopulating capacity (Ito et al., 2006). Similarly, increased ROS contributed towards cell cycle progression and proliferation (Kirova *et al.*, 2022). A family of transcription factors, forkhead box protein O (FOXO), activate the expression of antioxidant genes to balance ROS levels. Specifically, the loss of FOXO3 led to the accumulation of oxidative damage in HSPCs that contributed to stem cell ageing (Bigarella *et al.*, 2017). To assess mitochondrial mass in HSCs, Mito Tracker (MTG) dyes have been utilised by many in the field. HSCs possess efflux pumps that extrude MTG upon staining. Using verapamil (VP) to block efflux pumps, de Almeida M. and colleagues revealed that MTG fluorescence was higher in HSCs compared to downstream progenitors and associated with higher mitochondrial DNA (mtDNA). The mitochondrion-targeted Dendra2 (mitoDendra2) transgenic mouse expressing an EGFP fluorescent protein, used to thoroughly assess mitochondrial mass in HSCs, indicated that HSC with higher mito-Dendra2 fluorescent signal possess long-term repopulation activity (de Almeida et al., 2017). Moreover, Takihara Y. *et al.* showed that mito-Dendra2^{hi} HSCs, have larger mitochondria and low ECT activity suggesting that mitochondrial mass is coupled with HSC quiescence and reconstitution capacity (Ansó *et al.*, 2017; Takihara *et al.*, 2019). Other subsequent studies revealed that dHSCs are maintained in low metabolic activity (Vannini *et al.*, 2016b), low ROS (Haltalli et al., 2020), low membrane potential (Umemoto *et al.*, 2018) and low glycolysis (Ito et al., 2006; Takubo et al., 2010; Takihara et al., 2019; Hinge et al., 2020; Liang et al., 2020).

The dynamics and morphology of mitochondria in HSCs rely on antagonistic and balanced activities that assist mitochondria to fuse into a connected work (fusion) or divide into smaller units (fission). The fusion/fission machinery is needed to maintain mitochondrial homeostasis and the symmetric inheritance of mitochondria in daughter cells(Papa, Djedaini and Hoffman, 2019a). Impaired distribution of Drp1 (dynamin-related protein 1) during replicative stress, a regulator of mitochondrial fragmentation (fission), caused mitochondria to aggregate into a compact and polarised network in HSCs (Hinge *et al.*, 2020). Replicative stress, such as that induced by BM transplantation, led to inheritance of damaged mitochondria by daughter HSCs, and a transcriptional signature that failed to upregulate genes associated with metabolic and biosynthetic programs (Hinge *et al.*, 2020). This finding points towards the importance of mitochondria fission to maintain mitochondria morphology, which is coupled with HSC regeneration potential (Chakrabarty and Chandel, 2021).

Lysosomes are dynamic organelles that degrade and clear mitochondria through mitophagy (Luzio, Pryor and Bright, 2007; Deus *et al.*, 2020), and have been associated with low-mitochondrial membrane potential (MMP) HSCs (MPP-low). Liang *et al.* reported that MMP-low HSCs were enriched in large lysosomes and by restraining lysosomal activity, HSCs maintained their quiescence (Liang *et al.*, 2020c; Dong *et al.*, 2021). Equally important is mitophagy, the process of removing dysfunctional mitochondria through autophagy (Palikaras, Lionaki and Tavernarakis, 2018). The PINK1/PARK2 pathway is involved in mitochondria degradation thus clearing dysfunctional mitochondria and controlling oxidative metabolism. Ho T. and colleagues demonstrated that autophagy supressed HSC metabolism through the clearance of active mitochondria, maintaining HSC quiescence and stemness (Ho *et al.*, 2017). Similarly, chemical uncoupling of the ETC resulted in the reduction of mitochondrial mass by autophagy thus impacting HSC self-renewal (Vannini *et al.*, 2016). Moreover, Ito *et.al.,* showed that fatty acid oxidation favours the expansion of $Tie2^{+}$ HSCs through the recruitment of Parkin, indicating that mitophagy is a key component of HSC self-renewal (Ito *et al.*, 2016). Furthermore, the LKS ($Lin^{-}Sca\text{-}1^{+}c\text{-}Kit^{+}$) compartment in *Atg7*-deficient animals *(Atg7* is an autophagy gene), displayed high ROS, accumulation of mitochondria, increased proliferation and DNA damage, resulting in a functional decline and failure to reconstitute the haematopoietic system (Mortensen *et al.*, 2011).

Nucleosomes represents the basic unit of chromatin allowing 147base pairs (bp) of DNA to be compactly wrapped around four different histone proteins, H2A, H2B, H3 and H4. Physical interaction of histones with DNA is facilitated through chemical modifications such as methylation, acetylation, phosphorylation, hydroxylation, glycosylation, glycation and so forth (Dai, Ramesh and Locasale, 2020). Transposase accessible chromatin sequencing (ATAC-seq) combined with single and bulk RNA seq on human HSCs and HSPCs by Takayama N. and colleagues, revealed that activated HSPCs (Act/HSPCs) are enriched for binding sites for CTCF, a 3D genome organisation mediator, thus discriminating activated HSCs from LT-HSCs (Takayama *et al.*, 2021). Various TCA metabolites can diffuse through the plasma and nuclear membranes to be utilised as substrates or cofactors for epigenome-modifying enzymes that regulate chromatin modifications. Histone acetylation for example is catalysed by histone acetyltransferase (HATs) and requires citrate-derived acetyl-CoA (Ac-CoA) as the substrate. During glycolysis, glucose is converted into pyruvate which is then reduced into lactate. HSCs utilised glycolysis especially when entering the cell cycle, however excess levels of glycolysis correlate with high pyruvate kinase activity (PKA). PKA dependents on hypoxia-induced factor 1α (HIF1α) which in turn regulates a metabolic programme that sustains glycolysis essential for HSC activation (Takubo *et al.*, 2010). In HIF1α deficient mice, HSCs lost their quiescent status accompanied by a reduction in their numbers during BM transplantation or myelosuppression (Takubo *et al.*, 2010).

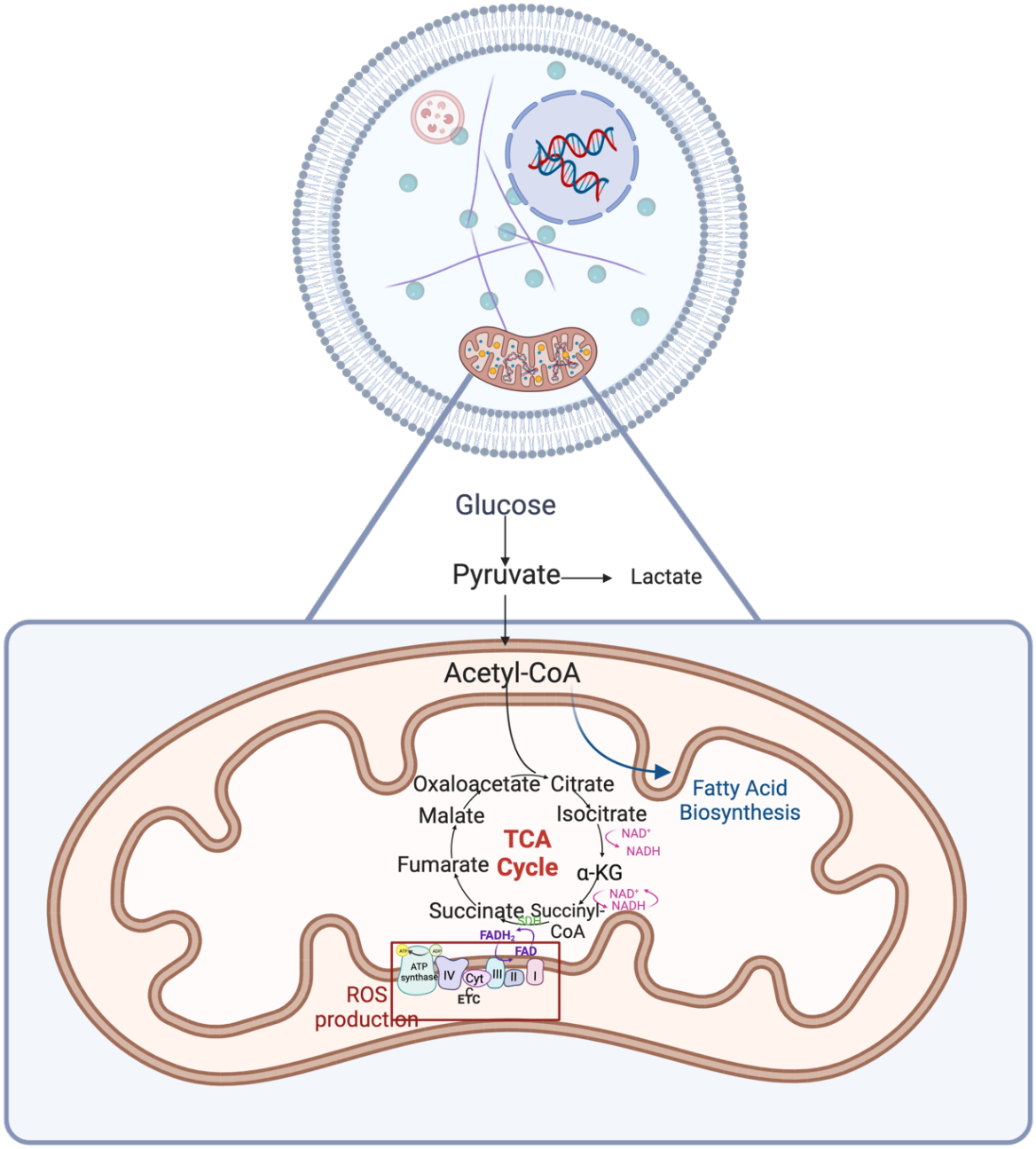


Figure 1. 4 Mitochondria support HSC maintenance and proliferation. Overview of mitochondrial bioenergetic and biosynthetic processes contributing to HSC-proliferation and differentiation. HSCs rely on glycolysis, the process of converting glucose into glucose-6P which results in pyruvate generation. HSCs reside in BM niches with low oxygen levels adapting to a relatively low energetic demand. Pyruvate enters the TCA cycle where it gets oxidised to generate citrate. In turn, citrate is converted into isocitrate and then α-ketogluterate. The TCA cycle is completed upon the generation of ATP and NADH and FADH2 that feed complexes I and II of the ETC respectevely. Electrons from complexes I and II are passed through the ETC to produce ATP through OXPHOS. Increase in glycolysis and OXPHOS is coupled with increased in mitochondrial mass, membrane potential, permeability and high ROS. Inspired from (Morganti, Cabezas-Wallscheid and Ito, 2022).

1.6 The HSC niche in homeostasis

It is evident from the studies highlighted above that HSC activity is regulated by cell-intrinsic mechanisms like epigenetic modifications, metabolism pathways and transcriptional regulators. However, HSC homeostasis is also attributed to cell-extrinsic cues such as neural signals from the BM microenvironment. Colleagues across the haematopoietic field refer to the "HSC niche" as the local microenvironment in which HSCs are maintained in a non-proliferative, undifferentiated state by secreting factors that determine HSC fate (Pinho and Frenette, 2019). Building from R. Schofield who was the first to propose this concept in 1978 (Schofield, 1978), a combination of mouse transgenic models that allowed genetic manipulation of niche cell types or depletion of niche factors, coupled with advanced microscopy techniques, shed light to understanding the BM microenvironment and its interactions with HSCs (Pinho and Frenette, 2019). Before embarking into the complex world of BM, the different niche constituents, their secreted factors and interactions with haematopoietic cells, it is important to briefly introduce the microarchitecture of the bone and bone marrow. The periosteum is a highly vascularised and innervated layer that covers the outer surface of the bone. The internal surface of the bone, adjacent to the BM, is the endosteum. A hard, calcified bone matrix surrounds the two and is referred to as compact bone which also includes the trabecular area that runs at the end of long bones. Typical long bones, like femur or tibia, contain a dense network of blood vessels. The central artery enters the cortical bone and reaches the BM where it brunches into a network of arteries and smaller arterioles. These arteries terminate into capillaries in epiphyseal and metaphyseal areas, in the endosteum and diaphysis (Ramasamy, 2017). Adjacent to the central artery is the central vein, which receives blood from capillaries and drains deoxygenated blood and waste products from the bone through sinusoidal vessels (Zhao and Li, 2016; Ramasamy, 2017). Arterioles and sinusoids are interconnected by type H vessels (also referred to as transitional vessels) at the trabecular bone and endosteum (transitional vessels). Type H vessels differ from the sinusoid (Type L capillaries) since they express high levels of endomucin (Emcn) and Pecam1 (CD31) (Ramasamy, 2017). Taken together, BM vasculature is crucial for haematopoiesis and at the same time very complex. Recent discoveries on haematopoietic cell interactions with BM components will pave the way towards therapeutic exploitations and

targeted interventions to support healthy HSC function in haematological malignancies and severe infection.

1.6.1 Different BM stroma cells shape HSC niche

A plethora of BM stroma cells such as osteoblasts, endothelial cells (EC), perivascular cells (PCs), mesenchymal stem cells (MSCs), adipocytes are implicated in regulating HSC activity. Currently, two main different HSC niches have been identified in the BM, the central and the endosteal niche. The central niche which locates in the central cavity of the BM, contains mostly sinusoids and arterioles whereas the endosteal niche, situated proximal to the bone surface both in the diaphysis and epiphysis, contains mostly transitional vessels (Méndez-Ferrer *et al.*, 2020). These niches not only differ anatomically but also contain different numbers of HSCs. As shown by Acar M. and colleagues, HSCs were more common in the central niche compared to the endosteal niche, with qHSCs more enriched in the former (Acar *et al.*, 2015).

Endothelial Cells (ECs)

The BM is a highly vascularised tissue with endothelial cells (ECs) being the most abundant cells within BM microenvironment, having a crucial role in haematopoiesis, especially after injury (Li *et al.*, 2010). ECs form monolayers lining the lumen of arterioles and sinusoids, hence their name arteriolar and sinusoidal ECs (AECs and SECs), comprising the arteriolar and sinusoidal niche respectively. To differentiate AECs from SECs, markers such as SCA1 and podoplanin (PDPN) are used; AECs are phenotypically described as $CD45^{-}Ter119^{-}SCA1^{high}PDPN^{-}$, whereas SECs are found as $CD45^{-}Ter119^{-}SCA1^{+}PDPN^{+}$ (Pinho and Frenette, 2019b). Nearly all AECs secrete detectable stem-cell factor (SCF). ECs and perivascular cells (PCs) have been identified as sources of essential haematopoietic mediators like SCF (also known as kit ligand-KITL) and CXCL12. Xu C. and colleagues showed that conditional deletion of *Scf* in AECs but not SECs, impacted significantly functional HSC numbers, suggesting that SCF is necessary for HSC maintenance (Xu *et al.*, 2018). SECs, on the other hand, regulate HSCs by secreting CXCL12 and expressing E-selectin (Winkler *et al.*, 2012). SECs also express VEGFR3 and VEGFR2 (Hooper *et al.*, 2009a). Hooper A *et al*. reported that VEGFR2 inhibition prevented damaged SECs regeneration thereby influencing HSPC engraftment and restoration

of haematopoiesis (Hooper *et al.*, 2009b). Notch1 receptor controls EC behaviour by promoting the formation of arteries. Based on Notch1 knock-in reporter mouse (NICD-Cre;Rosa26-mTmG), Kusumbe A. *et al*., reported that notch signalling in ECs leads to expansion of HSC frequency, type H capillaries (marked as $CD31^{hi}$), arteriole formation, perivascular cells expressing platelet-derived growth factor receptor-β (PDGFRβ) accompanied by increased SCF levels and MSC numbers (Kusumbe *et al.*, 2016). These findings demonstrate that Notch signalling can improve vascular niche function and enhance HSC frequency (Kusumbe *et al.*, 2016). Lastly, a small subpopulation of ECs expressing Apelin ($Apln^{+}$), a peptide ligand secreted during angiogenesis by ECs, is critical to maintain haematopoietic homeostasis. Using *Apln*-mTmG animals that lack the ability to generate the Apelin peptide, Chen Qi *et al*., showed that irradiation triggered the expansion of $Apln^{+}$ ECs that actively participate in the remodelling of the BM vasculature (Chen *et al.*, 2019).

Mesenchymal Stromal Cells (MSCs)

An important contributor to the generation of BM stromal cells are Mesenchymal stem cells (MSCs or mesenchymal stem and progenitor cells-MSPCs). MSCs are capable of generating colony-forming units-fibroblasts (CFU-F) *in vitro,* and when transplanted they were found to be the architects of a heterotypic haematopoietic niche (Pinho and Frenette, 2019a). MSCs are also multipotent, differentiating into cells of osteogenic, adipogenic and chondrogenic lineages (Wei and Frenette, 2018).

Early studies indicated that CXCL12 abundant reticular (CAR) cells were found with MSC characteristics based on their adipocytic and osteoblastic differentiation potential and the secretion of large amounts of CXCL12 and SCF cytokines (Omatsu *et al.*, 2010). In central BM (CBM) and endosteum, ECs and the associated perivascular MSCs maintain and regulate HSCs (Sacchetti *et al.*, 2007). As evaluated by Mendez-Ferrer S. *et al.*, MSCs expressing GFP under the regulatory elements of nestin promoter (Nes-GFP^{+}) were found to be associated with catecholaminergic nerve fibers (Méndez-Ferrer *et al.*, 2010a; Kunisaki *et al.*, 2013a). Nes-GFP^{+} lack expression of CD31 (or PECAM), CD34 or VE-Cadherin hence identified as bona fide MSCs (Méndez-Ferrer et al., 2010). These Nes-GFP^{+} MSCs were capable of self-renewal and differentiation into cartilage and bone forming cells sharing many characteristics with CXCL12-CAR cells (Méndez-Ferrer *et al.*, 2010b; Ho *et al.*, 2019). Furthermore, in a detailed three-

dimensional sternal and long bone BM images, Kunisaki Y. *et al.*, identified two distinct types of Nes-GFP cells based on the GFP intensity and cellular morphology (Kunisaki *et al.*, 2013b). Nes-GFP^{bright} were rare and associated with arterioles compared to the Nes-GFP^{dim} that were abundant and associated with sinusoids (Kunisaki *et al.*, 2013; Wei and Frenette, 2018). In addition, Nes-GFP^{bright} cells were labelled with the classical pericyte marker NG2 and α-smooth muscle actin. qHSCs preferably located near the arterioles ensheathed by neural-glial antigen 2 (NG2) pericytes (Kunisaki et al., 2013b). Another independent study recapitulated this result, NG2 expression labelled in Nes-GFP^{bright} stromal cells, and added that NG2-Cre transgenic animals produced high levels of CXC-chemokine ligand 12(CXCL12) (Asada, Takeishi and Frenette, 2017). Targeted deletion of Cxcl12 from arteriolar NG2^{+} cells led not only to a significant reduction in HSC numbers but also to HSC redistribution in the BM, specifically away from arterioles (Asada, Takeishi and Frenette, 2017). In contrast, Nes-GFP^{dim} largely overlapped with Lepr+ cells were distributed around sinusoids (Kunisaki *et al.*, 2013).

Generally, it is now accepted that MSCs are critical constituents of HSC niche in the BM and a major contributor of several factors such as SCF, CXCL12 and interleukin-7(IL7) (Wei and Frenette, 2018). It is obvious that MSC stromal populations marked by genetic labelling, Nes-GFP^{+}, Scf-GFP, Ng2-Cre^{+} or Lepr-Cre^{+}, largely overlap in the literature suggesting a complex heterogeneity and perhaps an underlying transcriptional profile relating to the identity and differentiation of BM MSCs that is yet to be uncovered. Surface markers used to identify MSCs and their progeny such as PDGFRa, αSMA, CD51, NG2, LepR still remain elusive due to different processing protocols used in studies i.e BM flushing and bone crushing (Wei and Frenette, 2018). Therefore, interpretation of data in which MSCs are included in the study to evaluate their progeny must be carried out with extreme precaution.

Perivascular Cells (PCs)

Perivascular cells (PCs), principally pericytes and progeny of MSCs, can be found in perivascular niches (Man *et al*., 2021). In murine BM, PCs are identified by their expression of leptin receptor (LepR), high levels of Scf and Cxcl12(Ding *et al.*, 2012; Ding and Morrison, 2013) and high/ low levels of Nestin-GFP (Méndez-Ferrer *et al.*, 2010b) and PDGFRα (Zhou *et al.*, 2014; Comazzetto, Shen and Morrison, 2021). Conditional deletion of *Scf* from LepR expressing PCs, resulted in a significant reduction of BM cellularity and depletion of HSCs from

the BM suggesting that LepR^{+} PCs are essential components that maintain HSCs (Ding *et al.*, 2012). However, these findings were challenged in a more recent study where Matsuoka S. *et al* showed that deletion of Scf or Kit ligand for LepR PCs did not alter HSC numbers in the BM failing to support the regulatory role of LepR PCs in HSCs (Matsuoka *et al.*, 20220). In another study, mobilisation of HSCs from the BM to peripheral blood (PB) and the spleen was observed upon deletion of CXCL12 chemokine from LepR PCs, concluding that CXCL12 expression by Lepr^{+} cells is important for HSC retention in the BM (Ding and Morrison, 2013). Heather A. and colleagues reported that upon conditional deletion of a heparin-binding growth factor, pleiotrophin (*Ptn*), from LepR+ PCs, HSC maintenance was impaired whereas deletion from ECs, osteoblasts or haematopoietic cells had no effect (Himburg *et al.*, 2018). Lastly, Acar M. *et al*., using α-catulin GFP reporter animals, showed that HSCs were located closely to Lepr^{+} and Cxcl12^{high} PCs and concluded that α-catulin GFP^{+} HSCs were found by sinusoids (hence perisinusoidal niche) and not arterioles (Acar *et al.*, 2015).

Osteolineage cells

During development, mesenchymal progenitors give rise to BM stromal cells of skeletal origin. Using a lineage tracing system, Pineault K. *et al.* showed Hoxa11-CreER^{T2} MSCs gave rise to chrondrocyte (Sox9), osteoblasts (Osteorix) and BM adipocytes (Perilipin) (Pineault *et al.*, 2019). Osteoblasts and osteoclasts are a group of cells that line the endosteal surface contributing towards bone formation and bone resorption respectively synchronously working to sustain bone homeostasis (Lee *et al.*, 2017). They were the first BM mesenchymal population shown to be a component of the HSC-niche by regulating haematopoiesis (Calvi *et al.*, 2003; Calvi and Link, 2015). Calvi L. and colleagues showed that pharmacological manipulation of osteoblasts by altering parathyroid hormone (PTH), an osteoblast activator, led to an increase in the number of osteoblasts and HSC *in vivo* pointing towards an osteoblastic niche that express Notch ligand jagged 1 (Jag1). Jag1 activated Notch signalling on HSCs resulting in their expansion based on long-term culture-initiating cell assay (LTC-IC) (Calvi *et al.*, 2003). Several regulatory molecules such as osteopontin (OPN)(Nilsson *et al.*, 2005), angiopoietin-1 (ANGTP1)(Zhou, Ding and Morrison, 2015) or Thrombopoietin (THPO) (Pinho and Frenette, 2019; Man *et al.*, 2021) are involved in the crosstalk between osteoblasts and HSCs in the endosteal niche. OPN, a phosphorylated matrix glycoprotein, is important for the retention, migration and negative regulation of proliferation in HSCs. Mice lacking OPN

were shown to have enhanced cycling of HSCs (Nilsson *et al.*, 2005). In addition, HSCs interact with osteoblasts through β1- integrin suggesting OPN to be a crucial component of the endosteal niche needed for the regulation of HSC location and proliferation (Nilsson *et al.*, 2005).

1.6.2 Bone marrow niche changes during stress

Viral (*pI:pC*), bacterial (LPS, *Mycobacterium avium*, *Mycobacterium tuberculosis*) and parasitic (*Plasmodium* species) infections lead to the recruitment of qHSC into cell cycle and subsequent proliferation of downstream progenitors. The effect on different BM niche components has only recently become an object of research in various studies (Fröbel *et al.*, 2021). Viral infections were shown to affect the BM microenvironment (Pascutti, Erkelens and Nolte, 2016).

A study conducted on HIV patients, showed that patients presented with lower bone mineral density (BMD) and with a higher risk of developing osteopenia/osteoporosis than non-HIV individuals (Beaupere et al., 2015). As a consequence of that, certain functional stages relating to MSCs such as proliferation, matrix maturation and mineralisation were impacted(Beaupere *et al.*, 2015). Treatment with two HIV proteins (tat and nef) was shown to inhibit the proliferation of MSCs thus promoting their senescence and leading to MSC metabolic dysfunction and oxidative stress (Beaupere *et al.*, 2015). Treatment with *pI:pC* on wt or INFa null animals led to rapid proliferation and activation of BM ECs, which associated with upregulation of EC related markers such as ESAM, VE-cadherin and laminin (Prendergast *et al.*, 2017). EC activation was facilitated by VEGF signalling (Prendergast *et al.*, 2017). Additionally, INFα compromised BM vascularity as shown by anti-laminin staining and vessel permeability (Prendergast *et al.*, 2017). Helbling P. *et.al.* investigated changes in the transcriptional landscape of SECs and CXCL12 abundant reticular cells (CAR) upon *pI:pC* or LPS infection and noted differentially expressed genes (DEGs) relating to interferon signalling and interleukins (Helbling *et al.*, 2019). Using *Tie2-Cre* mice which target ECs, Boettcher S. and colleagues reported that after LPS stimulation, ECs initiated emergency granulopoiesis through TLR/Myd88 signalling axis, and secreted G-CSF during the acute phase of bacterial

infection and VCAM-1 (Boettcher *et al.*, 2014). Moreover, *E coli* infected animals that lack the adaptor molecule Myd88, which is required for TLR signal transduction, led to severely defective granulocyte production (Boettcher *et al.*, 2014; Mun, Fazio and Arrieta, 2021). Signals coming from CAR cells and osteoblasts support B lymphopoiesis which is suppressed by G-CSF (Day *et al.*, 2015). Another study recapitulated alterations in the BM vasculature reporting increased number of sinusoids which was correlated with elevated levels of VEGF (Vandoorne *et al.,* 2018). Moreover, integrins are associated with angiogenesis and with TLR signalling triggering BM angiogenesis. Vandoorne K. *et al.* studied αVβ3 after liposaccharide injection (Vandoorne *et al.*, 2018) and reported that αVβ3 integrin participated in tissue remodelling since it allowed ECs migration to expand into vascularised regions during angiogenesis (Vandoorne *et al.*, 2018).

In another study contacted by Day R. *et.al.* animals were treated with G-CSF which not only drove CAR cell expansion but also it enhanced CAR cell potential towards osteogenic lineage, thus suppressing adipogenesis (Day *et al.*, 2015). Notably, G-CSF deprived the production of multiple factors associated with B cells like CXCL12 CAR cells, IL6, IL7 and IGF-1 (Day *et al.*, 2015). It is worth mentioning that BM microenvironment may facilitate pathogen long-term viability. For instance, Das B. and colleagues demonstrated that *Mycobacterium tuberculosis (Mtb)* affected BM MSCs which express CD271 even after these cells were treated with antitubercular drugs (Das *et al.*, 2013). Aside bacterial infection but in a similar context, BM acts as a reservoir for *Plasmodium* parasites. Immunohistochemical (IHC) analysis of BM specimens with *Plasmodium vivax* showed that the parasites persist in the BM parenchyma despite being undetectable in patients' PB (Silva-Filho *et al.*, 2020). This has been recapitulated in the molecular study contacted by Aguilar R. *et al.,* where it was shown that the gametocytes (see below parasite cycle) of *Plasmodium falciparum* were more prevalent in the BM compared to PB (Aguilar *et al.*, 2014). In bone histomorphometric analysis of animals infected with *Plasmoidum yoelii* nonlethal (*Py*NL), modelling *Plasmodium vivax* in humans, revealed OC and OB suppression and reduction in bone formation (Lee et al., 2017), suggesting that during acute infection bone associated cells were affected, which had a detrimental impact on bone growth (Lee *et al.*, 2017). Additionally, OCs and OBs were cultured *in vitro* with *Plasmodium falciparum* crude extract (PfCE), consisting of parasite proteins, hemozoin and nuclei acid, which did not affect OC maturation, however had a negative impact

on osteoclast progenitors (OCPs) and osteoblast precursors (OBPs), mediated by strong proinflammatory cytokine production such as IL-1α, IL-1β, IL-6 and TNF-α (Lee *et al.*, 2017). Proinflammatory cytokine expression on OCPs and OBPs was dependent on MyD88 indicating its role in controlling *Plasmodium*-induced chronic bone inflammation and bone loss(Lee *et al.*, 2017). Lastly, intravital microscopy (IVM) of osteoblast reporter (Co2.3 GFP) infected with the rodent malaria parasite, *Plasmodium berghei*, revealed loss of OBs and compromised vessel integrity associating with high ROS (Batsivari *et al.*, 2020; Haltalli *et al.*, 2020).

Together these findings not only highlight how complex the BM niche is but how we could utilise available tools such as RNAseq, genomic manipulations and confocal imaging to reveal the secrets of the BM niche. These secrets will either reveal possible targets relating to the maintenance or restoration of the microenvironment required for LT-HSCs during health, or gain knowledge on how to eradicate their competitors that lead to HSC exile and transformation of the healthy niche to a pre-malignant one (Mun, Fazio and Arrieta, 2021).

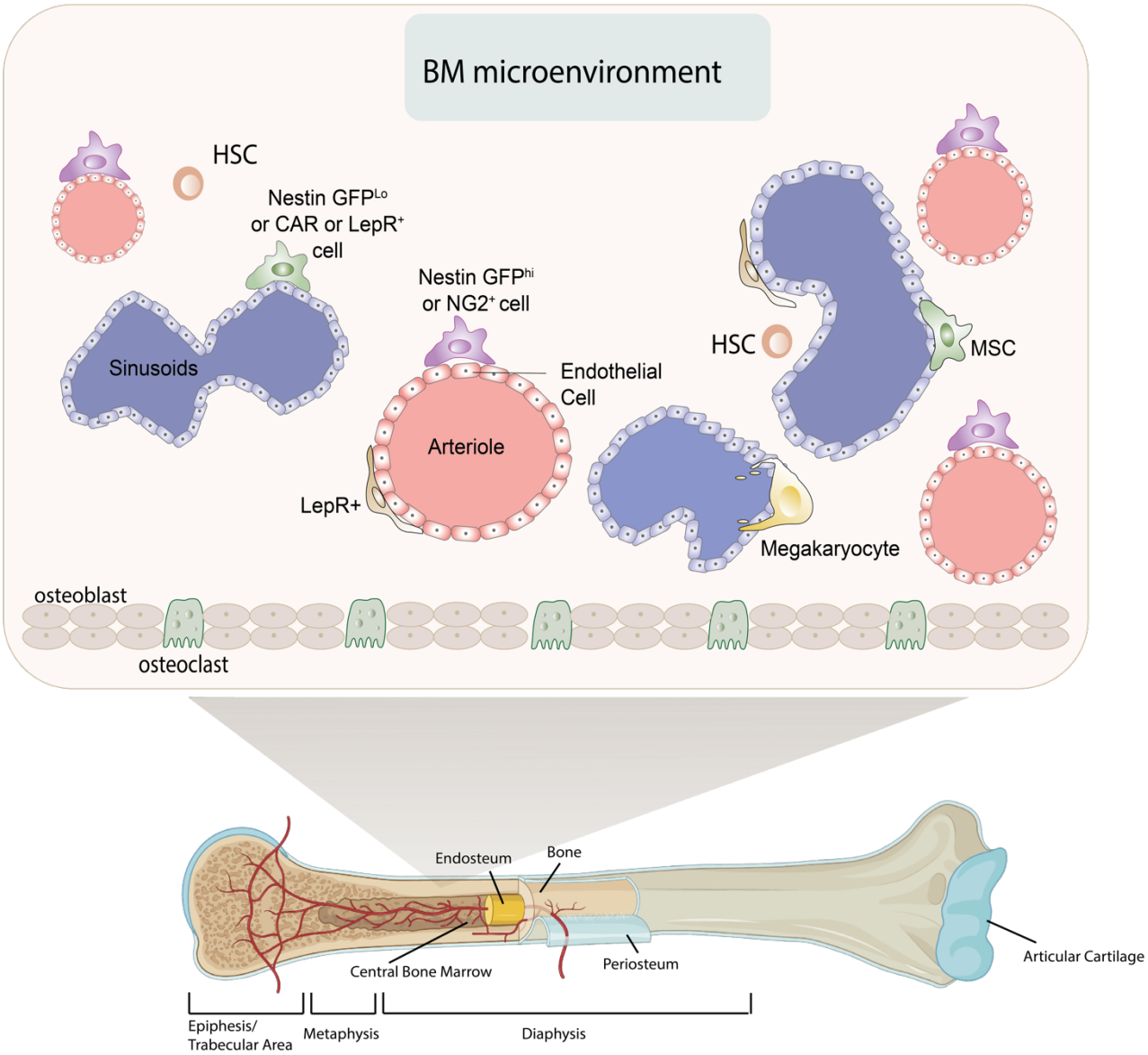


Figure 1. 5 Bone marrow microenvironment and interactions with HSCs. The bone architecture where the trabecular area marks the epiphysis, followed by metaphysis and then the diaphysis which consists of the central marrow. Inside the bone, in the BM, HSCs reside in specialised microenvironments called niches which support their maintenance, proliferation/differentiation and survival. There are two niches where HSC reside, the endosteal and central niche. These two niches are highly vascularised and consist of a myriad of stromal cells such as ECs, MSC, PCs, osteoblasts and other haematopoietic cells such as megakaryocytes. ECs-endothelial cells, PCs-perivascular cells, MSCs-mesenchymal stromal cells.

1.7 Malaria, a life-threatening disease

In humans, malaria is a life-threatening disease caused by *Plasmodium* parasites transmitted by the bite of female *Anopheles* mosquito (Coban, Lee and Ishii, 2018; Venugopal *et al.*, 2020; Arora *et al.*, 2023). In 2020, more than 240 million clinical infections and 620,000 deaths of malaria were reported with three-quarters of those cases occurring in sub-Saharan Africa (Arora *et al.*, 2023). These figures place malaria among the top lethal infectious disease in humans along with HIV and tuberculosis (Coban, Lee and Ishii, 2018). Among the five different *Plasmodium* species that cause malaria in humans (*P. falciparum, P vivax, P. ovale, P. malariae and P. knowlesi*), *P. falciparum* is the most prevalent in sub-Saharan Africa and considered to be the deadliest of all. On the other hand, *P. vivax* accounts for more than 50% of malaria cases in regions of Asia (Coban, Lee and Ishii, 2018; Venugopal *et al.*, 2020). During infection, parasites invade erythrocytes and undergo a round of intracellular replication either causing milder symptoms, such as fever, chills, headache, diarrhoea, body-aches, vomiting and anaemia or more severe complications, such as respiratory distress, renal injury and cerebral malaria (Ashley, Pyae Phyo and Woodrow, 2018; Coban, Lee and Ishii, 2018). Currently, anti-malaria interventions are utilised to treat *Plasmodium* symptoms in humans. While milder symptoms in *P falciparum* patients are treated with artemisinin, artesunate is given in more severe *P. falciparum cases* (White *et al.*, 2014; Lee, Waters and Brewer, 2018). Additionally, chloroquine is widely used to treat non-falciparum malarias such as *P. vivax* (White *et al.*, 2014). Taken together, anti-malarial drugs assisted drastically in the reduction of malaria cases worldwide in the past decade, however, this progress has been halted by the emergence of drug resistant parasites posing a great threat in controlling global malaria (Ashley, Pyae Phyo and Woodrow, 2018; Venugopal *et al.*, 2020).

Malaria infection begins when an infected female *Anophele* mosquito rests on the host skin to take a blood meal. While it feeds it inoculates sporozoites into the host dermis (*Figure 1.6 a*). The sporozoites through the bloodstream reach the liver where they cross the liver sinusoidal barrier and invade hepatocytes (*Figure 1.6 b)*. During the liver-stage, sporozoites replicate asexually and home in the hepatocytes until their maturation. After a couple of days, depending on the parasite species, sporozoites form schizonts which rupture into thousands

of daughter merozoites released back in the circulation, where they invade red blood cells (RBCs)(*Figure 1.6 c*). At this stage, some of the merozoites commit to a second asexual schizogony while others commit to gametogenesis to produce male and female gametocytes thus initiating the sexual cycle. Mature gametocytes enter the circulation and are taken up by another mosquito taking a blood meal from the host. In the mosquito's midgut (*Figure 1.6 d*), male and female gametocytes exit RBCs, differentiate and fuse to produce a zygote. The zygote transforms into ookinete and matures into an oocyst (White *et al.*, 2014; Venugopal *et al.*, 2020). Parasites in the oocyst stage undergo a third asexual replication to produce sporozoites, which migrate from the mosquito midgut to the mosquito's salivary glands where they remain until they are inoculated into the next host upon the next blood meal, marking the start of another cycle (*Figure 1.6 a*) (White *et al.*, 2014; Venugopal *et al.*, 2020).

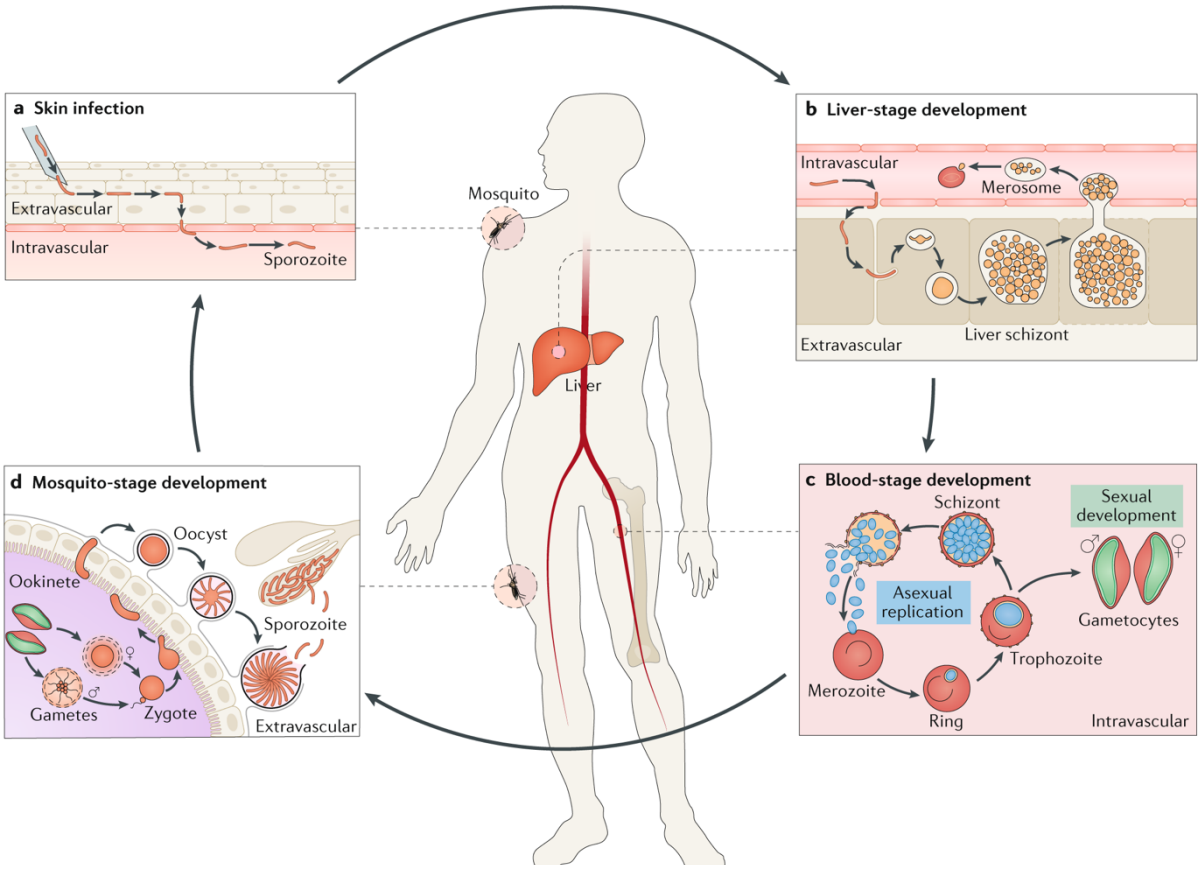


Figure 1. 6 *Plasmodium* life cycle in humans. A) Once an anopheline female mosquito takes a blood meal from the host it simultaneously inoculates sporozoites on the dermis. B) These sporozoites travel to the liver where they invade hepatocytes in which they remain until they mature into schizont. Schizonts then ruptured and released back in the circulation as C) merozoites where they invade red blood cells (RBCs). Merozoites undergo an asexual cycle. D) Merozoites circulate in the bloodstream until they are taken up by another mosquito ending up in its midgut where the sexual cycle begins and the male and female gametes fuse together to form the zygote. The zygote matures into an oocyst which further matures into a sporozoite. The sporozoite travels from the mosquito's midgut to its salivary glands and remains there until the next blood meal of the mosquito. Image adopted from (Venugopal *et al.*, 2020)

1.8 *Plasmodium berghei* parasite as a stressor of haematopoietic compartment

Tissue remodelling driven by malarial parasites reaches beyond erythrocytes. Murine-parasite models have started to shed light into the complexity of malaria infection and its detrimental effects upon haematopoietic cell and non-haematopoietic cell constituents. With the parasite adapting metabolically to the host cell environment, several *Plasmodium* parasite strains such as *P chabaudi*, *P berghei*, *P yoelii* and *P vinckei* exist (Lamikanra *et al.*, 2007) and enabled the characterisation and understanding of host-parasite interactions and their effects on haematopoiesis (Lee, Waters and Brewer, 2018; Venugopal *et al.*, 2020). Using the *P. berghei* parasite experimental model, published work from the Lo Celso research group showed haematopoietic perturbations in host animals infected through the bites of mosquito carrying *P. berghei* parasite (Vainieri et al., 2016). Vainieri *et al.* demonstrated phenotypic changes in the downstream haematopoietic progenitors, especially a dramatic expansion of SCA-1^{+} progenitors as a consequence of primitive HSC proliferation (Vainieri et al., 2016). The observed changes in haematopoietic cell populations during malaria were induced by a cytokine *milieu,* specifically INF-γ (Haltalli *et al.*, 2020). In addition, this second study showed that during *P. berghei* infection not only HSC lose their transcriptional identity and function, but also reside in the vicinity of leaky vessels containing high levels of ROS (Haltalli *et al.*, 2020). Lastly, Haltalli *et al.* demonstrated through IVM that malaria affects bone constituents, specifically the osteoblast (Haltalli *et al.*, 2020).

Deriving from the above work several questions arise on the cell-intrinsic and -extrinsic mechanisms on how *P berghei* infection perturbs haematopoietic and non-haematopoietic cells and their processes. Particularly:

1. Does the whole LT-HSC compartment become activated during malaria-induced stress or only certain HSC clones?
2. Does infection affect the distribution of HSCs in the BM?
3. What is the impact of reinfection on HSCs?
4. Could anti-malarial drugs preserve HSC functionality?
5. What are the effects of infection on other stromal components?

6. Do parasites continue to remodel stromal cells even after recovery from infection?

The search for understanding molecular and immunological pathways underlying the interactions between *Plasmodium* species and BM microenvironment and their effect on haematopoietic stem cells is of significant value. How these interactions are altered or not after parasite clearance of the initial infection need to be addressed too. This knowledge will pave the way towards developing novel therapies for patients to receive the most appropriate medical treatment and diagnosis to minimise the negative effects of malaria infection on HSCs (Coban, Lee and Ishii, 2018).

1.9 Project hypothesis and research questions

My overarching hypothesis is that a subset of quiescent HSCs exists that maintain stemness regardless of *P. berghei* proliferation induced stress.

In this project I focus on three main questions:

1. Does *P. berghei* infection induce the activation of all HSCs equally?

2. What cell intrinsic mechanisms underpin the HSCs' heterogeneous response?

3. Does the BM microenvironment play a role in HSC heterogeneous responses?

Chapter 2

Materials and Methods

2.1 Animal Models

All animal work was carried out in accordance with the animal ethics committee at Imperial College London and UK Home office regulations (ASPA 1986). C57BL/6.J animals or C57BL/6.N 8-12 wks old females were procured from Francis Crick Institute and ENVIGO respectively. CD45.1 (C57BL/6.SJL) 6-8 weeks old females were obtained from Francis Crick Institute. For the generation of parasite blood stocks (P0) Tuck-Ordinary (TO) or CD1 >5 weeks old animals were obtained from ENVIGO.

Transgenic reporters

To visualise the interactions of Biotin HSCs with BM microenvironment, the HSC transgenic reporter α-catulin GFP was used. Information was obtained from both males and females aged 8-12 wks old (Chapter 6).

The effect of *P. berghei* infection and its consequences to the BM niche was studied by using males and females aged 8-16wks from different niche reporters: osteoblasts- Col2.3 GFP^{+}, Endothelial cell (EC)- Flk1 GFP^{+} and Perivascular cell (PC)-$LepR^{+/-}$Cre;$Rosa26YFP^{+/-}$. Calvarium and long bones from these reporters were imaged for intravital microscopy (IVM) and immunofluorescence (Chapter 6).

Mouse Treatments

Parathyroid hormone (PTH) (rat PTH (1–34) Bachem; 80 µg kg−1 body weight) or PBS were administered i.p. five times a week for 2 weeks before infection and for a further week through infection until BM analysis at day 5.

Phenylhydrazine was administered i.p. at a dose of 10 µl/gm body weight three days before infection to induce reticulocytosis in mice.

Atovaquone was administered *i.p.* in mice at a dose of 0.5 mg/kg at day 5 *pbi* and parasitaemia was monitored every three days thereafter.

Doxycycline was administered in drinking water for seven days (2 mg/ml) before infection and throughout infection until day 5.

N-acetylcysteine (NAC) (130 mg/kg) or PBS (vehicle control) was injected *i.p.* in animals daily from 2 days before infection and through infection until BM analysis at day 5.

EZ-link-NHS-Biotin-Sulfo-LCLCLC label system was injected intravenously (*i.v.*) at a concentration of 1 mg/6 g at day 3 post blood injection (*pbi*) to study HSC proliferation kinetics in response to *P. berghei* infection. Label dilution was allowed for two days until the termination of the experiment on day 5 *pbi*.

The thymidine analogue 5-ethynyl-2'-deoxyuridine (EdU) was administered chronically in drinking water (0.3 mg/ml supplemented with 2% sucrose). EdU was also administered daily *i.p.* on day 3 and day 4 (*i.p.)* for each mouse at a dose of 1 mg/200 µl with a final *i.v.* injection at a dose of 1 mg/200 µl on day 5, 45 minutes before sacrifice.

CellROX deep red reagent was injected *i.v.* at a concentration of 2.5 mM in 200ul in control and infected $Flk1^{+}$ GFP animals to detect ROS in ECs. IVM was performed in the calvarium 30 minutes and 2 hrs post CELLROX injection.
Antibodies against c-kit, EPCR (Stem Cell Technologies or eBioscience), CD48 and VE-Cadherin were injected in α-catulin GFP transgenic mice at a concentration of 0.5 mg/ml. Col2.3 GFP animals were injected *i.v.* with anti-VE-Cadherin eFluor660 antibody at a concentration of 0.5 mg/ml.

2.2 *Plasmodium berghei* experimental model

For the generation of P0 stocks (performed at Cambridge University by Dr Andrew Blagborough), naïve C57BL/6.J animals were injected *i.p.* with freshly thawed infected blood containing wild-type parasite at passage 1 (P1). At three days post blood injection (*pbi*), sexual parasitaemia expanded to 10^{6} -10^{8} infected RBCs in PB. Throughout infection, parasitaemia

was monitored on day 3 and day 4 with cerebral malaria manifesting between days 6-8 where parasitaemia reaches >2-3% in PB. After ensuring that animals have sufficient levels of parasitaemia, PB is collected through cardiac puncture. The collected blood is injected into phenylhydrazine pre-treated TO animals and infection is followed for six days. After this time and when TO animals show detectable malaria (2-3% infected RBC in PB), naive mosquitos that have been starved (sucrose removed) for 72hrs are allowed to feed from deeply anaesthetised TO infected animals for 15 minutes inside a 37^{o}C incubator. From this stage, the asexual cycle of the parasite begins in the mosquito midgut. *Anophele* female mosquitos were maintained for 21 days until sporozoites were present in the mosquito's salivary glands. Once sporozoites were detected in the mosquitos, they were then starved to facilitate another feed of deeply anaesthetised naïve TO animals (each mouse exposed to 5 mosquitoes). Collection of peripheral blood, P0, from infected TO animals was facilitated through cardiac puncture at day 5 post blood feed (*pbf*). One unit of blood was mixed with 2 units of freezing medium which was prepared by mixing 9 units of Alsever's solution with 1 unit of glycerol. P0 stocks were stored in liquid nitrogen.

Blood infection model

To infect experimental cohorts, on day -5 P0 vials were freshly thawed in a 37^{0}C water bath for 5 minutes, injected *i.p.* into a donor mouse and infection was followed for 5 days. Fresh blood (containing 10^{6}-10^{8} infected RBCs) was collected (parasite passage P1) and injected into animals under the experimental cohort (day 0) with the collection of bones occurring at day 5 *pbi*.

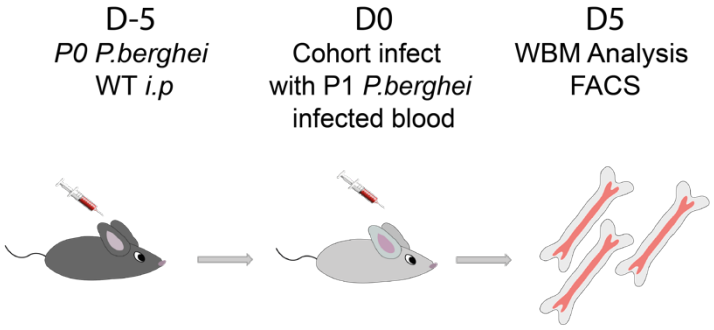


Figure 2. 1 Experimental model. Donor mouse is injected with P0 *P.berghei* vial at D-5 before the cohort is infected at D0. Cardiac puncture is performed at D0 where fresh blood is withdrawn from donor infected mouse that is then used to infect the cohort at D0. Bones from control and infected animals are collected on D5.

2.2.1 Counting infected parasites (parasitaemia)

A small drop of blood was gently squeezed out from the mouse's tail after making a small incision with a needle and directly into a glass slide. Then another glass slide was used to immediately and firmly sweep the other slide that contained the blood by drawing the blood along and forming a thin layer. After the slide was air-dried, it was fixed with methanol for 20 seconds and excess methanol was tipped off. Fixed blood smears were then stained with GIEMSA (1:4) for 20 minutes. Infected RBCs are visualised, identified and counted under a light microscope and at high magnification.

2.3 Flow Cytometry

Bones from infected and control animals were cleaned, crushed and processed for flow cytometry experiments. For most biotin experiments, CD117 (or c-kit) stem and progenitor cell enrichment was performed using $CD117^{+}$ magnetic beads. Beads were added to the cell suspension and incubated at $4^{0}C$ for 20 minutes in the dark. After LS MACs columns equilibration with PBS, filtered cells were loaded onto LS MACS columns for MAC separation. During this process, CD117+ cells were retained in the magnet and flushed into the tube. Enriched cells were then stained with directly conjugated antibodies for terminally differentiated cells referred to us Lineage (CD4, CD8, CD5, Ter119, Gr-1, B220/CD45), Flt3 (or Flk2), c-Kit , SCA1, CD48, CD150, Streptavidin, CD45 and EPCR. Cells incubated at RT for 15 minutes with Viability dyes (either 520 or 780), cells were washed and filtered in 5ml Falcon tube with a 40uM cell strainer. Fortessa analyser (Becton Dickinson), configured with blue, yellow-green, violet, ultraviolet and red lasers, was used in the acquisition of all experiments. For single colour controls and to set up the lasers, compensation beads were stained for each fluorophore and used to set up compensations to correct spectral spillover. Fluorescence minus one (FMOs) controls, including staining with all fluorophores apart from one per sample, were used to define positive and negative gates during analysis.

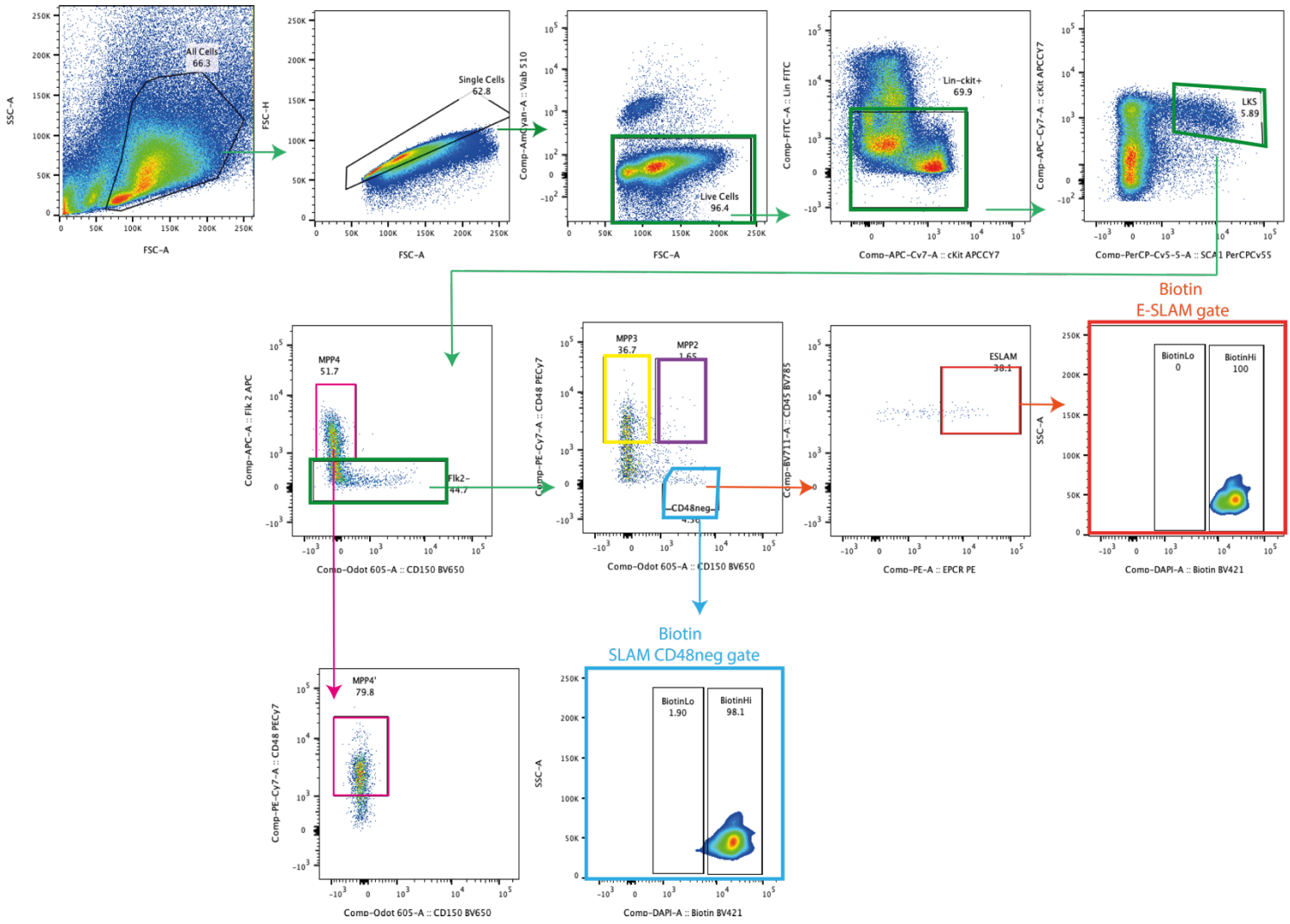


Figure 2. 2 Gating strategy to define Biotin high and low HSCs. Cells were c-Kit enriched and stained for the HSC panel to discriminate MPP subsets, $CD48^{neg}$ and E-SLAM Biotin high and low HSCs.

2.3.1 *EdU*

Click-iT EdU staining kit (ThermoFisher C10645) was used for the detection of cells in S-phase according to the manufacturer's instruction and after all necessary antibody stainings.

2.3.2 *Mitochondrial mass, membrane potential and ROS*

Cells were fully stained for LKS E-SLAM Biotin and viability dye and incubated at 37^0C in 5% CO_2 for 30 minutes with mitotracker dyes. Superoxide anions were measured with mitoSOX

Red (0.1mM), mitochondrial membrane potential (MMP) with TMRM (0.1mM) mitochondrial mass with MitoTracker Green (25nM) and as described in (Hinge et al., 2020; Liang et al., 2020). Probe responsiveness to MMP variations was tested using carbonyl cyanide 3-chlorophenyl hydra-zone (CCCP) incubated in samples before TMRM staining that blocks the mitochondria up taking of TMRM consequently decreasing TMRM fluorescence. Reactive oxygen species (ROS) were measured using CellROX Green (20nM) reagent. Briefly, cells were washed with the HSC FACS panel and stained for CellROX Green reagent following the manufacturer's instructions (Thermofisher). Cells were then acquired on BD Fortessa flow cytometer within 60 minutes of mitochondrial staining.

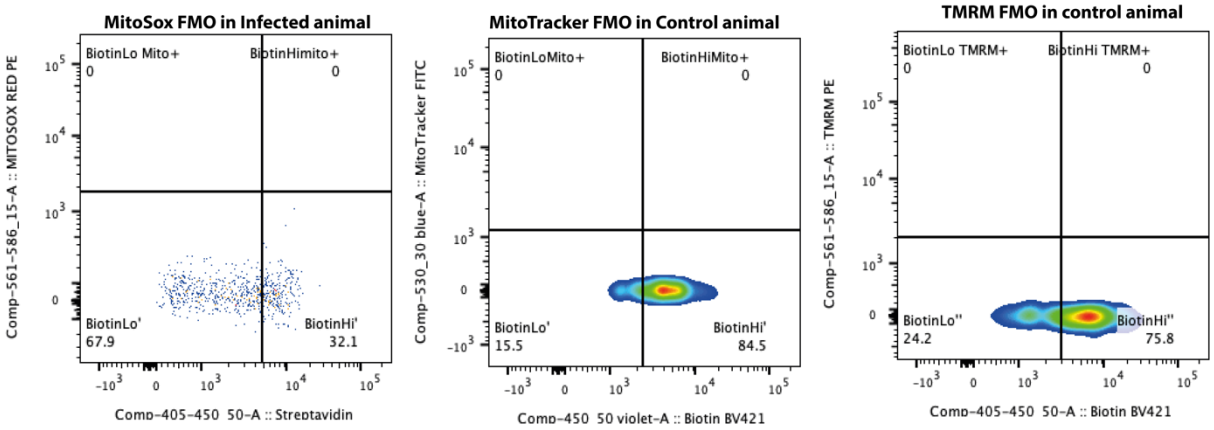


Figure 2. 3 Gating strategy associated with mitochondria health. Panels on the left shows gating strategy for MitoSOX probe, in the middle for mitoTracker Green and on the left shows gating strategy for MMP.

2.3.3 *Cell cycle analysis*

To assess SLAM and E-SLAM HSCs cell cycle statuses, after fixation and permeabilization steps, cells were incubated with anti Ki-67 antibody in the dark overnight in the cold room with gentle agitation. For nuclear staining, SYTOX Green was added to cells before running samples on Flow Cytometer.

2.3.4 *Biotin Localisation within BM*

To determine the localisation of SLAM CD48^{neg} (or CD48^{neg}) and E-SLAM Biotin cell subsets, the trabecular area/epiphysis/metaphysis (or endosteal BM area) were separated from the rest of the bone by dissecting them with a scalpel. The trabecular /epiphysis/metaphysis area

was then crushed using a pestle and mortar. Then diaphysis which contained central bone marrow (CBM) cells was flushed with a syringe. Both the endosteal and CBM fractions were stained separately for HSC panel markers.

2.4 BM stroma Staining

For the BM stroma cell quantification, bones were collected from infected and control animals and processed as two different fractions. The BM supernatant, labelled as the CBM, and the crushed bone, labelled as the bone lining cells, were processed as below:

a) Bones were extracted and crushed. Red dissociated marrow (CBM) was spun down and resuspended in 80 mg of collagenase IV/3 µg/ml of DNAse I/ 5% FACS buffer and incubated at 37^{o}C for 20 minutes. Afterwards, CBM cells were filtered with a 70uM cell strainer, washed with FACS buffer and centrifuged. To eliminate RBCs, lysis was performed using red blood cell lysis buffer (0.001g/ml Potassium bicarbonate, 0.008g/ml Ammonium chloride, 20mM EDTA, all from Sigma, and 5% (v/v) FBS diluted in Milli-Q water) and cells were washed again with FACS buffer to discard lysis buffer leftovers. CBM cells were incubated and labelled with anti-CD45 microbeads and through MACS column separation were depleted as CD45 negative cells. After CD45 depletion, CBM cells were stained for BM niche FACS panel.

b) For the bone lining cells (BLC), the bones were cut with scissors and into tiny pieces. The bone fragments were centrifuged and afterwards resuspended in Collagenase type I (3 mg/ml in DMEM/5% FCS, no EDTA) and incubated for 45 min at 37^{o}C with rotation. BLCs were filtered, treated with Collagenase I for a second time and then washed, centrifuged and stained with an antibody cocktail.

Both the CBM and BLC fractions were stained for the stroma antibodies against Sca1, Ter119, CD31, CD45.2, PDGFRα, LepR, CD51, ALCAM were used. The gating strategy for these populations is shown in Figure 2.3 (below).

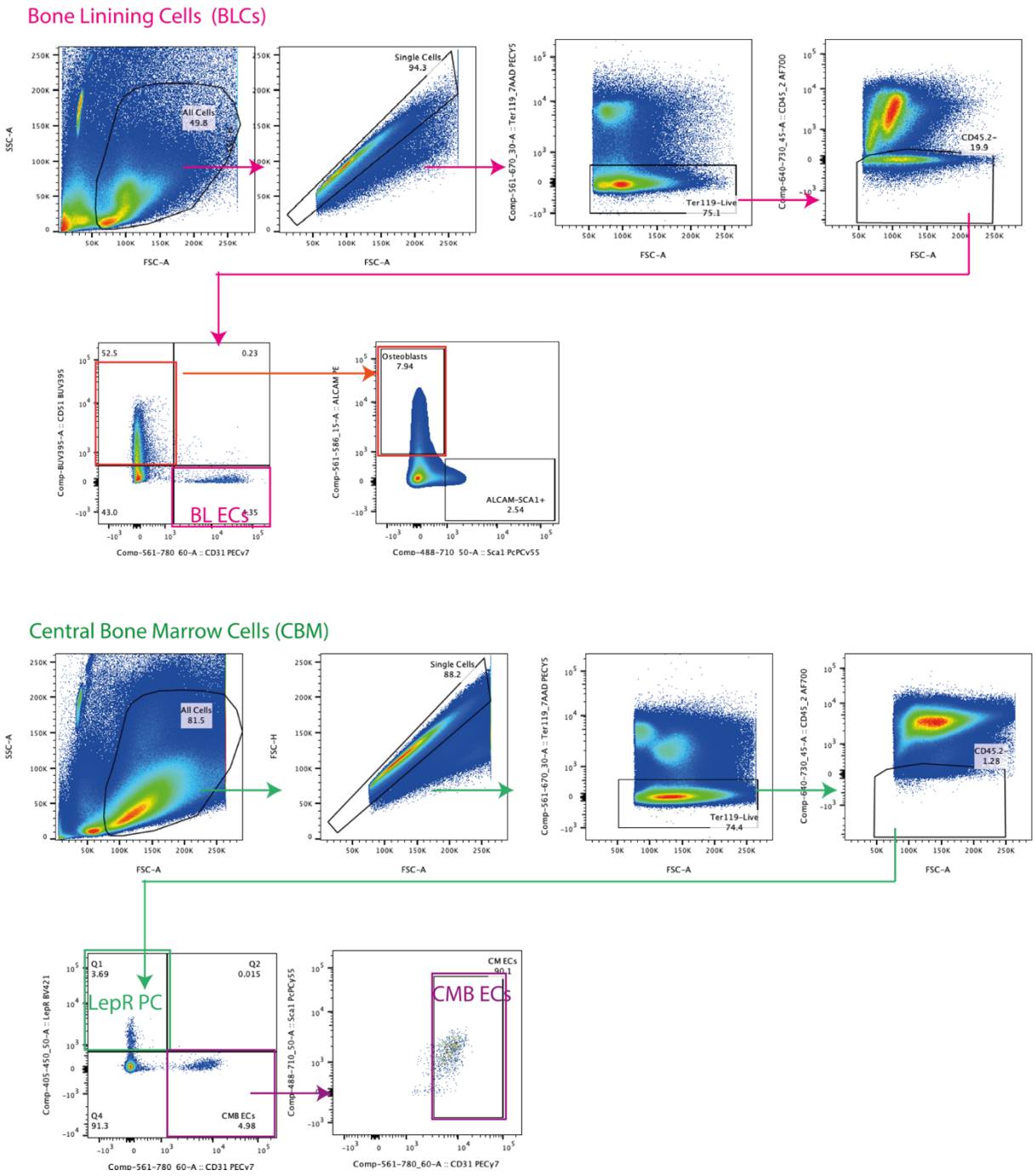


Figure 2. 4 Gating Strategy for BLC and CBM cells. Central bone marrow (CBM) and bone lining cells (BLCs) fractions were obtained from crushed bones. These fractions were processed separately but stained with the same antibody cocktail against Sca1, Ter119, CD31, CD45.2, PDGFRα, LepR, CD51, ALCAM. Thus, CBM PCs identified as CD45^{neg} Ter119^{neg} LepR^{+} and CBM ECs as CD45^{neg} Ter119^{neg} CD51^{neg} CD31^{+} SCA1^{+}. In the BL fraction, osteoblasts identified as CD45^{neg} Ter119^{neg} CD51^{+} CD31^{neg} ALCAM^{+} and BL ECs as CD45^{neg} Ter119^{neg} CD51^{neg} CD31^{+}.

2.5 Transplantation Assays

2.5.1 *Primary Transplants*

Bones (tibias, femurs, hips, sternum) from infected and control animals were collected and harvested under sterile conditions. Bones were crushed in FACS buffer (PBS+2%FBS+P/S) and filtered through a 70 µM cell strainer. Red blood cell lysis was performed to eliminate RBCs, with FACS buffer being added a minute later to stop lysis. Finally, cells were further washed and spun using a benchtop centrifuge at 500G for 5 minutes. To determine the number of cells per tube, Countess or Vi-Cell systems were used.

For the transplants in **Chapter 3,** cells purified from mTmG control and infected animals were Lineage depleted (EasySep Magnet Stem Cell Technologies (Cat# 18103)) and then stained with biotinylated lineage antibody cocktail as per EasySep Mouse Hematopoietic Progenitor Cell Isolation Kit from Stem Cell Technologies (Cat#19856A,Lot#00000) which included CD5, CD11b, CD19, CD45R/B220, Ly6G/C(Gr-1, TER119, CD4 and CD8. Lineage^{neg} cells were then stained for cKit, Sca-1, CD34, CD150, Flt3, CD48 and Viability dye and sorted on Aria Fusion Cell Sorter. Before transplantation, CD45.1 recipients (used in all transplants) were lethally irradiated receiving two doses of 5.5Gys, (administered 2 hours apart). Recipients were kept on Baytril for 5 weeks and transplanted HSC engraftment and reconstitution was recorded every 4 weeks until termination of the transplant.

A) **SLAM CD48^{neg} (or CD48^{neg} HSC) transplant (*Chapter 3*),** 120 HSCs (sorted as mTmG^{+}Lin^{neg}cKit^{+}SCA1^{hi}CD48^{neg}CD150^{+} or mTmG^{+}LKS SLAM CD48^{neg}) were sorted per condition and treatment. HSCs were injected into lethally irradiated CD45.1 recipients along with 300K CD45.1 WBM support. About 30-50ul of blood was obtained from recipients and stained for CD3, CD19, CD11b, CD45.2 and Viability 780 to visualise SLAM CD48^{neg} engraftment (see Chapter 2 section 2.5.3 multilineage reconstitution for further details) for 16 weeks by PB analysis every 4 weeks.

B) For the **Lineage^{neg}c-Kit^{+} (*Chapter 3*),** 161 x10^{3} uninfected and 272 x 10^{3} infected donor mTmG^{+} c-kit^{+}Lin^{neg} cells along with 300K CD45.1 WBM support were transplanted into CD45.1 recipients that received lethal irradiation dose 2 hours apart. The numbers

injected in the primary recipients were back-calculated based on the number of HSCs in the $Lin^{neg}cKit^{+}SCA1^{hi}CD48^{neg}CD150^{+}$ gate to match the **$CD48^{neg}$ HSC transplant (Chapter 3).** To obtain information on the engraftment and multilineage reconstitution, about 30-50ul of blood was obtained from recipients and analysed for CD3, CD19, CD11b, CD45.2 and Viability 780. The blood was obtained every 4 weeks for a period of 20 weeks (see Chapter 2 section 2.5.3 multilineage reconstitution for further details).

C) For the **ESLAM Biotin transplant** in **Chapter 4**, CD117 (or c-kit) stem and progenitor cell enrichment was performed as described in section 2.3. Enriched cells for CD117 were then stained with fluorescently conjugated c-Kit, SCA1, CD48, CD150, Flt2, EPCR, CD45 and antibodies for terminally differentiated cells, lineage cocktail (CD45/B220, Gr-1, Ter119, CD4, CD8, CD5). Cells were then stained with viability dye to determine live cells. Samples were sorted on Aria III sorter (Figure 2.4).Ten ESLAM $Biotin^{Hi}$ from control CD45.2, 10 ESLAM $Biotin^{Hi}$ from infected and ESLAM $Biotin^{Lo}$ from infected CD45.2 donors were transplanted along 250k CD45.1 WBM support. For the first four weeks, Baytril was administered in drinking water. After 4,8,12,16,20 and 24 weeks, 30-50ul of PB were obtained from recipients and stained with antibodies outlined in Chapter 2 section 2.5.3 to assess multilineage reconstitution.

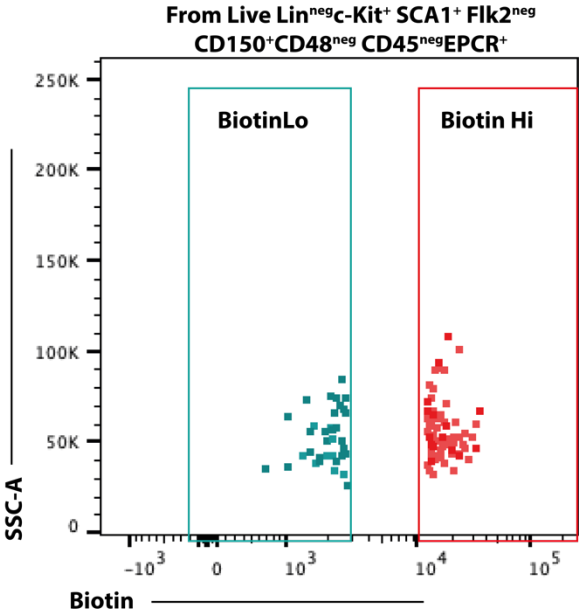


Figure 2. 5 Sort gates of E-SLAM Biotin high and low cells. Stringent gating strategy to sort the top 20% and bottom 20% of Biotin high and biotin low cells respectively.

2.5.2 *Secondary Transplants*

In **Chapter 3**, 1 x10^6 (**CD48^{neg}**)or 3 x10^6 (**Lineage^{neg}c-Kit$^+$)** WBM cells from CD45.1 primary recipients that received cells either from PTH-treated or PBS-treated control/Infected donor animals, were injected into lethally irradiated CD45.1 recipients. Engraftment was followed for a period of 16 weeks by monitoring the percentage of mTmG$^+$ primary donor cells in PB along with multilineage reconstitution.

In **Chapter 4**, 2 x10^6 WBM cells from primary recipients that receive either ESLAM-Biotin^{Hi}, ESLAM-Biotin^{Lo} cells purified from infected donors or ESLAM-Biotin^{Hi}cells from control donors were injected into lethally irradiated CD45.1 secondary recipients. Engraftments and multilineage reconstitution were monitored for 20 weeks. On week 20 WBM analysis of recipients' bones was carried out.

2.5.3 *Multilineage reconstitution assessment*

To assess multilineage reconstitution in primary and secondary transplant recipients from both **Chapters 3 and 4**, PB blood was lysed with RBL buffer, washed with FACS buffer (2% FCS+ PBS without Ca and Mg) and stained for antibodies against CD45.1 (to detect recipient's cells and support), CD45.2 (primary donor cells), CD19 (B Cells), CD3 (T cells), CD11b (other myeloid cells). Lysed cells were incubated with the antibody cocktail mix (containing the above antibodies) for twenty minutes in the dark and at 4^{o}C. Then, to exclude dead cells Viability 780 was used. Cells were then washed with FACS buffer, centrifuged, filtered through a nylon mesh filter and ran on a Fortessa BD analyser. To detect donor contribution to haematopoietic cell lineages in Chapter 3, antibodies against CD45.1, CD19, CD3 and CD11b and viability 780 were used. The transplanted cells from mTmG donor animals were visualised by using the PMT 586/15 which was switched onto the yellow-green laser during acquisition.

2.6 Single-cell (sc) and minibulk RNA sequencing

SLAM CD48^{neg} HSCs and E-SLAM BiotinHi/Lo cells purified from infected and control animals as described above were index sorted into 96-well plates as one cell/well across four plates for sc-RNA and multiple wells/15 cells for minibulk sequencing respectively. Single-cell (sc) and minibulk RNA sequencing experiments were run on 10x Chromium™ (10x Genomics,

Pleasanton, CA) at the University of Cambridge in Prof. Berthold Göttgens's laboratory. cDNA library preparation, clean up and quantification, sequencing and data analysis were performed by Dr Nicola Wilson, Mrs Sarah Kinston, Mr Shirom Chabra and Dr Qi Liu (MRC Stem Cell Institute, University of Cambridge, Cambridge) respectively. After quality control, differential expression analysis (DEA) was performed between SLAM Biotin^{Hi} control and SLAM Biotin^{Hi} infected cells and SLAM Bitoin^{Hi} infected and SLAM Bitoin^{Lo} infected cells. For both minibulk and sc-RNA sequencing, cell cycle analysis was performed along with hscScroring, repopulation ageing and p53 scorings. For more specific details and technical information from our collaborators please refer to Appendix A.

2.7 Bone processing, cryosectioning and immunofluorescence

Femurs from infected and control animals were harvested and fixed in 4% PFA, overnight at 4^{o}C. Bones were then washed in PBS to remove PFA and added into 10% EDTA (pH8) for 5 days at 4^{o}C. A sucrose gradient was prepared (10% <20%< 30% overnight) for cryoprotection and femurs were added in 10% and 20% sucrose for 2 hrs each and kept overnight in 30%. Afterwards, they were embedded in optimal cutting temperature (OCT) compound and blocks were stored at -80^{o}C until cryosectioning.

OCT blocks were sectioned at a thickness of 80µM using a Leica CM3050S Cryostat. Sections were passed on the Cryojane slide through the adhesive tape and placed under a UV block. Each bone plug was flushed three times with a 15-second interval between each flush, under UV light to enable sticking of bone section on to the slide. The slides were stored at -80^{o}C.

For immunofluorescence staining, slides containing bone sections were thawed and rehydrated in PBS at RT for 15 minutes. To prevent unspecific binding, sections were blocked in 10% donkey or horse serum at RT for 2hrs. Afterwards, sections were stained with primary antibodies (LepR biotinylated antibody (BAF497), or cKit (2B8)) diluted in blocking serum at 4^{o}C overnight. On the following day, sections were washed in PBS and incubated with secondary antibodies, donkey anti-goat AF555 or AF633 Life Technologies (to detect LepR), donkey anti-rat AF647 or AF594 (to detect c-Kit), Streptavidin AF647 (to detect biotin). After 2hr incubation of bone sections with secondary antibodies, bone plugs were washed again

with PBS, and 0.01% Triton was added to permeabilise the nuclear membrane for DAPI staining. DAPI was diluted 1:800 and bone sections were incubated with DAPI for 15 minutes at RT. At the final stage, bone plugs were washed in PBS and mounted using ProLong Diamond Antifade Mountant (Life Technologies P36961). Images were acquired on Zeis LSM980 upright confocal microscope and analysed using Fiji/Image J or Imaris softwares.

2.8 Microscopy

For all microscopy experiments a Zeis LSM980 upright confocal microscope equipped with 5 solid state confocal lasers (405, 488, 561, 594 and 639 nm), and two-lines infrared multiphoton laser (1045 fixed and 680-1300nm tunable), 6 non-descanned detectors (NDDs), and an array of 32 internal detectors was used.

2.8.1 Confocal microscopy of sections

Using internal detectors, GFP was detected through 488nm excitation; eFluor660 with 640nm excitation; AF555 and AF594 with 561 excitation and DAPI with 405nm excitation. Because of spectral spillover between AF555 and AF594 antibodies used to image EPCR and c-kit positive cells, single-colour slides were prepared and spectral unmixing was performed between the two parameters through Zeiss Zen Blue software.

2.8.2 Intravital Microscopy

Intravital microscopy was performed on Flk1 GFP and LepR Cre Rosa26YFP transgenic animals. Live imaging of the calvarium BM was performed as described in (Duarte et al., 2018). Briefly, animals were induced with 5% isofluorane in 3L/min O_2 and anaesthesia was maintained at 1%-2% isofluorane in 0.8-1L/min O_2 throughout the procedure. Animals were placed in the right lateral decubitus position and a small section in the skin was made. A metal window was adhered on the calvarium through a dental cement (Diamond carve). After the dental cement dried, animals were transferred to a microscope stage where they were kept under anaesthesia and monitored throughout the IVM.

2.9 Image processing and quantification

Zen Blue 3.3 was used to stitch three-dimensional BM tile scans obtained from animal calvariums and femur sections. A tilescan represents individual tiles fused to form an image. Fiji/Image J and Imaris software were used to visualise, process and analyse the tilescans.

For thresholding, segmentation and pixel quantification, a macro was used to create binary image that displays segmented pixels represented as a histogram obtaining the number of pixels above and below threshold. Size and circularity criteria were optimised based on the defined threshold. This was specifically set up for LepR+ and CellROX signal spots.

The vessel-lined endosteum was quantified by dividing the proportion of the vessel-lined endosteum by the total endosteum length.

To 3D reconstruct tile regions from the cortical bone and central bone marrow regions (CBM) Imaris software was utilised. For the vessels that appear less smooth in texture I refer to as "vessel roughness". Vessel roughness was calculated as Vessel roughness = vessel surface area/ vessel volume. For vessel length, the Imaris "filament" tool was used to manually draw all vessel surfaces. Filaments were represented as the vessel sum length. Lastly, area and volume quantifications in ECs and LepR+ PCs along with vessel roughness, which was defined as the irregular surface of the 3D reconstructed vessels, were obtained using the "surface" tools on Imaris.

2.10 Statistical analysis and reproducibility

For statistical analysis, raw data was visualised and processed using Microsoft Excel and GraphPad Prism. For transplant data or experiments that required multiple comparisons and as indicated in the figure legends, one-way or two-way ANOVA with post-hoc Tukey or Bonferroni corrections were used. For all other experiments, unpaired Student's *t*-test, was used to compare groups' means. Statistical differences were considered significant where (*) *p<0.05, (**) p<0.01; *** p<0.001; **** p<0.0001.*

2.11 Illustrated Figures

The majority of the illustrated images in the introduction were created with Biorender except Figure 1 and Figure 5 which were created with Adobe Illustrator. All other figures from Chapters 2-7 were created in Adobe Illustrator.

Table 2 List of Antibodies, chemicals, drugs, reagents, equipment, analysis software used for the project

Reagents/Chemicals/Buffers	Catalogue Number	Company	Clone
FACS Antibodies			
FITC anti-mouse/human CD45R/B220 Antibody	103206	Biolegend	RA3-6B2
FITC anti-mouse CD4 Antibody	100510	Biolegend	RM4-5
FITC anti-mouse CD5 Antibody	100606	Biolegend	53.7-3
FITC anti-mouse CD8a Antibody	100706	Biolegend	53-6.7
FITC anti-mouse Ly-6G/Ly-6C (Gr-1) Antibody	108406	Biolegend	RB6-8C5
FITC anti-mouse TER-119/Erythroid Cells Antibody	116206	Biolegend	TER-119
Brilliant Violet 421™ Streptavidin	405226	Biolegend	
PE/Cyanine7 anti-mouse CD48 [Clone: HM48-1] 100 µg	103424	Biolegend	HM48-1
Brilliant Violet 650™ anti-mouse CD150 (SLAM) Antibody	115931	Biolegend	TC15-12F12.2
Sca-1PerCP Cy5.5 anti-mouse Ly6A/E (Sca1)	108124	Biolegend	D7
Anti-Mouse EPCR Antibody, Clone RMEPCR1560 (1560)	60038PE	Stem Cell Technologies	RMEPCR1560 (1560)
APC/Cyanine7 anti-mouse CD117 (c-kit) [Clone: 2B8] 100 microg	105826	Biolegend	2B8
Brilliant Violet 785™ anti-mouse CD45 Antibody	103149	Biolegend	30-F11
CD45 BUV395 30-F11 50ug	564279	BD	30-F11
BUV395 anti-mouse CD4 Antibody	740208	BD	RM4-5
BUV395anti-mouse/human CD45R/B220 Antibody	563793	BD	RA3-6B2
BUV395 anti-mouse TER-119/Erythroid Cells Antibody	563827	BD	TER-119
BUV395 anti-mouse CD5 Antibody	740206	BD	53.7-3
BUV395 anti-mouse CD8a Antibody	563786	BD	53-6.7
BUV395 anti-mouse Ly-6G/Ly-6C (Gr-1) Antibody	563849	BD	RB6-8C5
Brilliant Violet 711TM anti-mouse CD45 [Clone: 30-F11] 50 microg	103147	Biolegend	30-F11
Fixable Viability stain 510	564406	BD Biosciences	
APC anti-mouse CD135 Antibody	135310	Biolegend	A2F10
Brilliant Violet 421™ Streptavidin	405225	Biolegend	
Fixable Viability Stain 780	565388	BD Horizon	
Brilliant Violet 510™ anti-mouse/human CD45R/B220 Antibody	103247	Biolegend	RA3-6B2
Brilliant Violet 510™ anti-mouse TER-119/Erythroid Cells Antibody	116237	Biolegend	116237
Brilliant Violet 510™ anti-mouse Ly-6G/Ly-6C (Gr-1) Antibody	108437	Biolegend	108437
Brilliant Violet 510™ anti-mouse CD4 Antibody	100553	Biolegend	100553
Brilliant Violet 510™ anti-mouse CD5 Antibody	100627	Biolegend	100627
Brilliant Violet 510™ anti-mouse CD8a Antibody	100751	Biolegend	53-6.7
CD201 (EPCR) Monoclonal Antibody (eBio1560 (1560)), APC, eBioscience	17-20120-82	eBioscience	1560
CD201 (EPCR) Monoclonal Antibody (eBio1560 (1560)), eFluor 710 eBioscience	46-2012-80	eBioscience	1560
CD144 (VE-cadherin) Monoclonal Antibody (eBioBV13 (BV13)), eFluor 660, eBioscience™	50-1441-82	ThermoFisher	50-1441-82

Ki67	564071	BD Biosciences	
SYTOX Green	M36008	Thermofisher	
PE/Cyanine7 anti-mouse CD45.1 Antibody	110730	Biolegend	A20
FITC anti-mouse CD45.2 Antibody	109806	Biolegend	104
APC anti-mouse CD3ε Antibody	100312	Biolegend	100312
Pacific Blue™ anti-mouse CD19 Antibody	115523	Biolegend	6D5
PE anti-mouse/human CD11b Antibody	101208	Biolegend	M1/70
Viability 780	565388	BD Horizon	
anti-CD45 microbeads, mouse 2ml	130-052-301	Miltenyi	
PerCP/Cy5.5 anti-mouse Ly-6A/E (Sca-1) Antibody	108124	Biolegend	D7
PE/Cy7 anti-mouse TER-119/Erythroid Cells Antibody	116221	Biolegend	TER-119
PE/Cy7 anti-mouse CD31 Antibody	102524	Biolegend	MEC13.3
Alexa Fluor® 700 anti-mouse CD45.2 Antibody	109821	Biolegend	104
CD140a (PDGFRA) Monoclonal Antibody (APA5)	17-1401-81	Thermofisher	APA5
Mouse Leptin R Biotinylated Antibody	BAF497	R&D Systems	
BUV395 Rat Anti-Mouse CD51	747834	BD	RMV-7
Mouse ALCAM/CD166 PE-conjugated Antibody	FAB1172P	R&D Systems	
BV421 Streptavidin	405226	Biolegend	
Commercial Assays			
CellROX™ Deep Red Reagent, for oxidative stress detection	C10422	Thermofisher	
CellROX® Green Reagent	C10444	Thermofisher	
Click-iT™ EdU Alexa Fluor™ 647 Flow Cytometry Assay Kit	C10424	Thermofisher	
mitoSOX Red	M36008	Invitrogen	
MitoTracker Green	M7514	ThermoFisher	
TMRM Assay Kit for Flow Cytometry	M20036	Thermofisher	
Chemicals			
EZ-Link™ Sulfo-NHS-LC-LC-Biotin Thermo Scientific PI21338; 50mg	21338	Thermofisher	
Doxycycline	D9891-5G	Sigma	
N-Acetyl-L-cysteine	A7250-5G	Sigma	
EdU (5-ethynyl-2’-deoxyuridine)	A10044	Thermofisher	
GIEMSA	48900-500ML-F	Sigma	
Solutions			
EDTA 0.5M pH8.0 +/-1 (100mL)	46-034-Cl	Corning	0.5 M stock
Dulbecco's Phosphate Buffered Saline,Modified, without calcium chloride and magnesium chloride	D8537	Sigma Aldrich	
Alsever's Solution	A3551	Sigma Aldrich	
BD Cytofix Cytoperm	561651	BD Bioscience	
DMEM	Gibco	11960-044	
Drugs			
Parathyroid Hormone	4012212	Bachem	rat PTH 1-34
Phenylhydrazine	P26252	Sigma	
Atovaquoe	A7986-50MG	Sigma	
Cryosectioning			

CFSA Cryojane adhesive slides	39475208	Leica Biosystems	
Cryojane Adhesive Tape Windows	39475214	Leica Biosystems	
Immunostaining			
Mouse Leptin R Biotinylated Antibody	BAF497	R&D Systems	
Purified anti-mouse CD117	105802	Biolegend	2B8
Streptavidin, Alexa Fluor™ 647 conjugate	S-32357	Thermofisher	
Normal donkey serum	ab7475	Abcam	
horse serum	31874	Life Technologies	
DAPI	D9542	Thermofisher	
Prolong Antifade Diamond Mountant	P36961	Thermofisher	

Chapter 3

Haematopoietic perturbations during *P.berghei* infection

3.1 Introduction

During steady state (health), LT-HSCs occasionally proliferate and differentiate to replenish downstream haematopoietic cell lineages, therefore maintaining haematopoiesis. Excessive stress imposed on LT-HSCs leads to detrimental effects on their functional properties consequently driving the disorganisation of the haematopoietic landscape. As shown previously, functional HSCs were severely depleted in animals infected with *Mycobacterium avium*, which causes pulmonary infection that resembles tuberculosis, depriving their repopulation capacity (Baldridge *et al.*, 2010). Furthermore, chronic infection drives exhaustion of the HSC compartment which is attributed to INF-γ, a product of the ensuing immune response and associated with HSC loss (Matatall et al., 2016). Other groups defined the effects of pathogens or viral infection on HSCs through the administration of lipopolysaccharide (LPS) or polyinosinic:polycytidylic (pI:pC) respectively (Boettcher et al., 2012; Zhang et al., 2016; Ostrander et al., 2020; Bogeska et al., 2022; Jacobs et al., 2022; Nguyen, Abidin and Heinonen, 2022; Grusanovic et al., 2023). While these studies showed attrition of HSC function and a phenotype associated with aged haematopoiesis (Bogeska *et al.*, 2022; Nguyen, Abidin and Heinonen, 2022), they were based on the artificial administration of biological agents rather than a natural route of infection. Natural stressors like *Plasmodium* infections recapitulate disease progression more accurately and translate more directly to human medicine.

To investigate infection-driven changes on HSCs, their downstream cell lineages and the BM niche, our research group employed *P. berghei* parasite that induces malaria in rodents. *P. berghei* is comparable with *P. falciparum's* pathogenesis in humans making it a robust model

to study the effects of severe malaria on haematopoiesis. Based on published work from our group, animals exposed to infected mosquitos carrying *P. berghei* parasite dramatically expanded their HSPC populations, which was coupled with early signs of anaemia (Vainieri et al., 2016). In a second study, the Lo Celso group showed that the primitive HSPC compartment shrunk substantially during malaria infection and that these changes were attributed to the increase of INF-γ in infected animals (Haltalli *et al.*, 2020). Furthermore, the BM microenvironment was shown to contain leaky vessels, suggesting that vascular permeability and increased ROS may be one of the mechanisms by which HSCs are lost during *P. berghei* infection (Haltalli *et al.*, 2020). Furthermore, ROS scavenger, *N*-acetyl-L cysteine (NSC), administration indicated a reduction of ROS in MPPs and HSPCs compared with untreated infected animals (Haltalli *et al.*, 2020). Parathyroid hormone (PTH) coupled with NAC reduced the proportion of proliferating HSPCs (Haltalli *et al.*, 2020) though it did not safeguard their function. Together, these studies did not address whether there may be a cell-intrinsic mechanism regulating HSC loss. While it is prominent that the majority of HSCs respond to infection/inflammation; the remainder of cells in the HSC pool were shown to have poor reconstitution ability following transplantation. Driven by the emerging evidence of heterogeneity within the HSC compartment, I specifically addressed whether a proportion of HSCs may maintain an unresponsive status towards infection and whether targeting the microenvironment could improve their function.

In this chapter, I establish a blood infection system avoiding animal exposure to infected mosquitos. Working with a more robust system, I ensure that the parasitaemia detected in the blood smears of infected animals is consistent and disease progression is even across all mice. Based on the functional distinction between SLAM HSPCs ($CD48^{neg/low}$) and $CD48^{neg}$ HSCs (Akinduro *et al.*, 2018), I studied $CD48^{neg}$ HSCs throughout this and subsequent chapters. Moreover, through transplantation assays, I question whether the remaining phenotypic LT-HSCs are still functional and whether pharmacological interventions targeting the osteolineage could rescue HSC functionality. FACS sorted $Lin^{-}cKit^{+}$ (LK) and $CD48^{neg}$ HSCs from infected and uninfected donor animals were transplanted into lethally irradiated syngeneic recipients. Transplanted cells were followed for 16 weeks and estimation of donor-derived cell engraftment and multilineage reconstitution was determined through FACS analysis of recipients' PB.

3.2 *P. berghei* as a natural infection model to study stress haematopoiesis

It was previously shown that animal exposure to *P. berghei* infected mosquitos drove changes in the HSPCs and recapitulated the natural development of the disease (Vainieri et al., 2016a; Haltalli et al., 2020); however logistically it was very demanding. Given that changes in the HSC niche were not detectable during the liver-stage (up to day 3 post sporozoite infection, *psi*), I worked towards establishing a robust blood infection system that delivered more consistent infection across all animals. Following infection of parasitised RBCs, malaria symptoms take around 5-6 days to manifest in the blood system compared to mosquito bite infection which took around 7-10 days. Low passage (P0) infected blood was thawed from stocks and injected intraperitoneally (*i.p*) into a donor mouse and five days post-infection, when parasitaemia reached 2-3% infected PB RBCs, P1 blood was collected and used to set up the experimental cohort (Figure 3.1 A). Passaged blood contains either ring stages, trophozoites or schizonts, that mark different asexual stages of the parasite. Mature schizonts burst and release merozoites invading host RBCs while other merozoites commit to producing gametocytes (Venugopal *et al.*, 2020).

First, I elucidated whether by skipping the liver stage of disease the HSC compartment will be equally affected by malaria pathogenesis. Visible signs of cerebral malaria developed 6 days post blood injection (*pbi*) hence my studies were focused on the first 5 days *pbi*. To determine the proportion of parasitaemia in peripheral blood (PB), blood was collected from the tail vein of animals and Giemsa-stained thin film smears were prepared. In animals injected *i.p* with infected blood, parasitaemia reached >3% in PB (Figure 3.1 B) at day 5, which was consistent with the mosquito bite model where parasitaemia reached between 3-5% (Haltalli et al., 2020) at day 7. Thereafter, I moved towards the characterisation of HSC pool through the phenotypic expression of cell surface markers such as Lineage cocktail, c-kit, SCA-1 and SLAM markers to identify HSCs as LKS $CD150^{+}CD48^{neg}$ (hereafter $CD48^{neg}$ HSCs). In infected animals, SCA1 was upregulated, hence the increased proportion of cells within the LKS gate, containing multipotent stem and progenitor cells along with HSCs (Figure 3.1 C), agreeing with previous findings from our group and others(Baldridge et al., 2010; Vainieri et al., 2016a; Haltalli et al., 2020). Moreover, malaria infection diminished HSC numbers as both the proportion and

number of CD48^{neg} HSCs were decreased suggesting their differentiation and/or possible depletion from the BM. This again was consistent with observations made at day 7 post-sporozoite infection (*psi*) in previous studies (Haltalli *et al.*, 2020).

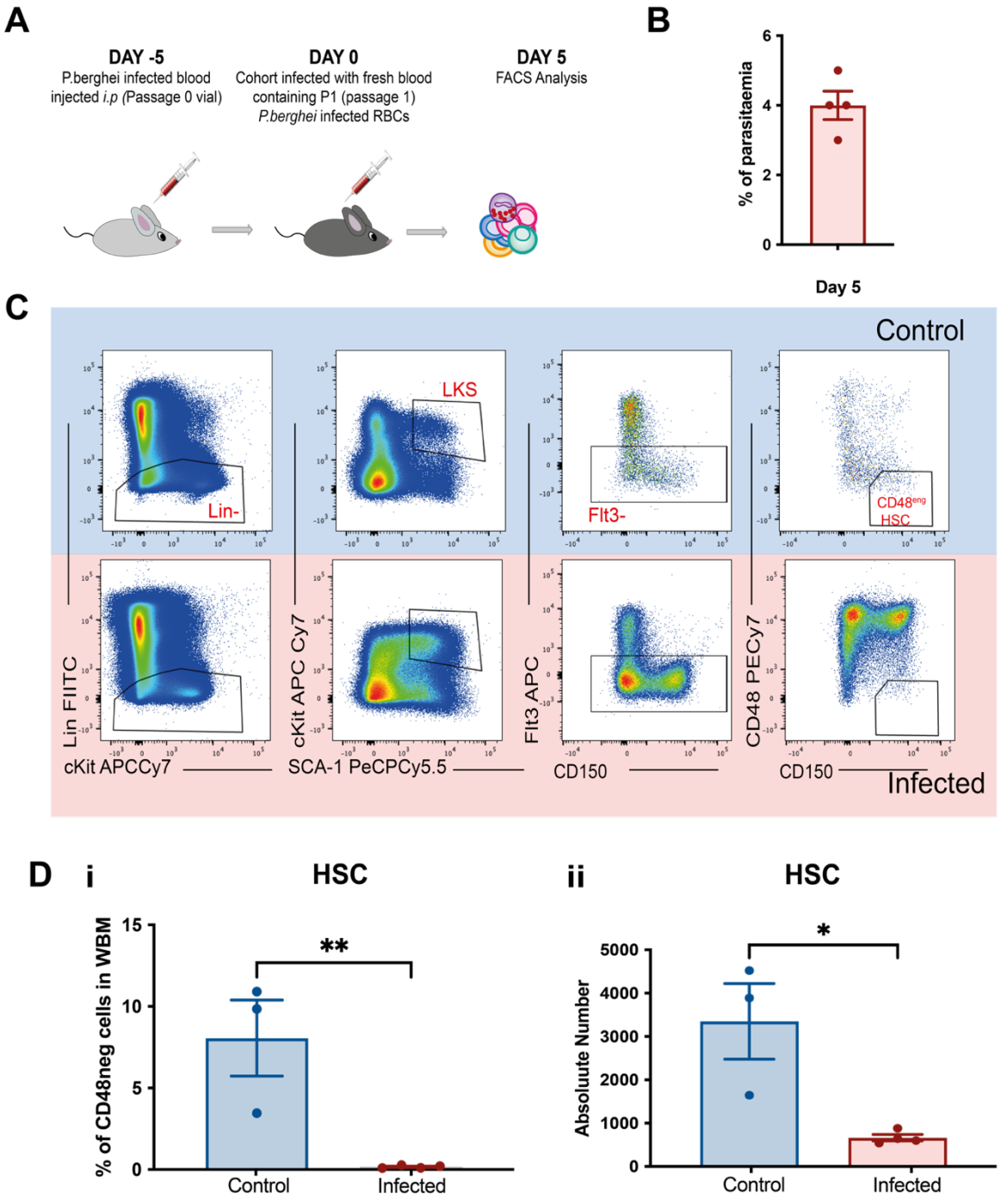
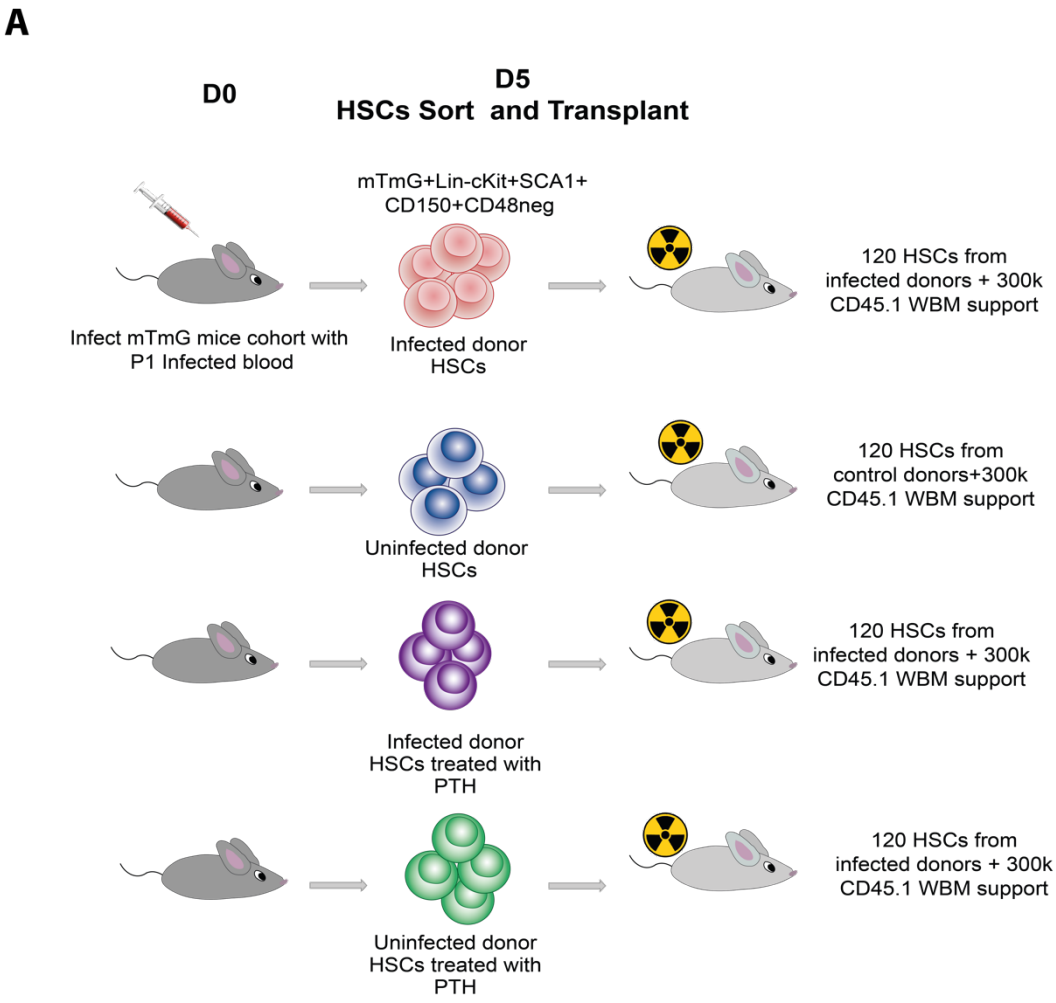


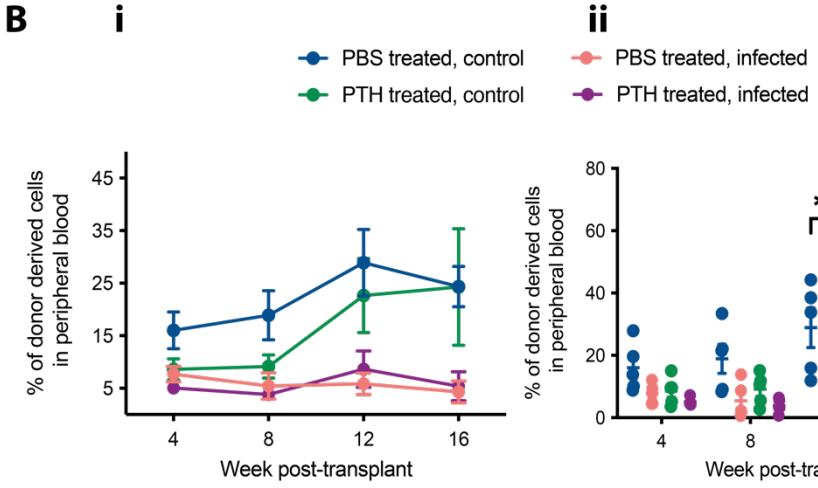
Figure 3. 1 Malaria infection induction through injection of *P. berghei* infected RBCs. A) Experimental set up. Passage 0 blood (P0) is injected into a donor mouse. Five days post blood injection (*pbi)* blood is collected through cardiac puncture and injected *i.p* in experimental animals. B) Parasitaemia quantification based on Giemsa-stained PB smears. C) Gating strategy for the identification of CD48^{neg} HSCs by flow cytometry of mouse BM. D) Frequency (i) and absolute numbers (ii) of CD48^{neg} HSCs in WBM live cells at day 5 *pbi* measured by flow cytometry in infected and healthy animals. Each dot represents one mouse. Error bars represent the mean ± s.e.m. Statistically significant differences were determined using Student's t-test. (** represent P ≤ 0.01; * P<0.05).

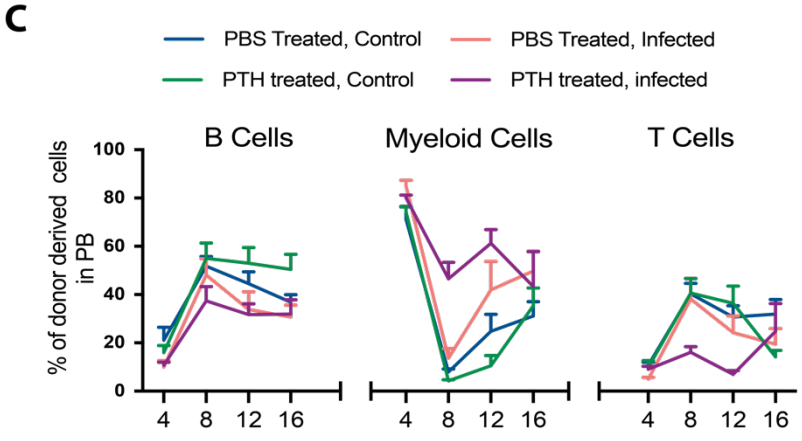
Taken together, these data highlight the robustness of the blood infection system and the changes in the HSCs and multipotent progenitors (LKS) associated with it, therefore recapitulating disease progression regardless of liver-stage.

3.3 PTH treatment does not rescue HSC function

Osteoblasts serve as regulators of HSC niche and treatment with parathyroid hormone (PTH) led to increased osteoblasts numbers which was associated with Notch-mediated activation and expansion of HSCs (Calvi *et al.*, 2003; Calvi and Link, 2015). PTH stimulates osteoblast proliferation and drives osteoblast progenitor differentiation (Calvi *et al.*, 2003; Calvi and Link, 2015). Our group demonstrated that during malaria infection osteoblasts are lost, suggesting that not only haematopoietic cells are affected but BM niche components too (Haltalli *et al.*, 2020). Treatment with PTH rescued osteoblast numbers in infected animals though it did not rescue the function of $CD48^{low}$ SLAM HSPCs (Haltalli *et al.*, 2020). As mentioned above, $CD48^{neg}$ HSCs are a small subpopulation of SLAM HSPCs more enriched for functional HSCs (Akinduro et al., 2018) and while their numbers were reduced in PTH-treated, infected mice (Haltalli *et al.*, 2020), their function specifically had not been tested. In this section, I aim to investigate whether pharmacological targeting of the osteolineage cells with PTH may control HSC proliferation and rescue primitive $CD48^{neg}$ HSC function. Therefore, I treated infected/uninfected donor animals that express a membrane-targeted Tomato (mT/mG) across all cells and tissues, with PBS- or PTH. To accomplish this, 120 $CD48^{neg}$ HSCs were extracted from infected animals at day 5 post blood infection (*pbi)* or control healthy mice, sort purified and transplanted into lethally irradiated CD45.1 recipients receiving 300K whole bone marrow (WBM) support (Figure 3.2 A). While irradiation eliminates a large proportion of haematopoietic cells and BM stromal cells, transplanted HSCs with stem-like properties will have the capacity to engraft and reconstitute (self-renew and differentiate) the recipient's haematopoietic system over a period of 16 weeks in a primary (Figure 3.2 B) and secondary (and even tertiary) transplants.


A
D0
D5
HSCs Sort and Transplant
mTmG+Lin-cKit+SCA1+
CD150+CD48neg
Infect mTmG mice cohort with
P1 Infected blood
Infected donor
HSCs
120 HSCs from
infected donors + 300k
CD45.1 WBM support
Uninfected donor
HSCs
120 HSCs from
control donors+300k
CD45.1 WBM support
Infected donor
HSCs treated with
PTH
120 HSCs from
infected donors + 300k
CD45.1 WBM support
Uninfected donor
HSCs treated with
PTH
120 HSCs from
infected donors + 300k
CD45.1 WBM support


B
i
ii
PBS treated, control
PTH treated, control
PBS treated, infected
PTH treated, infected
% of donor derived cells
in peripheral blood
Week post-transplant
*
*


C
PBS Treated, Control
PTH treated, Control
PBS Treated, Infected
PTH treated, infected
B Cells
Myeloid Cells
T Cells
% of donor derived cells
in PB

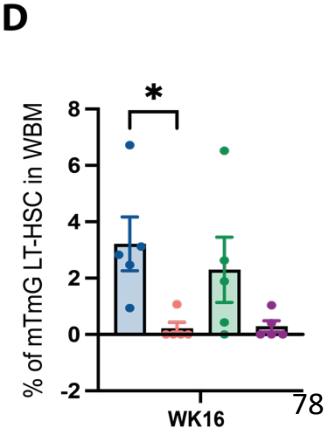

D
*
% of mTmG LT-HSC in WBM
WK16

Figure 3. 2 PTH treatment did not rescue HSC function. A) Experimental set up where 120 CD48^{neg} HSCs sorted from PTH/PBS healthy/*P berghei* infected mTmG donor animals and injected into lethally irradiated CD45.1 recipients supplemented with an extra 300,000 CD45.1 WBM support. B) Frequency of tomato+ cells measured in recipients' PB over time, with i) showing the average reconstitution and ii) reconstitution in each mouse individually per condition. C) Multilinegae output measured through B,T and Myeloid cells from donor derived HSCs. D) WBM analysis of recipients showing HSC as perecentage of live cells at wk16. Data pooled from two independed experiments. Error bars represent mean ± s.e.m. Statistically significant differences were determined using two way ANOVA with Bonferroni correction. (* represents P<0.05). No statistsically differences were found between PTH/PBS infected animals.

To identify donor derived cells, PB from recipients was stained for T, B and myeloid cells markers and analysed by flow cytometry at different time points. Normally after transplantation, haematopoiesis reaches "steady-state" up to week 8 and by week 16 the progeny observed in PB is the result of LT-HSC engraftment. According to Figure 3.2 B, by 16 weeks post-transplant, there was no difference in the engraftment of HSCs from PBS/PTH treated control mice, nor in that of HSCs from PBS/PTH treated infected mice, however, all HSCs harvested from infected mice showed poor engraftment (Fig 3.2 B). Moreover, multilineage reconstitution, which was measured through the proportion of donor-derived myeloid, T and B cells, showed no differences between any of the conditions, apart from HSCs from PTH treated, infected donors giving rise to more myeloid and fewer T cells in the short term (Figure 3.2 C). Interestingly, the highest myeloid reconstitution was observed at week 4 across all conditions, which was expected given that transplanted HSCs will differentiate into downstream multipotent progenitors. Analysis of whole bone marrow (WBM) from recipients of PTH and PBS treated infected donor cells, revealed reduced HSC numbers compared to the recipients of uninfected PTH- and PBS- treated donor cells (Figure 3.2 D) that prompts to a previous finding in which osteoblast rescue upon PTH treatment was not associated with HSC function (Haltalli *et al.*, 2020).

To reveal true stemness of transplanted HSCs from the primary transplanted mice, secondary recipients were lethally irradiated and injected with one million WBM harvested from primary reconstituted recipients (Figure 3.3 A). WBM derived from PTH- or PBS-treated infected primary recipients achieved low engraftment compared to PTH- or PBS-treated control donor derived cells (Figure 3.3 B). In agreement with the primary transplant, HSCs from PTH treated, infected donors gave rise to more myeloid and fewer T cells (Figure 3.3 C). Moreover, there were no differences detected in the B and T lineage output of HSCs derived from cells purified from PBS/PTH treated control/infected animals (Figure 3.3 C).

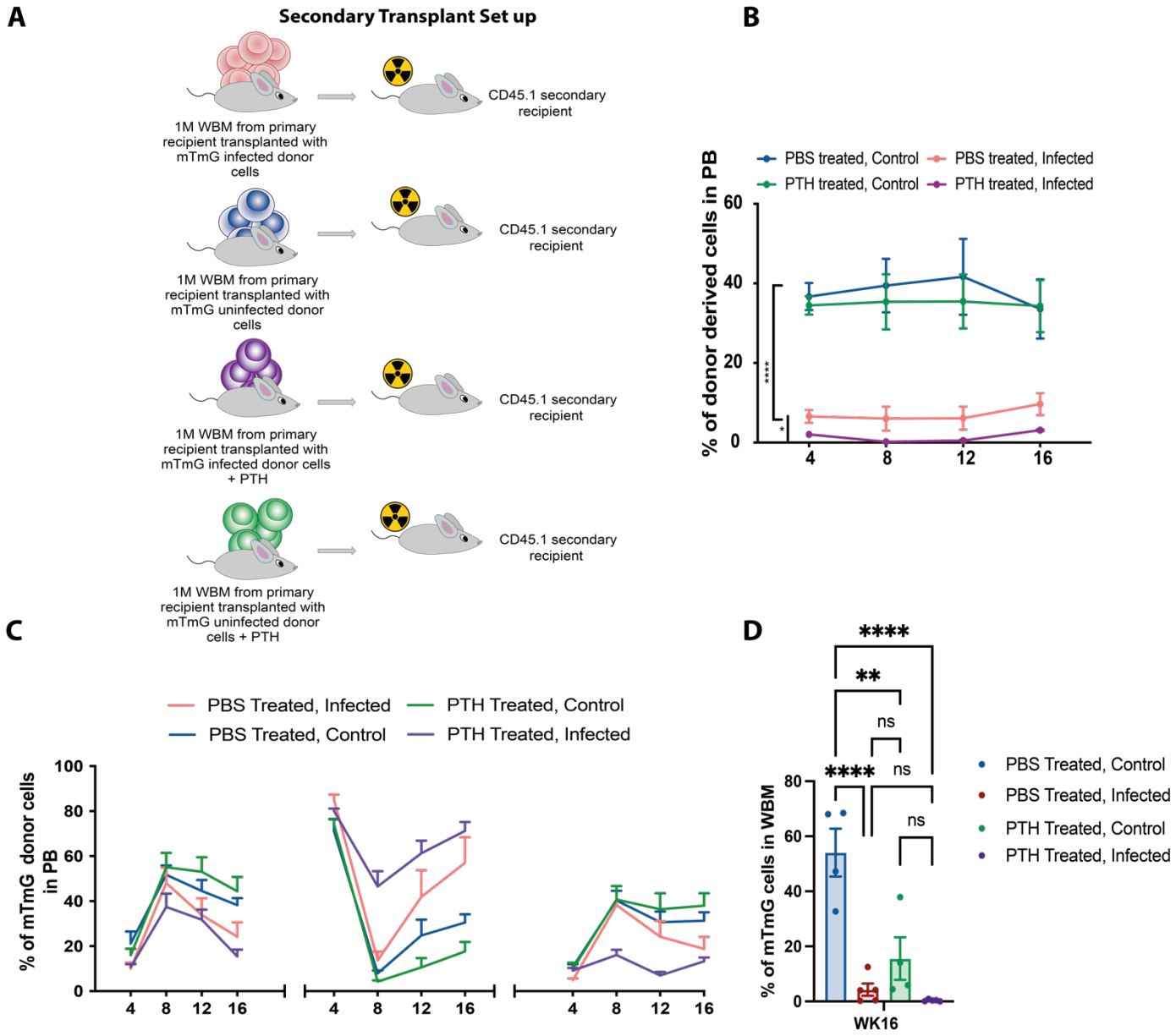


Figure 3. 3 HSC self-renewal is severely affected during *P. berghei* infection. A) Experimental set-up where 1M WBM primary recipient cells per condition were injected into secondary recipients. B) Proportion of donor derived cells in secondary recipients' PB over a period of 16 weeks. C) Multilineage reconstitution assessed by the percentage of tomato+ , T and Myeloid Cells in PB. D) Proportion of tomato+ cells in whole bone marrow (WBM). Error bars represent mean ± s.e.m. Statistically significant differences were determined using two-way ANOVA with Bonferroni correction. ****represent P ≤ 0.0001;** represent P ≤ 0.01; * P<0.05

WBM analysis of all recipients at week 16, revealed a dramatic reduction of tomato+ cells from primary PBS- and PTH-treated infected donors (Figure 3.3 D) indicating that these HSCs were ST-HSCs. PTH not only increased the number of osteoblasts in stromal structures but also led to the primitive haematopoeitic cell expansion *ex vivo* which was attributed to Notch activation (Calvi *et al.*, 2003). It is likely that upon PTH treatment, the primitive HSCs in

uninfected donors were activated affecting their stemness. Treatment with PTH not only led to their transient engraftment in the primary transplantation setting but also to a limited self-renewal ability showed in the secondary transplant (Figure 3.3 D) which was unexpected.

In conclusion, infection severely affected LT-HSCs but PTH treatment too. Pharmacological intervention of the osteolineage with PTH did not aid towards HSC functional rescue prompting to cell-intrinsic mechanisms possibly playing a significant role in the phenotypes observed.

3.4. Malaria infection severely affects HSC self-renewal

HSC stemness is severely affected by *P. berghei* infection which has an impact on HSC transcriptional identity too (Haltalli *et al.*, 2020). Single-cell RNA sequencing data performed on Lineage$^-$ c-Kit$^+$cells from control mice and mice at day 7 post sporozoite infection (*psi*), revealed decreased HSC scores (calculated based on a deep learning model based on HSC score database (Wilson et al., 2015) and substantial rewiring of haematopoiesis towards myeloid and basophil lineages (Haltalli *et al.*, 2020).

To investigate extensive loss of HSC transcriptional identity, 272 x 10^3 and 160 x 10^3 Lineage$^-$ c-kit$^+$ cells were extracted from infected animals at day 5 post blood infection (*pbi)* or control healthy mice sort purified and transplanted into lethally irradiated CD45.1 recipients receiving 300,000 whole bone marrow (WBM) support (Figure 3.4 A). The number of Lineage$^-$ c-kit$^+$ cells per condition was back-calculated to contain 120 CD48^{neg} HSCs to consistently match section 3.3 of this chapter. To identify donor derived cells, PB from recipients was stained for lineage markers (T, B and myeloid cell) and analysed by flow cytometry at different time points. The engraftment ability of donor cells was measured by the percentage of tomato+ cells in PB. Hence, transplanted cells purified from infected donors had reduced engraftment compared to control donor cells (Figure 3.4 B). Moreover, CD48^{neg} HSC lineage output showed no differences between any of the conditions (Figure 3.4 C). Interestingly the highest myeloid reconstitution was observed at week 4 in recipients injected with cells purified from infected

animals, which was expected given that transplanted HSCs will differentiate into downstream MPPs.

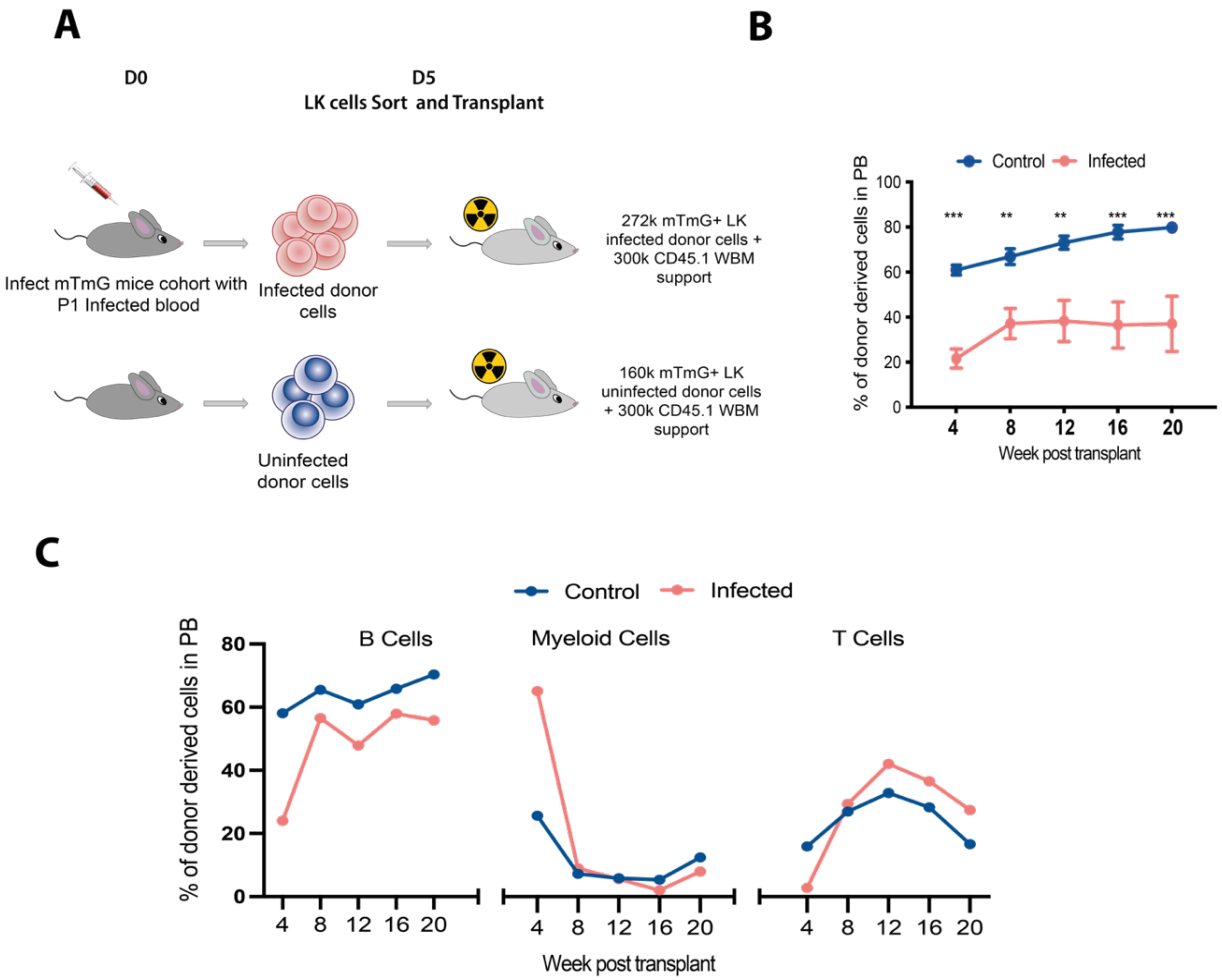


Figure 3. 4 HSCs display reduced engraftment after severe infection. A) Experimental set up where 272,000 and 160,000 sorted from healthy/ *P berghei* infected mTmG donor animals and injected into lethally irradiated CD45.1 recipients supplemented with an extra 300,000 CD45.1 cells. tomato+ LK and purified from infected and healthy donors. B) Percentage of tomato+ cells measured in recipients PB over time. C) Multilineage reconstitution measured through B, T and Myeloid cells from donor derived HSCs. Error bars represent mean ± s.e.m Statistically significant differences were determined using Student's *t* test. For multiple comparisons multiple comparisons test was used. *** represent P ≤ 0.001;** represent P ≤ 0.01.

To confirm that malaria severely affects haematopoiesis and that *P. berghei* infection deprives LT-HSCs from their stemness, I set-up a secondary transplant in which 3 x10^6 WBM cells from primary recipients were transplanted into lethally irradiated CD45.1 secondary recipients (Figure 3.5 A). As expected, the engraftment output as measured in PB of transplanted cells purified from infected donor cells was very low (Figure 3.5 B, C). Surprisingly, when multipotency was measured based on the proportions of B, T and myeloid cells in PB, myeloid cell output was low in the infected population at week 4 (Figure 3.5 C).

The data from all transplants, revealed that reconstitution from HSCs from infected animals is not completely abolished, prompting to investigate whether an even smaller population of HSCs may survive infection-derived stress.

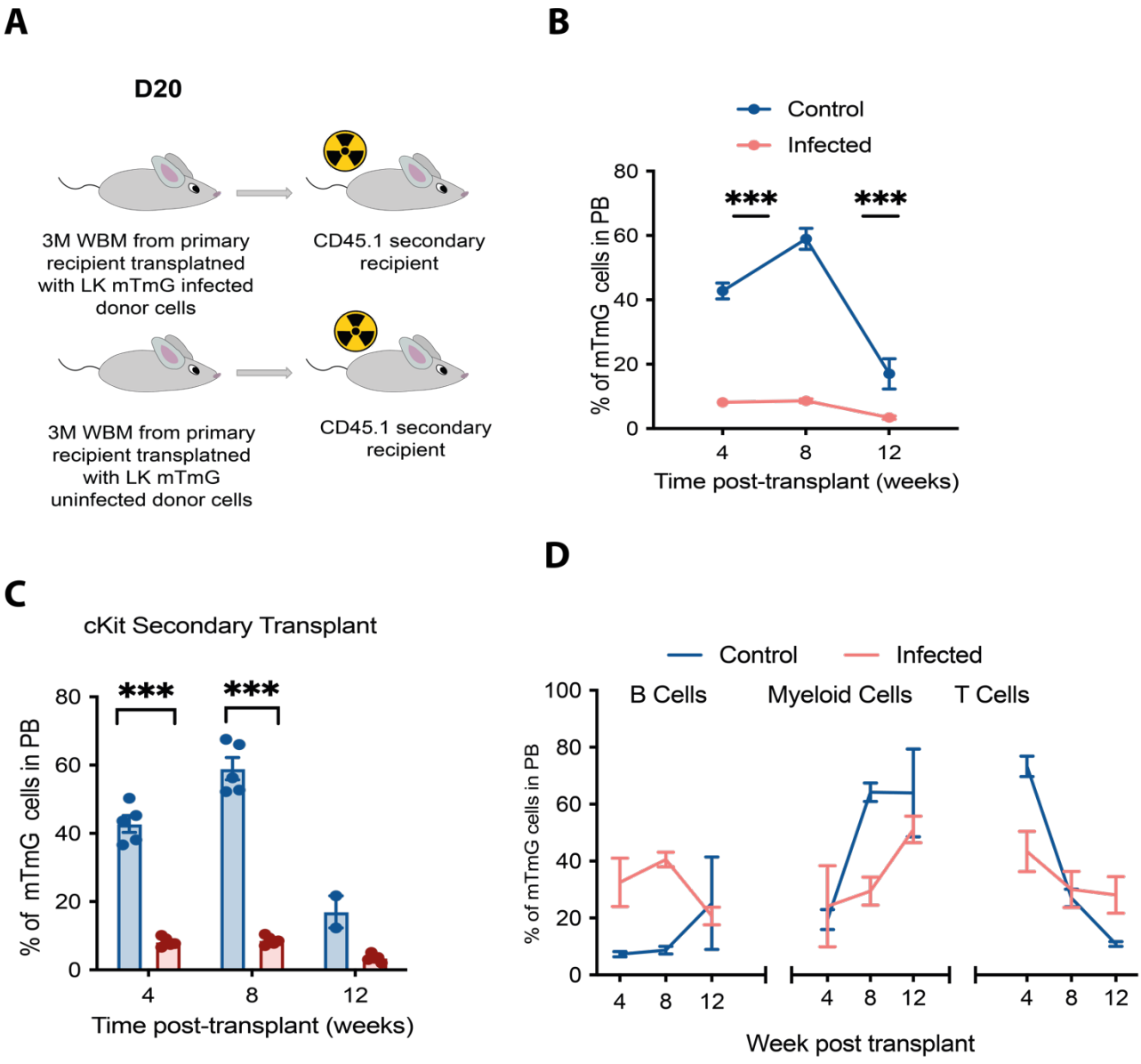


Figure 3. 5 Lineage- c-kit+ transplant shows reduced HSC self-renewal: A) Experimental set-up where 3x10^6 WBM from healthy/*P berghei* infected mTmG primary recipients is injected into lethally irradiated CD45.1 recipients supplemented with an extra 300,000 CD45.1 WBM support. Donor derived cells were measured as the proportion of tomato+ cells in PB over time with B) showing the average reconstitution and C) reconstitution in each mouse individually per condition. D) Multilineage output measured through B,T and Myeloid cells from donor-derived HSCs. Error bars represent mean ± s.e.m. Each individual dot represents a single replicate. Statistically significant differences were determined using Student's *t*-test. For multiple comparisons, multiple comparisons test was used.(*** represent P ≤ 0.001)

3.5 Discussion

The aims of this chapter were to gain a deeper perspective into the effects of *P. berghei* blood infection on primitive HSCs. Firstly, I established a blood infection system that gives consistent parasitaemia across all animals and within a shorter period of time, recapitulating haematopoietic perturbations. Previous published data from the Lo Celso lab showed that multiple cell populations of the haematopoietic hierarchy including primitive HSCs responded to *P.berghei* mosquito bite infection with an increase in proliferation (Vainieri et al., 2016b; Haltalli et al., 2020). Proliferation was evident in the LKS compartment through its increased size (SCA1 upregulation) and was further studied in detail using BrdU and EdU incorporation measurements (Haltalli *et al.*, 2020). Furthermore, HSC proliferation is controlled through the interaction of osteoblasts and HSCs at the endosteal surface (Nilsson *et al.*, 2005). Since *P. berghei* infection led to a dramatic loss of osteoblasts during sporozoite infection, through IVM our group demonstrated that PTH treatment, known to stimulate osteolineage cells proliferation and differentiation (Calvi *et al.*, 2003), partially rescued osteoblasts number in infected mice (Haltalli *et al.*, 2020). While positive outcome was seen on the osteoblasts previously (osteoblast rescue) (Haltalli *et al.*, 2020) I asked whether $CD48^{neg}$ HSCs surviving in PTH treated, infected mice could still be functional. PTH did not have an effect in safeguarding HSCs from proliferation which subsequently led to a reduction in HSC engraftment and self-renewal confirming previous findings (Haltalli *et al.*, 2020). The lack of functional recovery was reported in inflammatory challenges where LT-HSCs functionality was studied. After pI:pC exposure, HSCs carried transcriptional signatures relating to ageing (Bogeska *et al.*, 2022). Moreover, impairment in HSC self-renewal was also noted in *Mycobacterium avium* infection in which INFγ induced HSC differentiation which was linked to *Batf2* transcription factor (Matatall *et al*., 2016; Florez *et al*., 2020). These studies agree with the findings from this chapter prompting to investigate whether a more quiescent subset of HSCs may survive infection-derived stress.

Single-cell RNA sequencing analysis of $Lineage^{-}$ $c\text{-}kit^{+}$cells extracted from sporozoite mosquito bite infected animals, revealed a reduced HSC scoring, loss of HSC transcriptional identities (Wilson et al., 2015) and substantial rewiring of haematopoiesis towards myeloid and basophil

lineages (Haltalli *et al.*, 2020) in the expense of primitive HSPCs (a mixture of HSCs $CD48^{neg/low}$ and MPPs) and megakaryocytes (Haltalli *et al.*, 2020). Based on this, sort purified $Lineage^{-}$ c-kit^{+}cells from healthy and infected donors were transplanted into lethally irradiated recipients. The results reveal a reduction of HSC repopulation ability of cells purified from infected donors confirming that the HSC transcriptional identity is lost hence agreeing with previous sc-RNA sequencing data (Haltalli *et al.*, 2020).

In conclusion, *P. berghei* infection imposes a huge stress on LT-HSC compartment since they are primed to respond. Repetitive HSC activation may induce transcriptional changes which are linked to HSC attrition (Essers *et al*., 2009) and ageing phenotypes (Matatall *et al*., 2016; Hormaechea-Agulla *et al.,* 2021). The changes observed, such as the limited repopulation ability of HSCs in the transplants, might be associated with DNA damages due to HSC proliferation as a response to *P. berghei* infection. It was shown previously that mammalian cells manage DNA repairs by pausing the replication fork and actively converting it into a reverse replication fork to fix the errors before restarting DNA synthesis (Jacobs *et al.*, 2022). Whether the DNA machinery in HSCs is unable to fix DNA repairs and if that is associated with their stemness could be a potential avenue to explore. HSCs loss is not attributed to apoptosis since preliminary experiments from Annexin V and Caspase 3 were inconclusive (data not shown here) based on the high proportion of Annexin V+ cells not only in the infected but also in control animals. There is a possibility that some HSCs die, while others survive stress.

In conclusion, HSC engraftment observed in the transplant was reduced and not zero which prompted me to investigate whether an even smaller population of HSCs may survive infection-derived stress.

Chapter 4

A subset of primitive HSCs maintain their stemness despite INFγ

4.1 Introduction

During homeostasis HSCs reside in a quiescent state and only occasionally proliferate and/or differentiate into downstream lineage-biased cells, and these fate choices and the rate at which they happen change as a response mechanism to stress. Dormant HSCs are preserved in a low glycolytic state (de Almeida et al., 2017; Zhang, Menzies and Auwerx, 2018; Papa, Djedaini and Hoffman, 2019; Hinge et al., 2020; Liang et al., 2020),being dependant on autophagy (Mortensen *et al.*, 2011; Ho *et al.*, 2017) and are marked by low metabolic activity (Vannini et al., 2016; Ansó et al., 2017; Papa, Djedaini and Hoffman, 2019; Haltalli et al., 2020) and low oxidative phosphorylation (Fernández-Vizarra *et al.*, 2022; Kirova *et al.*, 2022). Dormancy is also associated with hyaluronic acid GPRC5C signalling (Zhang *et al.*, 2022), vitamin A-retinoic acid signalling (Cabezas-Wallscheid *et al.*, 2017) and low levels of p57 and Myc (Laurenti *et al.*, 2008; Cabezas-Wallscheid *et al.*, 2017).

As discussed in Chapter 1, transplantation assay is a powerful tool to determine whether HSCs are capable of repopulating primary and secondary recipients for more than 16 weeks. If repopulation occurs, then HSCs are considered to have long-term function and high self-renewal capacity. On the contrary, cells that produce multilineage output but engraft transiently in a primary set-up are downstream populations, such as ST-HSCs or MPPs. Experiments based on single cell transplants led to identification of variability in reconstitution kinetics within HSC subpopulations (Sanjuan-Pla *et al.*, 2013; Carrelha *et al.*, 2018) and of lineage-biased HSCs. Moreover, heterogeneity is also found when looking at the length of time an HSC spends in quiescence or cycling as reported in label-retaining cell studies (LRCs) (Wilson et al., 2008a). Analysis of single cell transcriptomes revealed that heterogeneity is

associated with differences in cell-cycle status since slow-cycling HSCs correlated with enriched LRCs (Lauridsen *et al.*, 2018). It is now apparent that HSCs respond to infection/inflammation via PRRs which detect DAMPs and PAMPs or get activated by proinflammatory cytokines released by immune cells. Numerous studies, as depicted in Table 3, investigated the direct impact of chronic infection or inflammation and their consequences on HSCs. Responses to several types of infection/inflammatory stress share common features, for example, decline of HSC function, impacting their repopulation capacity. Inflammatory cytokines also act on HSCs either directly or through the BM microenvironment, which serve as a secondary inflammatory signal on HSCs (Caiado, Pietras and Manz, 2021; Luis *et al.*, 2023). Several insults initiate the disruption of HSC quiescence and promote excessive terminal differentiation through IFN signalling axes. The Lo Celso research group and others reported that excess proliferation led to a decline in the repopulation ability of HSPCs which was transcriptomically associated with interferon-related genes (IRGs) (Baldridge et al., 2010; Matatall et al., 2016; Haltalli et al., 2020). Similarly, chronic exposure of HSPCs to IFNα resulted in their activation leading to their functional attrition (Essers et al., 2009a; Haas et al., 2015; Bogeska et al., 2022). IFNs also act indirectly on HSPCs through BM stroma that senses and responds to elevated levels of IFNγ (Haltalli *et al.*, 2020). Osteolineage is dramatically depleted in response to IFNγ with HSPCs found proximal to leaky vessels that possibly correlate with high ROS (Haltalli *et al.*, 2020). Lastly, IFNγ stimulation facilitates displacement of HSCs from CXCL12-abundant reticular cells (CAR), associated with increased expression of BST2, which binds with high affinity to the vascular endothelial cell ligand E-selectin (Florez et al., 2020).

It is visible from the literature summarised in Table 3 that after an acute or chronic inflammatory stress most of the LT-HSCs will be depleted and those that remain will be dysfunctional. While in Chapter 3 I reported a nearly complete loss of repopulation capacity of transplanted $CD48^{neg}$ SLAM HSCs, in this chapter I aim to dissect out LT-HSC heterogeneity by further characterising the HSCs within the surviving quiescent pool. Motivated by my hypothesis from Chapter 1 and given the reported heterogeneity in the HSC compartment, I question if *P. bergei* infection drives heterogeneous HSC responses marked as $EPCR^{+}$ $CD48^{neg}$, hereafter E-SLAM HSCs and whether a proportion of E-SLAM cells may remain unresponsive to IFNγ challenge and maintain their stem cell properties.

Secondly, I utilised an injectable NHS-ester-LC-LC-biotin probe as reported previously (Nygren and Bryder, 2008a; Luis *et al.*, 2023b) which allows to mark proliferation kinetics in cells using flow cytometry analyses where fluorophore-conjugated streptavidin is used to measure the degree of label on the cells of interest. Immediately after injection of the probe, all cells are brightly labelled. After a few rounds of proliferation, there is a linear reduction of biotin distributed on the daughter cell membranes. This biotin system aided towards identifying two sub-populations within the E-SLAM HSC pool that proliferate either minimally or not, which I refer to as E-SLAM Biotin^{Hi}, or cells that already proliferated, E-SLAM Biotin^{Lo}. Thirdly, using the thymidine analog EdU to mark cells in the replication phase of cell cycle (S phase), I marked the majority of E-SLAM^{Lo} cells and a proportion of E-SLAM Biotin^{Hi} as EdU^{neg}. Additionally, using cell cycle marker Ki67 I was able to define the cell cycle stages of CD48^{neg} Biotin and E-SLAM Biotin subsets. Through primary transplantation assay, I proved that E-SLAM Biotin^{Hi} cells preserve their stemness regardless IFNγ secretion due to *P. berghei* infection. Furthermore, a secondary transplant confirmed the self-renewal ability of E-SLAM Biotin^{Hi} as opposed to Biotin^{Lo} HSCs.

4.2 Defining primitive E-SLAM HSCs and MPP subpopulations

To visualise surviving HSPCs at the peak of *P.berghei* infection, I optimised a flow cytometry panel to phenotypically characterise HSPC and MPP subpopulations by combining cell surface markers reported in Chapter 3 with additional markers like Flk2, endothelial protein C receptor (EPCR) and CD45 (Figure 4.1 A). MPP2 is known to preferentially differentiate into cells of erythroid/megakaryocytic lineage, MPP3 into myeloid cells such as basophiles, eosinophiles, macrophages etc., and MPP4 cells are biased towards lymphoid cell lineages. Both MPP2 ($FLK2^{-}$ $CD150^{+}$ $CD48^{+}$) and MPP3 ($FLK2^{-}$ $CD150^{-}$ $CD48^{+}$) do not express FLK2 on their cell surface, however during *P. berghei* infection there is an upregulation of CD48 expression resulting in a dramatic enlargement of both cell populations (Figure 4.1 A, C). EPCR (*Procr* gene), a type 1 transmembrane glycoprotein, is expressed mainly on the surface of endothelial cells of larger vessels. EPCR has a significant role in anticoagulation and together with activated protein C (APC) and protease-activated receptor 1 (Par-1) exert anti-apoptotic and anti-inflammatory actions (Iwasaki *et al.*, 2010). Aside from the endothelium, EPCR was found to be expressed in higher levels on HSCs (Goodell *et al.*, 1996; Balazs *et al.*, 2006; Rao, Esmon and Pendurthi, 2014; Cohen *et al.*, 2015) hence it was used by multiple studies as a tool to study long-term repopulating HSCs (Kent *et al.*, 2009; Iwasaki *et al.*, 2010; Rabe *et al.*, 2020; Lin and Trumpp, 2023). Here, I do too and combined with CD45 I identify a small number of cells that maintained EPCR expression (Figure 4.1 B) during malaria infection.

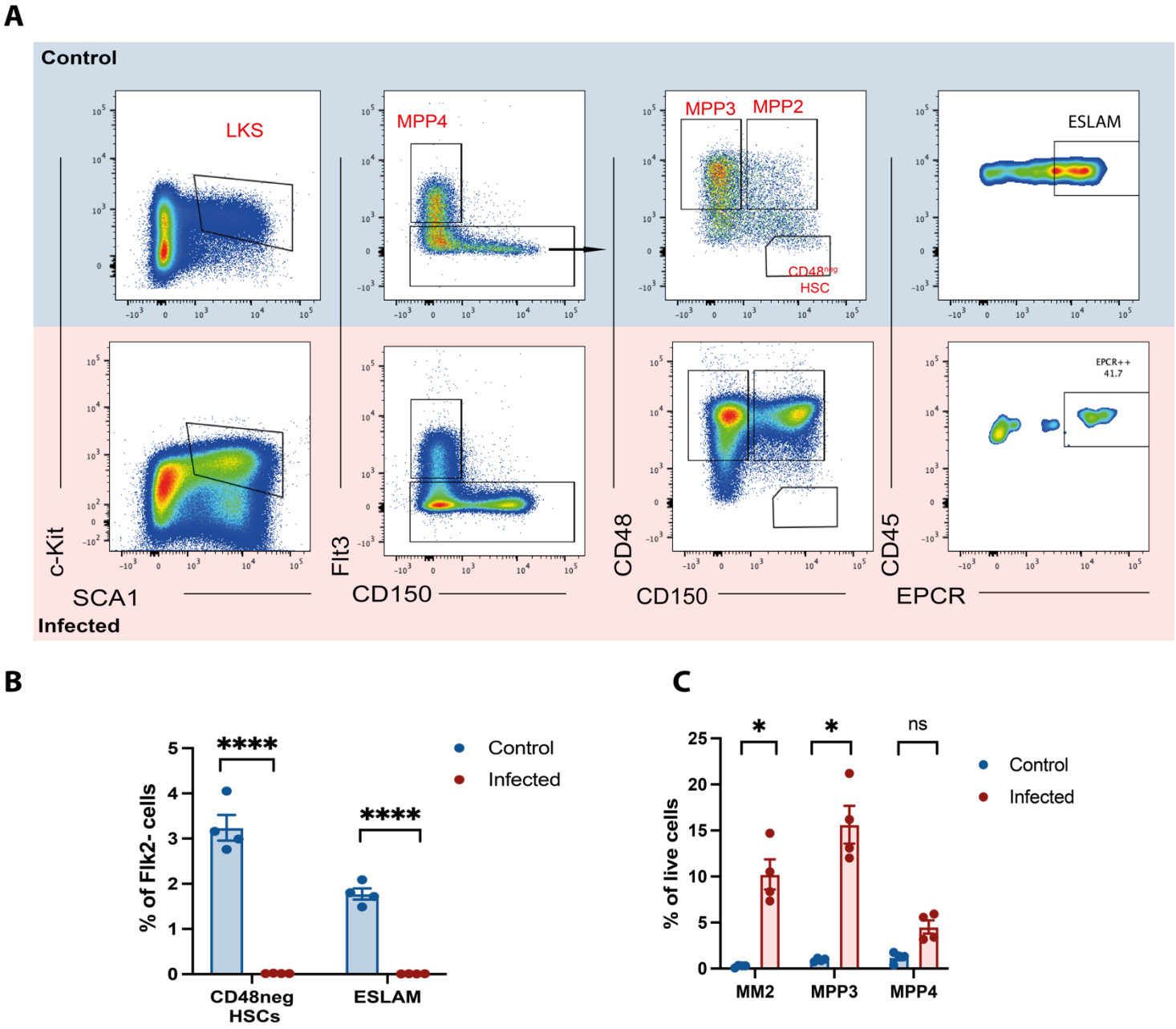


Figure 4. 1 Phenotypic characterisation of E-SLAM CD48^{neg} HSCs and MPP subsets. A) Markers such as FLK2, EPCR and CD45 were employed to investigate MPP subsets and primitive HSCs (ESLAM). MPP subsets were differentiated based on Flk2 expression and into MPP2, MPP3 and MPP4. EPCR is expressed on primitive HSCs. B) Bar plots showing percentage of HSCs and ESLAM. C) Bar plots showing percentage of MPP2, MPP3 and MPP4. Error bars represent mean ± s.e.m Each individual dot represents a mouse. Statistically significant differences were determined using Studet's *t* test for HSCs and ESLAMs and multipe *t* test for MPPs. ****represent P ≤ 0.0001; * P<0.05.

4.3 Failure in establishing a tetracycline-regulated histone H2B GFP system to mark LRCs during *Plasmodium berghei* infection

To study HSC proliferation dynamics during steady state and inflammation, multiple studies have used the tetracyclin (tet) regulated histone 2B-green fluorescent protein system (SCL-tTA:H2B GFP). When the tTA version of Tet-transactivator is used, animals are treated with doxycycline (DOX) leading to expression of GFP in all cells. Upon termination of DOX treatment, H2B-GFP transcription stops and a long chase period (up to sixty-days depending on the study) will define HSC label retention or reduction based on their cellular division. Over time, GFP expression in cycling cells will be further diminished eventually becoming undetectable. On the contrary, quiescent cells will retain the GFP expression since they may or not undergo very few rounds of proliferation (Wilson *et al*., 2008; Foudi *et al.,* 2009; Bogeska *et al*., 2022; Guo *et al*., 2022; Yang *et al*., 2022). Therefore, this pulse-chase system allows the quantitative assessment of H2B-GFP dilution in cells making it a powerful tool to study their biology and behaviour.

In relation to my experiments, first, I checked whether DOX would interfere with *P. berghei* infection before importing SCL:tTA TRE:H2B GFP transgenic animals for my analyses. To examine the effect of DOX treatment as during the chase phase of the H2B-GFP label retention assay, DOX administration was initiated seven days before infection in wild-type animals and continued throughout the experiment until BM analysis on day 8 (Figure 4.2 A). Here I asked, does doxycycline effectively clear the parasite in *P. berghei* infected animals and if so does it have an effect on HSPCs? Parasitaemia was counted from Giemsa-stained blood smears for each mouse, indicating low levels of the parasite in PB (Figure 4.2 B). During blood stage infection merozoites should invade RBCs, though this was not the case here as DOX effectively cleared the parasite. As expected, in the absence of infection, no HSPC proliferation was observed, which was coupled with the absence of SCA1 upregulation and the limited expansion of MPPs (Figure 4.2 C, H, I). The percentages of LKS cells in infected animals remained between 0.12%-0.14%, which was similar to the healthy control (Figure 4.2 D). Additionally, the proportion of $CD48^{neg}$HSCs and E-SLAM HSCs (Figure 4.2 F) was slightly elevated in infected animals compared to control which agreed with the increase observed in

absolute numbers (Figure 4.2 G). The proportion of different MPP subsets (Figure 4.2 H) and MPP absolute numbers (Figure 4.2 I) from infected animals was similar to the treated control. Cerebral malaria manifests at day 6 and in this case, and DOX-treated animals looked healthy past this time point.

Taken together, it is apparent from the data that although the H2B-GFP pulse-chase system could be a valuable tool to address E-SLAM HSC heterogeneity during *P.berghei* infection, DOX treatment will eradicate effectively any live parasite malaria infection.

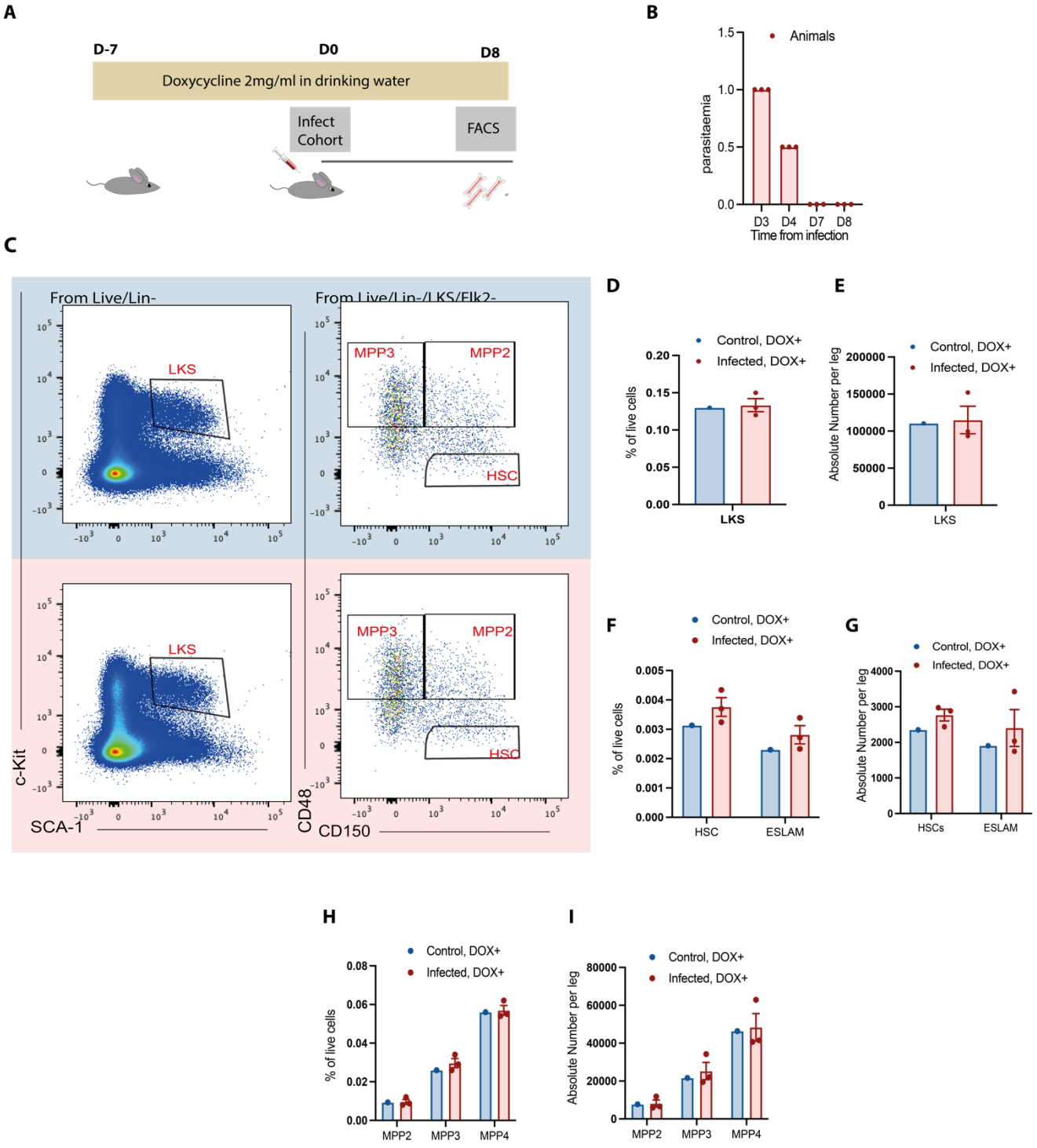


Figure 4. 2 Doxycyclie effectively clears the parasite. A) Experimental set-up. B) Graph showing parasites detected in PB over a period of 8 days *pbi*. C) Representative FACS plots showing no SCA1 upregulation in infected animals, D) proportion of LKS cells in WBM estimated from live cells and E) absolute numbers per leg. F) Proportion of $CD48^{neg}$ and ESLAM HSCs in WBM estimated from live cells and G) absolute numbers per leg. H) Proportion of MPPs in WBM estimated from live cells and I) absolute numbers per leg. *N* of 3 infected animals and *N* of 1 used for control animals. No statistical test were performed in this experiment due to the limited number of control animals.

4.4 NHS-ester Biotin as a pulse-chase labelling system to study HSC heterogeneity

With the technical limitations of the H2B GFP label system in mind, I turned towards an *in vivo* N-hydroxysulfosuccinimide (NHS) biotin labelling system, hereafter referred to as biotin, which was reported firstly in literature by David Bryder (Nygren and Bryder, 2008) and later by Luis T. *et al.* (Luis *et al.*, 2023). Upon biotin injection, NHS biotin will react with amino groups ($-NH_2$) forming amide bonds. Proteins expressed on cell membranes of all haematopoietic cells have primary amines which are labelled upon biotin injection. Once a cell proliferates, the labelled membrane proteins are equally distributed among daughter cells resulting in a linear reduction of biotin. Biotin dilution is assessed through streptavidin-based detection thus allowing the assessment of proliferation history of cells over time. (Figure 4.3 A). Of note, because proteins have their own half life, this system is not amenable to very long chases, such as the ones lasting several weeks used with the DOX system. Instead, it is recommended to not chase for longer than a few days (Nygren and Bryder, 2008). To confirm that all BM haematopoietic cells, are uniformly labelled with NHS-ester Biotin (hereafter biotin), animals were intravenously injected (*i.v.)* with biotin and culled 15 minutes prior to analysis. Flow cytometry analysis confirmed that biotin labelled all $CD48^{neg}$ HSCs, MPP2, MPP3 and MPP4 (Figure 4.3 A-E).

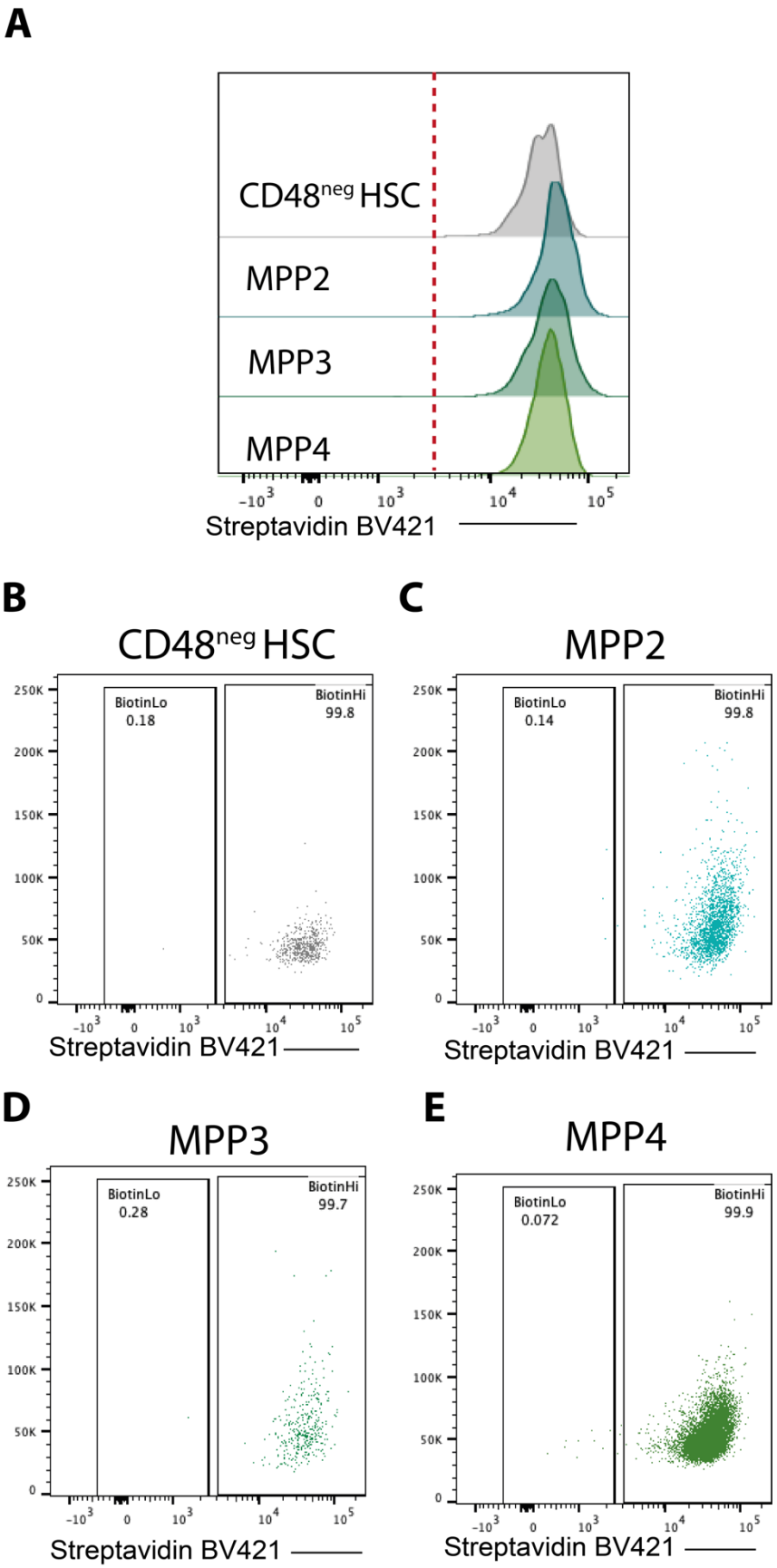


Figure 4. 3 Biotin labels all haematopoietic stem and progenitor cells. A) NHS-ester biotin is injected intravenously *(i.v.)* for a 15 minutes labelling in HSCs, MPP2, MPP3 and MPP4. Streptavidin based detection of Biotin in B) HSC, C)MPP2, D) MPP3 and E) MPP4.

After ensuring that biotin labels all cells, I then proceeded by injecting biotin label in infected animals on day 3 *pbi* and allowed two day label dilution to determine heterogeneous responses of HSCs and MPPs subsets (Figure 4.4 A,B).

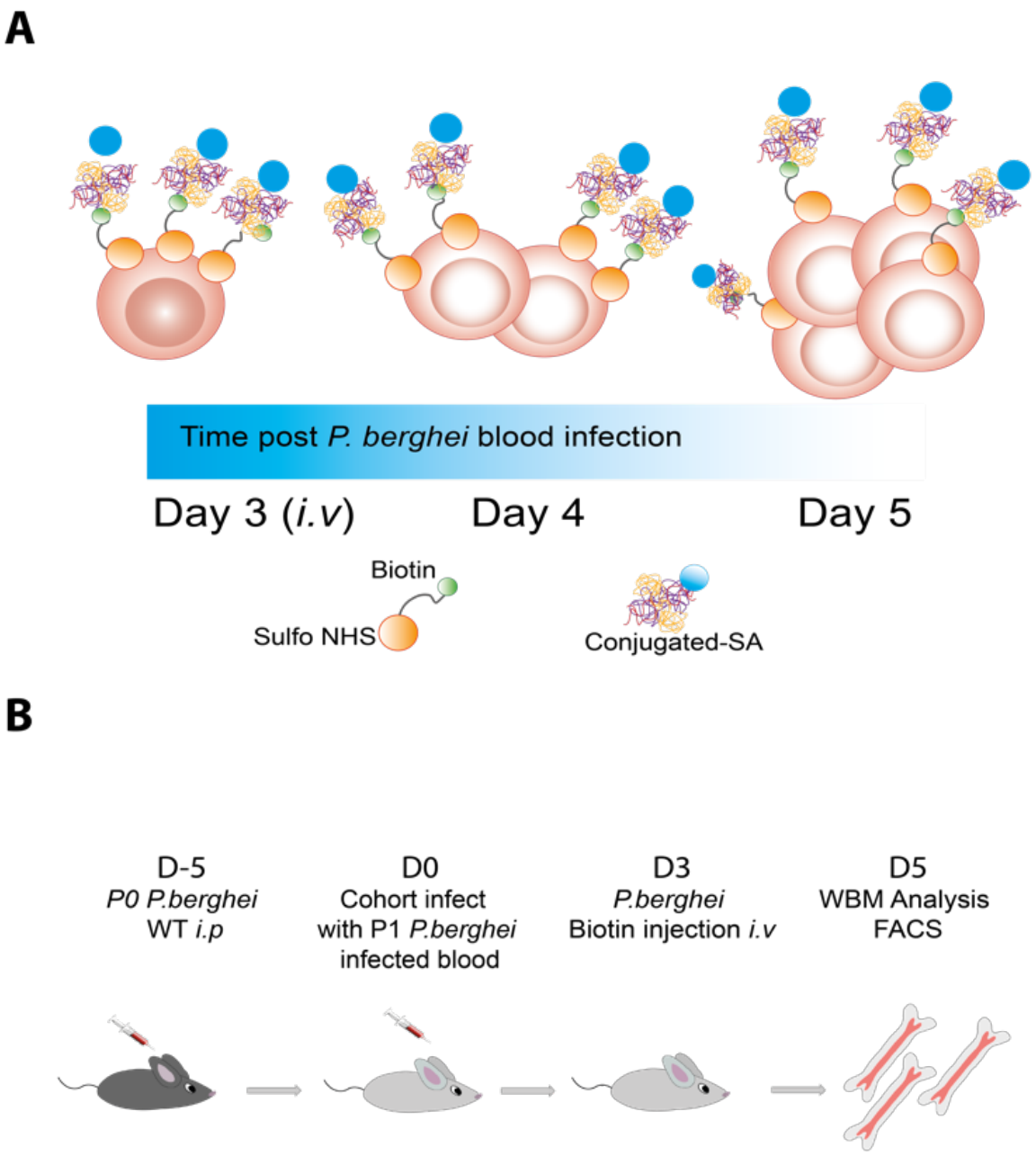


Figure 4. 4 NHS-Biotin labelling system enables measurement of proliferation kinetics in cells. A) Cells are labelled upon NHS-Biotin injection on day 3 *pbi* and dilution is allowed for 2 days. When cells proliferate they will share biotin with their daughter cells resulting in a linear reduction of label assessed through streptavidin detection. B) Experimental set-up where infected and control animals are injected with biotin at day 3 *pbi* and information on proliferation kinetics obtained on day 5.

Thereafter, I investigated heterogeneity within HSPCs. Based on streptavidin intensity I was able to define two sub-populations with different proliferation statuses in $CD48^{neg}$ HSCs and E-SLAMS. Higher intensity in the label identified $Biotin^{Hi}$, whereas a dimmer streptavidin signal identified $Biotin^{Lo}$. As expected, there was a proportion of $CD48^{neg}$ HSCs that retained biotin labelling, identified as $CD48^{neg}$ $Biotin^{Hi}$, that presented with no proliferation (Figure 4.5 A). Similarly, a population with no to limited proliferation was also observed in the E-SLAM compartment, E-SLAM $Biotin^{Hi}$ (Figure 4.5 B). Histograms representing unfractionated $CD48^{neg}$ HSC and E-SLAM populations indicated a shift in biotin labelling in infected animals (Figure 4.5 C, D). This shift was plotted and quantified as the reduction of streptavidin Mean fluorescence intensity (MFI) marking the proliferation of $CD48^{neg}$ HSC population (Figure 4.5 E) or E-SLAMs (Figure 4.5 F) in infected animals compared to controls. Because control E-SLAMs remained essentially all $Biotin^{Hi}$ and are known to be quiescent, the biotin dilution suggested that $Biotin^{Lo}$ cells had proliferated more than $Biotin^{Hi}$ ones (Figure 4.5 B). Emergency myelopoiesis develops in the *P. berghei* mosquito bite model (Belyaev *et al.*, 2013; Haltalli *et al.*, 2020) and based on my data I observed a particular increase in MPP2, compared to other MPP subsets, MPP3 and MPP4 (Figure 4.5 G-I) suggesting a megakaryocyte/erythroid (MK/Er) bias (Figure 4.5 J).

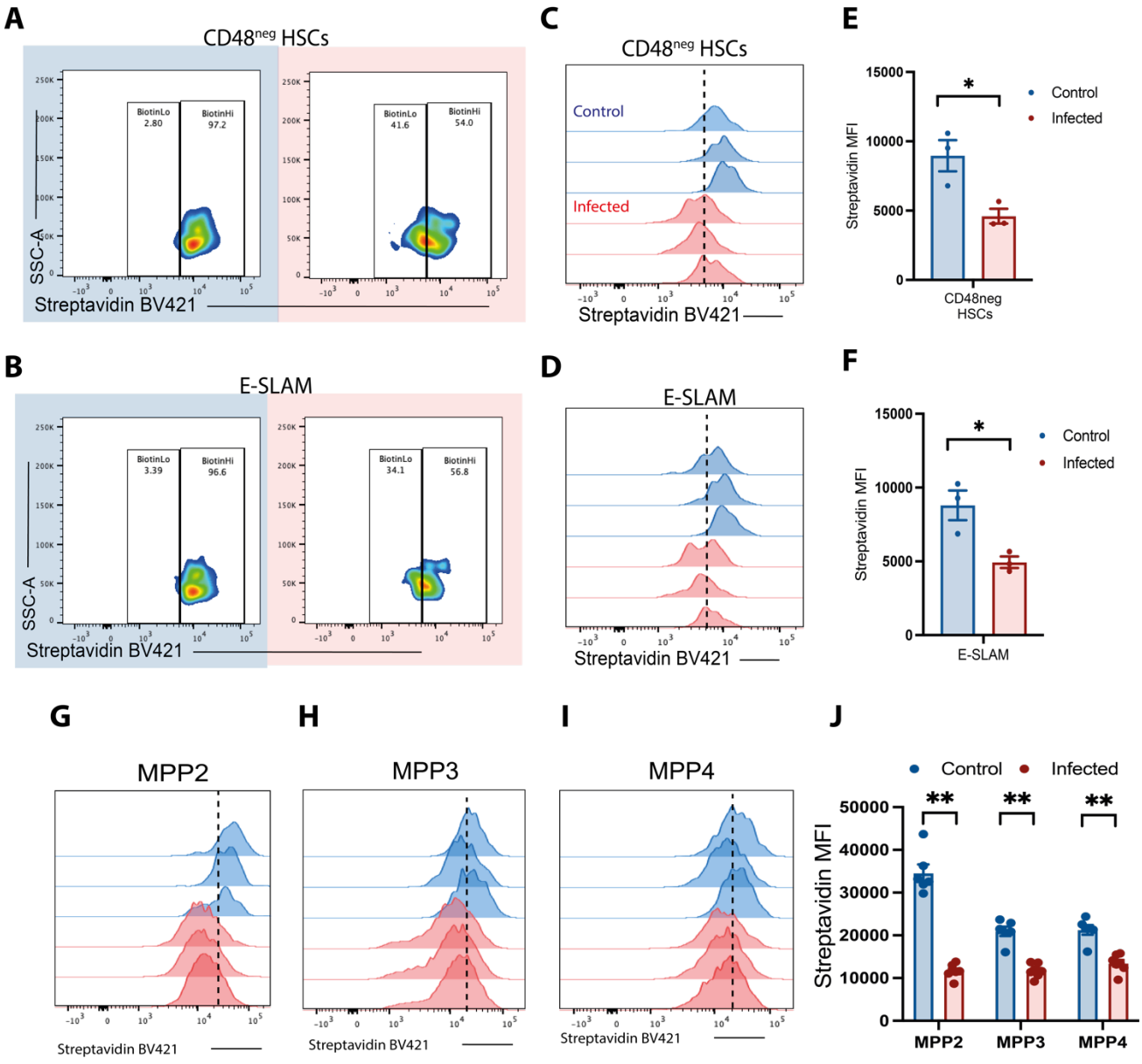


Figure 4. 5 Biotin^{Hi} and Biotin^{Lo} HSPCs identified as a result of malaria infection. Two day dilution allowed the identification of two subsets within the HSPC compartments, Biotin^{Hi} and Biotin^{Lo} cells. Representative dot plots of A) CD48^{neg} and B) E-SLAM. Histograms show C) CD48^{neg} and D) E-SLAM HSCs from control and infected animals. Biotin dilution plottes as streptavidin MFI for E) CD48^{neg} and F) ESLAM. MPP subsets such as G) MPP2, H) MPP3 and I) MPP4 proliferate during malaria infection. Dotted line represents cut-off between Biotin Hi and BiotinLo gates. For the MPP subsets data was substracted from a two independent experiments. HSPC data from one independent experiment. Each dot represents one mouse. Error bars represent the mean ± s.e.m. Statistically significant differences were determined using Student's *t*-test. (** represent P ≤ 0.01; * P<0.05).

4.5 Biotin dilution correlates with the proliferation of HSPCs

To validate that reduction of biotin label in HSCs was attributed to proliferation-induced labelling dilution I next asked if biotin dilution correlates with DNA replication. Continuous administration of EdU during the pulse-chase and on the day of BM analysis ensured that all cycling cells were caught in S phase leaving no window for replicating cells to fail up-taking EdU and stay unlabelled. For this reason, EdU was added to drinking water starting on day 3 and also administered by EdU intraperitoneal (*i.p*) injections at days 3 and 4 with a final *i.v* EdU injection on day 5 just 30 minutes before termination of the experiment (Figure 4.6 A).

I analysed biotin retention/dilution and EdU uptake in both $CD48^{neg}$- and E-SLAM Biotin HSCs by staining both with streptavidin and for EdU (Click-it reaction). Therefore, I could further fractionate $CD48^{neg}$ and E-SLAM HSCs based on their EdU profiles and correlate with biotin dilution. In the $CD48^{neg}$ compartment of infected animals, I found that the majority of $CD48^{neg}$ $Biotin^{Lo}$ had uptaken EdU (hence $Biotin^{Lo}$ EdU^{hi}) (Figure 4.6 B, D) marking DNA replication (S phase). While around 25% of $CD48^{neg}$ $Biotin^{Hi}$ HSCs were EdU^{+}, a small fraction was still EdU^{-} presumably displaying a quiescent phenotype (Figure 4.6 B, D). This was similar to the $CD48^{neg}$ $Biotin^{Hi}$ HSCs from healthy animals that remained EdU^{-} (Figure 4.6 B,D) and presented with a non-proliferative profile. Consistent with this, 35% of E-SLAM $Biotin^{Hi}$ cells did not uptake EdU (EdU-) prompting me to assume that these cells could have preserved their stemness regardless of malaria stress (Figure 4.6 E).

Taken together, these data confirmed that Biotin proliferation correlates with DNA replication and that the biotin labelling system is a reliable tool to study heterogeneous HSC responses during stress.

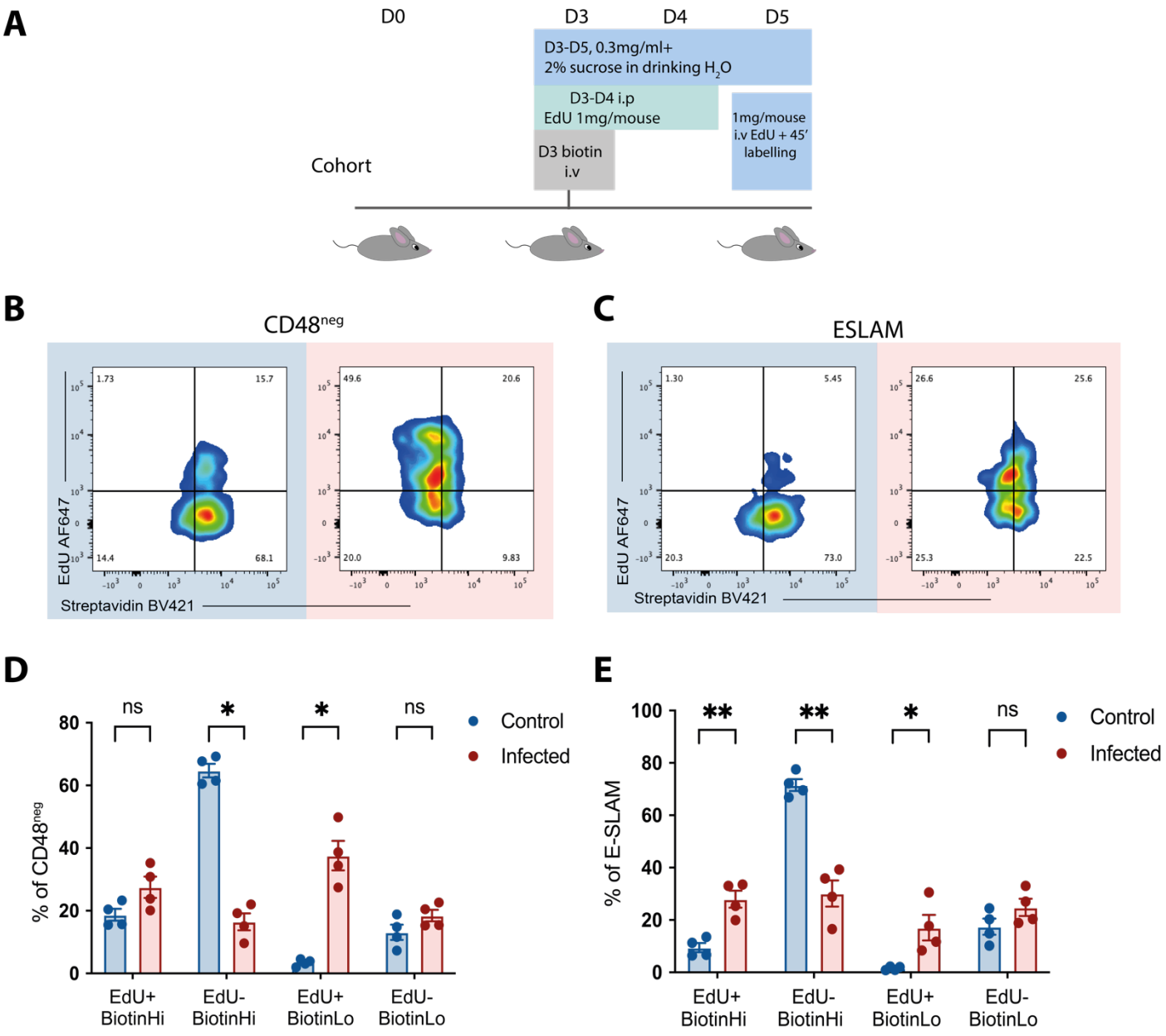


Figure 4. 6 Proliferation of biotin correlates with DNA replication. A) Chronic administration of EdU in drinking water followed by *i.p* injections at days 3 and 4 with a final *i.v* injection 45 minutes before termination of experiment. FASC plots of EdU versus Biotin in LKS B) $CD48^{neg}$ HSCs and C) ESLAM showing a large D) proportion of $CD48^{neg}Biotin^{Lo}$ in S phase compared to Biotin Hi infected cells. E) A large proportion of Biotin Hi control cells were not labelled with EdU and not associated with DNA replication. Each dot represents one mouse. Error bars represent the mean ± s.e.m. Statistically significant differences were determined using Student's *t*-test (** represent P ≤ 0.01; * P<0.05). Plots represent *N*=1 experiment.

Based on the above results, so far, I have presented the heterogeneous responses of both CD48^{neg} and E-SLAM cells during *P. berghei* infection. Biotin aided towards the identification of cells with limited (Biotin^{Hi}) or faster proliferation kinetics (Biotin^{Lo}). When EdU profiles from biotin subsets were measured, the majority of CD48^{neg} and E-SLAM Bitoin^{Lo} cells were EdU^{+}, hence found in the replication phase, while a small fraction of HSCs did not uptake EdU (Biotin^{Hi} EdU^{-}) displaying a quiescent phenotype. To confirm that a proportion of Biotin^{Hi} HSCs are in quiescence (cell cycle G_0), I analysed the cell cycle statuses of Biotin^{Hi} and Biotin^{Lo} subsets in the CD48^{neg} and E-SLAM compartments isolated from control and infected animals. The combination of Ki67, a cell cycle protein upregulated during S/G2/M cell cycle phases, with nuclear dye SYTOX, allowed the quantification of the proportion of cells in the G_0, G_1 and S/G_2/M stages of the cell cycle (Figure 4.7 A and B). As confirmed from the analysis, CD48^{neg} and E-SLAM Biotin^{Hi} uninfected cells were quiescent since the majority was found in G_0. A large proportion of Biotin^{Lo} from the CD48^{neg} HSC compartment was found in S/G_2/M phase (Figure 4.7 C ii) confirming cell cycle entry as a response to malaria infection. On the contrary, a clear fraction of CD48^{neg} HSC and a large proportion of E-SLAM Biotin^{Hi} HSCs remained in G_0 regardless of infection-induced stress (Figure 4.7 Ci, D). One possible limitation, which became a challenge later was that the more I fractionated HSCs from infected animals, from which numbers were dramatically reduced, the more challenging it was/is to obtain sufficient numbers for robust statistical analysis, particularly within the E-SLAM CD48^{neg} cells.

With a focus on the data obtained so far and for this section, I conclude based on Ki67 experiments that Biotin^{Hi} are indeed quiescent and regardless of malaria infection there is still a primitive HSC subset that remains in G_0. Ki67 distribution changes during cell cycle progression and this was observed in Biotin^{Lo} HSCs. Whether this variability is an intrinsic property reflecting environmental or metabolic influences is a question that I seek to answer in later sections.

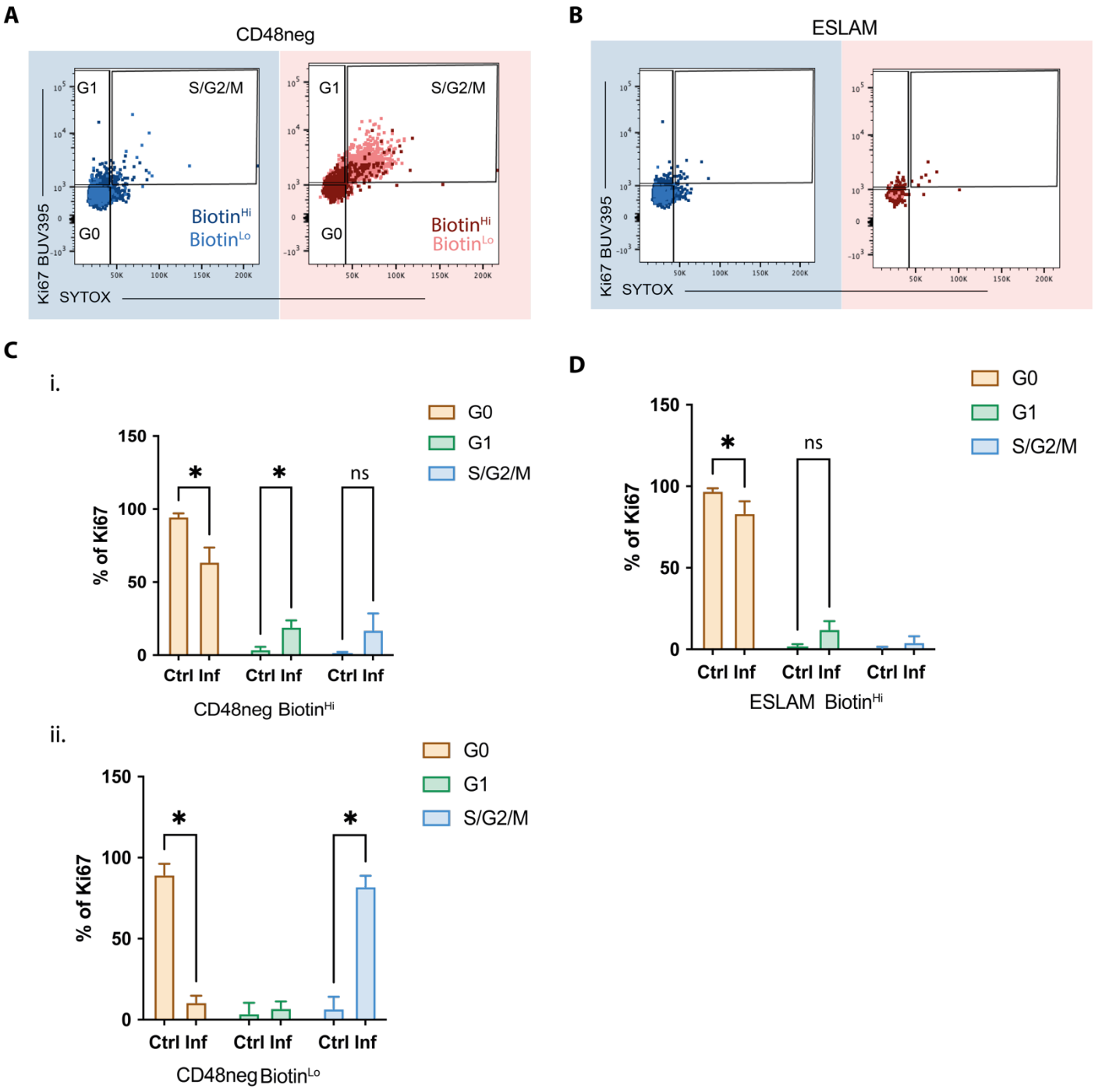


Figure 4. 7 BiotinHi cells are quiescent. Representative FACS plots of KI67 versus SYTOX nuclear dye to determine cell cycle statuses of Biotin subsets in A) CD48^{neg} HSCs and B) ESLAM. C) The majority Biotin^{Hi} CD48^{neg} cells in both control and infected animals were found in G_0. Biotin^{Lo} CD48^{neg} displayed cycling activity. D) The majority of E-SLAM CD48^{neg} Biotin^{Hi} cells were found in G_0. Each dot represents one mouse. Error bars represent the mean ± s.d. Dot plots show concatenated data from 4 control and 3 infected animals. Statistically significant differences were determined using Student's *t*-test. (**** represent P≤0.001, ** represent P ≤ 0.01).

4.6 A proportion of Biotin E-SLAM HSCs retain their functional properties

Given the heterogeneous responses of E-SLAM Biotin cells during infection, which was associated with differences in their proliferation status, I then sought to determine whether E-SLAM Biotin^{Hi} and -Biotin^{Lo} HSCs differ in their capacity to reconstitute the hematopoietic system in transplantation experiments. Animals were infected with fresh blood, injected with biotin at D3 and purified BM cells were sorted on day 5. Because little to no proliferation was present in Biotin^{Lo} from uninfected animals, I focused on sorting the top 20% in the E-SLAM Biotin^{Hi} control/ Biotin^{Hi}infected groups and the bottom 20% in the E-SLAM Biotin^{Lo} infected group. Ten cells from each E-SLAM population were transplanted into CD45.1 lethally irradiated recipients receiving 250,000 CD45.1 BM support (Figure 4.8).

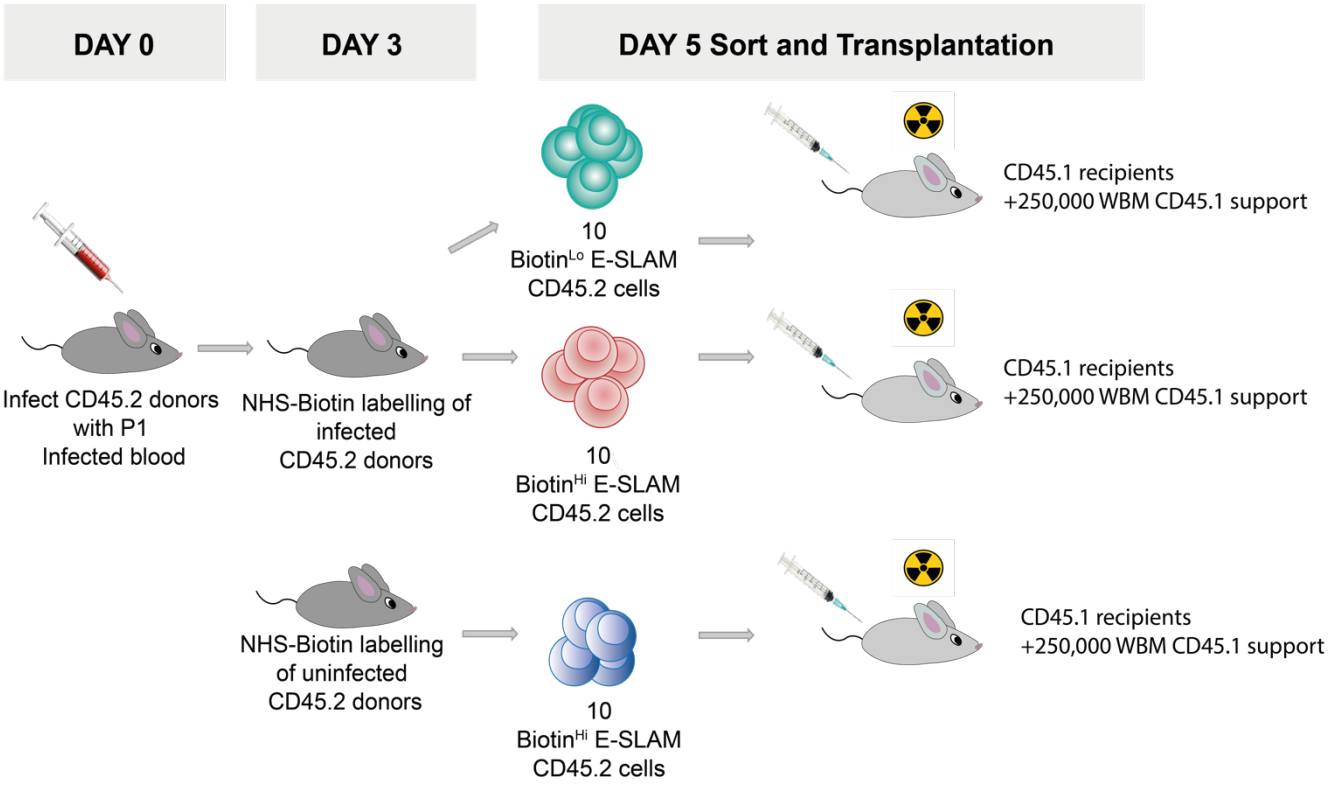


Figure 4. 8 Experimental set-up to test reconstitution potential of biotin high and low HSCs. A) E-SLAM Biotin^{Hi} and Biotin^{Lo} were sort purified from control and infected donors. Ten cells per group per condition were injected into lethally irradiated CD45.1 recipients along with 250,000 CD45.1 WBM cells.

During the primary transplant, in which engraftment and repopulation capacity were assessed, PB was analysed every 4 weeks to follow reconstitution for a total of 24 weeks. The use of the CD45.1 and CD45.2 congenic system enabled the identification of host or donor derived haematopoiesis, respectively. Although at 8 weeks peripheral blood cells already derived from the transplanted HSCs, I kept the transplant running for longer to better assess long-term HSC output. Donor derived reconstitution was evaluated either as an average (Figure 4.9 A) or per individual recipient (Figure 4.9 B) per group, indicating that E-SLAM Biotin^{Hi} HSCs purified from infected animals displayed the highest repopulation ability compared to E-SLAM Biotin^{Lo} from infected donors. Roughly 64% and 73% of recipients that received E-SLAM Biotin^{Hi} control/infected respectively engrafted. It was surprising to see that a high percentage (66%) of E-SLAM Biotin^{Lo} infected cells reconstituted recipients's haematopoietic system (Figure 4.9 C). This suggests that E-SLAM Biotin^{Lo} still possess stem-like properties despite the low engraftment observed PB of these recipients (Figure 4.9 A, B). Of note was the high engraftment in E-SLAM Biotin^{Hi} purified from infected animals compared to healthy donors (Figure 4.9 C) which was not significantly different (Figure 4.8 D). E-SLAM Biotin^{Lo} cells showed reduced engraftment ability as opposed to E-SLAM Biotin^{Hi} from infected donors. Despite the non-significant differences between the two transplanted populations, there is a trend in the data potentially suggesting a functional heterogeneity within the primitive ESLAM HSC compartment. In addition, data from the E-SLAM Biotin^{Lo} cells resembled the low engraftment observed in the CD48^{neg} HSC transplant from Chapter 3, confirming my hypothesis that the low level of reconstitution achieved was driven by some rare functional HSCs. Next, the multilineage reconstitution potential for each cell population transplanted was assessed by measuring their contribution to B, T and myeloid lineages (Figure 4.9 D). Data obtained from the recipient's PB cells showed a spike in the myeloid cells observed in the recipients of E-SLAM Biotin^{Lo} cells at week 24 (Figure 4.9 D). The lineage output seen in E-SLAM Biotin^{Lo} HSCs presumes a possible bias towards myeloid cells. Overall, B, T and myeloid cell lineage output of transplanted E-SLAM Biotin subsets per condition (Figure 4.9 D) showed no significant differences. WBM reconstitution at week 24 was 38% and 22% for E-SLAM Biotin^{Hi} cells purified from infected and control donors, respectively, and about 19% for E-SLAM Biotin^{Lo} cells from infected donors, however no statistically significance was achieved because of the wide spread of the data (Figure 4.9 E).

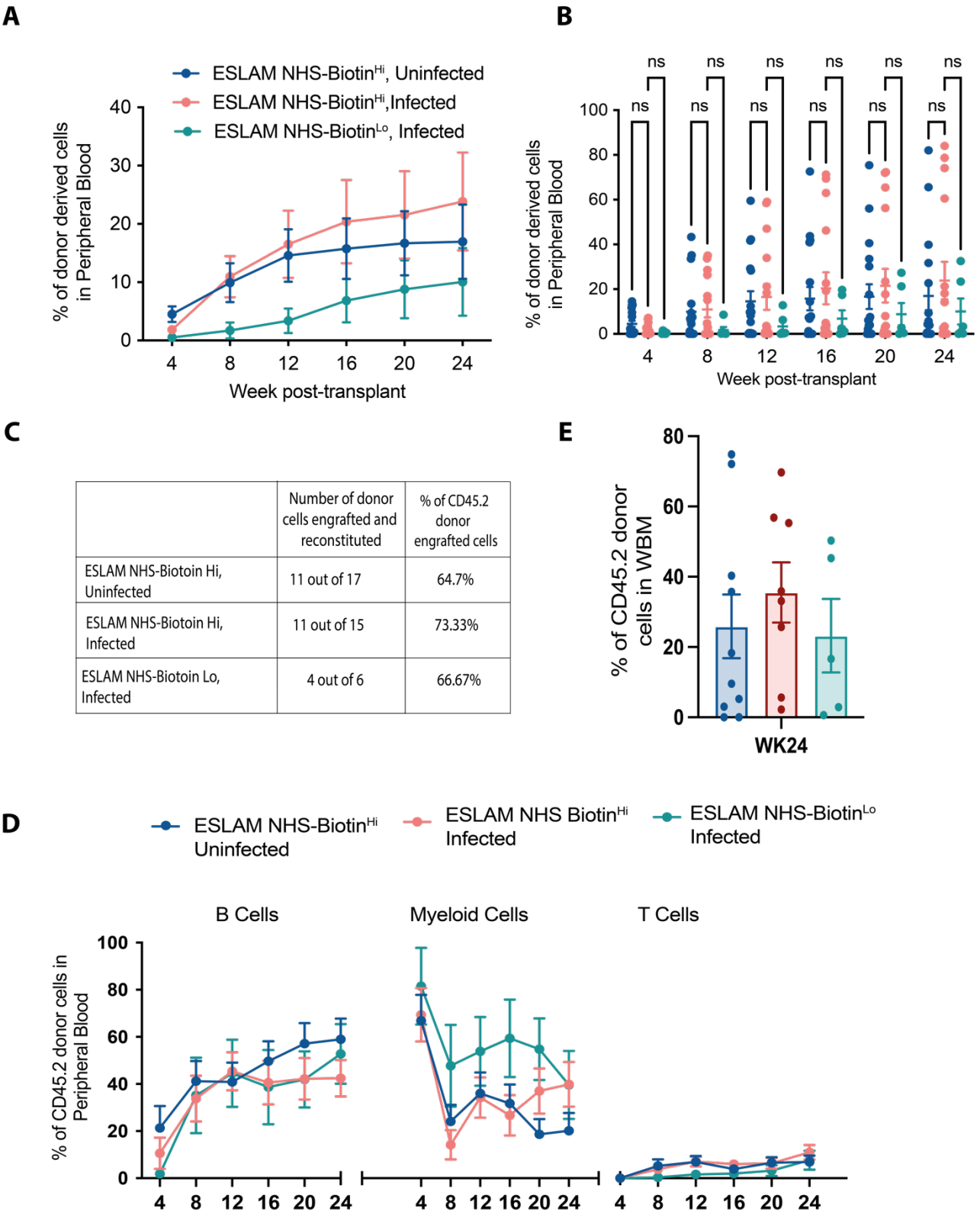


Figure 4. 9 E-SLAM Biotin ^{Hi} HSCs display the highest repopulation ability. Donor derived cells calculated as A) an average of or B) individual values of CD45.2 cells in recipients' PB. C) Table shows the number and average percentage of reconstited recipients per cell-type transplanted. D) Lineage output of transplanted cells assessed by measuring the contribution to Myeloid, B and T cell outputs. No differences were detected between lineage cells across different conditions.E) Percentage of CD45.2 donor derived cells in WBM at week 24. Each dot represents one mouse. Error bars represent the mean ± s.e.m. *N* from two independent experiments. No statistical differences were found across conditions and for each transplanted cell population.

To assess the self-renewal potential of donor cells from E-SLAM Biotin^{Hi} control/infected and -Biotin^{Lo} infected animals, I set up a secondary transplant. What was notable in the primary transplant was the high repopulation ability of E-SLAM CD48^{neg} Biotin^{Hi} purified from infected donors the stemness of which looked promising. Functional HSCs will have the ability to reconstitute secondary recipient's haematopoiesis in the long-term. Therefore, I injected 2 million cells from reconstituted primary recipients from each group containing into lethally irradiated CD45.1 secondary recipients (Figure 4.10 A). Based on FACS analysis, I estimated that each secondary recipient received fewer than 100 E-SLAMs per condition/group. Engraftment was measured over 20 weeks by sampling the recipients' PB every 4 weeks. As expected, E-SLAM Biotin^{Hi} cells from infected donors engrafted and maintained haematopoiesis in secondary recipients at higher percentages than E-SLAM ^{g} Biotin^{Lo} cells from infected donors (Figure 4.10 B). Most notably, infected donor-derived E-SLAM Biotin^{Hi} cells repopulated secondary recipients to a higher degree than E-SLAM Biotin^{Hi} HSCs from uninfected donors (Figure 4.10 B). E-SLAM BiotinHi HSCs exposed to infection may have a clonal advantage over those from uninfected donors associated with epigenetic regulation. According to recent scientific evidence, IFNγ signalling is sufficient to drive the expansion of Dnmt3a-loss of function in HSCs after *M. avium* infection outcompeting HSCs from wild-type animals (Hormaechea-Agulla D. *et.al.,* 2020). E-SLAM Biotin^{Lo} cells, as expected, led to poor engraftment and their functional decline was clear since they sustained haematopoiesis only transiently (Figure 4.10 B). Lineage contribution of donor cells was measured in PB based on T, B or Myeloid lineages in all cell donor groups (Figure 4.10 C). In terms of lineage potential, E-SLAM Biotin^{Lo} had the lowest myeloid reconstitution compared to E-SLAM Biotin^{Hi} cells from control and infected donors (Figure 4.10 C). Lastly, as observed from WBM analysis at week 20, the percentage of CD45.2 donor cells in secondary recipients of E-SLAM Biotin^{Hi} cells from infected donors was significantly higher than that of secondary recipients of either E-SLAM Biotin^{Hi} control and -Biotin^{Lo} infected cells (Figure 4.10 D).

Findings from this section suggest that although severe infection activates a proportion of primitive HSCs that respond to *P. berghei* infection, there is a fraction of HSCs that remain in quiescence, maintaining their stemness.

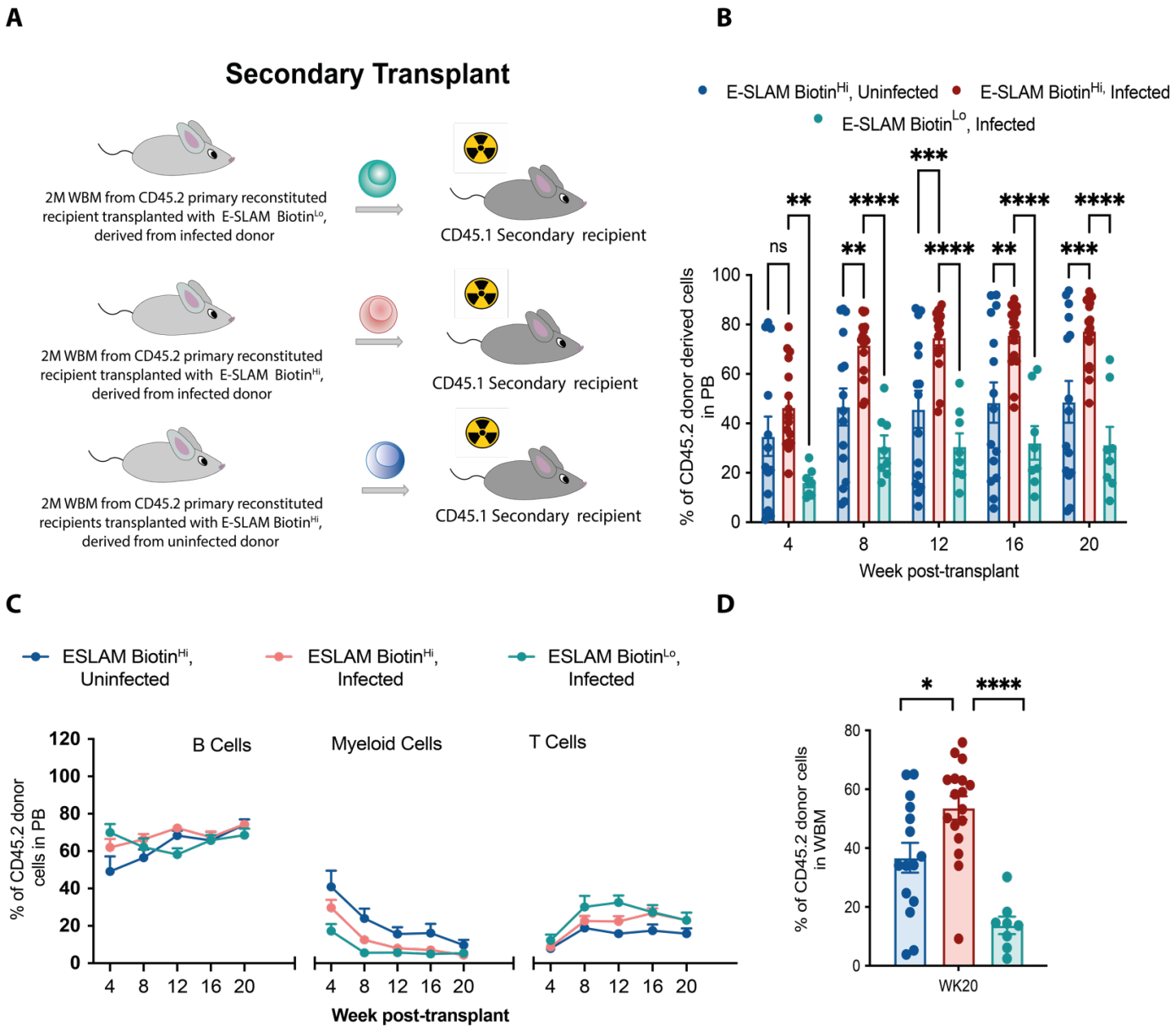


Figure 4. 10 E-SLAM Biotin^{Hi} maintain their stemness during secondary transplantation. A) Experimental set up where 2x10^6 WBM cells from primary reconstituted recipients were tranplanted into lethally irradiated CD45.1 secondary recipients. B) Proportion of CD45.2 cells in recipients' PB plotted as average per group per condition. C) Lineage output of transplanted cells assessed by measuring their contribution to Myeloid, B and T cells. D) Percentage of CD45.2 donor derived cells in WBM of secondary recipients at week 20. E) Frequency of ESLAM in reconstituted secondary recipients that received Biotin$^{Hi/Lo}$ infected and Biotin^{Hi} control primary donor cells at week 20 after WBM analysis. Each dot represents one mouse. Error bars represent the mean ± s.e.m. *N* from two independent experiments. Statistically significant differences were determined using Two-way ANOVA and Student's t-tests with post-hoc Bonferroni corrections for multiple comparisons. (*** represents P≤0.001, ** represent P ≤ 0.01; * P<0.05)

4.7 Discussion

To study HSC cellular dynamics during unperturbed or challenged haematopoiesis, transgenic animal reporters combined with sc-RNA sequencing, functional studies and multi-photon confocal microscopy are becoming the go-to tools nowadays. Although heterogeneity within the HSC compartment exists in steady-state haematopoiesis, information becomes more sparse when disease comes into play. With a focus on infection/inflammation a plethora of studies proved that exposure of HSCs to acute or chronic stress has detrimental consequences on their functionality. To identify HSC subsets, a mouse reporter system allowed the identification of cells based on label dilution where cycling cells diluted the label over time with more quiescent HSCs retaining H2B GFP expression. Upon exposure of H2B-GFP animals with pI:pC, LRCs display a functional attrition and a transcriptional phenotype associated with ageing (Bogeska *et al.*, 2022). Considering the outcomes from a myriad of studies which showed that HSC stemness is almost abolished during stress (Essers et al., 2009; Baldridge *et al*., 2010; Matatall *et al.,* 2016; Yamashita and Passegué, 2019; Haltalli *et al*., 2020; Bogeska e*t al*., 2022), I questioned that this might not be true as a pool of qHSCs still preserve their stemness despite of stress. To gain an in-depth understanding of LT-HSC heterogeneous responses to *P. berghei* infection and because the H2B GFP system proved not to be the right tool to use, in this chapter I established an NHS-biotin labelling system from which meaningful readouts can be obtained regarding HSC proliferation kinetics. Upon Biotin injection at D3 *pbi* and with two-day dilution, I was able to further fractionate LKS SLAM into cells with no or limited proliferation, referred to as $CD48^{neg}$ $Biotin^{Hi}$, or cells that actively cycled and proliferated, $CD48^{neg}$ $Biotin^{Lo}$. Upon proliferation, HSC will distribute an equal amount of biotin to their daughter cells leading to a linear reduction of label, observed through streptavidin-based detection. Moreover, EPCR and CD45 are used as additional markers along with Biotin to further characterise the dormant HSC pool referred to us E-SLAM $Biotin^{Hi}$ and - $Biotin^{Lo}$. In addition, data also showed that MPP2 and MPP3 but not MPP4 responded to malaria infection since there was a reduction of label present in infected animals which was attributed to proliferation as a response to emergency myelopoiesis. Thereafter, I asked whether proliferation kinetics, as observed in biotin dilution, correlated with DNA replication. To answer this question, EdU was administered chronically ensuring that all proliferated/ing cells incorporated EdU DNA *de novo*. The majority of $CD48^{neg}$ HSCs $Biotin^{Lo}$ and a fraction of E-SLAM

Biotin^{Lo} cells were caught in the S phase, hence they were EdU^{+}, which was expected considering that these cells proliferated due to infection. Conversely, CD48^{neg} and ESLAM - Biotin^{Hi} HSCs remained EdU negative hence no DNA labelling, in both control or infected animals. This finding comes in agreement with a similar setting using BrDu instead of EdU, where H2B GFP^{LRC} did not alter their DNA content and were enriched in dormant HSCs(Wilson et al., 2008b). If I simulate proliferation using a quantitative inference mathematical model based on kinetics from two populations, it will be highly likely that CD48^{neg} Bitoin^{Lo} cells will turnover at least once contributing to the production of new cells as a consequence of stress (Haltalli *et al.*, 2020).

Since I observed that a proportion of CD48^{neg} Biotin^{Hi} did not uptake EdU but the majority of CD48^{neg} Biotin^{Lo} did, I wondered what are the cell cycle statuses of these HSCs? To obtain information in G_0/S/G_2/M cycle stages, Ki67 combined with a nuclear dye SYTOX identified a high proportion of Biotin^{Hi} cells (CD48^{neg} and E-SLAM) in a quiescent state and CD48^{neg} - Biotin^{Lo} primed for cell cycle based on the upregulation of Ki67 (reflecting in S/G_2/M stages). Both EdU and Ki67 readouts confirmed that CD48^{neg} or E-SLAM cells respond to infection heterogeneously; while a proportion of cells enter cell cycle, there still is a fraction of HSCs that remain quiescent. Whether these “dormant” HSCs preserve their stemness is something that I sought to determine next in functional assays.

Flow cytometry cell sorting enabled the purification and transplantation of 10 E-SLAM Biotin^{Hi} control/infected or E-SLAM Biotin^{Lo} infected donor cells into lethally irradiated CD45.1 recipients. Over a period of 24 weeks and as expected, E-SLAM Biotin^{Hi} infected donor cells engrafted and repopulated recipient’s haematopoietic system at high percentages which was not the case for animals receiving E-SLAM Biotin^{Lo} infected donor cells. There were no differences observed in the donor chimerism between E-SLAM Biotin^{Hi} purified from infected and control animals suggesting a possible stemness. As for lineage reconstitution, there were no differences detected in the lineage output of cells between the three subsets transplanted. Since ST-HSCs or MPPs can repopulate the haematopoietic system transiently, in the case of a secondary transplant they will fail to engraft and reconstitute haematopoiesis. To assess the long-term function, hence stemness, of E-SLAM Biotin^{Hi} cells purified from control and infected animals, I set up a secondary transplant where secondary recipients were injected

with $2x10^6$ primary reconstituted recipient cells. From this, it was evident that a) E-SLAM $CD48^{neg}$ $Biotin^{Hi}$ cells from primary infected donors engrafted and reconstituted haematopoiesis for an additional 20 weeks, long-term, b) when I compared the proportion of primary donor cells in PB, not only E-SLAM $Biotin^{Hi}$ purified from infected animals had the highest engraftment ability which was statistically different to recipients receiving E-SLAM $Biotin^{Lo}$ from infected donor cells but also from E-SLAM $Biotin^{Hi}$ control cells. At the end of the secondary transplant, almost 55% of CD45.2 from E-SLAM $Biotin^{Hi}$ infected primary donor cells were statistically significant compared to CD45.2 E-SLAM $Biotin^{Hi}$ control donor cells. The low percentage observed in CD45.2 E-SLAM $Biotin^{Lo}$ in secondary CD45.1 recipients was expected.

From the above I conclude that a) even though some proliferation was evident in $Biotin^{Hi}$ E-SLAMs as a response to malaria infection, they did not compromise their stemness; b) E-SLAM $Biotin^{Lo}$ displays poor engraftment and repopulation ability, a phenotype reflected in cycling HSCs; c) E-SLAM $Biotin^{Hi}$ cells are dormant HSCs bearing long-term reconstitution functional properties. Having identified a subpopulation of HSCs that retains function despite strong stress, the next question is whether these cells do so by remaining insensitive to infection and therefore molecularly identical to biotin hi HSCs from control animals, or through other mechanisms. I will tackle this in the next chapter.

Chapter 5

The Biotin^{Hi} HSCs are transcriptionally and metabolically distinct from the Biotin^{Lo}

5.1 Introduction

Advances in gene expression profiling of HSCs have allowed a deeper insight into the regulation of HSC molecular programs. Conditions, such as severe infection, cause HSCs to excessively proliferate which is accompanied by transcriptional and metabolic changes (Haltalli *et al.*, 2020; Bogeska *et al.*, 2022). Active HSCs for example have increased metabolic activity compared to quiescent HSCs that are preserved in a low glycolytic state (de Almeida et al., 2017; Zhang, Menzies and Auwerx, 2018; Papa, Djedaini and Hoffman, 2019; Hinge et al., 2020; Liang et al., 2020),being dependant on autophagy (Mortensen *et al.*, 2011; Ho *et al.*, 2017) and are marked by low metabolic activity (Vannini et al., 2016; Ansó et al., 2017; Papa, Djedaini and Hoffman, 2019; Haltalli et al., 2020) and low oxidative phosphorylation (Fernández-Vizarra *et al.*, 2022; Kirova *et al.*, 2022). Dormancy is also associated with hyaluronic acid GPRC5C signalling (Zhang *et al.*, 2022), vitamin A-retinoic acid signalling (Cabezas-Wallscheid *et al.*, 2017) and low levels of p57 and Myc (Laurenti *et al.*, 2008; Cabezas-Wallscheid *et al.*, 2017). Several studies that looked into the cell cycle and transcriptome profiling of activated HSCs, suggested that albeit HSC return to G_0 cell cycle phase, they sustain injury from their activation (Wilson et al., 2008; Hinge et al., 2020). The associated activation signalling pathways relating to stress include p38^{MAPK}, TGFβ (Ito et al., 2006). Mitochondria are dynamic organelles constantly fusing into a connected network (fusion) and dividing into smaller units (fission) (Filippi, 2021). Defects in mitochondrial dynamism were observed upon transplantation of HSCs that had lower Drp1 expression causing mitochondria to aggregate into a polarized and compact network (Hinge *et al.*, 2020). The inability of mitochondrial machinery to remove or repair damaged mitochondria resulted in their inheritance by the daughter HSCs (Hinge *et al.*, 2020).

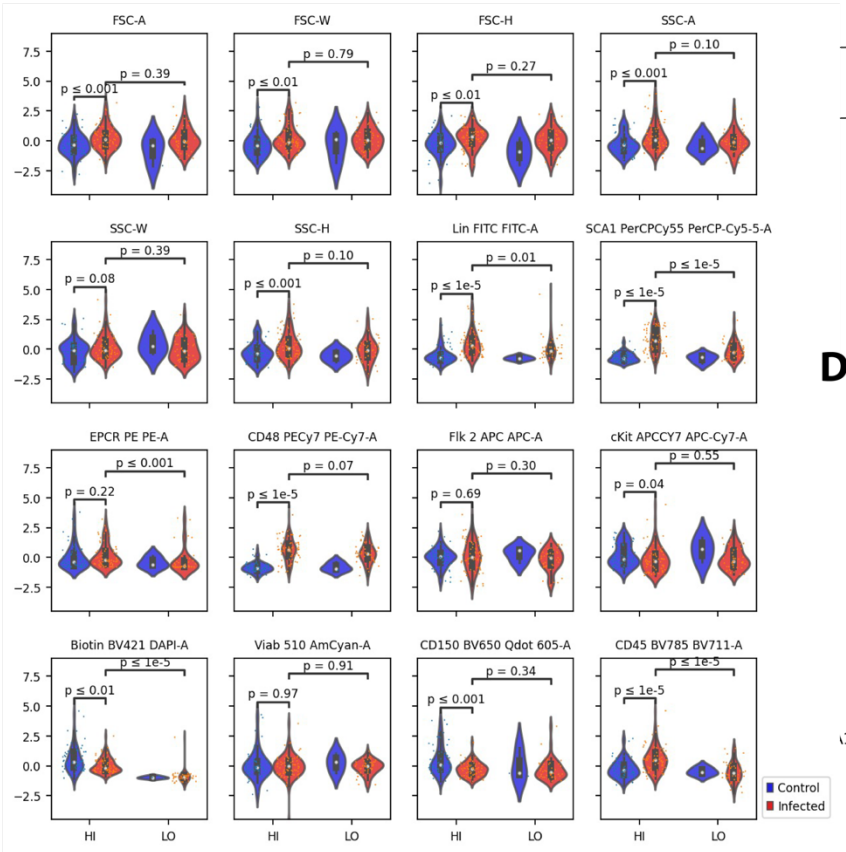
In Chapter 4, I showed heterogeneous responses of Biotin HSC subsets and that E-SLAM Biotin^{Hi} HSCs maintain stemness even after strong infection. Here, I decipher molecular changes between CD48^{neg} Biotin^{Hi} and Biotin^{Lo} HSCs during *P. berghei* infection. To gain a global understanding of the transcriptional profiles of CD48^{neg} Biotin^{Hi} and Biotin^{Lo} HSCs, I index sorted single cells (sc) for RNA sequencing purified from control and infected animals. Lastly, I worked towards identifying a possible mechanism by which E-SLAM Biotin^{Hi} maintain their self-renewal potential compared to E-SLAM Biotin^{Lo} HSCs. With a particular focus on the metabolism, I utilised certain probes and asked whether differences between E-SLAM - Biotin^{Hi} and Biotin^{Lo} are attributed to cell-intrinsic mechanisms associated with metabolism alone or combined with epigenetic mechanisms.

5.2 Deciphering the molecular signatures of CD48^{neg} Biotin HSC subsets during steady state and stress

Having identified a functional HSC subpopulation that retains its function I then asked what molecular signatures CD48^{neg} Biotin^{Hi} HSCs possess that make them different from CD48^{neg} Biotin^{Lo} HSCs? To address molecular signatures in HSCs, I took an integrated single-cell (sc) and minibulk (Appendix B) approach where sorted cells were processed for sc- and mini bulk RNA sequencing by Dr. Nicola Wilson and Mrs Sarah Kinston and analysed by Dr Qi Liu from Bertie Göttgens's group at Cambridge University. Of 275 overall sorted cells (125 Biotin^{Hi} control 90 Biotin^{Hi} infected and 60 Biotin^{Lo} infected), over 170 cells passed stringent quality control (see Chapter 2 for details) with 27,028 genes to be detected. Because the E-SLAM subpopulations are very small and it is challenging to work with a small number of cells that may have relatively few transcriptional differences, I index sorted single CD48^{neg} HSCs based on 12 flow cytometry parameters (FSC, SSC, viability, Lineage, c-Kit, Sca-1, FLK2, CD150, CD48, EPCR, CD45 and Biotin) which were recorded for every single cell (Figure 5.1 A). Index sorting allows for the retrospective identification of each cell based on the immunophenotypic intensities of the parameters used, here presented as violin plots (Figure 5.1 A). Due to thesis time constraints, scRNA sequencing data analysis for E-SLAM Biotin^{Hi} control/infected and E-SLAM Biotin^{Lo} infected cells is still ongoing and data will be available to me after my thesis submission. Here, I focused on finding transcriptional differences between the CD48^{neg} Biotin

subsets from control and infected animals. Using the indexed sort values for Biotin, 64 Biotin^{Hi} and 3 Biotin^{Lo} 'control', 65 Biotin^{Hi} and 42 Biotin^{Lo} 'infected' CD48^{neg} HSCs were identified (Figure 5.1 B). Due to their small number, Biotin^{Lo} CD48^{neg} HSCs were excluded from the sc-RNA sequencing analysis. Mean fluorescence intensity (MFI) per indexed value showed several phenotypic changes in the markers used.

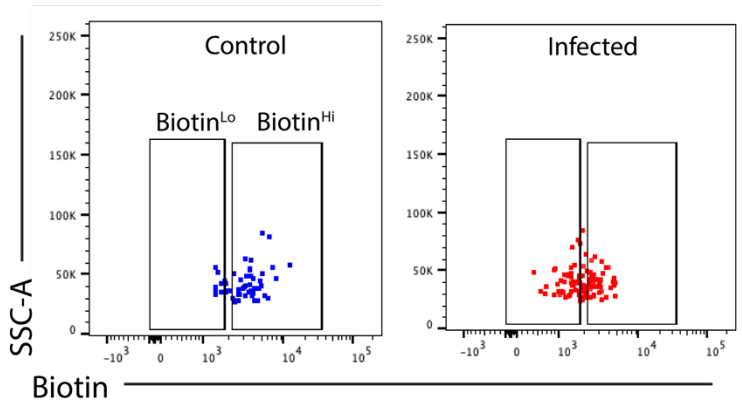
A



B

Biotin	Condition	Cells
SLAM CD48^{neg} Hi	Control	64
SLAM CD48^{neg} Hi	Infected	65
SLAM CD48^{neg} Lo	Infected	42
SLAM CD48^{neg} Lo	Control	3

C



D

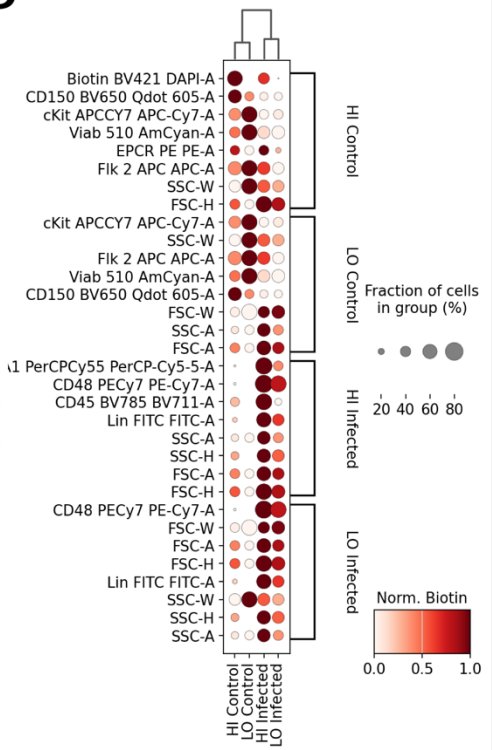


Figure 5. 1 Indexed sort values of SLAM CD48^{neg} HSCs. A) MFI of indexed values for parameter were plotted in violin plots and for each Biotin population. B) Number of CD48^{neg} HSCs identified based on Biotin dilution. C) Gating of CD48^{neg} HSCs Biotin^{Hi} and Biotin^{Lo} correlates with biotin dilution shown in violin plots A. D) Dot plot shows normalised Biotin expression in SLAM CD48^{neg} HSCs across a bubble plot. The size of each dot represents the frequency of cells in each group with normalised expression levels at >0. The intensity in the colour of each dot shows the expression levels for Biotin. Data was compiled from 2 independent experiments. Each dot represents a sorted cell. *N* of infected animals= 6, *N* of control animals = 6.

From the violin plots, biotin was retained in CD48^{neg} Biotin^{Hi} control/infected cells and diluted in CD48^{neg} Biotin^{Lo} infected sorted cells (Figure 5.1 A). This finding is reflected in the FACS plots of CD48^{neg} Biotin^{Hi} and Biotin^{Lo} in Figure 5.1 C. Cell granularity and size are measured with forward (FSC) and side (SSC) scatter parameters respectively in Flow cytometry. Therefore, Biotin^{Hi} and -Biotin^{Lo} 'infected' HSCs have increased -FSC and SSC values compared to 'control' cells when visualised on a bubble plot (Figure 5.1 A, D). In addition, SCA1 and CD48 expression was upregulated in the Biotin subsets of infected animals which is consistent with findings in Chapters 3 and 4. Lastly, EPCR is highly expressed in the CD48^{neg} Biotin^{Hi} of both 'control' and 'infected' cells (Figure 5.1 D) but not in CD48^{neg} Biotin^{Lo} 'infected' cells. After establishing the numbers of cells based on biotin dilution, for each subtype, differential expression analysis comparing Biotin^{Hi} 'control' and Biotin^{Hi} 'infected' cells revealed 116 differentially expressed genes (DEGs) of which 107 were upregulated and 9 were downregulated (Figure 5.2 A). Mean gene expression was plotted on a bubble plot where each dot represents the proportion of cells expressing each gene and the red colour variations the intensity of normalised gene expression levels across the population (Figure 5.2 C). Amongst upregulated genes, I noticed CD74 (Figure 5.2 C, D) to be differentially expressed in Biotin^{Hi} 'infected' cells. CD74 is essential for the trafficking and assembly of MHCII for antigen presentation (Li *et al.*, 2022). HSCs with high MHCII and CD74 expression levels were described to represent a quiescent subset and were protected from stress-induced proliferation(Li *et al.*, 2022). Additionally, four other genes caught my attention that were found to be associated with HSC maintenance (*Il2rg* and STAT1), transcriptional response to type I interferon (*Irf7*), or negative regulation of IFNγ signalling (*Irgm1*) (Figure 5.2 C, D). Next, Gene ontology (GO) pathway enrichment analysis using the list of differentially expressed genes (cutoff of adjusted $P<0.05$) revealed pathways relating to defence response to symbiont and virus, cellular response to type I and II interferon and positive regulation of interferon-beta production (Figure 5.2 B). Interestingly, regulation of hormone biosynthesis process, positive regulation of hormone metabolic process and regulation of epithelial cell proliferation were among significantly downregulated terms (Appendix B). Additionally, considering CD74 expression and its association with MHC-II, Gene set enrichment analysis (GSEA) revealed that Biotin^{Hi} 'infected' cells were enriched for MHC-II expression (Figure 5.2 E).

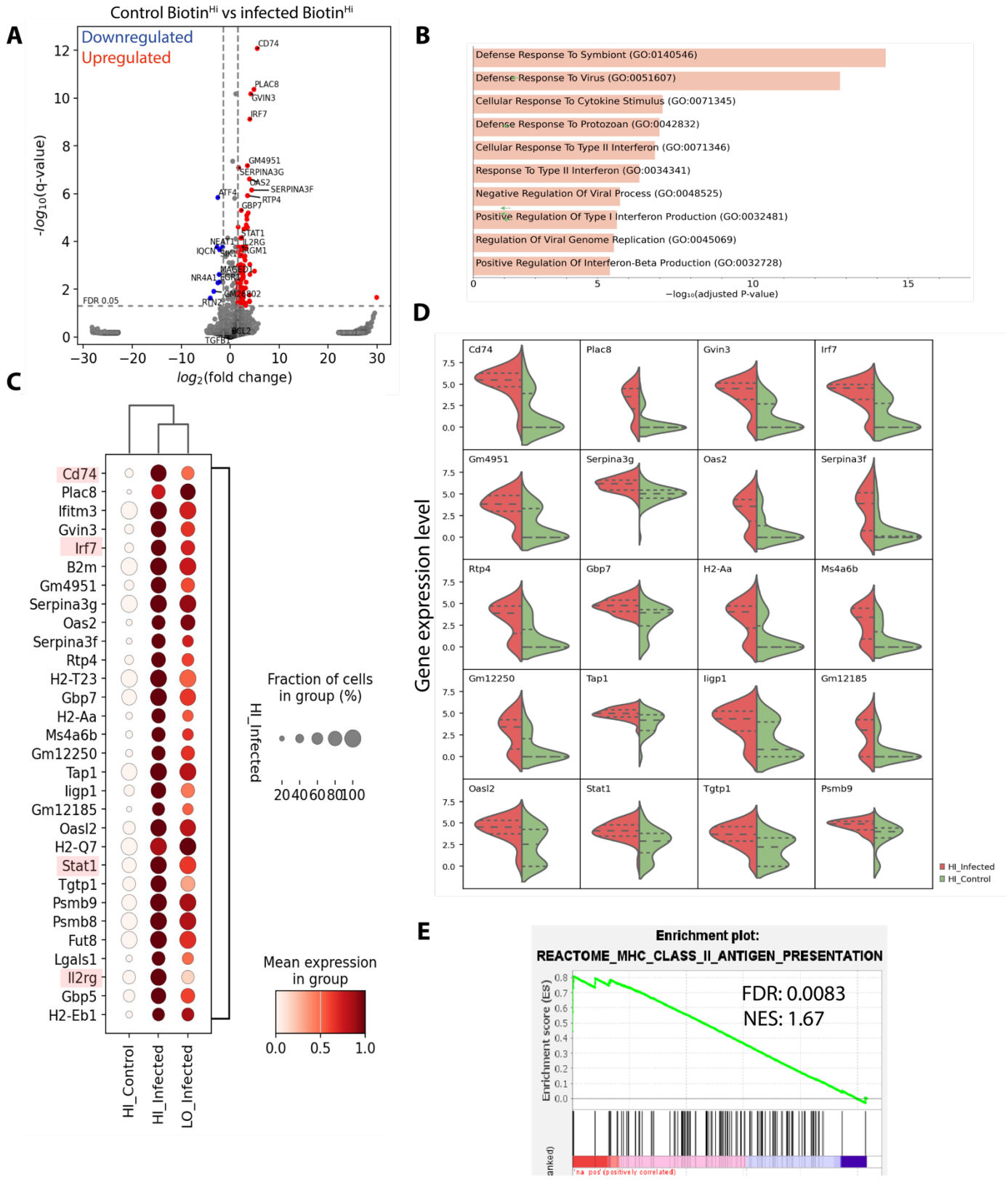


Figure 5. 2 Differentially expressed genes between Biotin^{Hi} control and infected HSCs. A) Volcano plot showing 107 upregulated and 9 downregulated genes. B) Gene ontology enrichment pathway analysis (GO) revealed pathways associated with defence response to symbiont and virus, type I and II interferon and positive regulation of interferon beta production. C) Dahlin plot showing normalised gene expression in 30 DEGs in CD48^{neg} HSC biotin high/low infected/control. The size of each dot represents the frequency of cells in each group with normalised gene expression levels at >0. The intensity in the colour of each dot shows the levels of gene expression. D) Top 20 differentially expressed genes in control vs infected Biotin^{Hi} cells. D) Violin plots representing gene expression levels between control vs infected Biotin^{Hi} cells. E) Gene set enriched analysis (GSEA) of MHC II in Biotin^{Hi} infected cells. False discovery rate (FDR) Normalised enrichment score (NES). Statistical differences were determined with Student's t-test. Differences for GO analysis were determined with Fisher exact test

When Biotin^{Hi} and Biotin^{Lo} 'infected' cells were compared, *Crzl1* was found to be downregulated in CD48^{neg} Biotin^{Lo} HSCs (Figure 5.3 A, B). In addition, genes associated with proliferation (placenta-specific 8 (Plac8)) and HSC maintenance (transforming growth factor β (Tgfb1)), were found with the highest score ranked among 20 genes (Figure 5.3 C). Next, to gain a global understanding of the mean gene expression levels in Biotin high and low 'infected' HSCs, the bubble plot was used to visualise these data (Figure 5.3 D). The mean expression of Tgfb1 and *Bcl2* genes was high in Biotin^{Lo} compared to Biotin^{Hi} 'infected' cells (Figure 5.3 D). On the contrary, the mean expression of genes associated with type I IFN (*Irf7*), negative regulation of IFN (*Irgm1*), MHC II antigen presentation (CD74) and HSC maintenance (*Ilrg2, Stat1*) was higher in the Biotin high compared to low infected cells (Figure 5.3 D).

To capture nuanced relationships between CD48^{neg} HSCs in each of the 3 groups (Biotin high; infected/control) a uniform manifold approximation and projection (UMAP) algorithm was used (Figure 5.4 A), whereby all cells were positioned within a 2D plot, with more similar cells localised closer to each other and more different cells further apart from each other. A total of 2,239 highly variable genes (HVGs) were detected and used in UMAP analysis. On this landscape, cells cluster per condition/biotin expression (control vs infected) and cell cycle phase (each of the resulting 3 groups biotin high vs low control/infected) (Figure 5.4 A). Biotin^{Hl} and Biotin^{Lo} HSCs appeared quite interspersed with each other (Figure 5.4 A). Next, I asked if CD48^{neg} Biotin^{Lo} may be transcriptionally primed for cell division compared to other HSC subpopulations and each cell was assigned to the G0/G1, S, or G2/M phases of the cell cycle as previously shown (Kowalczyk *et al.*, 2015; Nestorowa *et al.*, 2016)(Figure 5.4 B).

Consistent with my previous flow cytometry data (Chapter 4 section 4.5), the majority of CD48^{neg} Biotin^{Hi} infected and control cells had a G_0/G_1 transcriptional signatures and related to *Egr1* and *Fos*, transcription factors (TF) that promote HSCs quiescence (Figure 5.4 B). On the contrary, 40% and 20% of CD48^{neg} Biotin^{Lo} 'infected' cells were found in S and G_2/M cell cycle stages respectively (Figure 5.4 B) and carried transcriptional signatures relating to cellular division (Cdk1, Cdk6, Cdk19, Cdk2).

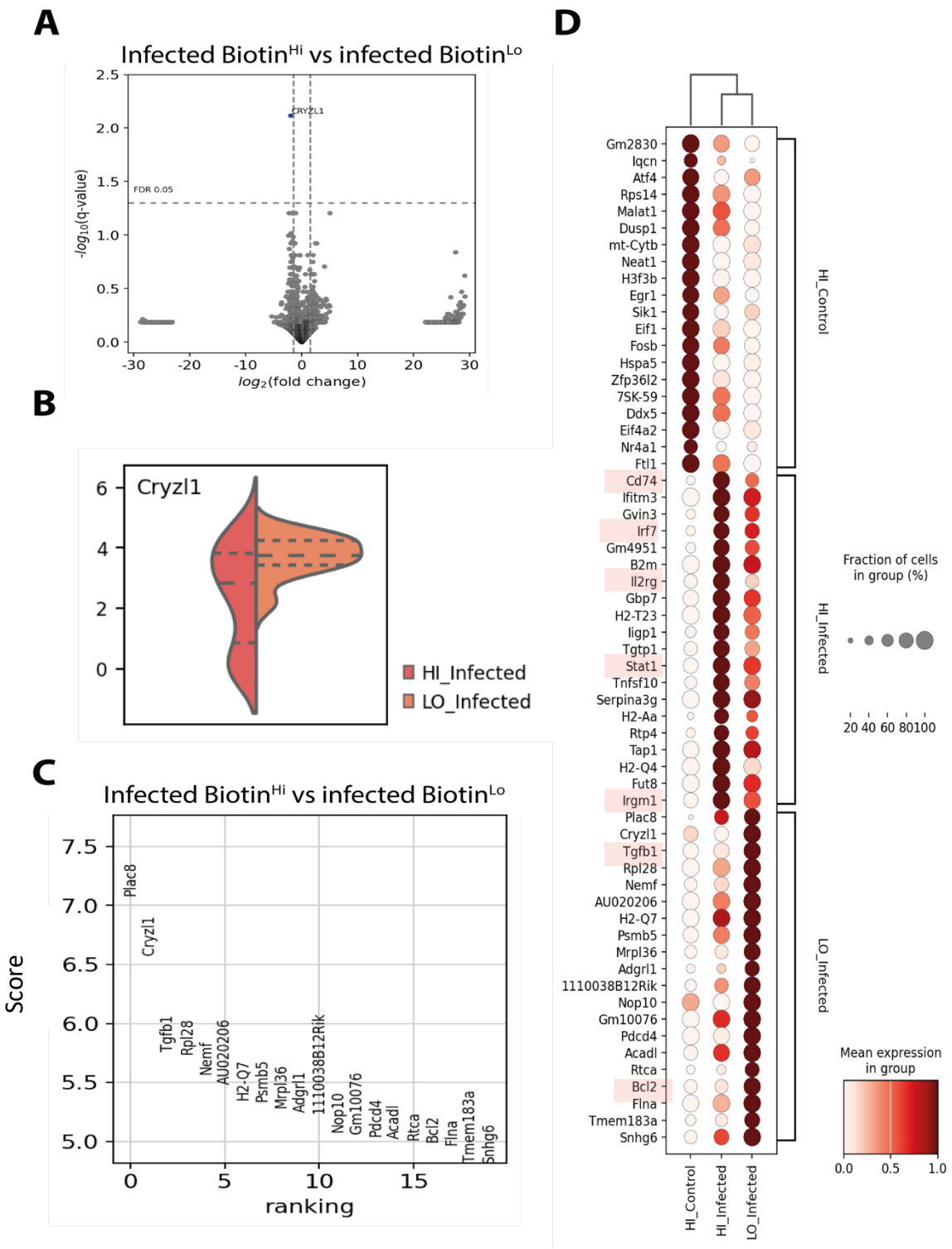


Figure 5. 3 Differentially expressed genes between Biotin$^{Hi/Lo}$ in infection. A) Volcano plots showing DEGs gene in blue between bitoin subsets in infection.Vertical lines represent the threshold of 1.5 for absolute logarithmic fold change and horizontal lines (FDR) represent the threshold of 0.05 for adjusted p-value. B) Violin plot showing Cryzl1 expression between Biotin Hi and Lo infected cells. C) Top 20 gene ranked based on the expression levels in BiotinHi vs Bitoin Lo cells. D) Dot plots showing gene expression in cell types per condition across a bubble plot. The size of each dot represents the frequency of cells in each group with normalised gene expression levels at >0. The intensity in the colour of each dot shows the levels of gene expression.

Based on this, I next assessed whether further similarities could be found between the transcriptional profiles of CD48^{neg} Biotin^{Hi} infected and control cells, and what may differentiate them from CD48^{neg} Biotin^{Lo} infected cells. To check if Biotin high control/infected and Biotin low infected cells were indeed true HSCs, we score them based on an hscScore algorithm (Hamey and Göttgens, 2019), here presented as UMAP and violin plots (Figure 5.4 C). The hscScore is a robust multiplayer perception deep learning model where the cells in question are scored based on the sc-transcriptomes of known HSCs thus investigating whether they are true HSCs (Hamey and Göttgens, 2019). The Biotin^{Hi} control and infected cells, had a significantly higher HSC score compared to Biotin^{Lo} (Figure 5.4 C) but similar to Biotin^{Hi} infected cells. Noteworthy, Biotin^{Lo} infected cells had a reduced hscScore compared to the Biotin^{Hi} infected HSCs (Figure 5.4 C) which was significantly different.

Continues exposure of HSCs to endogenous DNA damage promoted HSC accelerated ageing associated with p53 activation and myeloid bias differentiation (Wang M. *et al.,* 2023). Considering HSC activation as a response to malaria infection, we then asked if proliferation induced stress promotes ageing and upregulation of p53 target genes in Biotin^{Lo} infected compared to Biotin^{Hi} control and infected subpopulations. When we compare Biotin high control/infected and Biotin low infected cells we found that p53 scoring (Wang M. *et al.,*2023) was higher in the Biotin^{Lo} cells as opposed to Biotin^{Hi} HSCs from infected mice, whose score was similar to that of CD48^{neg} Biotin^{Hi} control cells (Figure 5.4 D). Then we calculated the ageing signature score based on the expression of top 20 of the 220 ageing signature genes reported in Wang M. *et al.,* 2023. Ageing scores (AS) for CD48^{neg} Biotin^{Lo} cells were higher but not significantly different to those of CD48^{neg} Biotin^{Hi} cells purified from infected or control animals (Figure 5.4 D). Therefore, AS in CD48^{neg} Biotin^{Hi} does not correlate with the functional data demonstrated earlier in the chapter and disagrees with a previous study where H2BGFP LRCs were found to have strong ageing signatures after proliferation-induced stress (Bogeska *et al.*, 2022). Lastly, utilising repopulation signature (RepopSig) that enriches for HSCs as described previously (Che *et al.*, 2022) I showed that CD48^{neg} Biotin^{Hi} infected cells are highly functional HSCs compared to CD48^{neg} Biotin^{Lo} HSCs and similar to Biotin^{Hi} control cells (Figure 5.4 D), agreeing with transplantation data demonstrated in Chapter 4 section 4.6.

In summary, scRNAseq analysis of CD48^{neg} HSCs indicated that the Biotin^{Hi} cells from infected mice do sense the infection, as they have a different transcriptional profile compared to that of Biotin^{Hi} cells, however, they retain gene expression associated with stemness when compared with Biotin^{Lo} HSCs from the same infected mice. In particular, this was likely achieved by upregulating genes such as CD74, STAT1 and IRGM1 known to protect cells from interferon and other inflammatory stresses, while retaining high HSC scores and signatures relating to quiescence. Consistently GO pathway enrichment analysis identified processess associated with defence response to virus and biosynthetic processes. This raised the question of whether metabolic differences between biotin high and low cells from infected animals would be identifiable.

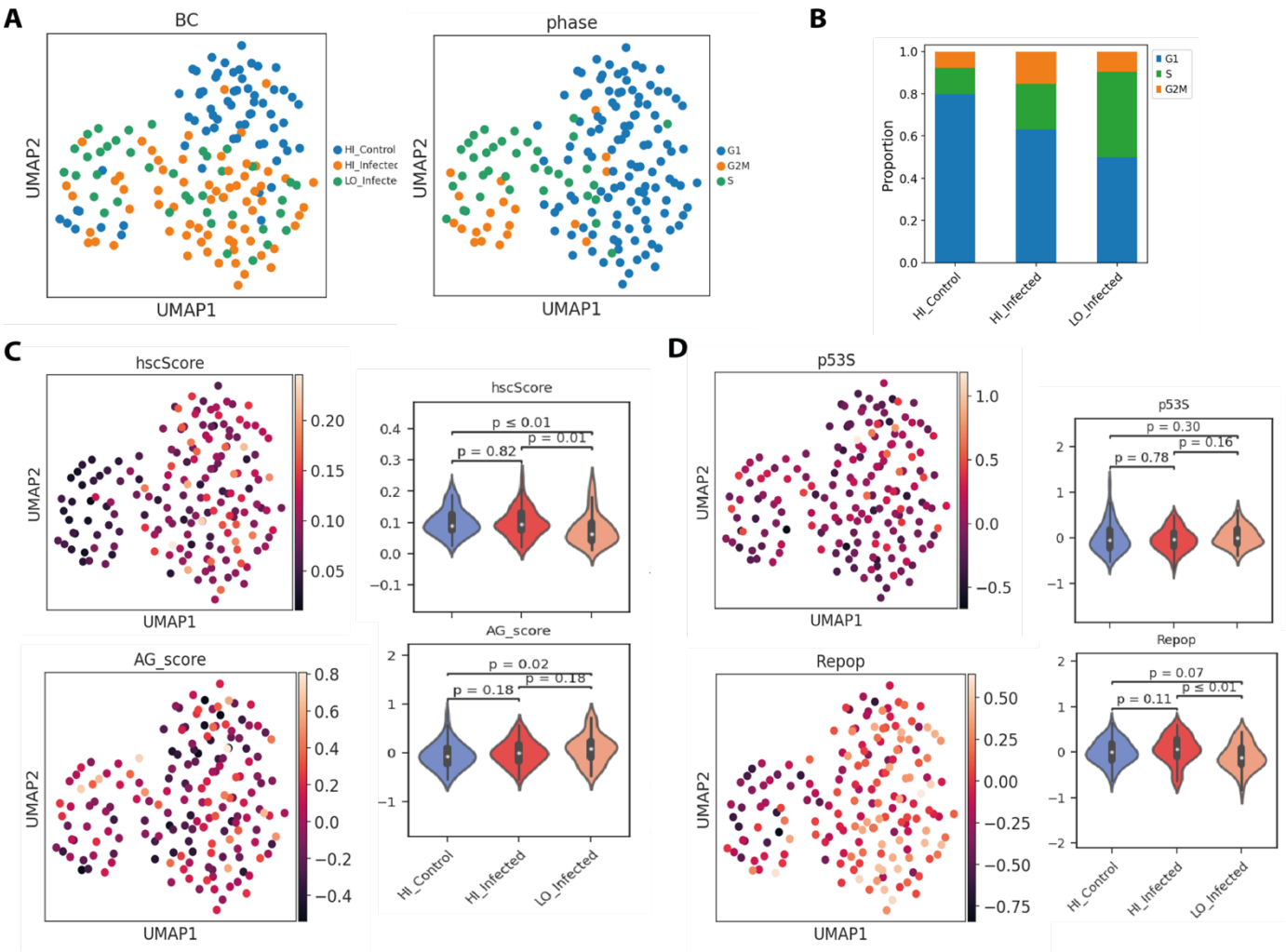


Figure 5. 4 CD48^{neg} Biotin^{Hi} cells have high HSC Score regardless of condition. UMAP analysis based on A) condition, Biotin expression and G_0/G1, S, G_2/M cell cycle stage, C) for hscScore, ageing, D) *Trp53* and *RepopSig.* B) Bar graphs showing G_0/G1, S, G_2/M cell cycle stage of Biotin^{Hi} Control/Infected and Biotin^{Lo} Infected. Violin plots per condition and biotin subsets are shown in C) for hscScore and ageing and D) for *p53* and RepopSig. Statistical differences were determined with the Mann-Whitney U test for all four parameters.

5.3 CD48^{neg} Biotin^{hi} are metabolically less active compared to CD48^{neg} Biotin^{Lo} HSCs during infection

The evidence so far directed me to think of the CD48^{neg} Biotin^{Hi} infected cells as LT-HSCs with similar phenotype and hscScoring with CD48^{neg} Biotin^{Hi} control cells but dissimilar to CD48^{neg} Biotin^{Lo} infected cells. Considering gene signatures in Biotin^{Hi} infected/ control and Biotin^{Lo} infected HSCs and relevant GO pathway enrichment analysis of downregulated genes, in the former, relating to hormone biosynthesis or positive regulation of metabolic processes, I turned towards metabolism. What drew my attention was Bcl2 expression in Biotin^{Lo} cells too. Bcl2 protein can prevent or induce intrinsic apoptosis but it can also regulate mitochondria apoptotic responses (Hata, Engelman and Faber, 2015). Based on the literature that BCL-2 expressing cells exhibit an increase in their mitochondria metabolism (Norddahl *et al.*, 2011; Kollek *et al.*, 2016) I questioned, are CD48^{neg} Biotin^{Lo} cells from infected mice, metabolically different from CD48^{neg} Biotin^{Hi}?

Considering that LT-HSCs are known to have low OXPHOS, ROS, mitochondria membrane potential (MPP) and highly depend on glycolysis (Papa, Djedaini and Hoffman, 2019; Hinge et *al*., 2020; Liang *et al*., 2020; Fernández-Vizarra *et al*., 2022) I hypothesised that E-SLAM Biotin^{Hi} from control/infected animals will maintain a low metabolic profile compared to E-SLAM Biotin^{Lo} from infected animals. To pursue this, I used multiple mitochondria dyes to assess superoxide production by mitochondria (MitoSox), mitochondrial mass (MitoTracker Green) and mitochondrial membrane potential (MPP) (TMRM) using flow cytometry to compare Biotin in E-SLAM and CD48^{neg} compartments. First, cells from control and infected mice were stained with my HSC phenotypic antibody panel, and subsequently incubated with MitoSOX Red superoxide indicator to measure mitochondrial ROS as an indicator of active OXPHOS. MitoSox indicator will permeate live cells and fluorescently label oxidised products released by the mitochondria. As my FACS panel was incompatible with staining E-SLAM cells, I was unable to obtain any data relating to this population, hence I decided to focus on CD48^{neg} HSCs, MPP2 and MPP3 instead (Figure 5.5 A). From the FACS dot plots in Figure 5.5 A and based on the results summarised in Figure 5.5 B, CD48^{neg} Biotin^{Hi} cells produced low levels of mitochondrial superoxide ROS, hence the low MitoSOX fluorescence (Biotin^{Hi}Mito^{neg}), in both

control and infected mice, suggesting a limited metabolic activity by these cells (Figure 5.5 A, B). On the contrary, a proportion of CD48^{neg} Biotin^{Lo} cells displayed high MitoSOX staining, indicating high mitochondrial superoxide oxidation (Figure 5.5 B). This was consistent with my earlier findings that these cells are cycling, and therefore their mitochondria are responding to the increased energy and metabolic demand (Figure 5.5 B). In MPP2 and MPP3 populations, it was unexpected to see only a small proportion of Biotin^{Lo} cells stained positive for MitoSOX (Figure 5.5 C, D) considering that they respond to infection by replenishing downstream haematopoietic populations.

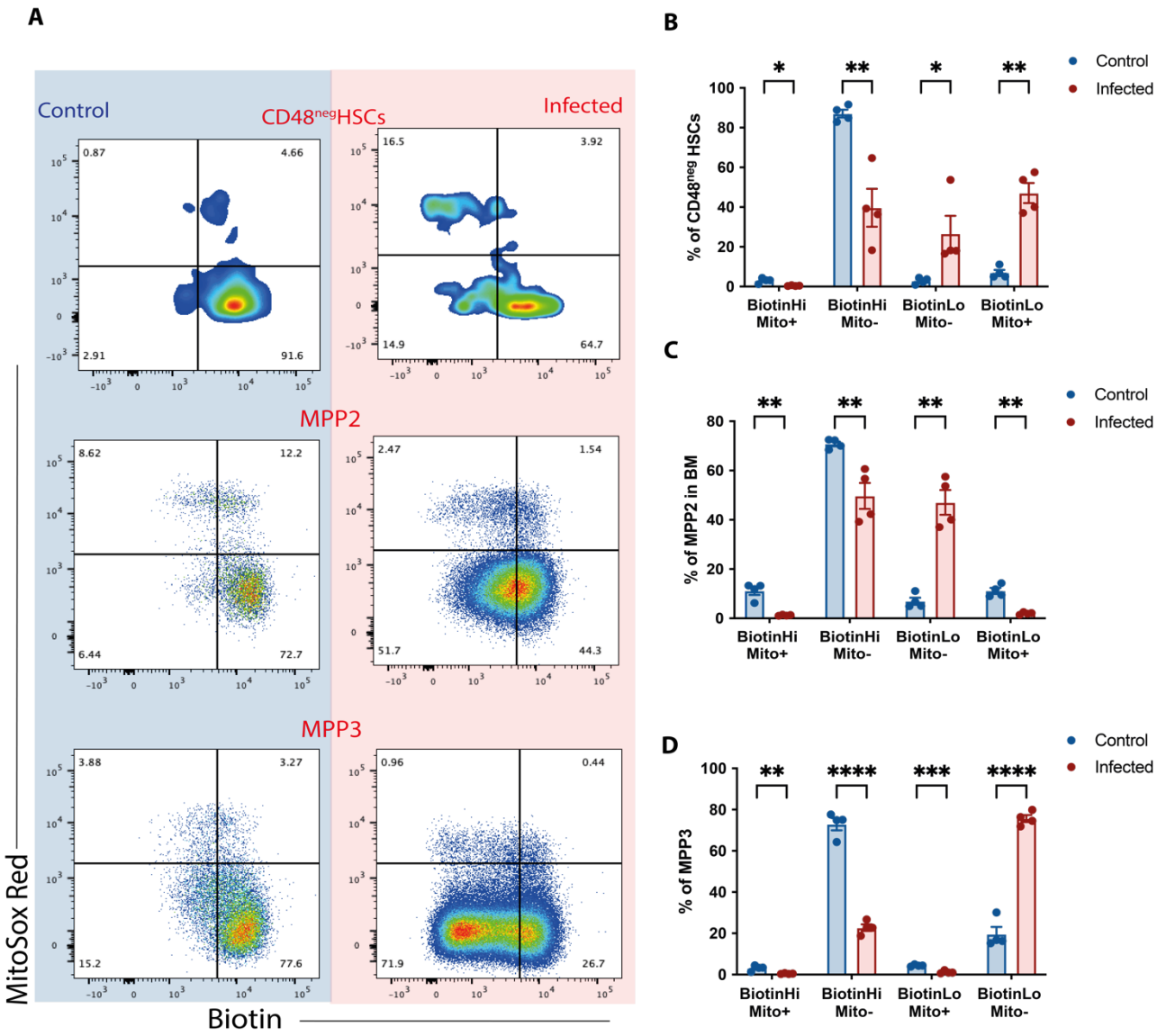


Figure 5. 5 MitoSox as a superoxide ROS indicator. A) Gating strategy of MitoSox and Biotin in CD48^{neg} , MPP2 and MPP3 populations. B) Proportion of MitoSox +/- in Biotin Hi/Lo CD48^{neg} C) Proportion of MitoSox +/- in BiotinHi/Lo MPP2. D) Proportion of MitoSox +/- in 3 BiotinHi/Lo MPP3. Error bars represent the mean ± s.d. Statistically significant differences for multiple comparisons were determined using Student's *t*-test. (*** represent P≤0.001, ** represent P ≤ 0.01; * P<0.05).

Next, I sought information on the mitochondrial mass of Biotin high and Low HSCs. Multiple studies revealed heterogeneity in HSC mitochondria mass across HSC populations when the mitochondrial content of cells was measured with Mitotracker probe (Mitotracker Green), TOM20 antibody, or mitoDendra2 transgenic animals (Takihara *et al*., 2019; Hinge *et al*., 2020; Liang *et al*., 2020; Kirova *et al*., 2022). Despite the controversy about whether LT-HSCs have low or high mitochondrial mass, I was curious to measure mitochondrial mass in HSCs using MitoTracker Green (hereafter MTG) in my experimental model. Mitotracker accumulates in the mitochondria matrix where it binds to mitochondria proteins (Filippi and Ghaffari, 2019).

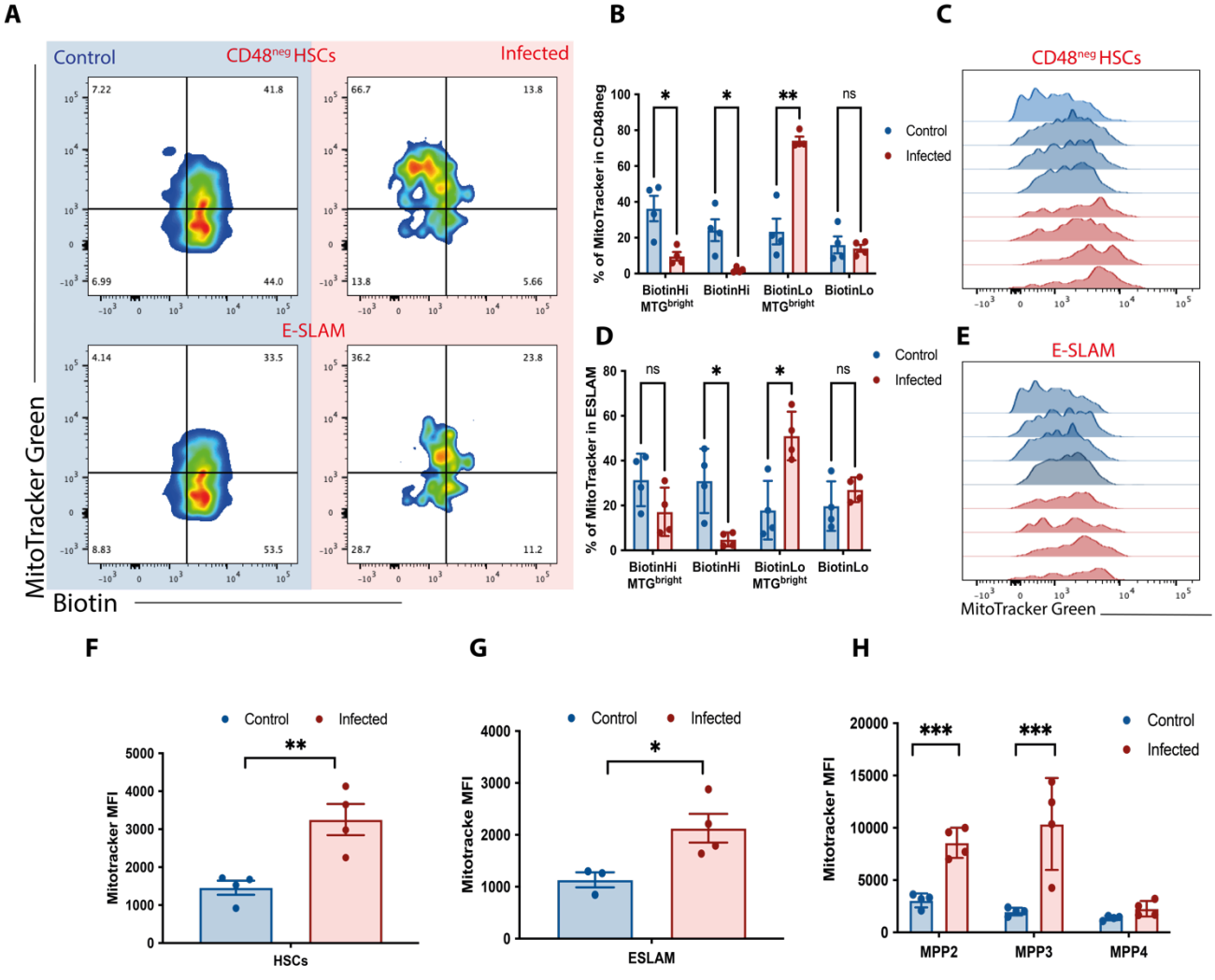


Figure 5. 6 MitoTracker Green as an indicator of mitochondrial mass. A) Gating Strategy to Discriminate Biotin Hi/Lo MTG ±- in CD48^{neg} HSCs and ESLAMS. B) Proportion of MTG^{bright} in Biotin Hi/Lo CD48^{neg} C) MTG fluorescence plotted as histograms in CD48^{neg} HSCs. D) Proportion of MTG^{bright} in BiotinHi/Lo E-SLAMs. E) MTG fluorescence plotted as histograms in E-SLAMs. F) MFI of MTG in CD48^{neg} HSCs, G) E-SLAMs and H) MPP2, MPP3 and MPP4. Each dot represents one mouse. Error bars represent the mean ± s.d. Statistically significant differences were determined using Student's *t*-test (**** represent P≤0.0001*** represent P≤0.001, ** represent P ≤ 0.01; * P<0.05).

Consistent with both CD48^{neg} and E-SLAM -Biotin^{Lo} diluting biotin due to proliferation (Figure 5.6 A) and because largely these cells were actively cycling during infection, I detected increased proportions of MTG^{bright} Biotin^{Lo} cells in both control and infected animals (Figure 5.6 B, D). When I looked at the CD48^{neg} (Figure 5.6 C, F) and E-SLAM (Figure 5.6 E, G) cells, I found that both compartments were brighter for MTG in infected compared to control animals. Furthermore, it was not surprising to see higher MTG MFI in MPP2 and MPP3 but not in MPP4 during infection (Figure 5.6 H) indicating higher mitochondria mass as a response to malaria infection.

Generally, quiescent cells, are maintained in low metabolic state possessing low mitochondrial metabolic activity, mitochondrial membrane potential (MPP) and OxPHOS (Hinge *et al.*, 2020). Considering the increase of mitochondria ROS (MitoSox) and mitochondrial mass (MTG) in CD48^{neg} Biotin^{Lo} HSCs, I asked whether they exhibit depolarised MPP. Rhodamine-based sensors such as TMRM-Tetramethylrhodamine methyl ester is capable to distinguish highly and negative polarised MPP. To ensure accurate readout in the TMRM probe I used the mitochondrial uncoupler carbonyl cyanide *m*-chlorophenylhydrazone (CCCP) to alter MMP leading to a reduced TMRM fluorescent signal which was detected by Flow cytometry (Figure 5.7 D). Both CD48^{neg} and ESLAM populations when plotted against TMRM showed increased TMRM uptake (Figure 5.7 A). From the data, it was evident that a high proportion of CD48^{neg}Biotin^{Lo} HSCs in infected animals exhibited depolarised MPP (Figure 5.7 B), which was not the case in ESLAM Biotin^{Lo} in infected animals (Figure 5.7 C). In addition, about 60% of ESLAM Biotin^{Hi} from control mice were not stained by TMRM, indicating that they maintained a negative, polarised MMP (Figure 5.7 C). Instead, there was a higher frequency of ESLAM Biotin^{Hi} cells from malaria infected animals positive for TMRM (Figure 5.7 C). When TMRM fluorescence intensity was measured in CD48^{neg} and ESLAM compartments, in either histograms (Figure 5.7 D, F) or graphs (Figure 5.7 E, G), it was clear that HSCs from infected animals had higher MMP compared to control animals. Consistently with previous findings, MPP2 and MPP3 populations displayed depolarised MMP during infection, while MPP4 cells did not (Figure 5.7 H, I).

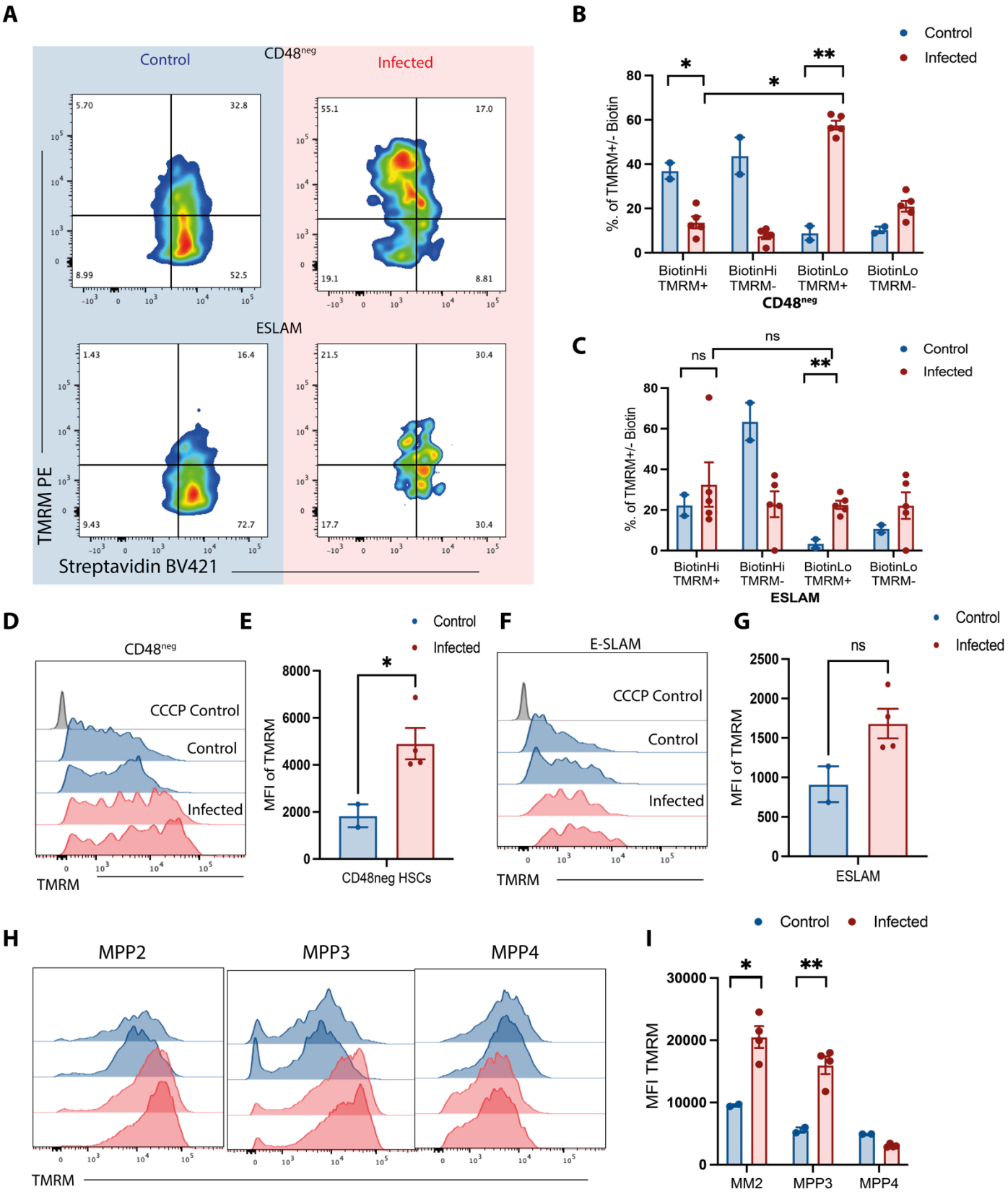


Figure 5. 7 TMRM studies MMP in CD48^{neg}, E-SLAM and MPPs. A) Gating Strategy to discriminate Biotin Hi/Lo TMRM +/- in CD48^{neg} HSCs and ESLAMS. B) Proportion of TMRM± in Biotin Hi/Lo CD48^{neg} and C) Biotin Hi/Lo ESLAMs. D) TMRM fluorescence shown as histogram for CD48^{neg} HSCs or E) plotted as MFI. F) TMRM fluorescence shown as histogram for ESLAM HSCs or G) plotted as MFI. H) TMRM fluorescence shown as histograms for MPP2, MPP3 and MPP4 or I) plotted as MFI between MPP2, MPP3 and MPP4 in control and infected animals. Each dot represents one mouse. Error bars represent the mean ± s.d. For multiple comparisons statistically significant differences were determined using Student's *t*-test (*** represent P≤0.001, ** represent P ≤ 0.01; * P<0.05).

5.4 CD48^{neg} and ESLAM Biotin^{Lo} cells exhibit higher ROS during infection

Based on the earlier findings from this Chapter, I then asked, do Biotin^{Lo} HSCs exhibit higher ROS compared to Biotin^{Hi} cells in malaria burden animals? CELLROX reagent was used to stain for ROS in cells from control and infected animals. ROS was elevated in CD48^{neg} (Figure 5.8 A) and E-SLAM (Figure 5.8 C) compartments in infected animals. When I looked more closely, CD48^{neg} Biotin^{Lo} HSCs (Figure 5.8 B) and E-SLAM Biotin^{Lo} (Figure 5.8 D) from infected animals exhibited higher ROS compared to Biotin^{Hi} cells from these animals. (Figure 5.8 B, D). ROS was relatively low in HSCs from control animals, consistent with HSCs being maintained in low ROS in steady-state (Figure 5.8 B). Additionally, in agreement with previous data showing higher mitochondrial activation (MitoSOX probe) in MPP2 and 3 but not 4 harvested from infected animals, I detected higher ROS in MPP2 and 3 but not 4 (Figure 5.8 E).

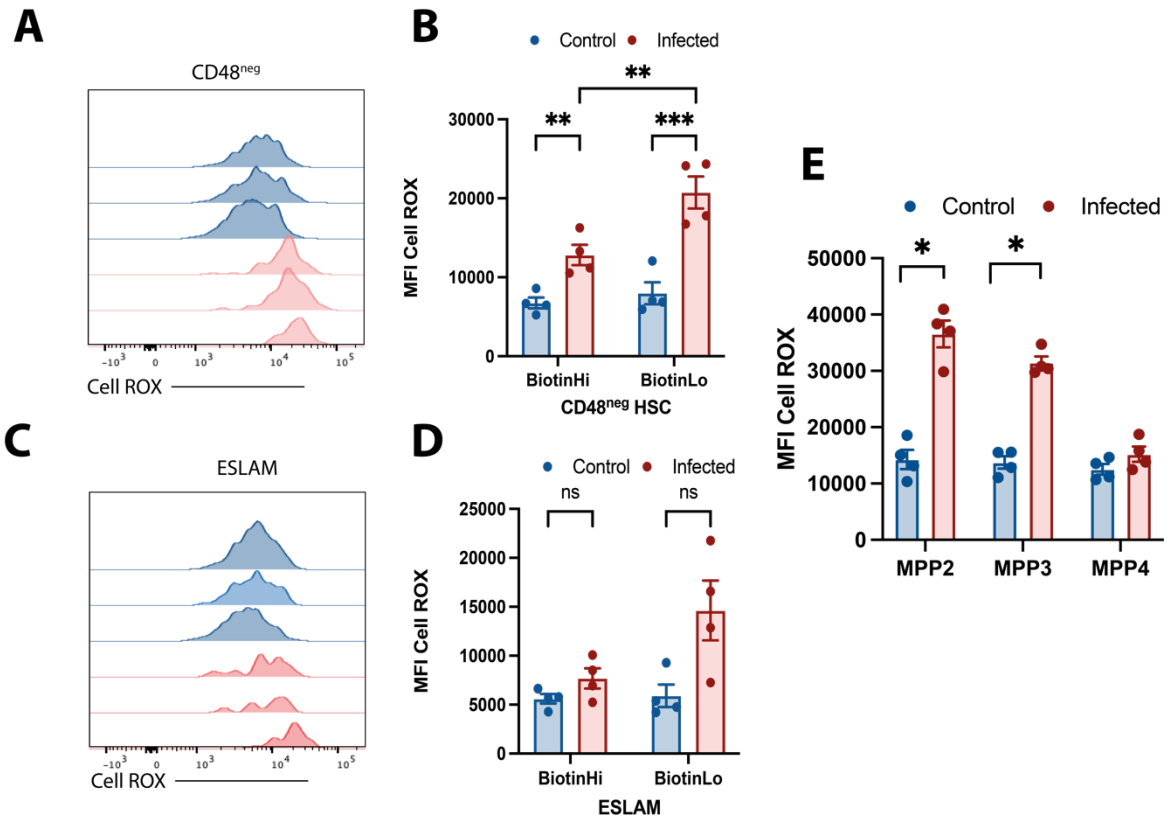


Figure 5. 8 Biotin^{Lo} HSCs have increased ROS compared to Biotin^{Hi}. CELLROX fluorescence plotted as histograms for A) CD48^{neg} HSCs B) ESLAM. MFI of biotin hi and low in CD48^{neg} (B) and ESLAM (D) populations in control and infected animals. E) MFI of CellROX in MPP2, MPP3 and MPP4. Each dot represents one mouse. Error bars represent the mean ± s.e.m. For multiple comparison statistical significant differences were determined using multiple comparison test (B, D). Student's *t*-test was used in E. (*** represent P≤0.001, ** represent P ≤ 0.01; * P<0.05).

In an attempt to inhibit ROS and achieve a global ROS reduction in infected treated animals compared to untreated infected animals in the HSC compartment, *N*-Acetylcysteine, NAC, was used. Starting at two days before infection, animals were treated with NAC or PBS, and at D0 were infected or PBS treated followed by WBM analysis at D5 *pbi* (Figure 5.9 A). Analysis revealed a decrease in ROS release in CD48^{neg} purified from NAC- treated in comparison to NAC untreated animals (Figure 5.9 B). Similarly, MPP2 displayed lower ROS in the NAC-treated infected relatively to infected NAC-untreated (Figure 5.9 B).

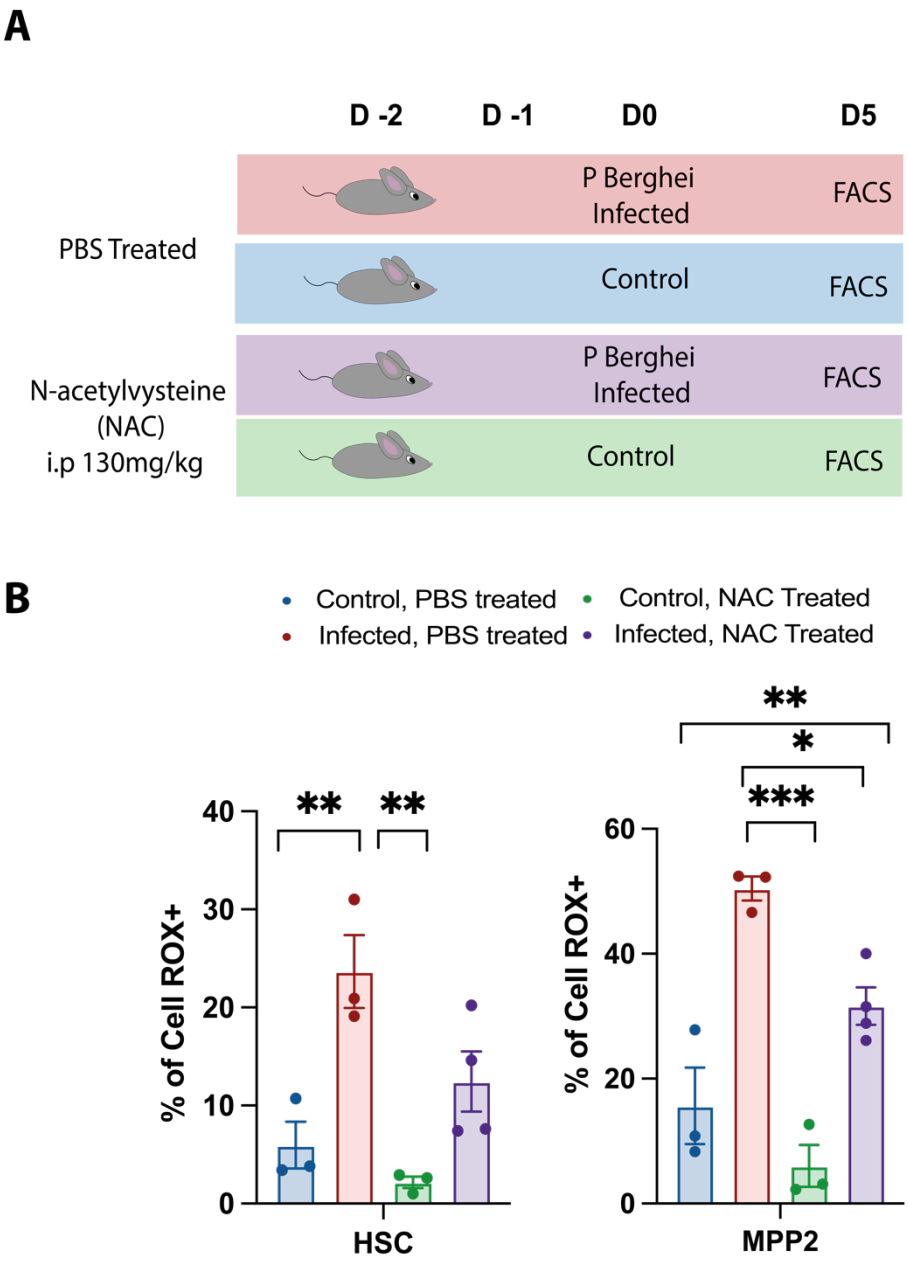


Figure 5. 9 NAC treatment abolishes ROS in HSCs. A) Experimental set up to scavenge ROS by treating infected/uninfected animals with NAC. B) Proportion of CD48^{neg} HSCs and MPP2 in NAC treated/untreated infected/control. Each dot represents one mouse. Error bars represent the mean ± s.d. For multiple comparisons statistically significant differences were determined using Two-way ANOVA with Bonferroni correction (*** represent P≤0.001, ** represent P ≤ 0.01; * P<0.05)

These findings indicate that NAC could be used as a potential inhibitor of ROS. As this was a preliminary experiment, I intend to repeat this experiment with Biotin injection at day 3 *pbi* after I submit my thesis. The next question thereafter is to ask, could I rescue E-SLAM Biotin^{Lo} functionality in infected animals treated with NAC to scavenge released ROS?

In this section, mitochondria metabolism was studied using multiple strategies. Therefore, from the data obtained, I can conclude that: a) E-SLAM Biotin^{Hi} from infected animals have similar mitochondria metabolism to E-SLAM Biotin^{Hi} from control animals suggesting that indeed these cells remain unresponsive to malaria stress, b) there is some variability already in the metabolism at steady-state which becomes more disrupted and more heterogeneous with infection, c) metabolic activity of MPP2 and MPP3 but not MPP4 is in agreement with their proliferation profile in the context of emergency myelopoiesis.

5.5 Discussion

Severe infection causes HSC excessive proliferation leading to changes in their molecular signatures. Because the E-SLAM subpopulations are very small and might have nuanced transcriptional differences, I index sorted single CD48^{neg} HSCs. In this chapter I addressed the transcriptional differences in CD48^{neg} Biotin subsets in control and infected animals. Based on the indexed sort biotin values, cells were labelled as Biotin^{Hi} control, Biotin^{Hi} infected and Biotin^{Lo} infected. Gene expression analysis revealed 116 genes to be associated with CD48^{neg} Biotin^{Hi} from cells purified from control and infected animals. While CD48^{neg} Biotin^{Hi} HSCs displayed dormant characteristics regardless of stress there is a possibility that infection altered the expression of certain genes in CD48^{neg} Biotin^{Hi} HSCs but not to a bigger extent as in CD48^{neg} Biotin^{Lo} cells. Focusing on the differentially expressed genes between CD48^{neg} Biotin^{Hi} control and infected, CD74 was prominent. CD74 is known for its role in the presentation of antigens via the MHC class II pathway and for cross-presentation of class I (Basha *et al.*, 2012; Schröder, 2016). Recently, it was shown that CD74^{hi} HSCs with high levels of MHC II (MHCII^{hi}), remained in G_0 and were less responsive to proliferation-induced stress and apoptosis compared to MHCII^{lo} HSCs (Li *et al.*, 2022). Infected CD48neg Biotin^{Hi} cells have higher CD74 gene expression from CD48^{neg} Biotin^{Lo} HSCs marking the possibility that the former might express higher levels of MHCII too (Li *et al.*, 2022). Furthermore, MHC molecule

expression (STAT1) is found at lower levels during steady state (Li *et al.*, 2022) which agrees with the levels observed in CD48^{neg} Biotin^{Hi} control cells. Moreover, IRGM1 a gene associated with negative regulation of IFN signalling (King *et al.*, 2011), had increased expression in CD48^{neg} Biotin^{Hi} infected than -Biotin^{Lo}, confirming that CD48^{neg} Biotin^{Hi} and possibly E-SLAM Biotin^{Hi} remain unresponsive to IFN. STAT1 was recently shown to maintain transcriptional protection and cell cycle inhibition of HSCs after stress-induce challenge (Li *et al.*, 2022) which might be the case in CD48^{neg} Biotin^{Hi} infected HSCs. Molecular signatures in the CD48^{neg} Biotin^{Lo} infected cells revealed high levels of TGFB1 and BCL2. While some studies report TGF-β1 role in HSC maintenance and quiescence(Wang *et al.*, 2018) others claim its involvement in HSC activation and HSC attrition due to accumulated DNA damage (Zhang et al., 2016). TGF-β1 was seen to be differentially regulated in HSC subtypes (Challen *et al.*, 2010) which agrees with the low and high expression levels in Biotin^{Hi} and Biotin^{Lo} cells from infected animals respectively. GO analysis for the CD48^{neg} Biotin^{Lo} revealed processes associated with signal transduction in response to DNA damage, DNA damage response, negative regulation of epithelial cell proliferation. BCL2 was among the genes that exhibited high expression in CD48^{neg}Biotin^{Lo} infected cells which was associated with oxidative stress and mitochondria metabolism (Norddahl *et al.*, 2011). This is supported by another study where loss of BID phosphorylation, a BH3-only BCL2 family member found in apoptosis, correlated with an increase in mitochondria (Maryanovich et al., 2012; Mortensen et al., 2022). Furthermore, accumulation of DNA damage in CD48^{neg} Biotin^{Lo} cells as a response to severe infection is attributed to the activation of p53 signalling pathway. I believe these cells lose their ability to repair any double-strand DNA breaks (Yamashita, Nitta and Suda, 2015) as seen in p53 violin plots. CD48^{neg} Biotin^{Hi} cells from control and infected animals were scored with high hscScore as opposed to -Biotin^{Lo}. The similarity in hscScoring between control and infected CD48^{neg} Biotin^{Hi} cells comes in agreement with the functional assay previously reported for the CD48^{neg} HSCs (Akinduro et al., 2018) and the cell cycle FACS analysis from Chapter 4 section 4. Taken together, these results demonstrate that CD48^{neg} Biotin^{Hi} contain functional stem cells and represent a more quiescent subset which is less responsive to malaria-induced proliferation compared to CD48^{neg} Biotin^{Lo} cells. While I only showed sc-RNA seq analysis of CD48^{neg} HSCs in this chapter, analysis for the sc-RNA seq ESLAM analysis is in progress and will follow.

Among the terms from GO pathway enrichment analysis, regulation of hormone biosynthesis and positive regulation of metabolic process were two of the terms that came up among downregulated terms between CD48^{neg} Biotin^{Hi} control/ infected cells. With that in mind, I asked, do Biotin^{Hi} control and Biotin^{Hi} infected cells present with low metabolic activity compared to Biotin^{Lo} infected cells? Looking at both CD48^{neg} and E-SLAM cellular pools, I demonstrated that Biotin^{Lo} infected cells have increased mitochondrial (mtROS) and cytoplasmic ROS (CellROX) compared to CD48^{neg} and E-SLAM Biotin^{Hi} HSCs from controls and infected animals. Since CD48^{neg} Biotin^{Lo} infected HSCs are cycling it is a possibility that ROS might accumulate in S/G2 stages. In a non-transformed cell cycle model, retina pigment epithelial cells (RPE-1) presented with an increase in mitochondria ROS accumulating in S and G2 cell cycle phases which correlated with increased mitochondria mass or a switch from glycolysis to oxidative phosphorylation (Kirova *et al.*, 2022). Thereafter, I seek to find information based on mitochondrial mass. I used MitoTracker (MTG) as mitochondria mass read-out to answer this question despite (Norddahl *et al*., 2011; Vannini *et al*., 2016; Ho *et al.*, 2017; Nakamura-Ishizu *et al*., 2018); previous report showing that MTG dye could be extruded by the xenobiotic efflux pumps harboured by HSCs; consequently leading to signal reduction than increase not truthfully correlating with mitochondrial mass (de Almeida *et al.*, 2017). De Almeida M. and colleagues found that upon verapamil treatment, which blocked efflux pump intake of MTG, MTG staining was increased in all haematopoietic cells instead of being reduced (de Almeida *et al.*, 2017b). Controversy, another study reported a spike in MTG fluorescence intensity 7 days post 5-FU treatment in HSPCs (Hinge et al., 2020). Lastly, Takihara *et al.* utilised mito-Dendra2 reporter animals, which possess a fluorescent protein fused to the signal of cytochrome c oxidase of subunit VII, and showed that a proportion of cells with high mito-Dendra2 GFP intensity (mito-Dendra2^{hi}) expressed EPCR, had a more quiescent phenotype and greater reconstitution compared to mito-Dendra2^{lo} EPCR$^{lo/-}$HSCs (Takihara *et al.*, 2019; Chakrabarty and Chandel, 2021). Under the effect of a chemotherapy drug, 5-fluorouracil (5-FU), mito-Dendra2^{hi} EPCR^{+} Lin^{-} SLAM cells were metabolically primed compared to the untreated cells due to cellular proliferation and exit from quiescence, suggesting a decline in mitochondria mass.

Taken together it is obvious that mitochondrial mass varies in HSCs and between studies. Only a small fraction of these studies reported changes in mitochondrial content relating to

proliferation-induced stress, however, there is no information in the literature relating to how severe infection affects mitochondria health in HSCs. In agreement with older studies, $CD48^{neg}$ and E-SLAM $Biotin^{Lo}$ HSCs showed a dynamic change of mitochondrial content upon their activation and differentiation. Furthermore, H2B GFP^{LRC} displayed a more dispersed and homogeneously distributed mitochondrial network compared to H2B GFP^{lo} cells (de Almeida *et al.*, 2017a; Zhang, Menzies and Auwerx, 2018) which is something I am expecting to see upon TOM20 antibody staining of $CD48^{neg}$ and E-SLAM $Biotin^{Lo}$ infected HSCs. Lastly, in infected animals, there was a ROS decrease which was reduced upon NAC treatment. The next step is to combine NAC with TMRM and MitoTracker mitochondria dyes to see whether by scavenging ROS mitochondrial mass and MMP is similar to E-SLAM $Biotin^{Hi}$ infected cells. If results look promising I could further ask, is E-SLAM $Biotin^{Lo}$ HSC functionality rescued upon NAC treatment in infected animals?

In conclusion, this chapter confirmed that transcriptional and metabolic differences between $CD48^{neg}$ $Biotin^{Hi}$ and $Biotin^{Lo}$ cells from infected animals exist making a strong argument that primitive HSCs are not entirely lost during severe infection and that the very few that remain preserve their stemness. Whether the differences between E-SLAM Biotin high and low cells are purely a reflection of a cell-intrinsic mediated system i.e stochastic behaviour or deterministic or environmental influences attributed to the BM niche where they reside it remains to be determined.

Chapter 6

Searching for Biotin HSCs in the BM microenvironment

6.1 Introduction

The BM microenvironment plays a pivotal role in regulating haematopoiesis. The current paradigm is that specialised environments, or niches, secrete various factors that promote HSC maintenance, quiescence and survival. Early studies reported that BM endothelial cells and stromal-derived cells promote granulopoiesis over a long period of time consequently supporting the maintenance of HSCs (Dexter, Allen and Lajtha, 1978; Li *et al.*, 2004). Since the cellular composition and location of certain BM niche cells remain to be determined, over the past years there has been a tremendous effort to expand this knowledge. Transcriptional data from single-cell analyses transformed our understanding of the relationship between haematopoietic cells and the BM niche (Baryawno *et al.*, 2019; Tikhonova *et al.*, 2019; Baccin *et al.*, 2020). Furthermore, it elucidated the composition of the niche as heterogeneous and identified more than 20 different independent subsets of cells associated with pro-haematopoietic factors, membrane-bound ligands and chemokines (Xu *et al.*, 2018; Tikhonova *et al.*, 2019; Dolgalev and Tikhonova, 2021; Fröbel *et al.*, 2021). While other studies investigated the niche in both steady-state and disease, specifically irradiation and cancer, (Hooper et al., 2009; Xu et al., 2018; Chen et al., 2019; Ho et al., 2019) the effect of infection on BM stromal cells remains an unsolved mystery.

Several perturbations such as *pI:pC*, LPS or parasitic, bacterial and viral infections induce the release of pro-inflammatory cytokines leading not only to HSC activation but to profound alterations in the BM stroma. Transient activation of BM niche after acute inflammatory stress led to the rapid activation and proliferation of endothelial cells (ECs) accompanied by vessel permeability and vasculature remodelling (Prendergast *et al.*, 2017). BM vasculature activation is associated with increased production of vascular endothelial growth factor (VEGF) (Prendergast *et al.*, 2017). In a similar context, interferon was found to affect not only haematopoietic cells but also mesenchymal BM stroma cells. Specifically, animals suffering

from malaria were shown to develop a dramatic loss of osteoblasts and leaky vessels (Haltalli *et al.,* 2020). Pharmacological treatment with osteo-active PTH led to the abolishment of proliferation in HSCs caused by infection and osteoblast rescue (Haltalli *et al.*, 2020). It was shown that during *P. falciparum* asexual cycle, gametocytes home to BM extravascular space for their sequestration (Joice *et al.*, 2014; Venugopal *et al.*, 2020). In the BM parenchyma, terminal erythropoiesis occurs in erythroblastic islands. Although these niches serve as a protective site for gametocyte development *per se*, however, the presence of parasite affects terminal differentiation of erythroid cells (Drive and Email, 2023). While several studies investigated the complexity and deregulation of some BM niche components during infection, the question remains on how the remodelled niche interacts with HSCs. During *Mycobacterium avium* infection, IFNγ promoted displacement of HSCs by disrupting the interaction between CXCL12-abundant reticular (CAR) cells (Florez *et al*., 2020). BST2 expression was detected in HSCs stimulated by IFNγ, accompanied by an increase in the adhesive molecule E-selectin contributing to HSC homing through transendothelial migration (Winkler *et al.,* 2012; Florez *et al*., 2020).

Given the BM stroma is remodelled during severe infection, several open questions remain to be elucidated:

A) Does BM remodelling affect the localisation of HSCs?
B) What are the mechanisms driving BM niche remodelling?
C) How does the BM niche regenerate after recovery from severe infection?
D) What is the transcriptional landscape of remodelled niche components during severe infection?

In this Chapter, I aim to investigate first the localisation of E-SLAM Biotin cells by asking, do E-LSAM Biotin^{Hi} cells localise in specific areas of the BM that facilitate dormancy compared to E-SLAM Biotin^{Lo} cells? By combining confocal microscopy and flow cytometry approaches, I answer this question with the help of an endogenous HSC reporter α-catulin GFP. Secondly, having in mind that malaria affects osteolineage and remodels BM vasculature (Haltalli *et al.*, 2020), I embark on a journey to identify other niche components that might be affected. My hypothesis here was that perhaps the loss of functionality in E-SLAM Biotin^{Lo} might be attributed to not only cell-intrinsic mechanisms but also to the remodelled niche. With the

help of osteoblast, Col2.3 GFP and LepR^{+}Cre; RosaYFP reporters and by combining flow cytometry, confocal microscopy and IVM, I study LepR^{+} PCs and ECs and the impact of *P. berghei* infection upon these cells. Thirdly, given the BM remodelling in infected animals, I endeavour to investigate possible mechanisms that relate to their loss.

6.2 No preferential bone location for E-SLAM Biotin^{Hi} HSCs during malaria infection

Data so far has shown that there is a proportion of dormant HSCs that proliferate minimally, since they retain the biotin label, preserving their stemness and maintaining a low metabolic status. To explore further possible mechanisms, I went ahead and explored cell extrinsic signals that help dormant Biotin HSCs preserve their functionality. Therefore, I asked, is there a "preferred" location in the BM that shields E-SLAM Biotin^{Hi} HSCs from total activation caused from *P. berghei* infection? To capture localisation changes, I decided to inject animals with biotin at different time points, on days one and three *pbi* (Figure 6.1 A) specifically and collect bones on days 3 and 5 *pbi* respectively. Given that the first signs of parasitaemia in animals' PB appear from day 3 onwards accompanied by the activation of the HSC compartment, HSCs might not relocate before day 3 but changes could be noticeable on day 5. To gain insights into preferential locations of CD48^{neg} and E-SLAM Biotin^{Hi} and Biotin^{Lo} HSCs, bones were fractionated into two groups, central bone marrow (CBM) and trabecular area/epiphysis/metaphysis (Figure 6.1 B). In leukaemic animals, Duarte *et* al. a) flushed the cells from the central marrow, located in the diaphysis of the bone, and b) crushed the cells of the trabecular area, located in the epiphysis mainly but metaphysis was included in their analysis too (Duarte et al., 2018). Using the same methodology, CBM and trabecular area fractions had a high percentage of CD48^{neg} and E-SLAM Biotin^{Hi} HSCs on day 3 (Figure 6.1 C, E), which was expected. However, the proportion of CD48^{neg} but not E-SLAM Biotin^{Hi} was diminished in the CBM area as infection progressed (Figure 6.1 D). In addition, CD48^{neg} Biotin^{Lo} HSCs were found in higher proportions on day 5 (Figure 6.1 D) in both CBM and trabecular areas compared to day 3 (Figure 6.1 C). Interestingly, the percentage of E-SLAM Biotin^{Hi} HSCs in control and infected animals was similar in the CBM and trabecular areas earlier in the time course (Figure 6.1 E, F). Taken together, these data show that although the proportion of both

CD48^{neg} and E-SLAM Biotin^{Hi} HSCs decreased at day 5 *pbi* there were not supported by a preferred niche during malaria infection.

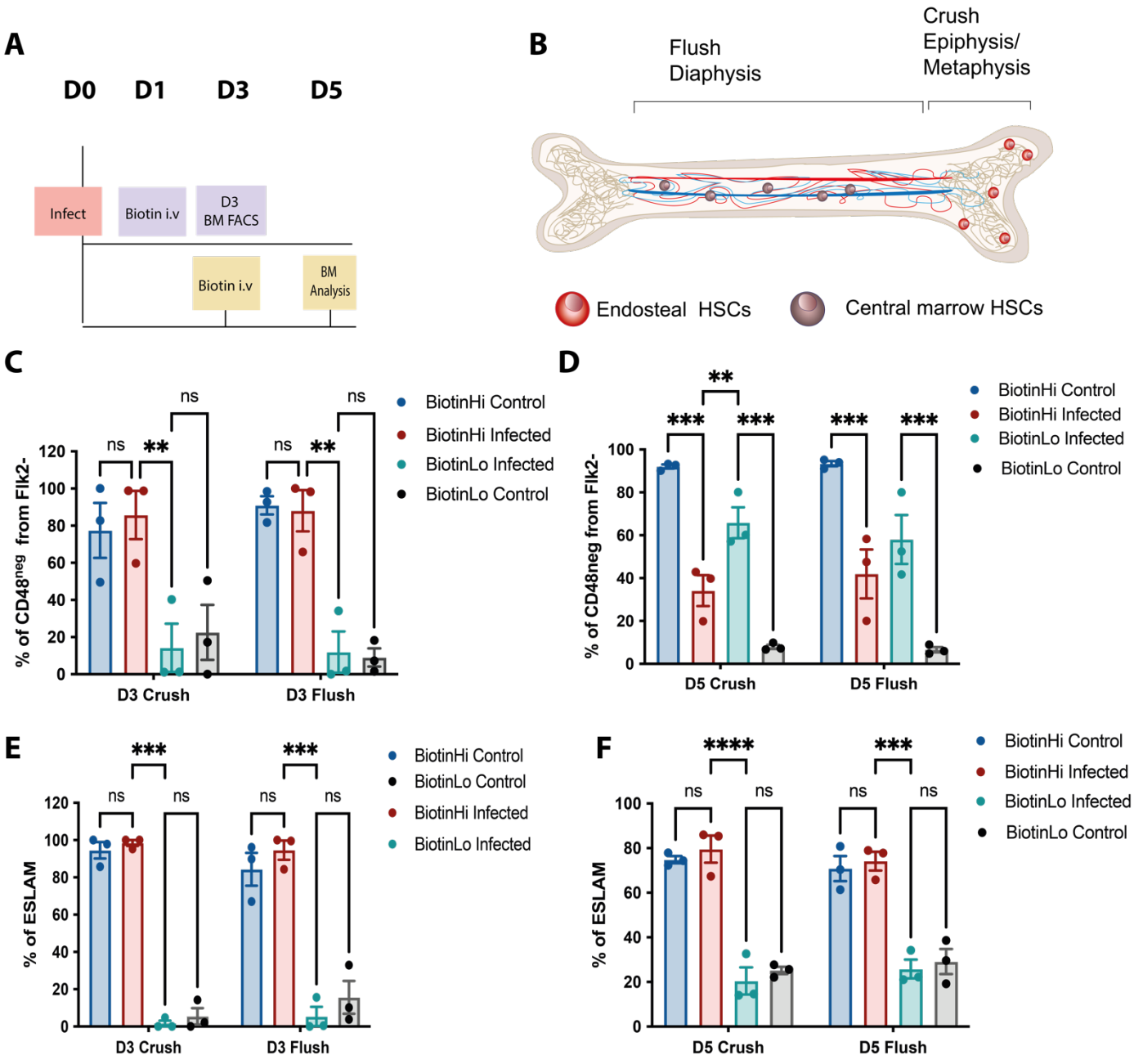


Figure 6. 1 Dormant or proliferating HSCs evenly distributed in the BM. A) Experimental set up where animals are injected with biotin label at days 1 and 3 and analysed at day 5 *pbi*. B) To assess the proportion of HSCs in specific BM areas, bones were compartmentalised into flush (Diaphysis) and crush (epiphysis/metaphysis) fractions. The flush fraction contained CBM cells whereas the crush fraction contained cells from both epiphysis/metaphysis areas as previously described (Duarte et al., 2018). Proportion of CD48^{neg} Biotin^{Hi} and Bitoin^{Lo} cells in infected and control animals from flush/crush fractions on days C) 3 and D) 5. E,F) Proportion of E-SLAM Biotin^{Hi} and Bitoin^{Lo} cells in infected and control animals from flush/crush fraction on days E) 3 and F) 5. Error bars represent the mean ± s.d. Each dot represents one mouse. Statistical differences were determined using two-way anova with Bonferroni correction. (*** represent P≤0.001,** represent P≤0.01, * P<0.05).

6.3 Endogenous α-catulin GFP HSC reporter enables the identification of E-SLAM Biotin^{high} HSCs

HSCs are rare and until recently Flow cytometry was the go-to tool to study them from different angles. Since the first publication emerged in 2015, all attention turned towards endogenous HSC reporters as HSCs could now be studied in their natural environments. Some examples of these reporters are the α-catulin GFP mouse line, where the green fluorescent protein is knocked-in into the *Ctnnal1* gene (Acar *et al*., 2015), or the homeobox B5 (Hoxb5-tri-mCherry)(Chen *et al*., 2016). Only a small fraction of HSCs express α-catulin GFP, nevertheless when their long-term multilineage reconstitution ability was questioned it was found that α-catulin GFP HSCs were functional LT-HSCs (Acar *et al.*, 2015). The α-catulin GFP HSCs also expressed c-kit on their cell surfaces. Therefore, to gain an understanding of the localisation of biotin-retaining HSCs, I worked with the α-catulin GFP mouse line (Acar *et al*., 2015) where I first injected biotin at day 3 post blood infection (*pbi*) and anti-EPCR antibody on day 5. Bone sections from control and infected animals were then stained for c-kit and Streptavidin, to detect positive expression for c-Kit and biotin, and afterwards were visualised under a confocal microscope. Thereafter to identify HSCs, I looked for combined membranous c-Kit and cytoplasmic α-catulin GFP signals on cells. When co-localisation was detected, I then moved to identify cells with a positive expression of EPCR and Biotin. From control animals, I was able to detect close to 20 ESLAM Biotin^{Hi} HSCs (Figure 6.2 A, B) in different areas of a single bone. However, this was not the case in the infected animals as E-SLAM Biotin^{Hi} HSCs were extremely rare to be found, hence only two cells were identified (Figure 6.2 C, D) as α-catulin GFP+, c-Kit+, Biotin+. This led me to think that a) although α-catulin GFP cells were easier to locate in steady-state GFP expression in HSCs possibly could be diminished during infection, and b) it is a possibility that due to infection-induced proliferation, precursors could also express the GFP. To answer these questions, I proceeded and analysed WBM from control and infected α-catulin GFP animals through Flow cytometry.

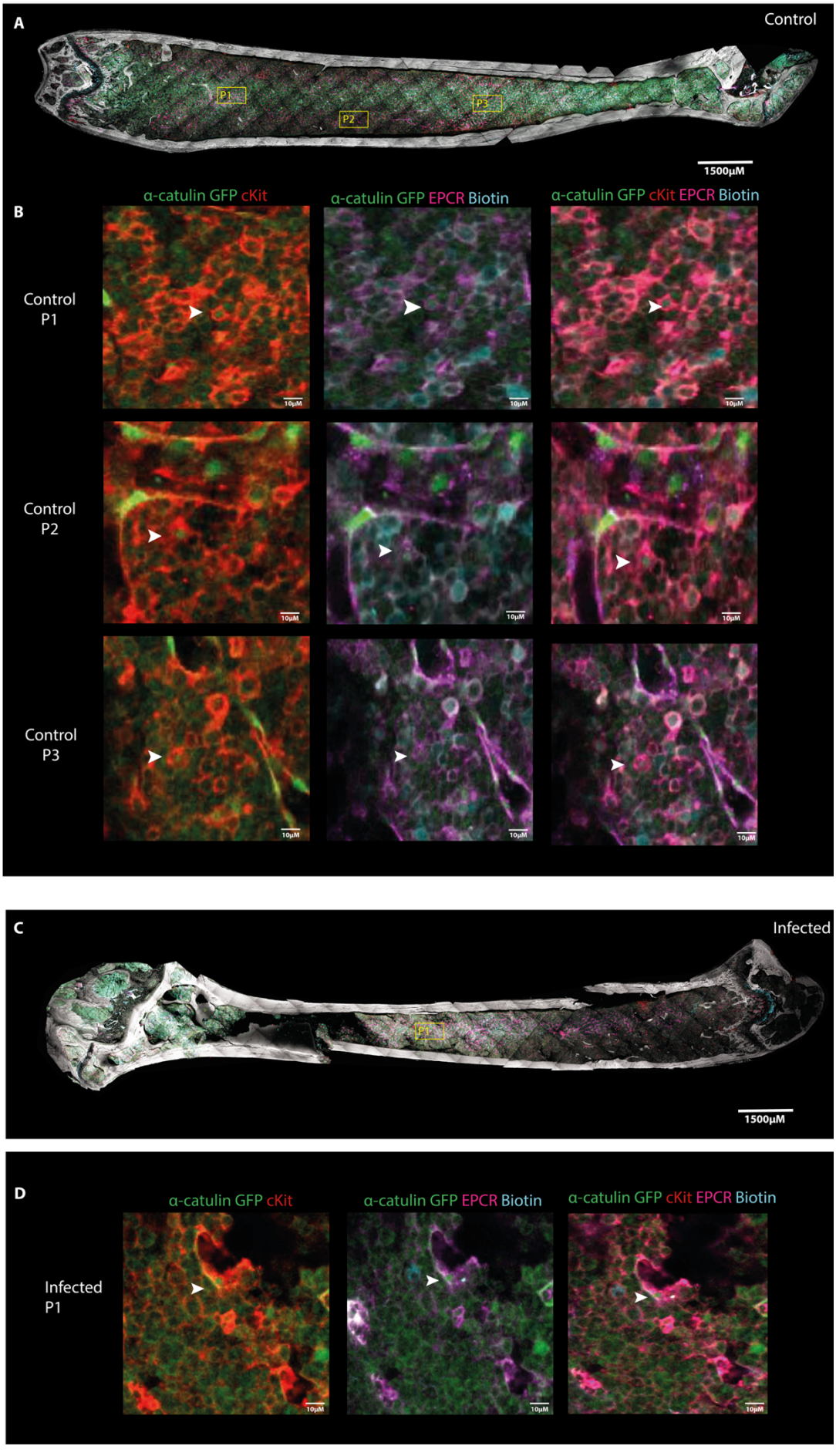

A
Control
P1
P2
P3
1500μM
B
α-catulin GFP cKit
α-catulin GFP EPCR Biotin
α-catulin GFP cKit EPCR Biotin
Control P1
Control P2
Control P3
10μM
C
Infected
P1
1500μM
D
α-catulin GFP cKit
α-catulin GFP EPCR Biotin
α-catulin GFP cKit EPCR Biotin
Infected P1
10μM

Figure 6. 2 Localisation of α-catulin GFP E-SLAM Biotin cells A) Bones were processed, sectioned and stained for c-Kit and Streptavidin (Biotin). Biotin and EPCR were injected *iv.* B) Positions from α-catulin GFP E-SLAM^{+} Biotin^{+} cells in different areas of the bone in A. α-catulin GFP^{+} cytoplasmic expression was identified followed by a membranous c-Kit staining (left column). Middle column shows α-catulin GFP^{+}c-Kit^{+} HSCs with positive signals for Streptavidin and EPCR. Images in the right column represent "merge" of all staining parameters.P, positions. Data substracted from *N*= 2 control bones and *N*=2 infected bones and from two independent experiments.

For flow analysis, I first plotted α-catulin GFP (x axis) and c-Kit (y-axis) and focused on the α-catulin GFP^{+} c-kit+ cells (Figure 6.3 A). Then I followed the usual gating strategy outlined in Chapter 2 section 2.3 and looked for possible changes in the proportion of MPP2, CD48^{neg} and E-SLAM HSCs (Figure 6.3A). In α-catulin infected animals I observed fewer CD48^{neg} and E-SLAM

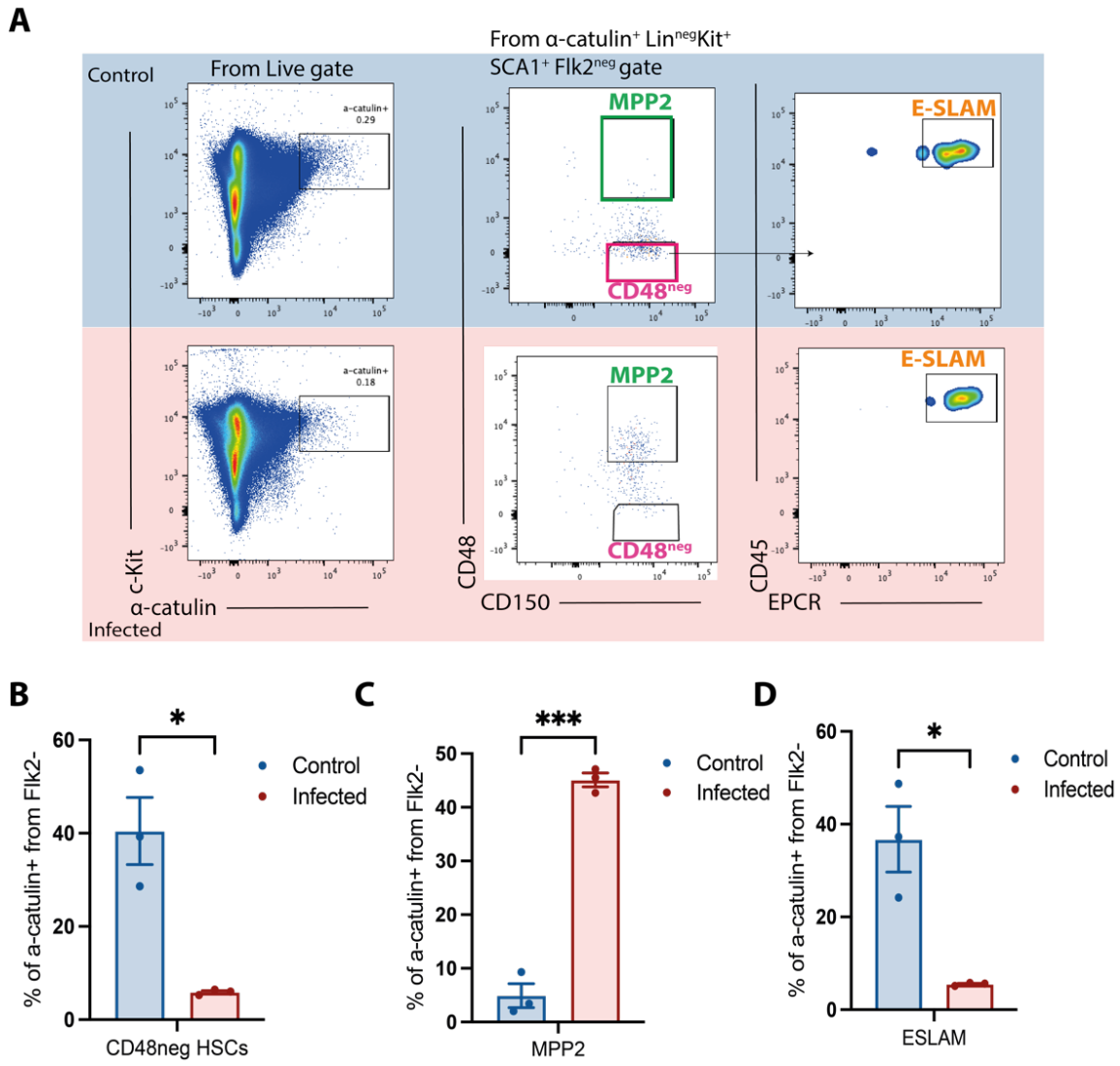
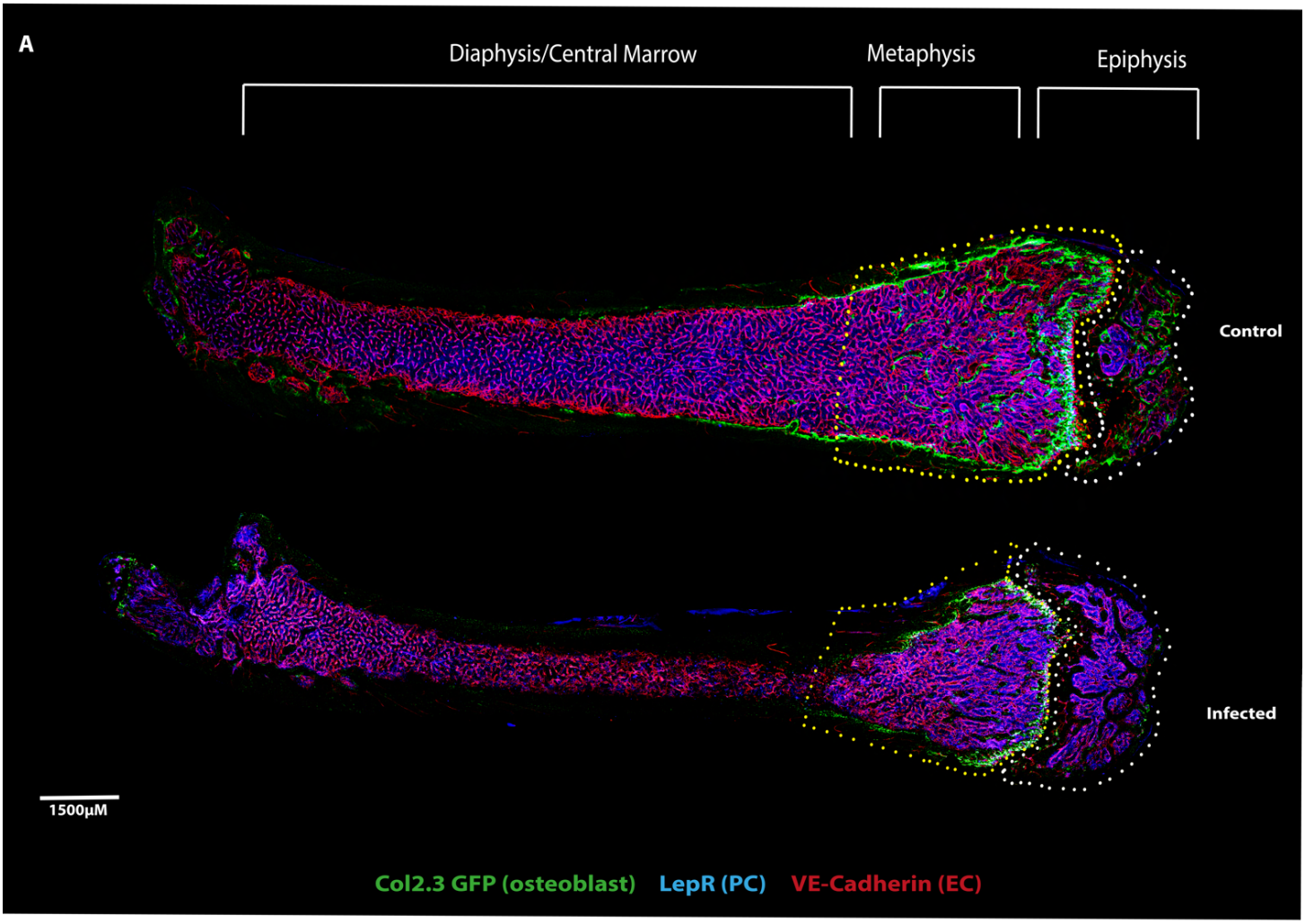


Figure 6. 3 α-catulin GFP HSCs BM analysis A) To clarify that all HSCs in the bone plugs are positive for α-catulin, flow cytometry analysis was used. FACS plot shows cells from the cKIT+, α-catulin GFP $^{+}$, then I followed the usual gating strategy outlined in material and methods in Chapter 2 to identify CD48^{neg}-HSCs, ESLAM and MPP2. Proportion of B) CD48^{neg}-HSCs, C) E-SLAM was reduced during infection. D) The percentage of MPP2 was increased in infected animals compared to control. Each dot represents one mouse from one independent experiments. Error bars represent the mean ± s.e.m. Statistically significant differences were determined using student's *t*-test (*** represent P≤0.001, * P<0.05) .

HSCs compared to control animals (Figure 6.3 B, D) which agreed with previous data in Chapters 3 and 4. When I investigated MPP2 subset, it was evident that these cells have proliferated in infected animals, which was reflected in the high proportion shown in Figure 5.3 C.

6.4. *P. berghei* infection causes alternations in the BM stroma.

The effect of malaria on the BM stroma has recently begun to unravel. Recent work pointed towards the loss of osteoblasts and vasculature remodelling based on IVM and haematoxylin and eosin (H&E) immunohistochemical stainings (Haltalli *et al.*, 2020). Given these findings, it is crucial to understand, what other stroma components are affected? and what happens to those cells after recovery? Here, I seek to understand the first part of the question. The osteoblast reporter animals, Col2.3GFP, were injected *i.v* with fluorophore-conjugated anti VE-Cadherin antibody. After femurs from control and infected animals were processed and cryosectioned, femurs were rehydrated, blocked with serum and stained for LepR antibody (Figure 6.4 A). A pre-defined threshold macro was used for the analysis which enabled the segmentation of pixels based on the green fluorescent intensity. The signal from green pixels in both the cortical bone and epiphysis but not the diaphysis was reduced in infected animals (Figure 6.4 B) since osteoblasts are located in the endosteum and not in the central bone marrow (diaphysis). This finding agreed with previously published data where osteoblasts were dramatically affected in *P. berghei* sporozoite infection (Haltalli *et al.*, 2020). However, the question still remained for the other stroma components. Hence, I focused on studying the effect of malaria infection on Endothelial cells (ECs) and LepR^{+} perivascular cells (PCs).



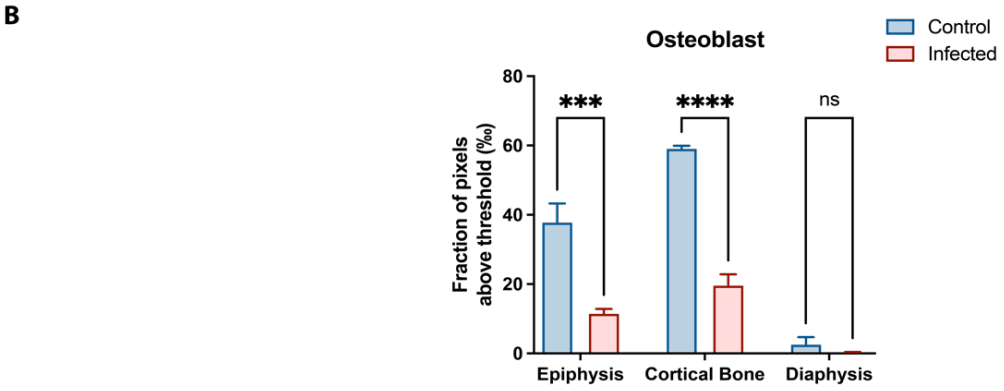


Figure 6. 4 Loss of osteoblast in infected Col2.3 GFP animals. A) Osteoblasts, ECs and PCs were examined based on GFP expression, VE-Cadherin and LepR stainings respectively. B) Percentage of green pixels in epiphysis, cortical (entire) bone and diaphysis measured from the bone of control and infected animals. Error bars represent the mean ± s.e.m. Statistically significant differences were determined using student's *t*-test (**** represent P≤0.0001, ns no significance). Data substracted from *N*= 2 control bones and *N*=2 infected bones and from independent experiments.

First, given the dramatic loss of osteoblast I investigated whether the vessels found in endosteum (endosteal vessels) are remodelled. Animals were injected with fluorophore-conjugated anti-VE-Cadherin antibody to visualise ECs. The vascular adhesion molecule VE-Cadherin is found at EC junctions. Based on VE-Cadherin expression in femoral bones from both conditions (Figure 6.5 A), I calculated the proportion of the endosteal vessels (EVs) (Figure 6.5 A, B) by dividing different endosteum areas covered by vessels with the total endosteum length. This measurement was firstly described in acute myeloid leukaemia (AML) (Duarte et al., 2018).

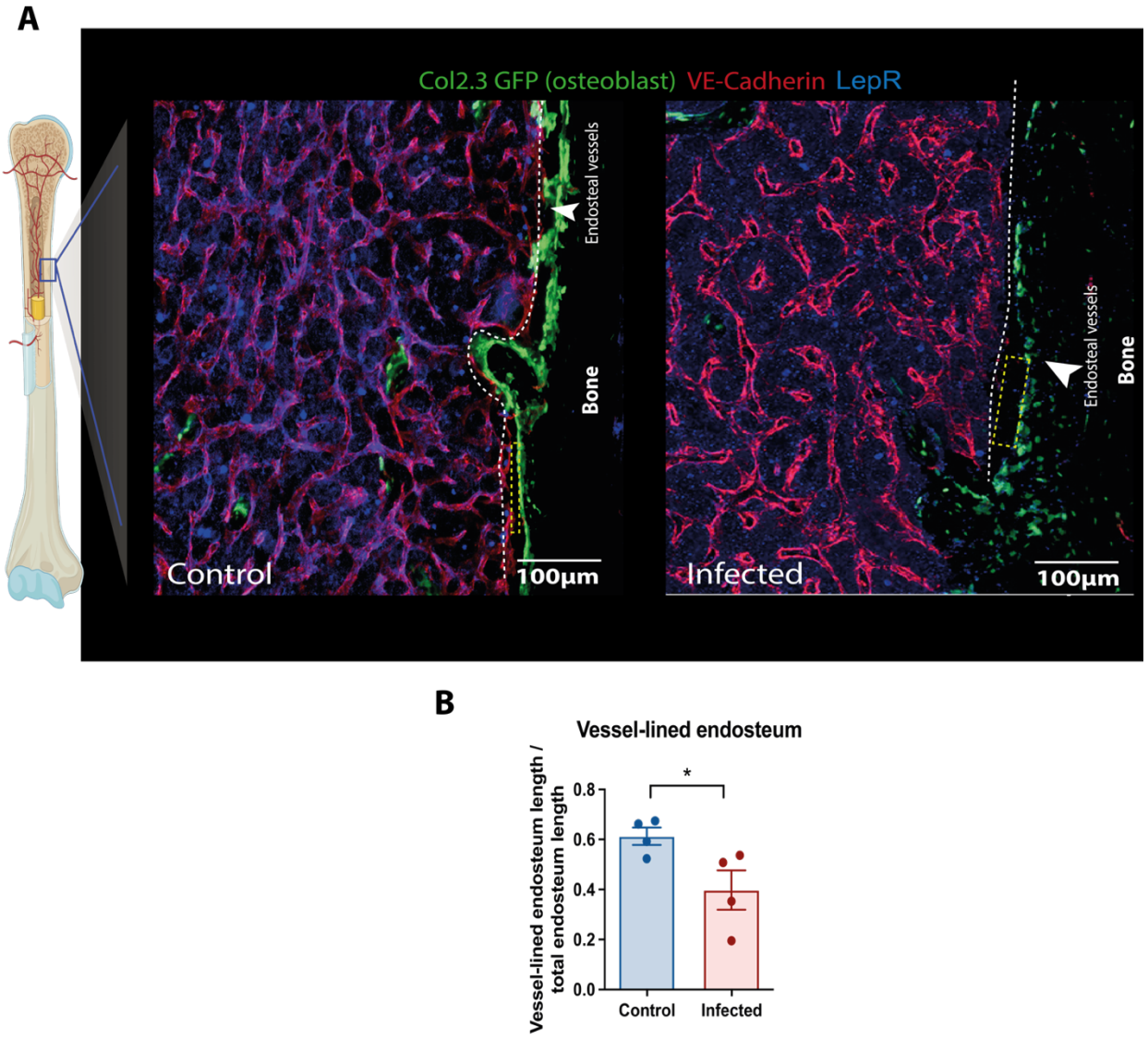


Figure 6. 5 Osteoblasts loss uncovered in bone sections. A) Endosteum (dotted white line) and vessels (red) including endosteal ones in control and infected bones. Yellow box represents distance from the bone. B) the proportion of endosteal vessels was calculated. C) EV volume represented as the percentage of EVs that occupy endosteal marrow calulcated per fiedl of view. Each dot represents filed of view occupied by either osteoblasts (green) or endosteal vessels (red). Error bars represent the mean ± s.e.m of the fields of vews analysed. Statistically significant differences were determined using student's *t*-test (*** represent P≤0.001, ** represent P ≤ 0.01; * P<0.05). Data substracted from *N*= 2 control bones and *N*=2 infected bones and from 2 independent experiments.

Based on the calculation, the endosteal vessels were significantly reduced in the infected compared to control animals, pointing towards endosteal vessel loss (Figure 6.5 B). In addition, the endosteal-lined vessels (dotted white line) were noted to be further away from the bone in the infected bones, compared to healthy ones (yellow dashed box) (Figure 6.5 A). This observation was made by observing individual tiles from two infected and control bones. Further analysis on the BM stroma was performed with the help of Amaia Ochandorena Saa. Using a 3D reconstructed volume of endosteal vessels per field of view, we calculated the percentage of the endosteal marrow (yellow dashed line) occupied by the reconstructed vessels (Figure 6.6 A). The lack of EV volume was seen in the malaria-burdened bones compared to healthy (Figure 6.6 B) ones suggesting that the endosteal marrow occupied less space. Moreover, the remaining vessels appeared thinner, raising the question whether they may have been remodelled more generally. For this reason, we used Imaris image analysis software and placed filaments along the length of each vessel so that the sum of filaments represented the total length of the vascular network per field of view. From the analysis it was evident that the total length of EVs was significantly decreased (Figure 6.6 C) in infected animals compared to controls, suggesting a reduction in vessel branching. Published work from Haltalli M and colleagues showed that in the mouse endothelial cell reporter, Flk1 GFP, animals exposed to infected mosquitos carrying *P. berghei* parasite had leakier vessels compared to healthy control prompting to vasculature remodelling (Haltalli *et al.*, 2020). To obtain more information on the blood infection model, I then asked does vessel texture, a form of vasculature remodelling, changes as a consequence of malaria infection? The vessel texture, referred to as roughness, in control bones seemed smoother but in the infected bones did not. These changes were calculated by dividing reconstructed endosteal area by endosteal vessel volume. Figure 6.6 D, shows that vessels in infected animals have slightly different surface roughness, which was significantly increased when compared to healthy vessels which was shown for the first time.

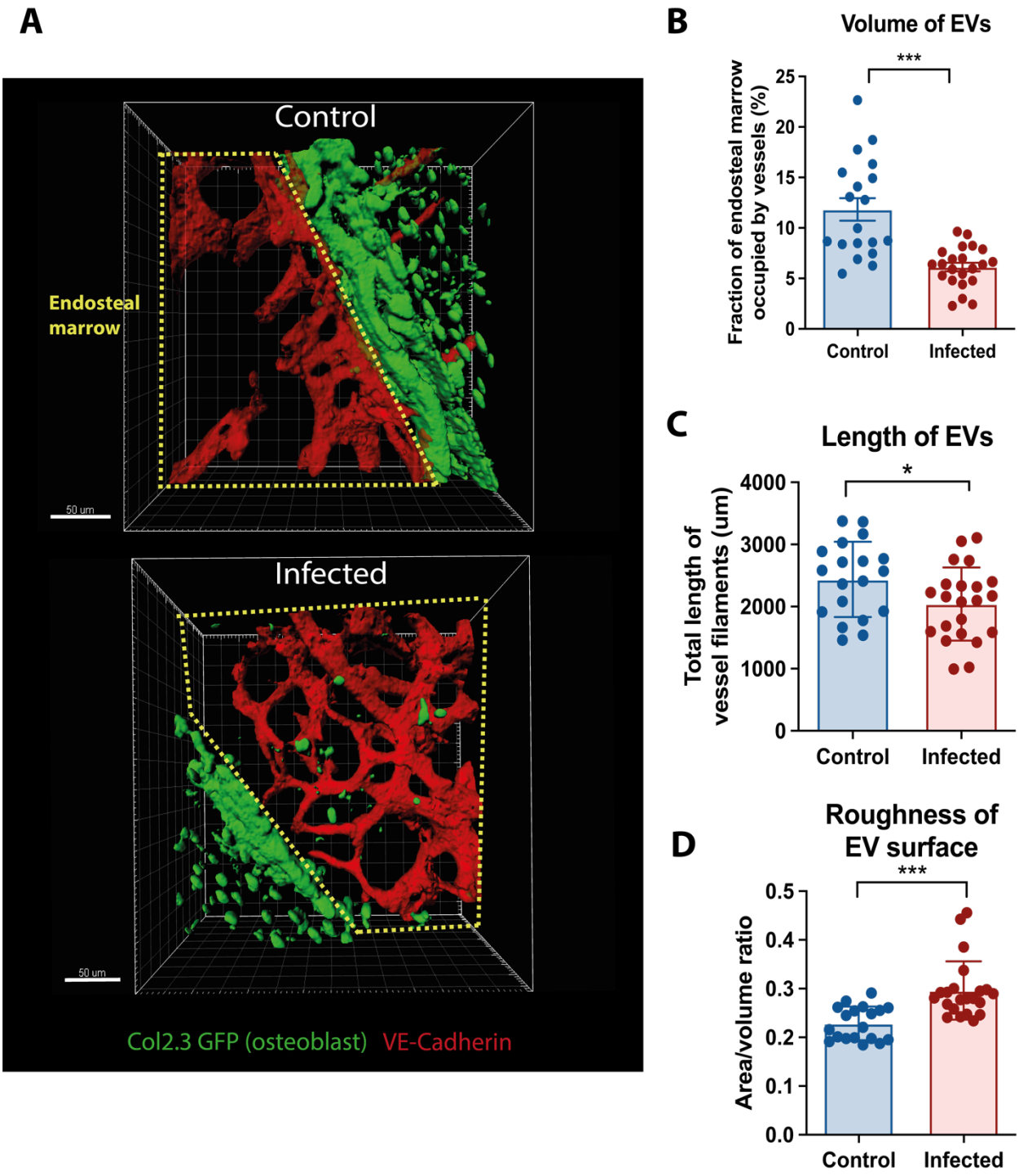


Figure 6. 6 Endosteal vessel remodelling in severe infection. A) 3D reconstructed volumes of endosteal vessels and endosteal marrow (encased in yellow dashed line) in control and infected animals. Quantifiction of B) vessel volume, C) levessel length defined by filaments, and D) roughness surface texture Each dot represents filed of view occupied by either endosteal vessels. Error bars represent the mean ± s.e.m. Statistically significant differences were determined using student's *t*-test (*** represent P≤0.001, * P<0.05). Data substracted from *N*= 2 control bones and *N*=2 infected bones and from different animals.

6.5 Severe infection remodels vasculature in central bone marrow areas.

Since I observed osteoblast loss and endosteal vessel remodelling in the field of view that contained the endosteum, I then asked whether such changes are visible, for length, volume and vessel surface, on the CBM vessels as a consequence of infection. Firstly rendered vessels (Figure 6.7 A,C) after maximum projection were 3D reconstructed (Figure 6.7 B, D). Thereafter, I calculated the volume (percentage of the CBM occupied by the reconstructed vessels) and observed that in the infected animals, CBM ECs occupied less volume (Figure 6.7 E). By dividing the area of reconstructed vessels by CBM vessel volume I concluded that the vessel surface was "rougher" in infected as opposed to those in healthy bones (Figure 6.7 F). These data indicated that not only vasculature in the endosteal areas is remodelled but also vasculature in the CBM is too. While the changes in the CBM ECs were noted I then asked, are LepR^{+} PCs that surround ECs also affected by *P. berghei* infection? To answer this question, I first visualised LepR^{+} perivascular protrusions wrapping around the vessels in 3D reconstructed images (Figure 6.7 G). Then I measured the LepR^{+} PC volume in one field of view and found that it decreased in the malaria-burdened animals suggesting that not only CBM ECs are affected but PCs too (Figure 6.7 H). Thereafter, intravital microscopy (IVM) was used to acquire information on LepR$^{+/-}$Cre; Rosa26YFP reporter animal that were injected with a fluorophore-conjugated anti VE-Cadherin antibody (Figure 6.8 A) before acquisition took place. A tilescan (Figure 6.8 A) and high-resolution images from four fields of view obtained from the mouse calvarium were used to quantify possible changes in LepR$^{+/-}$Cre; Rosa26YFP animals in both conditions. For the analysis, I first segmented LepR^{+} PCs using a Fiji algorithm to separate the brightest pixel clusters (yellow outlines) (Figure 6.8 B), which I called LepR^{+} patches. Based on the number of LepR^{+} patches per total number of pixels within the entire BM area (Figure 6.8 C) of the calvarium, I concluded that LepR^{+} PCs in the calvarium are 4-fold reduced in infected BM compared to control animals. Lastly, I quantified the number of LepR^{+} (cyan) pixels alone based on the number of pixels above a set intensity threshold normalised by the number of pixels within the available BM space in each tile and concluded that perivascular cells in the CBM of LepR$^{+/-}$Cre; Rosa26YFP infected animals are dramatically lost (Figure 6.8 D)

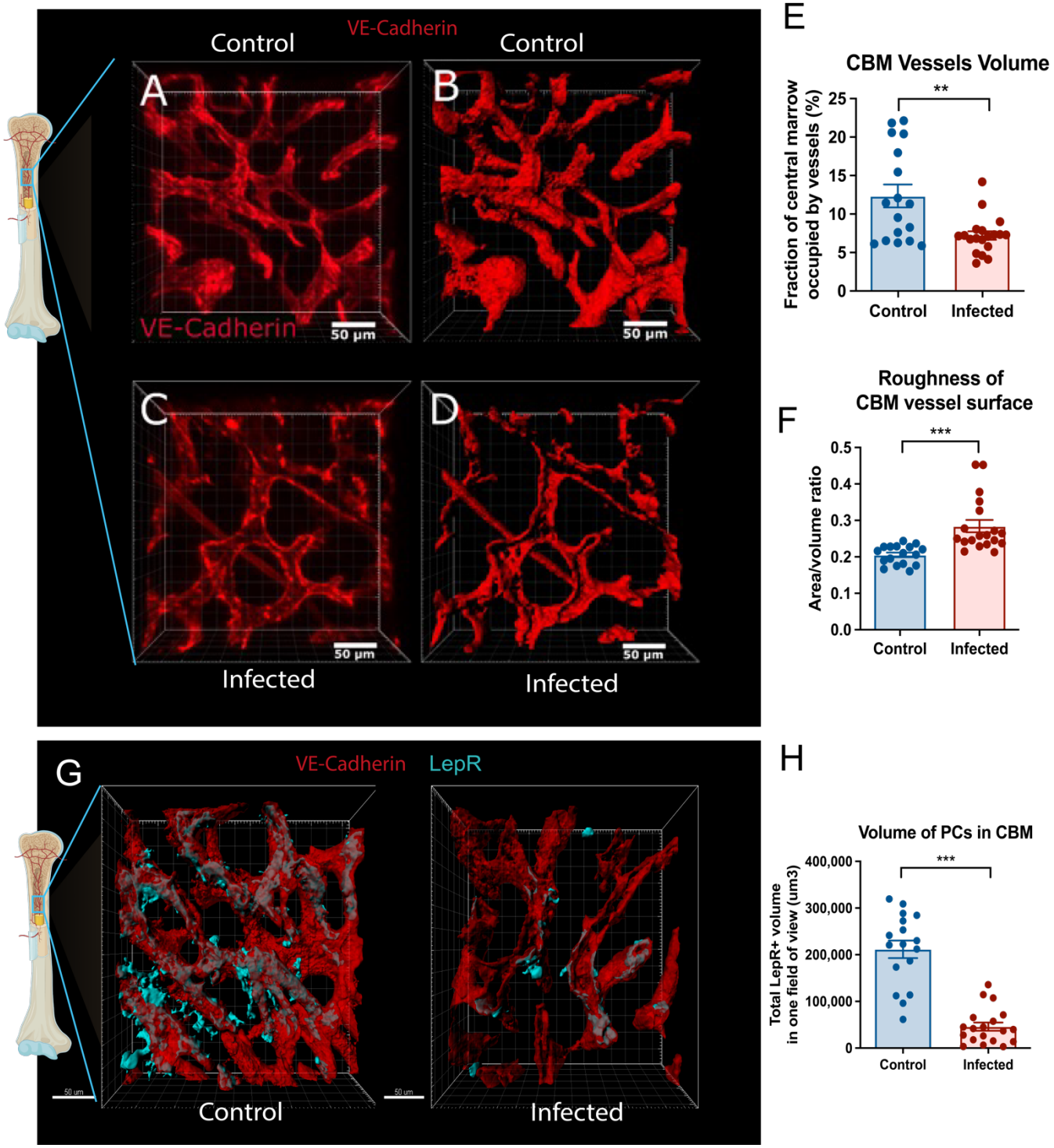


Figure 6. 7 *P. berghei* impacts CBM ECs and PCs. A,C) normal images and B,D) 3D reconstructed images of infected and control bone tile regions. Measurements on CBM occupied by vessels to define E) the vessel volume, and F) Roughness of CBM vessel surface. G) 3D images showing vasculature (red) and LepR$^+$ PCs (blue) in both conditions. H) Measurements of the LepR$^+$ PCs volume in the CBM. Each dot represents one filed of view per bone analyses. Data substracted from two infected and two control long bones from 2 independent experiments. Error bars represent the mean ± s.e.m. Statistically significant differences were determined using student's *t*-test (*** represent P≤0.001, ** represent P ≤ 0.01).

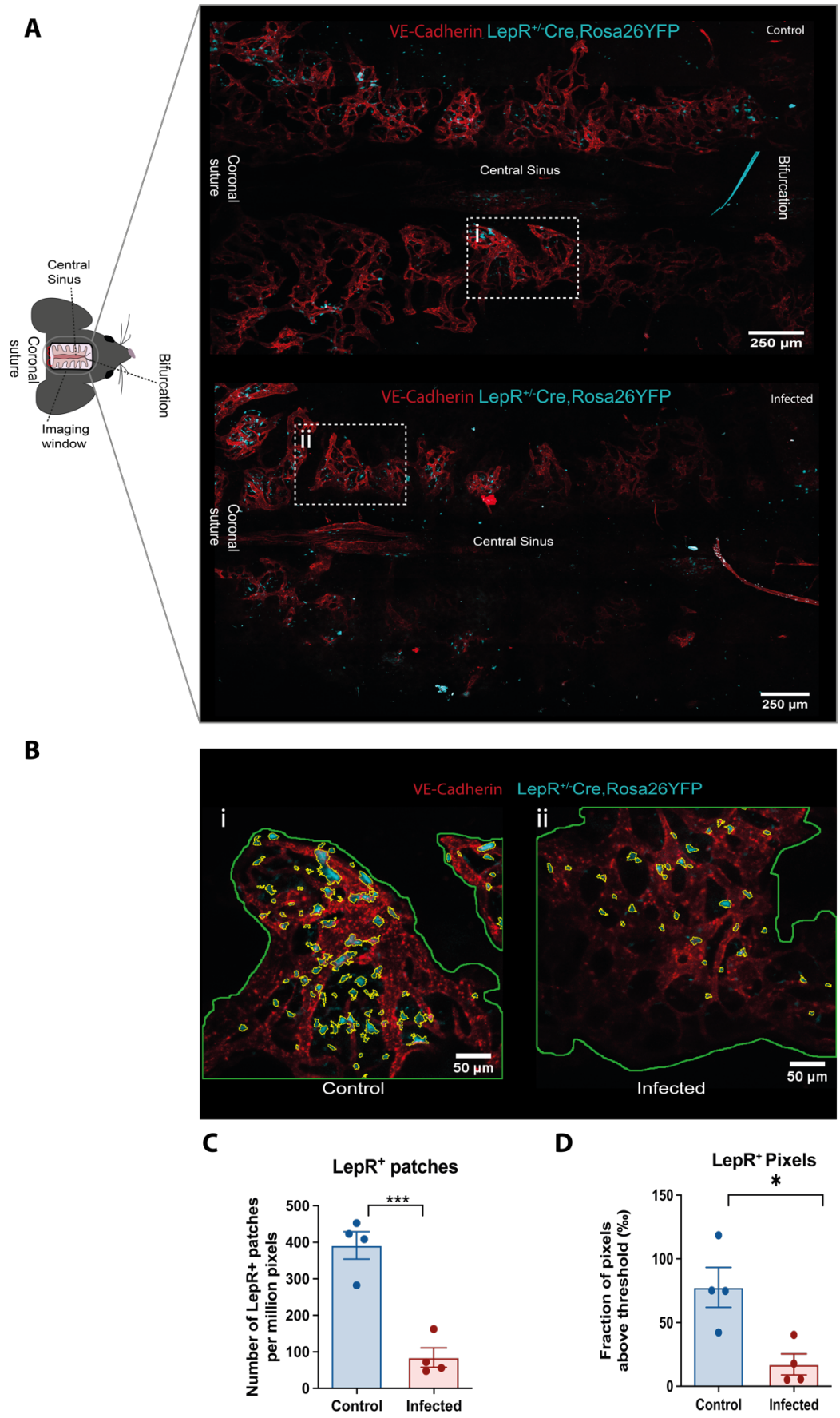


Figure 6.8 IVM of LepR$^{+/-}$Cre; Rosa26YFP transgenic reporter mice to confirms the loss of LepR^{+} PCs in malaria. A) Representative mages of animal calvarium obtained by intravital microscopy (IVM) on LepR$^{+/-}$ Cre; Rosa26YFP control and infected animals. A small incision is made on mouse skull to insert imaging window. Tilescan from control (top) and infected (bottom) calvaria. B) Higher resolution images from animal calvaria. Green outline is the result of the automated counting algorithm (yellow outline) and represents the area of the tile where bone marrow is present. C,D) Fiji algorithm segments the brightest pixels to discriminate LepR patches. C) represents the number of pixels above threshold. F) Number of pixels above threshold normalised. By the number of pixels within the available BM space in each tile. *N*= 4 fields of view from one control calvarium and *N*=4 fields of view from 1 infected calvarium. Statistical differences were determined by Student's *t*-test. (*** represent P≤0.001, * represent * P<0.05).

confirm these findings, bones from both conditions were divided into two fractions and analysed by flow cytometry. One fraction related to central bone marrow (CBM) cells, and the second to bone lining cells (BL). CBM cells were incubated with anti-CD45 microbeads to deplete haematopoietic cells (that have positive expression for CD45). Thereafter, these two fractions were stained with a cocktail of BM stroma antibodies to identify osteoblast, $LepR^{+}$PC, ECs from fractionated bones and as previously described(Luis et al., 2023). Based on flow cytometry analysis of BM stroma from control and infected animals, in the BL fraction osteoblast were identified as $CD45^{neg}$ $Ter119^{neg}$ $CD51^{+}$ $CD31^{neg}$ $ALCAM^{+}$ and ECs as $CD45^{neg}$ $Ter119^{neg}$ $CD51^{neg}$ $CD31^{+}$. In the CBM fraction, $LepR^{+}$PC were identified as $CD45^{neg}$ $Ter119^{neg}$ $LepR^{+}$ and CBM ECs as $CD45^{neg}$ $Ter119^{neg}$ $CD51^{neg}$ $CD31^{+}$ $SCA1^{+}$. A detailed gating strategy can be found in Chapter 2, section 2.4. FACS analysis revealed a reduction in the bone lining ECs and osteoblast (Figure 6.9 A, B) which agreed with the quantification shown in the long bones. Furthermore, the proportions of both ECs and $LepR^{+}$PCs in CBM were decreased (Figure 6.9 C, D) in the malaria-burdened animals compared to controls, suggesting that *P. berghei* infection leads to BM stroma alterations and depletion of ECs, $LepR^{+}$PCs and osteoblasts.

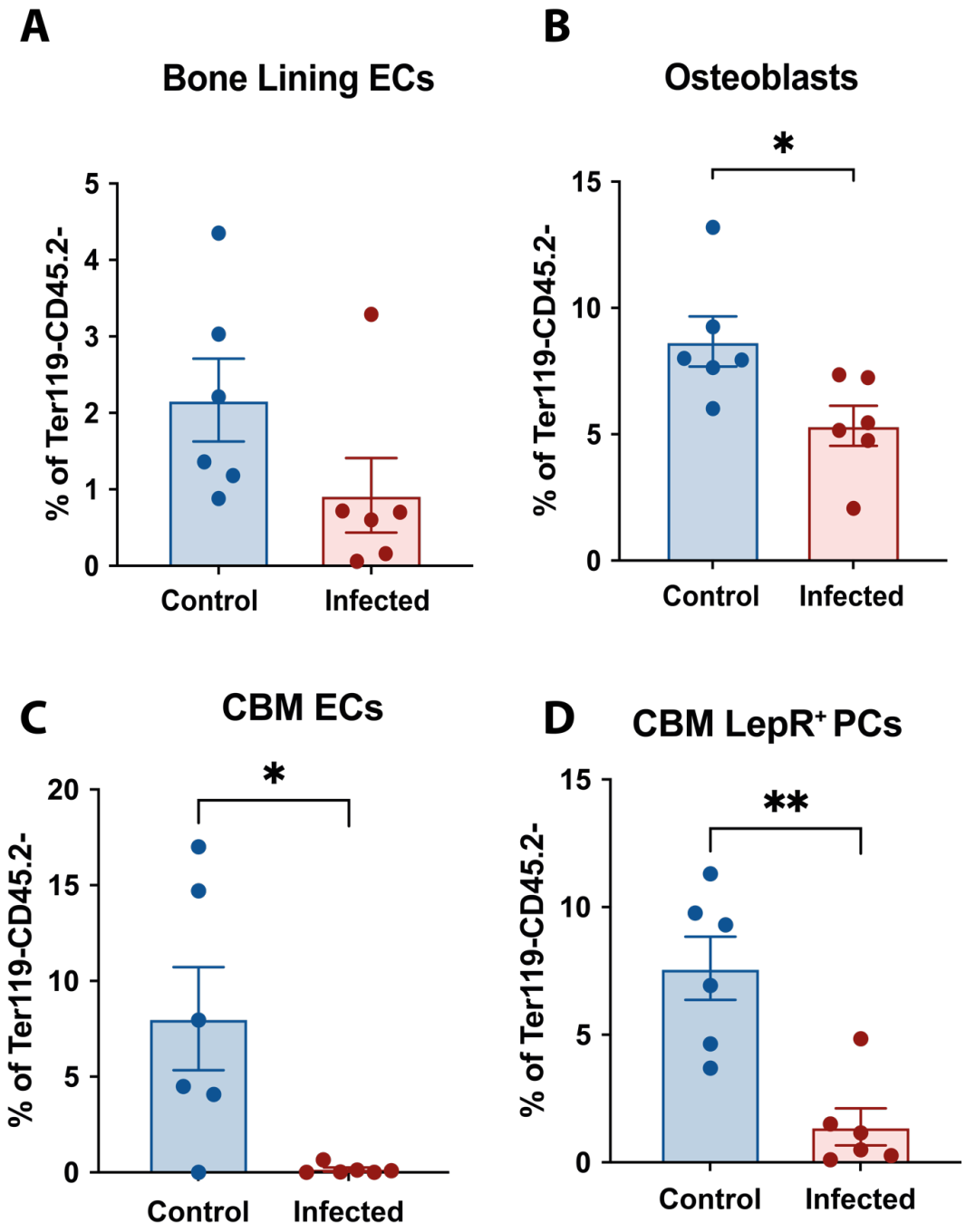


Figure 6. 9 BM stroma cells are lost during severe infection. Bone lining cells (BL) were stained for ECs (A) and osteoblasts (B) and their proportions were measured in both conditions. Central bone marrow (CBM) cells were stained for ECs (C) and LepR^{+} PCs (D) and their proportions were measured in control and infected animals was reduced in CBM in infected animals compared to controls. Each dot represents one mouse, *N*=5 control and *N*=5 infected from three independent experiments *N*=3. Error bars represent the mean ± s.e.m. Statistically significant differences were determined using Student's *t*-test (** represent P ≤ 0.01; * P<0.05).

6.6 Stromal ROS as a possible mechanism of HSC damage

Previous observations revealed that highly permeable sinusoids promoted HSPC activation due to augmented levels of ROS (Itkin *et al.*, 2016). Similarly, in malaria burdened animals it was shown that increased vascular leakiness was associated with elevated ROS concentrations in HSPCs (Haltalli *et al.*, 2020). Given the observations on the BM stroma remodelling in the above section I next asked, can BM stroma cells secret ROS and if so, could this lead to a possible mechanism that promotes HSC damage?

To investigate ROS release by ECs, fetal liver kinase 1 (Flk1) GFP transgenic animals were used. Flk1-GFP infected and control animals were administered CellROX Deep Red reagent intravenously (Figure 6.10 A) on day 5 *pbi*. Here, I focused on ECs as LepR^{+}Cre; Rosa26 YFP transgenic was not available at the time to subtract possible ROS information from LepR^{+} PCs. The calvaria of Flk1 GFP animals from both conditions were imaged by IVM (Figure 6.10 B). Therefore, to decide on the optimal time when ROS could be visualised, I imaged animals 30 minutes and at 2 hours post CellROX reagent intravenous injection (Figure 6.11 A). CellROX reagent is dim and red fluorescence appears when ROS are released, which is detected by 647 nm red laser excitation. Moreover, an empty channel, generated using 584 nm excitation, was also used on top of the red and green lasers, to ensure signal specificity and to avoid autofluorescence (background noise). From the high-resolution images obtained 30 minutes post CellROX injection, ROS signal is visually low in both control and infected animals (Figure 6.11 A) however after quantification of CellROX signal with a counting algorithm, control animals had more red (ROS^{+}) spots compared to infected animals (Figure 6.11 B). In the calvaria of animals from both conditions, I noticed a variability in spot size (patches) which I evaluated as “occupied area” (Figure 6.11 C). The “occupied” area by red spots seemed low in both control and infected calvaria at 30 minutes (Figure 6.11 C) and remained unchanged after 2 hours (Figure 6.11 E). Similarly, at 2 hours post CellROX injection, the red spots appeared to be visually increased in control (Figure 6.11 A) though the numbers obtained at 2 hours were similar to the 30 minutes timepoint (Figure 6.11 B, D). The number of red spot patches measured as “occupied area” was unchanged in both conditions (Figure 6.11 E).

Although there is some signal detectable under this setup I anticipated more ROS released in the infected rather than control animals, which was not the case. In conclusion, while I was able to see CellROX deep Red reagent in the mouse calvarium this experiment needs to be repeated in irradiated FLK1 GFP animals as a positive control for high ROS levels to determine whether CellROX is localised within ECs.

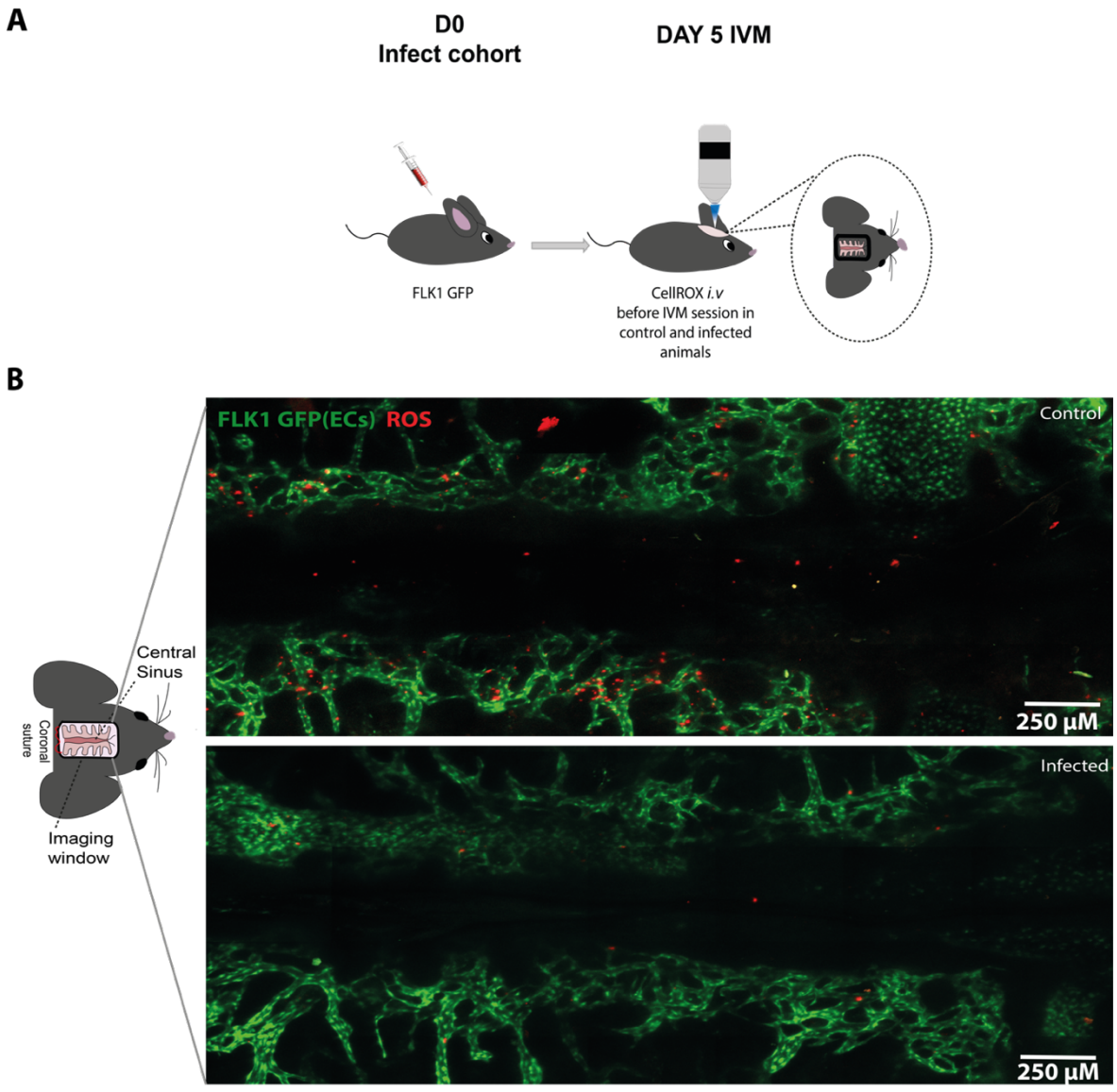


Figure 5. 10 Assessing ROS in FLK1 GFP calvaria A) Experimental set-up where control and infected animals were injected with CellROX deep red reagent 30 minutes before IVM. B) IVM showing a representation of mouse head, the window (on the right) and calvarium tilescan on the left. Green endothelial cells and Red CellROX Deep Red.

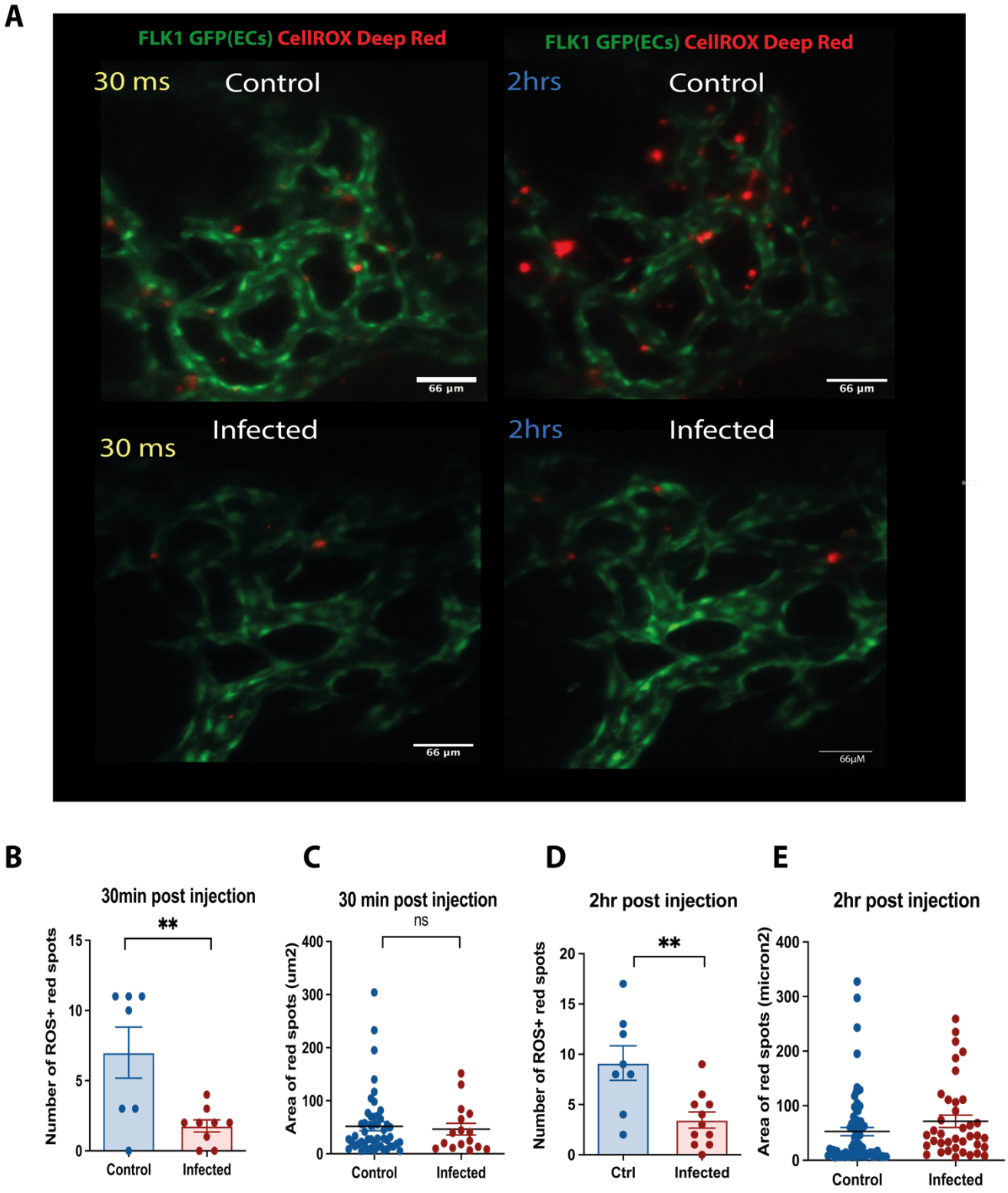


Figure 6. 11 Quantification of CELLROX signal in the calvaria of mice A) High-resolution positions obtained from same fields of view at 30 minutes and 2 hours post CellROX probe injection. The number of red (ROS^+) spots was determined by Fiji counting algorithm at B) 30 minutes and D) 2hrs apart obtained from the same field of view images. Spots of variable sizes defined as "occupied area" were counted for C) 30 minutes and E) at 2 hours in the control and infected Flk1 GFP animals. Each dot represents one spot. In C) *N*=49 spots were measured in the control and N=16 spots in infected. In D) *N*=8 spots were measured in the control and N=11 spots in infected. In E) *N*=73 spots were measured in the control and N=38 spots in infected. Mouse calvaria used *N*=1 control, *N*=1 infected Error bars represent the mean ± s.e.m. Statistically significant differences were determined using Student's *t*-test (** represent $P \leq 0.01$).

6.7 Discussion

In this chapter, I set out to identify a) Biotin^{Hi} HSCs in α-catulin GFP control/infected transgenic animals, b) changes in the Bm microenvironment of infected animals, c) possible mechanisms relating to BM stroma that contribute towards HSC damage. Quiescent HSCs were shown to associate with small arterioles and are preferentially found in the endosteal region of the BM compared to active HSCs that are distributed significantly further from arterioles *(Kunisaki et al.,* 2013). However, it is still unclear whether these cells reside in a preferential niche. Moreover, osteoblasts also serve as a side for quiescent HSPCs (Calvi *et al.*, 2003; Haltalli *et al.*, 2020). My hypothesis was that Biotin^{Lo} HSCs will be found in different locations on day 5 compared to day 3 *pbi* as HSCs and progenitor cells respond to infection from day 4 onwards. On the contrary, quiescent Biotin^{Hi} HSCs will be supported by the same niche and its secreted factors. Therefore, to study the location of HSC Biotin Hi and Lo cells in the central BM and endosteal (trabecular) areas, the bone was fractionated as previously described for AML-burdened animals (Duarte et al., 2018). The proportion of CD48^{neg} and E-SLAM Biotin^{Hi} control cells remained unchanged for days 3 and 5 though there was a drop at day 5 in the CD48^{neg} and E-SLAM Biotin^{Hi} cells purified from infected animals. As for their location, I did not find differences in CD48^{neg} and ESLAM Biotin^{Hi} locations in infected animals which was expected given that dormant HSCs are found in both CBM and endosteal regions(Calvi et al., 2003; Kunisaki et al., 2013). To study E-SLAM Biotin HSCs *in situ,* I then employed a green fluorescent protein knock-in mouse reporter for the *Ctnnal1* gene called *α*-catulin GFP. HSCs are rare and in the *α*-catulin GFP animals and only 0.02% of *α*-catulin GFP^{+} HSCs, defined as *α*-catulin GFP^{+} c-Kit^{+}, were highly functional (Acar *et al.*, 2015). In this chapter, I sought to identify E-SLAM Biotin HSCs and used EPCR, c-Kit and Biotin to study E-SLAM interactions with specialised BM niches. Here, only the first part of this aim was defined. Long bones from control and infected *α*-catulin GFP^{+} animals were processed and stained for c-Kit and Streptavidin (Biotin). In the control long bones, I identified around 20 E-SLAM Biotin^{Hi} cells compared to infected bones in which I could only locate one or two cells. FACS analysis of α-catulin GFP+ in control animals revealed GFP+ cells only in the HSC compartment which was consistent with previous findings (Acar et al., 2015). On the contrary, FACS analysis from infected α-catulin GFP+ animals revealed an increased proportion of α-catulin GFP^{+} MPP2. Two explanations arise from this, a) α-catulin GFP^{+} HSCs differentiated to downstream MPP2 as a response to malaria infection,

or b) the MPP2 subset responded to infection and preferentially expanded. When the other two MPP subsets, MPP3 and MPP4, were investigated were not found with positive GFP expression. Staining with other antibodies like CD48 could be a possibility to discriminate MPP2 from HSCs since the former upregulates CD48 compared to HSCs in the malaria setting. Although I tried clone HM48-1 and did not work, in the future more bones will be stained with antibodies against CD48, made from different clones. As soon as I can identify E-SLAM Biotin^{Hi} cells, I will move to identify preferential BM locations of Biotin HSCs in the long bones.

Second, I asked whether *P. berghei* infection causes alterations in the BM stroma. Here I hypothesised that if infection causes remodelling of the vasculature in both the CBM and the endosteal regions, then E-SLAM Biotin^{Lo} HSCs are possibly located in those areas compared to the E-SLAM Biotin^{Hi} HSCs. Using confocal microscopy imaging on long bones coupled with IVM, I found that in the bones of infected Co2.3 GFP animals, osteoblasts are lost which agreed with previous findings in the calvarium (Haltalli *et al.*, 2020). Osteoblast loss is associated with HSPC proliferation linked to loss of function (Haltalli *et al.*, 2020). PTH treatment led to osteoblast maintenance which was associated with rescuing proliferating HSPCs but did not preserve their function (Haltalli *et al.*, 2020). Moreover, analysis in the endosteal area of the bone revealed that endosteal vessels are remodelled. This comes in agreement with previous findings where AML leads to endosteal vessel remodelling for which the capacity to support non-leukaemic HSCs was reduced (Duarte et al., 2018). In addition, injection of tetramethyl rhodamine (TRITC) labelled dextran in infected animals revealed highly permeable vessels (Haltalli *et al.*, 2020) and HSCs that were found to localise proximal to leaky vessels had higher ROS (Itkin *et al.*, 2016). Further analysis in the CBM, revealed a reduction of LepR^{+} PCs and ECs. It will be intriguing to investigate mesenchymal stromal cells (MSCs) the progenitors of LepR+ cells. These findings were supported by FACS analysis of infected and control bones suggesting that malaria infection leads to loss of ECs in the endosteal areas as well as PCs and ECs in the CBM. BM is affected by infection and by staining further BM niche components in the Hoxb5 KuO (endogenous HSC reporter) animals I will address whether certain remodelled niches lead to HSC differentiation, hence supporting Hoxb5 KuO Biotin^{Lo} HSCs while other niches maintain hypoxic conditions favouring HSC quiescence and maintenance. Hypoxyprobe for instance, could be used to visualise hypoxia in BM areas as previously reported in the vasculature of AML animals (Passaro et al., 2017).

Lastly, I investigated a possible mechanism of ROS release by the vessels, particularly ECs by asking, do proliferating HSCs reside in high ROS BM regions during infection? Endothelial cell reporter animals, Flk1 GFP, were firstly injected *i.v* with CellROX deep reagent. High-resolution images were obtained at 30 minutes and 2hrs to determine changes in CellROX signal. CellROX reagent is dim and when superoxide ROS is released it turns red. Although I could detect ROS based on the IVM on the mouse calvarium in both control and infected animals, readouts were similar according to the measurements made on ROS red patches. The best alternative is to use Bis-sulfonyl chalcone or BODIPY, in either Flk1 GFP or $LepR^{+/-}$ Cre; Rosa26 YFP animals to indirectly measure ROS through lipid peroxidation, oxidative degradation of lipids by free radicals from ROS (Lv *et al.*, 2021). This measurement could be facilitated in long-bones or mouse calvarium through IVM.

The data showed that the BM vasculature is remodelled during *P. berghei* infection and that possibly these niches might support E-SLAM $Biotin^{Lo}$ cells in infected animals. On the other contrary, there is still a supporting niche for the quiescent HSCs that remains unaffected by the malaria parasite helping E-SLAM $Biotin^{Hi}$ HSCs to preserve their stemness. In conclusion, the location of the E-SLAM Biotin HSCs is an open question which I am still exploring.

Chapter 7

Summary, conclusions and future directions

The haematopoietic system is responsible for the production of blood cells and transportation of oxygen throughout the body (erythrocytes), immune surveillance and defence (immune cells) and hemostasis (platelets). In health, it has been estimated that in the BM of adult humans, fifty to seventy billion cells are produced (or twenty to sixty billion cells in mice). This number exponentially increases upon viral, bacterial or parasitic invasions (Sender and Milo, 2021). To replenish increased cellular demand as a response to severe infection, the haematopoietic system relies on a rare stem cell population that localises in protective BM niches. Haematopoietic stem cells (HSCs) reside at the apex of a hierarchical system and are characterised by their ability to generate daughter cells that retain HSC activity (self-renew) or produce terminally differentiated cells (multilineage differentiation). HSCs are maintained in BM niches in a quiescent state (G_0 phase of cell cycle), and upon pathogen entry, HSCs can sense environmental signals, initiating demand-adapted haematopoiesis and consequently promoting HSC activation, proliferation and differentiation (Takizawa, Boettcher and Manz, 2012; Caiado, Pietras and Manz, 2021). In the last decade, there has been a tremendous effort to understand the consequences of severe infection on quiescent HSCs. Multiple studies agreed that HSC proliferation-induced stress leads to the inability of HSCs to self-renew or give rise to terminally differentiated cells coupled with related transcriptional signatures (Essers et *al*., 2009; Baldridge *et al*., 2010; Choi *et al.,* 2011; Haas *et al.,* 2015; Matatall *et al*., 2016; Vainieri *et al*., 2016; Nakagawa, Chen and Rathinam, 2018; Haltalli *et al*., 2020; Cinat, Coppes and Barazzuol, 2021) and a phenotype associated with ageing (Bogeska *et al.*, 2022). Though, it is arguably and evolutionary impossible for an organism to lose almost completely its functional HSCs after a stressful encounter. Surely, there is a possibility of an LT-HSC "reserve" that responds minimally to infection without compromising their stemness.

In this thesis, I investigated the effects of *Plasmodium berghei*, a parasite that causes rodent malaria, on primitive HSCs, their interactions with the BM niche and its impact on the BM microenvironment *per se*. While it is generally accepted that infection triggers the loss of quiescence and long-term self-renewal and multipotency in HSCs, to date, no studies addressed directly the existence and functionality of this "reserve" pool. Considering this, it is important to investigate the localisation and interactions of these HSCs with their niche, investigating whether the BM niche associated with the HSC "reserve" pool does not undergo changes attributed to the cytokine *milieu* as a consequence of the immune response. The panoptic hypothesis for this work is:

"A *reserve pool of primitive HSCs exists that reacts minimally to infection, preserving their stemness"*

To study LT-HSCs in response to severe infection, I used a rodent malaria parasite, *P. berghei,* and investigated alterations in the long-term function of HSCs (Chapter 3). Thereafter, I studied heterogeneity within the LT-HSC population based on their proliferation kinetics (Chapter 4) and found populations that differ in their cell cycle statuses, functionality, transcriptional and metabolic signatures (Chapter 4 and 5). I then explored the localisation of HSC sub-populations and the effect of malaria in the BM niche trying to understand if alterations in the BM stroma support a niche for proliferating cells (Chapter 6). By combining phenotypic, functional, transcriptional, immunofluorescence and IVM approaches, malaria-burdened animals were studied in search of insights for the proposed research questions and hypothesis. In Chapter 7, I summarise and conclude my findings relating to each research question asked, introduce new ground for research suggestions or proposals relating to the continuation of this research as well as touch on the translational implications this work has for the malaria field.

Does *P. berghei* infection induce the activation of all HSCs equally?

In Chapter 3, I studied the consequences of malaria on the primitive HSC compartment (identified as LKS SLAM CD48^{neg} or CD48^{neg} HSCs) and whether their stemness could be rescued through the osteo-active parathyroid hormone (PTH). *Plasmodium* parasites were shown to reside in the parenchyma of patients' bones even after treatment and affecting niche components (Joice *et al.*, 2014). Consistent with this observation, BM stromal cells, specifically the bone-forming osteoblasts, were dramatically lost during infection (Haltalli *et al.*, 2020). Because HSCs were previously found residing in the osteoblastic niche (Calvi *et al.*, 2003), pharmacological targeting with PTH in malaria burden animals led to osteoblast rescue and the abolishment of infection-triggered HSC proliferation (Haltalli *et al.*, 2020). Although PTH reduced proliferation caused by malaria, haematopoietic stem and progenitor cells (LKS SLAM CD48$^{neg/low}$) or HSPCs failed to repopulate irradiated recipients in transplantation assays (Haltalli *et al.*, 2020). Due to a functional distinction between CD48^{neg} and CD48^{low} (Akinduro et al., 2018), I tested a more primitive HSC population by focusing on CD48^{neg} HSCs. Functionally, HSCs (sorted as LKS SLAM CD48^{neg}) purified from PTH or PBS-treated control/infected animals were found to be “stem-less” based on my primary and secondary transplantations. Transcriptional analysis based on sc-RNA sequencing of sorted Lin^{neg}c-Kit^{+} cells from control and day 7 *psi* animals, indicated decreased HSCscoring and substantial haematopoietic rewiring towards myeloid and basophil cell lineages at the expense of primitive HSCs (Haltalli *et al.*, 2020). To investigate a possible link between changes in HSC transcription and function, transplantation of Lin^{neg}c-Kit^{+} cells from infected/uninfected donors revealed poor engraftment and multilineage reconstitution. According to both transplants, most HSCs are activated during *P. berghei* infection and their dysfunctional identity highlighted a uniform response to stress disagreeing with previous work on heterogeneity in both steady-state and disease (Wilson *et al.,* 2008, 2015; Kwak and Ghazizadeh, 2015; Laurenti et al., 2015; Cabezas-Wallscheid *et al*., 2017; Kaufmann *et al*., 2021; Zhang *et al*., 2022). Highly motivated to solve the HSC survival conundrum in malaria infection, I then questioned whether there was an alternative way to exclude highly proliferative HSCs and obtain better resolution of quiescent cells that could be sorted for transplantation experiments.

Based on the observations from Chapter 3, in Chapter 4 I elucidated for the first time LT-HSCs heterogeneous responses to severe infection. I have achieved this through NHS-Ester-Biotin labelling, whereby the Ester reagent was injected in animals allowing discrimination of HSC subpopulations based on their proliferation kinetics *in vivo*. Upon stress, HSCs proliferate, distributing labelled membrane proteins among their daughter cells, resulting in a linear reduction of biotin assessed through streptavidin-based detection. According to biotin dilution (Nygren and Bryder, 2008; Luis *et al*., 2023), I identified two HSC populations, one that proliferated minimally, named LKS SLAM CD48^{neg} Biotin^{Hi} (hereafter CD48^{neg} Biotin^{Hi}) and another which was highly proliferative, named LKS SLAM CD48^{neg} Biotin^{Lo} (hereafter CD48^{neg} Biotin^{Lo}). Primitive HSCs with the highest repopulation ability express the *Procr* gene which encodes the Endothelial protein C receptor (EPCR) (Rabe *et al.*, 2020; Oedekoven *et al.*, 2021). Building on this, EPCR antibody helped me to identify LKS SLAM CD48^{neg} EPCR^{+} (hereafter E-SLAM) HSCs. Combining EPCR with Biotin, I detected E-SLAM HSCs retaining label, E-SLAM Biotin^{Hi}, or not, E-SLAM Biotin^{Lo}, suggesting a potential heterogeneity of the E-SLAM compartment as a response to infection-induced stress. To correlate DNA replication and biotin proliferation, I administered EdU chronically through drinking water, and combined it with *i.p* and *i.v* injections, to label all proliferating cells in S phase (cell cycle phase where DNA replication takes place) throughout the development of the infection. Hence, I found a high proportion of CD48^{neg} and E-SLAM -Biotin^{Lo} HSCs from infected animals in DNA replication stage, which was expected given that these cells proliferated during infection. Although the majority of E-SLAM Biotin^{Hi} HSCs were EdU^{-}, there was a proportion of both E-SLAM Biotin^{Hi} and E-SLAM Biotin^{Lo} that incorporated EdU, suggesting a heterogeneous response. Taking this result on board, I turned towards cell cycle analysis. Consistent with the EdU data, Ki67 staining showed all CD48^{neg} Biotin^{Lo} cells in S/G2/M phases (DNA replication or synthesis, genetic material condensation and mitosis/division) while CD48^{neg} Biotin^{Hi} cells were found in G_0 stage. When cell cycle analysis of E-SLAM Biotin^{Hi} and -Biotin^{Lo} cells was checked, I found the majority of E-SLAM Biotin^{Hi} cells in G_0 phase though the number of E-SLAM Biotin^{Lo} cells obtained was very small to draw any conclusions. Exit from quiescence is associated with differential regulation of CDK6 protein levels in HSC subsets (Laurenti et al., 2015). Transcriptional analysis of *CDK6* could potentially reveal higher expression in E-SLAM Biotin^{Lo} cells than E-SLAM Biotin^{Hi} since ST-HSCs are known to express high levels of CDK6 protein (Laurenti et al., 2015).

Given the cellular dynamics between the E-SLAM Biotin cells, I sought to investigate their functional properties. To visualise transplanted cells, I injected ten E-SLAM Biotin^{Hi} and Biotin^{Lo} cells purified from CD45.2 control and infected animals into lethally irradiated CD45.1 recipients. Engraftment and multilineage potential were monitored over a period of 24 weeks by looking at the a) percentage of CD45.2^{+} donor-derived cells and the b) proportion of terminally differentiated cells, measured as B, T and Myeloid cells, in PB of recipients. From both primary and secondary transplants, I concluded that infection did not affect the stemness of E-SLAM Biotin^{Hi} cells purified from infected animals which was not the case for E-SLAM Biotin^{Lo} cells that displayed poor engraftment. This data confirmed for the first time E-SLAM heterogeneity and identified a "reserve" pool of quiescent HSCs that maintained stemness despite *P. berghei* infection agreeing with a similar study on primitive HSCs (Munz *et al*., 2023).

What cell intrinsic mechanisms underpin the HSCs' heterogeneous response?

Based on the observation that some rare, NHS-ester (biotin) retaining HSCs maintain their function despite the severe infection affecting the rest of the haematopoietic tree, I sought to identify molecular players that possibly underpin SLAM or E-SLAM fate decisions. To retrospectively identify single cells based on their immunophenotypic intensity, I indexed sorted CD48^{neg} HSC for single-cell RNA sequencing (sc-RNA seq) based on 12 flow cytometry parameters. Mini bulk and sc-RNA sequencing allowed an unbiased understanding of the molecular changes taking place in CD48^{neg} Biotin^{Hi} and Biotin^{Lo} cells purified from control and infected animals. When SLAM Biotin cells were compared across conditions, *Cd74* gene was found to be differentially expressed between CD48^{neg} Biotin^{Hi} in control and Biotin^{Hi} infected cells. CD74 protein is expressed on antigen-presenting cells (APCs) and functions as a major histocompatibility complex (MHC) class II chaperone (David *et al.*, 2022). Since CD74 expression was upregulated in SLAM Biotin^{Hi} infected cells it suggested that MHCII expression may be regulated by signal transducer and activator of transcription 1 (STAT1) (Becker-Herman *et al.*, 2021), a downstream mediator of IFN signalling. STAT1 was also found to be differentially expressed in SLAM Biotin^{Hi} infected cells along with negative regulation of IFN gene (*Irgm1*) signature and GO pathways relating to defence response to virus. STAT1 was shown to inhibit cell cycle entry of HSCs (Li *et al.*, 2022). Moreover, a subset of MHCII^{hi} HSCs

expressed STAT1 and subsequent loss of STAT1 led to the depletion of these cells (Li *et al.*, 2022). Additionally, *Tgfβ1* and *Bcl2* genes were highly expressed in SLAM Biotin^{Lo} HSCs prompting to investigate Tgfβ1R role as an activation rather than a quiescent marker. TGFβ signals by binding to two types of receptors, type I and type II triggering a cascade of signalling events that include Smad and non-Smad pathways (Sweatt,S.K, Gower, B.A, Chieh, A.Y, Liu, Y, Li, 2016). Activated TGFB receptor type I (or TGFBR1) phosphorylates Smad family members. Smad 4 has a key role in self-renewal and HSC maintenance since its deletion led to impaired BM reconstitution (Karlsson *et al.*, 2007). It is a possibility that TGFβ1 gene is differentially regulated in Biotin^{Lo} HSCs rather than Biotin^{Hi} since it was previously reported that Myeloid biased HSCs when stimulated with high levels of TGF-β1 engaged the cell cycle. Controversly, when lymphoid biased HSCs cultured with low levels of TGF-β1 they were retained in G_0 cell cycle stage (Challen *et al.*, 2010). Lastly, CD48^{neg} Biotin^{Hi} control and infected cells had higher hscScores compared to CD48^{neg} Biotin^{Lo} which agreed with the transplantation assays. Interestingly, given that a number of genes were differentially expressed between Biotin^{Hi} control and Biotin^{Hi} infected HSCs, my data suggest that Biotin^{Hi} HSCs from infected animals are not completely insensitive to the infection, but rather they do sense it, and have a molecular machinery that allows them to cope with it.

According to scRNA sequencing analysis, transcriptional differences between Biotin high and low HSCs seemed nuanced. Possible changes happening cell intrinsically might be attributed to epigenetic modifications that allow HSCs with certain mutations to gain a selective advantage over other HSC clones in specific environmental settings (Hormaechea-Agulla et al., 2021). HSCs lacking *DNMT3A* had defective differentiation and enhanced self-renewal in *M. avium* infected animals (Hormaechea-Agulla et al., 2021). Theoretically, Biotin^{Hi} HSCs from infected animals might carry DNMT3A mutations as opposed to Biotin^{Lo} HSCs making them resistant to infection. Even though I have not explored epigenetic modifiers (DNMT3A, TET2) in Biotin subsets for my Thesis, single-cell ATAQ sequencing could aid towards understanding why Biotin^{Hi} HSCs can maintain stemness compared to Biotin^{Lo} cells underpining possible epigenetic players. Furthermore, it will be interesting to explore whether Biotin^{Hi} HSCs carry an epigenetic memory after infection insult. Recent data brought to light showed that two human HSC subsets (HSC-I and II) exist harboring distinct transcriptional and epigenetic states. The second subset, called HSC-II, displayed a quiescence enrichment signature similar to

human LT-HSCs while HSC-I did not. Intriguingly, HSC-II retained an inflammatory memory after hTNFα or LPS challenge (Zeng *et al.*, 2023). Similarly, de Laval B. *et al.,* indicated that after repeated LPS challenges, HSCs harboured an immune epigenetic memory (Hormaechea-Agulla et al., 2021a). Building on the findings reported by Dick's and Sieweke groups, I speculate that Biotin^{Hi} HSCs, from malaria recovered and then re-infected animals, will carry an immune epigenetic memory of the initial infection.

In steady state, LT-HSCs maintain low metabolic profiles since they are associated with low oxidative phosphorylation (OXPHOS), low ROS and low mitochondrial membrane potential (MPP). Evidence based on cell cycle and EdU data directed me to explore metabolic differences in the "reserve" pool of cells that retained biotin label versus no-label retaining cells. CD48^{neg} and E-SLAM Biotin^{Hi} infected cells displayed a quiescent phenotype compared to CD48^{neg} and E-SLAM Biotin^{Lo} infected cells. Specifically, a variety of metabolic probes indicated high membrane potential and high ROS in the CD48^{neg} and E-SLAM Biotin^{Lo} cells and as expected low metabolism output in the CD48^{neg} and E-SLAM Biotin^{Hi} infected cells. This suggests dynamic mitochondrial changes associated with HSC activation and differentiation. ROS scavenging by *N*-acetyl cysteine (NAC) rescued SLAM HSCs as the proportion of ROS was decreased in infected cells.

Does the BM microenvironment play a role in HSC heterogeneous responses?

In Chapter 6, I first tried to unravel possible interactions of E-SLAM Biotin HSCs with BM niche and the effect of *P. berghei* infection on the BM stroma itself. Specifically, I showed that there is not a preferential location for E-SLAM Biotin subsets in metaphysis versus diaphysis at days 3 and 5 *pbi*. Using a green fluorescent protein knock-in for the *Ctnnal1* gene transgenic mouse line, *α*-catulin GFP, I successfully identified Biotin E-SLAM *α*-catulin GFP^{+} HSCs in the long-bones of control animals. However, due to the activation of HSCs in infected animals and the subsequent reduction of numbers as a response to emergency myelopoiesis, I was unable to confidently identify a sufficient number of Biotin E-SLAM *α*-catulin GFP^{+} HSCs in the long-bones of infected animals to draw definitive conclusions on the micro-localisation of biotin retaining HSCs. Moreover, FACS analysis revealed *α*-catulin expression in MPP2 cells too from

infected animals, therefore the E-SLAM α-catulin GFP^{+} cells identified could be either a MPP2 or HSC. Staining with CD48 could discriminate the two populations in the future. Though, I am highly confident from what I discovered to be a Biotin^{Hi} HSC in the control long bones, since the biotin cells detected were HSCs and not MPP2 cells. Flow cytometry analysis from α-catulin control animals confirmed a high proportion of HSCs and not MPP2 to positively express GFP. Moreover, HSCs could be explored using an alternative HSC reporter like the Hoxb5 mCherry (Chen et al., 2016). Lastly, low HSC numbers observed in the bones of infected animals could be an indication of their dislodgment from the BM. This was shown in AML burden animals where leukaemia outcompeted healthy haematopoietic cells leading to extramedullary haematopoiesis (Pirillo *et al.*, 2022).

Second, I have uncovered for the first time that BM ECs and LepR^{+} PCs are dramatically affected during malaria infection along with the osteoblast (Haltalli *et al.*, 2020) based on IVM and immunofluorescence of long bones from infected mice. Furthermore, I identified structural changes in the vasculature of infected animals, since ECs and LepR^{+} PCs presented with "rough" surface compared to healthy controls. FACS analysis confirmed that CBM ECs and PCs are dramatically reduced due to a possible activation or proliferation. Considering the loss of ECs and the structural changes observed, I lastly investigated a possible mechanism of ROS release from the FLK1 expressing ECs in the FLK1 GFP mouse reporter. Other avenues need to be explored to identify ROS *in vivo* and during IVM along with Ki67 or TUNEL experiments to determine actively cycling or apoptotic PCs and ECs.

Future work

In summary, in this thesis I have explored the heterogeneous primitive HSC responses during *P. berghei* infection. I combined phenotypic, functional, metabolic, transcriptomic and microscopic approaches to identify a "reserve" pool of quiescent HSCs that maintain their function regardless of IFNγ release. The BM microenvironment and interactions with HSCs were examined too, shedding light on the detrimental effects *P. berghei* infection on BM stroma components. Considering these data, I propose a number of short and long avenues, to be explored. Based on the transcriptomic analysis, first, sc-RNA seq revealed genes relating

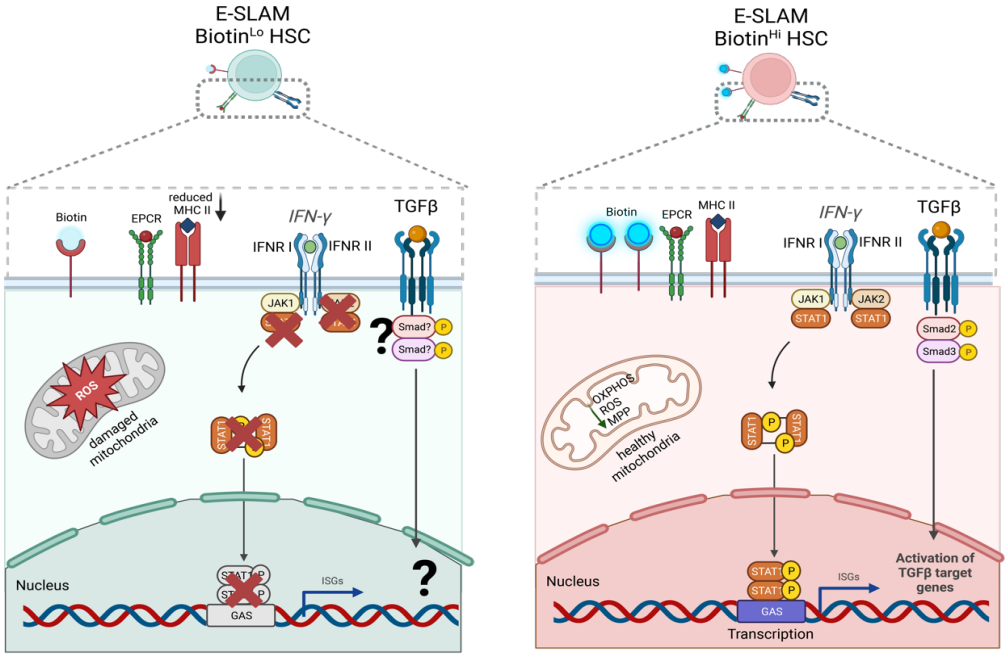
to mediators downstream of IFNγ signalling. This could be achieved by exploring STAT1 and phosphorylated STAT1 in CD48^{neg} and E-SLAM Biotin HSCs staining through Flo cytometry. If STAT1 levels are lower in Biotin^{Lo} and higher in Biotin^{Hi} HSCs, a transplantation assay could be set-up by injecting cells purified from STAT1-deficient animals, determining its crucial role in HSC self-renewal. I expect the absence of STAT1 from E-SLAM Biotin^{Hi} cells will lead to their loss of function and reduced engraftment (Figure 6.1 A). Second, TGFβ might be differentially regulated in Biotin^{Hi} and Biotin^{Lo} HSCs since it's important in modulating HSC fate decisions and identity. Because Biotin^{Hi} expressed higher levels of TGFβ1 it is a possibility that they remained longer in G_0 than Biotin^{Lo} HSCs. While TGFβ1 signals through Smad transcription factors, Smad2/3 and Smad 4 have been implicated in quiescence and self-renewal respectively (Chadwick *et al.*, 2005; Karlsson *et al.*, 2007). Therefore, assessing the levels of phosphorylated Smad2/3 and Smad 4 phenotypically in Biotin^{Lo} HSCs could give an indication of whether TGFβ1 receptor or Smad2 or 3 expressions are reduced compared to Biotin^{Hi} HSCs. Alternatively, by inhibiting TGFβ1R signalling through an antagonist it could be a potential mechanism towards Biotin^{Hi} HSCs loss of quiescence (Kim *et al.*, 2021) (Figure 7.1 A). Third, taking the differences in Biotin^{Hi} and Biotin^{Lo} HSC cell cycle status and with the information obtained from the transplantation data, where I saw Biotin^{Lo} expanding towards cells of the myeloid lineage, it will be interesting to show if Biotin HSC subsets have biases towards certain lineages. Lastly, it will be crucial to repeat the above analysis on the E-SLAM Biotin HSCs.

Metabolic analysis pointed towards low metabolic activity in the E-SLAM Biotin^{Hi} compared to E-SLAM Biotin^{Lo}HSCs in infected animals (Figure 7.1 A). Considering this, one can investigate the immunometabolic profile of E-SLAM Biotin HSCs by acquiring information on their energy metabolism through the single-cell energetic metabolism by profiling translation inhibition (SCENITH) method (Argüello *et al.*, 2020). SCENITH, a flow cytometry-based method, allows the measurement of metabolic profiles in heterogeneous cell populations by using metabolic inhibitors to block ATP synthesis, aerobic glycolysis and OXPHOs. Combined with these data, mito-Dendra2^{Hi} HSCs have greater reconstitution capacity than mito-Dendra2^{Lo} HSCs based on mitochondrial mass content (Takihara *et a*l., 2019; Mortensen *et al*., 2022). This could be a potential path one could take to study HSC activation or quiescence in mito-Dendra2 GFP animals to assess not only mitochondria mass in E-SLAM Biotin^{Hi} and E-SLAM Biotin^{Lo} HSCs after severe infection but also the carry-over of damaged mitochondria in daughter HSCs

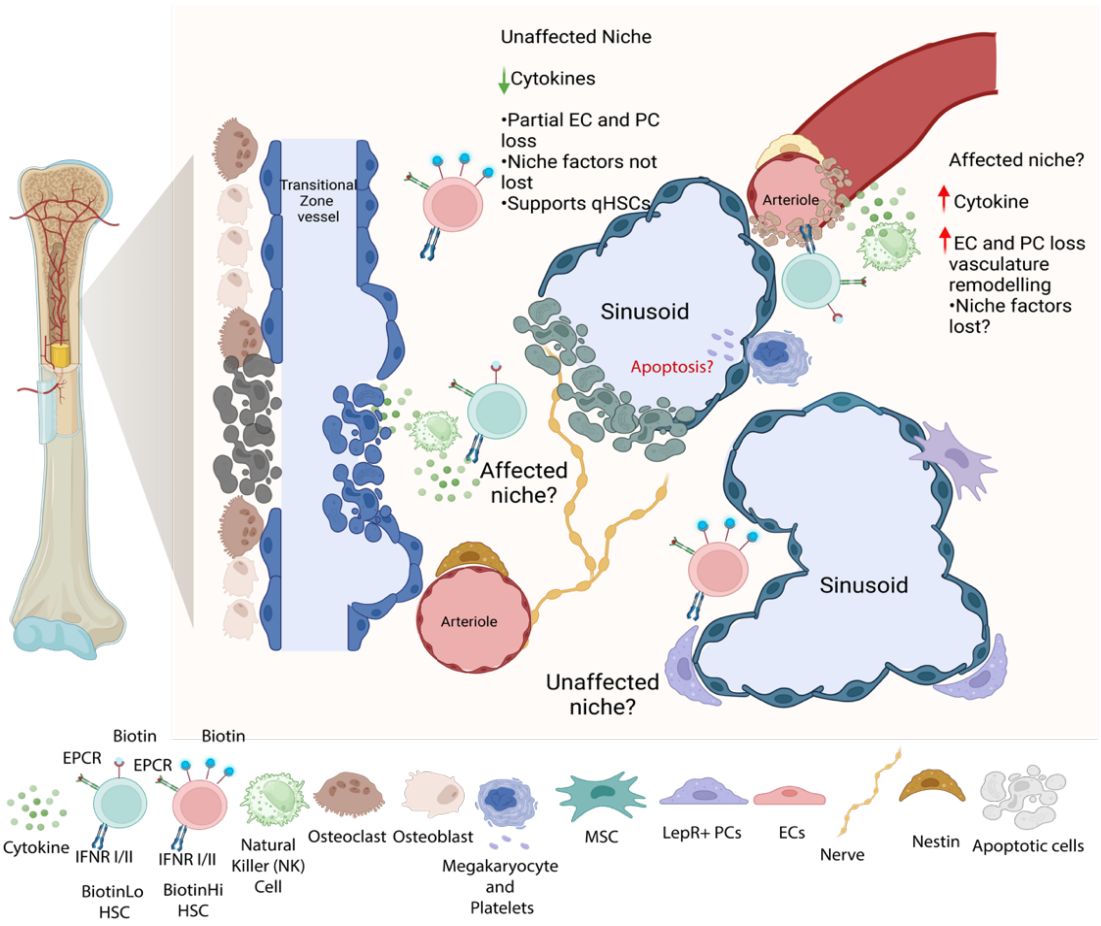
potentially affecting their stemness (Hinge *et al.*, 2020). Furthermore, since higher ROS were detected in SLAM and E-SLAM Biotin^{Lo} HSCs, ROS scavenge with NAC could shed light into the rescuing of E-SLAM Biotin^{Lo} functionality upon transplantation (Haltalli *et al.*, 2020).

A further avenue to explore is to study the interactions of the "reserve" HSC pool with the BM microenvironment. Although I reported that LepR+ and ECs are lost during infection it will be interesting to study the lost factors secreted by the niche. I believe there are still a number of niches that remain intact from the consequences of severe infection maintaining HSC quiescence while other niches push HSCs towards activation (Figure 7.1B).

A



B



Legend below

Figure 7. 1 Outlined summary of Thesis and open questions. The differences observed in Biotin high and low HSCs might be attributed to A) Cell intrinsic mechanisms or B) extrinsic signals coming from the BM microenvironment influencing or not Biotin HSC subsets.

A) IFNγ binds to type II IFN receptor composed of IFNGR1 and IFNGR2 associated with JAK1 and JAK2 respectively. Activation of JAK regulate downstream activation and phosphorylation resulting in STAT1-STAT1 homodimer formation which translocate to the nucleus and binds to an IFNγ activated site, cGAS elements which in turn initiates transcription (Platanias, 2005) of pro-inflammatory genes. This could be a potential mechanism by which Biotin^{Hi} cells (right panel) are protected from exhaustion. On the contrary, STAT1 in Biotin^{Lo} is not phosphorylated therefore it fails to bind to GAS consequently leaving Biotin^{Lo} unprotected (left panel). Biotin^{Hi} HSCs (right panel) possibly express high levels of MHC II which helps them to be less responsive to stress (Li et al., 2022) compared to Biotin^{Lo} HSCs. In addition, in Chapter 5, Biotin^{Lo} cells in infected animals were seen metabolically active (high levels of ROS and OXPHOS) and with poor mitochondrial health (TMRM, mass) compared to Biotin^{Hi} HSCs. TGFβ signalling might be hyperactive in Biotin^{Lo} HSCs which consequently leads to their activation and exhaustion (left panel) (Challen *et al.*, 2010).

B) Although the BM microenvironment is remodelled during malaria infection (Chapter 6) there is a possibility that Biotin^{Hi} reside in niches unaffected by *IFNγ* compared to Biotin^{Lo} cells that possibly reside in areas where BM stroma cells (LepR^{+} PCs, and ECs) are lost. Whether the loss is attributed to apoptosis it remains an open question.

Relevance

Lastly, it will be of great significance to explore the consequences of reoccurring infections on the HSC compartment and whether haematopoiesis recovers after treatment (Appendix C). In endemic areas, individuals tend to get re-infected hence these experiments will give an insight into the effects of re-activation on the stem cell pool. As for the treatment, it will be interesting to see if haematopoiesis returns back to normal after administration of anti-malaria drugs, such as phenylhydrazone or atovaquone and assess whether the parasites that remain in the BM parenchyma, even after treatment, affect BM regeneration.

In conclusion, I believe that the data presented in this thesis contributes significantly to our knowledge and understanding of the haematological implications malaria has on haematopoiesis and emphasises the necessity for further investigation, including translational work, aiming to improve the morbidity and mortality of not only malaria survivors but also those who suffer from severe infections.

Bibliography

Acar, M. *et al.* (2015) 'Deep imaging of bone marrow shows non-dividing stem cells are mainly perisinusoidal', *Nature*, 526(7571), pp. 126–130. Available at: https://doi.org/10.1038/nature15250.

Aguilar, R. *et al.* (2014) 'Molecular evidence for the localization of plasmodium falciparum immature gametocytes in bone marrow', *Blood*, 123(7), pp. 959–966. Available at: https://doi.org/10.1182/blood-2013-08-520767.

Akinduro, O. *et al.* (2018) 'Proliferation dynamics of acute myeloid leukaemia and haematopoietic progenitors competing for bone marrow space', *Nature Communications*, 9(1). Available at: https://doi.org/10.1038/s41467-017-02376-5.

Alagpulinsa, D.A. *et al.* (2022) 'Advances in understanding the molecular basis of clonal hematopoiesis', *Trends in Molecular Medicine*, 28(5), pp. 360–377. Available at: https://doi.org/10.1016/j.molmed.2022.03.002.

de Almeida, M.J. *et al.* (2017a) 'Dye-Independent Methods Reveal Elevated Mitochondrial Mass in Hematopoietic Stem Cells', *Cell Stem Cell*, 21(6), pp. 725-729.e4. Available at: https://doi.org/10.1016/j.stem.2017.11.002.

Ansó, E. *et al.* (2017) 'The mitochondrial respiratory chain is essential for haematopoietic stem cell function', *Nature Cell Biology*, 19(6), pp. 614–625. Available at: https://doi.org/10.1038/ncb3529.

Argüello, R.J. *et al.* (2020) 'SCENITH: A Flow Cytometry-Based Method to Functionally Profile Energy Metabolism with Single-Cell Resolution', *Cell Metabolism*, 32(6), pp. 1063-1075.e7. Available at: https://doi.org/10.1016/j.cmet.2020.11.007.

Arora, G. *et al.* (2023) 'Malaria: influence of Anopheles mosquito saliva on Plasmodium infection', *Trends in Immunology*, 44(4), pp. 256–265. Available at: https://doi.org/10.1016/j.it.2023.02.005.

Asada, N., Takeishi, S. and Frenette, P.S. (2017) 'Complexity of bone marrow hematopoietic stem cell niche', *International Journal of Hematology*, 106(1), pp. 45–54. Available at: https://doi.org/10.1007/s12185-017-2262-9.

Ashley, E.A., Pyae Phyo, A. and Woodrow, C.J. (2018) 'Malaria', *The Lancet*, 391(10130), pp. 1608–1621. Available at: https://doi.org/10.1016/S0140-6736(18)30324-6.

Baccin, C. *et al.* (2020) 'Combined single-cell and spatial transcriptomics reveal the molecular, cellular and spatial bone marrow niche organization', *Nature Cell Biology*, 22(1), pp. 38–48. Available at: https://doi.org/10.1038/s41556-019-0439-6.

Balazs, A.B. *et al.* (2006) 'Endothelial protein C receptor (CD201) explicitly identifies hematopoietic stem cells in murine bone marrow', *Blood*, 107(6), pp. 2317–2321. Available at: https://doi.org/10.1182/blood-2005-06-2249.

Baldridge, M.T. *et al.* (2010) 'Quiescent haematopoietic stem cells are activated by IFN-γ in response to chronic infection', *Nature*, 465(7299), pp. 793–797. Available at: https://doi.org/10.1038/nature09135.

Baryawno, N. *et al.* (2019) 'A Cellular Taxonomy of the Bone Marrow Stroma in Homeostasis and Leukemia', *Cell*, 177(7), pp. 1915-1932.e16. Available at: https://doi.org/10.1016/j.cell.2019.04.040.

Basha, G. *et al.* (2012) 'A CD74-dependent MHC class i endolysosomal cross-presentation pathway', *Nature Immunology*, 13(3), pp. 237–245. Available at: https://doi.org/10.1038/ni.2225.

Batsivari, A. *et al.* (2020) 'Dynamic responses of the haematopoietic stem cell niche to diverse stresses', *Nature Cell Biology*, 22(1), pp. 7–17. Available at: https://doi.org/10.1038/s41556-019-0444-9.

Beaupere, C. *et al.* (2015) 'The HIV proteins tat and nef promote human bone marrow mesenchymal stem cell senescence and alter osteoblastic differentiation', *Aging Cell*, 14(4), pp. 534–546. Available at: https://doi.org/10.1111/acel.12308.

Becker-Herman, S. *et al.* (2021) 'CD74 is a regulator of hematopoietic stem cell maintenance', *PLoS Biology*, 19(3), pp. 1–24. Available at: https://doi.org/10.1371/journal.pbio.3001121.

Belenguer, G. *et al.* (2021) 'Adult Neural Stem Cells Are Alerted by Systemic Inflammation through TNF-α Receptor Signaling', *Cell Stem Cell*, 28(2), pp. 285-299.e9. Available at: https://doi.org/10.1016/j.stem.2020.10.016.

Belyaev, N.N. *et al.* (2013) 'Extramedullary Myelopoiesis in Malaria Depends on Mobilization of Myeloid-Restricted Progenitors by IFN-γ Induced Chemokines', *PLoS Pathogens*, 9(6). Available at: https://doi.org/10.1371/journal.ppat.1003406.

Beneyto-Calabuig, S. *et al.* (2023) 'Clonally resolved single-cell multi-omics identifies routes of cellular differentiation in acute myeloid leukemia', *Cell Stem Cell*, 30(5), pp. 706-721.e8. Available at: https://doi.org/10.1016/j.stem.2023.04.001.

Bernitz, J.M. *et al.* (2016) 'Hematopoietic Stem Cells Count and Remember Self-Renewal Divisions', *Cell*, 167(5), pp. 1296-1309.e10. Available at: https://doi.org/10.1016/j.cell.2016.10.022.

Bigarella, C.L. *et al.* (2017) 'FOXO3 transcription factor is essential for protecting hematopoietic stem and progenitor cells from oxidative DNA damage', *Journal of Biological Chemistry*, 292(7), pp. 3005–3015. Available at: https://doi.org/10.1074/jbc.M116.769455.

Boettcher, S. *et al.* (2012) 'Cutting Edge: LPS-Induced Emergency Myelopoiesis Depends on TLR4-Expressing Nonhematopoietic Cells', *The Journal of Immunology*, 188(12), pp. 5824–5828. Available at: https://doi.org/10.4049/jimmunol.1103253.

Boettcher, S. *et al.* (2014) 'Endothelial cells translate pathogen signals into G-CSF-driven emergency granulopoiesis', *Blood*, 124(9), pp. 1393–1403. Available at: https://doi.org/10.1182/blood-2014-04-570762.

Bogeska, R. *et al.* (2022) 'Inflammatory exposure drives long-lived impairment of hematopoietic stem cell self-renewal activity and accelerated aging', *Cell Stem Cell*, 29(8), pp. 1273-1284.e8. Available at: https://doi.org/10.1016/j.stem.2022.06.012.

Bondar, T. and Medzhitov, R. (2010) 'p53-Mediated Hematopoietic Stem and Progenitor Cell Competition', *Cell Stem Cell*, 6(4), pp. 309–322. Available at: https://doi.org/10.1016/j.stem.2010.03.002.

Cabezas-Wallscheid, N. *et al.* (2017) 'Vitamin A-Retinoic Acid Signaling Regulates Hematopoietic Stem Cell Dormancy', *Cell*, 169(5), pp. 807-823.e19. Available at: https://doi.org/10.1016/j.cell.2017.04.018.

Caiado, F., Pietras, E.M. and Manz, M.G. (2021) 'Inflammation as a regulator of hematopoietic stem cell function in disease, aging, and clonal selection', *Journal of Experimental Medicine*, 218(7), pp. 1–19. Available at: https://doi.org/10.1084/jem.20201541.

Calvi, L.M. *et al.* (2003) 'Osteoblastic cells regulate the haematopoietic stem cell niche', *Nature*, 425(6960), pp. 841–846. Available at: https://doi.org/10.1038/nature02040.

Calvi, L.M. and Link, D.C. (2015) 'The hematopoietic stem cell niche in homeostasis and disease', *Blood*, 126(22), pp. 2443–2451. Available at: https://doi.org/10.1182/blood-2015-07-533588.

Carrelha, J. *et al.* (2018) 'Hierarchically related lineage-restricted fates of multipotent haematopoietic stem cells', *Nature*, 554(7690), pp. 106–111. Available at: https://doi.org/10.1038/nature25455.

Chadwick, K. *et al.* (2005) 'Smad7 alters cell fate decisions of human hematopoietic repopulating cells', *Blood*, 105(5), pp. 1905–1915. Available at: https://doi.org/10.1182/blood-2004-03-0881.

Chakrabarty, R.P. and Chandel, N.S. (2021) 'Mitochondria as Signaling Organelles Control Mammalian Stem Cell Fate', *Cell Stem Cell*, 28(3), pp. 394–408. Available at: https://doi.org/10.1016/j.stem.2021.02.011.

Challen, G.A. *et al.* (2010) 'Distinct Hematopoietic Stem Cell Subtypes Are Differentially Regulated by TGF-β1', *Cell Stem Cell*, 6(3), pp. 265–278. Available at: https://doi.org/10.1016/j.stem.2010.02.002.

Che, J.L.C. *et al.* (2022) ' Identification and characterization of in vitro expanded hematopoietic stem cells ', *EMBO reports*, 23(10), pp. 1–19. Available at: https://doi.org/10.15252/embr.202255502.

Chen, J.Y. *et al.* (2016) 'Hoxb5 marks long-term haematopoietic stem cells and reveals a homogenous perivascular niche', *Nature*, 530(7589), pp. 223–227. Available at: https://doi.org/10.1038/nature16943.

Chen, Q. *et al.* (2019) 'Apelin+ Endothelial Niche Cells Control Hematopoiesis and Mediate Vascular Regeneration after Myeloablative Injury', *Cell Stem Cell*, 25(6), pp. 768-783.e6. Available at: https://doi.org/10.1016/j.stem.2019.10.006.

Cheng, H., Zheng, Z. and Cheng, T. (2020) 'New paradigms on hematopoietic stem cell differentiation', *Protein and Cell*, 11(1), pp. 34–44. Available at: https://doi.org/10.1007/s13238-019-0633-0.

Choi, H.H. *et al.* (2011) 'Effects of mycobacterial infection on proliferation of hematopoietic precursor cells', *Microbes and Infection*, 13(14–15), pp. 1252–1260. Available at: https://doi.org/10.1016/j.micinf.2011.08.001.

Cinat, D., Coppes, R.P. and Barazzuol, L. (2021) 'DNA Damage-Induced Inflammatory Microenvironment and Adult Stem Cell Response', *Frontiers in Cell and Developmental Biology*, 9(October), pp. 1–18. Available at: https://doi.org/10.3389/fcell.2021.729136.

Coban, C., Lee, M.S.J. and Ishii, K.J. (2018) 'Tissue-specific immunopathology during malaria infection', *Nature Reviews Immunology*, 18(4), pp. 266–278. Available at: https://doi.org/10.1038/nri.2017.138.

Cohen, S.G. *et al.* (2015) 'PAR1 signaling regulates the retention and recruitment of EPCR-expressing bone marrow hematopoietic stem cells', *Nature Medicine*, 21(11), pp. 1307–1317. Available at: https://doi.org/10.1038/nm.3960.

Colom Díaz, P.A., Mistry, J.J. and Trowbridge, J.J. (2023) 'Hematopoietic stem cell aging and leukemia transformation', *Blood*, 142(6), pp. 533–542. Available at: https://doi.org/10.1182/blood.2022017933.

Comazzetto, S., Shen, B. and Morrison, S.J. (2021) 'll Review Niches that regulate stem cells and hematopoiesis in adult bone marrow', *Developmental Cell*, pp. 1–13. Available at: https://doi.org/10.1016/j.devcel.2021.05.018.

Dai, Z., Ramesh, V. and Locasale, J.W. (2020) 'The evolving metabolic landscape of chromatin biology and epigenetics', *Nature Reviews Genetics*, 21(12), pp. 737–753. Available at: https://doi.org/10.1038/s41576-020-0270-8.

Das, B. *et al.* (2013) 'CD271+ bone marrow mesenchymal stem cells may provide a niche for dormant mycobacterium tuberculosis', *Science Translational Medicine*, 5(170), pp. 1–11. Available at: https://doi.org/10.1126/scitranslmed.3004912.

David, K. *et al.* (2022) 'CD74 as a regulator of transcription in normal B cells', *Cell Reports*, 41(5). Available at: https://doi.org/10.1016/j.celrep.2022.111572.

Day, R.B. *et al.* (2015) 'Granulocyte colony-stimulating factor reprograms bone marrow stromal cells to actively suppress B lymphopoiesis in mice', *Blood*, 125(20), pp. 3114–3117. Available at: https://doi.org/10.1182/blood-2015-02-629444.

de Laval, B. *et al.* (2020) 'C/EBPβ-Dependent Epigenetic Memory Induces Trained Immunity in Hematopoietic Stem Cells', *Cell Stem Cell*, 26(5), pp. 657-674.e8. https://doi.org/10.1016/j.stem.2020.01.017.

Demerdash, Y. *et al.* (2021) 'Yin and Yang: The dual effects of interferons on hematopoiesis', *Experimental Hematology*, 96, pp. 1–12. Available at: https://doi.org/10.1016/j.exphem.2021.02.002.

Deus, C.M. *et al.* (2020) 'Mitochondria–Lysosome Crosstalk: From Physiology to Neurodegeneration', *Trends in Molecular Medicine*, 26(1), pp. 71–88. Available at: https://doi.org/10.1016/j.molmed.2019.10.009.

Dexter, T.M., Allen, T.D. and Lajtha, L.G. (1978) 'Factors controlling the proliferation of haemopoietic stem cells in vitro.', *The symposium / The Society for Developmental Biology. Society for Developmental Biology. Symposium*, (35), pp. 149–160. Available at: https://doi.org/10.1016/b978-0-12-612981-6.50014-4.

Ding, L. *et al.* (2012) 'Endothelial and perivascular cells maintain haematopoietic stem cells', *Nature*, 481(7382), pp. 457–462. Available at: https://doi.org/10.1038/nature10783.

Ding, L. and Morrison, S.J. (2013) 'Haematopoietic stem cells and early lymphoid progenitors occupy distinct bone marrow niches', *Nature*, 495(7440), pp. 231–235. Available at: https://doi.org/10.1038/nature11885.

Dolgalev, I. and Tikhonova, A.N. (2021) 'Connecting the Dots: Resolving the Bone Marrow Niche Heterogeneity', *Frontiers in Cell and Developmental Biology*, 9(March), pp. 1–11. Available at: https://doi.org/10.3389/fcell.2021.622519.

Dong, S. *et al.* (2021) 'Chaperone-mediated autophagy sustains haematopoietic stem-cell function', *Nature*, 591(7848), pp. 117–123. Available at: https://doi.org/10.1038/s41586-020-03129-z.

Drive, P. and Email, C.A. (2023) 'Plasmodium falciparum infection of human erythroblasts induces transcriptional changes associated with dyserythropoiesis associated with dyserythropoiesis 1 . Department of Pediatrics , Stanford University School of Medicine , Stanford , CA 94305 Medicine'.

Duarte, D. *et al.* (2018) 'Inhibition of Endosteal Vascular Niche Remodeling Rescues Hematopoietic Stem Cell Loss in AML', *Cell Stem Cell*, 22(1), pp. 64-77.e6. Available at: https://doi.org/10.1016/j.stem.2017.11.006.

Dykstra, B. *et al.* (2007) 'Long-Term Propagation of Distinct Hematopoietic Differentiation Programs In Vivo', *Cell Stem Cell*, 1(2), pp. 218–229. Available at: https://doi.org/10.1016/j.stem.2007.05.015.

Essers, M.A.G. *et al.* (2009) 'IFNα activates dormant haematopoietic stem cells in vivo', *Nature*, 458(7240), pp. 904–908. Available at: https://doi.org/10.1038/nature07815.

Fanti, A.K. *et al.* (2023) 'Flt3- and Tie2-Cre tracing identifies regeneration in sepsis from multipotent progenitors but not hematopoietic stem cells', *Cell Stem Cell*, 30(2), pp. 207-218.e7. Available at: https://doi.org/10.1016/j.stem.2022.12.014.

Fernández-Vizarra, E. *et al.* (2022) 'Two independent respiratory chains adapt OXPHOS performance to glycolytic switch', *Cell Metabolism*, 34(11), pp. 1792-1808.e6. Available at: https://doi.org/10.1016/j.cmet.2022.09.005.

Filippi, M.D. (2021) 'Hematopoietic stem cell (HSC) divisional memory: The journey of mitochondrial metabolism through HSC division', *Experimental Hematology*, 96, pp. 27–34. Available at: https://doi.org/10.1016/j.exphem.2021.01.006.

Filippi, M.D. and Ghaffari, S. (2019) 'Mitochondria in the maintenance of hematopoietic stem cells: New perspectives and opportunities', *Blood*, 133(18), pp. 1943–1952. Available at: https://doi.org/10.1182/blood-2018-10-808873.

Florez, M.A. *et al.* (2020) 'Interferon Gamma Mediates Hematopoietic Stem Cell Activation and Niche Relocalization through BST2', *Cell Reports*, 33(12), p. 108530. Available at: https://doi.org/10.1016/j.celrep.2020.108530.

Florez, M.A. *et al.* (2022) 'Clonal hematopoiesis: Mutation-specific adaptation to environmental change', *Cell Stem Cell*, 29(6), pp. 882–904. Available at: https://doi.org/10.1016/j.stem.2022.05.006.

Foudi, A. *et al.* (2009) 'Analysis of histone 2B-GFP retention reveals slowly cycling hematopoietic stem cells', *Nature Biotechnology*, 27(1), pp. 84–90. Available at: https://doi.org/10.1038/nbt.1517.

Fröbel, J. *et al.* (2021) 'The Hematopoietic Bone Marrow Niche Ecosystem', *Frontiers in Cell and Developmental Biology*, 9(July), pp. 1–19. Available at: https://doi.org/10.3389/fcell.2021.705410.

Goodell, B.M.A. *et al.* (1996) 'Isolation and F u n c t i o n a l Properties o f M u r i n e H e m a t o p o i e t i c S t e m Cells that are R e p l i c a t i n g In Vivo By Margaret A. Goodell, Katja Brose, Glenn Paradis,* A. Stewart Conner,* and Richard C. Mulligan', 183(April).

Grusanovic, S. et al. (2023) ' Chronic inflammation decreases HSC fitness by activating the druggable Jak/Stat3 signaling pathway ', *EMBO reports*, 24(1), pp. 1–19. Available at: https://doi.org/10.15252/embr.202254729.
Guo, P. *et al.* (2022) 'Histone variant H3.3 maintains adult haematopoietic stem cell homeostasis by enforcing chromatin adaptability', *Nature Cell Biology*, 24(1), pp. 99–111. Available at: https://doi.org/10.1038/s41556-021-00795-7.

Haas, S. *et al.* (2015a) 'Inflammation-Induced Emergency Megakaryopoiesis Driven by Hematopoietic Stem Cell-like Megakaryocyte Progenitors', *Cell Stem Cell*, 17(4), pp. 422–434. Available at: https://doi.org/10.1016/j.stem.2015.07.007.

Haas, S., Trumpp, A. and Milsom, M.D. (2018) 'Causes and Consequences of Hematopoietic Stem Cell Heterogeneity', *Cell Stem Cell*, 22(5), pp. 627–638. Available at: https://doi.org/10.1016/j.stem.2018.04.003.

Haltalli, M.L.R. *et al.* (2020) ''Manipulating niche composition limits damage to haematopoietic stem cells during Plasmodium infection', *Nature Cell Biology*, pp. 1–47.

Hamey, F.K. and Göttgens, B. (2019) 'Machine learning predicts putative hematopoietic stem cells within large single-cell transcriptomics data sets', *Experimental Hematology*, 78, pp. 11–20. Available at: https://doi.org/10.1016/j.exphem.2019.08.009.

Hata, A.N., Engelman, J.A. and Faber, A.C. (2015) 'The BCL2 family: Key mediators of the apoptotic response to targeted anticancer therapeutics', *Cancer Discovery*, 5(5), pp. 475–487. Available at: https://doi.org/10.1158/2159-8290.CD-15-0011.

Helbling, P.M. *et al.* (2019) 'Global Transcriptomic Profiling of the Bone Marrow Stromal Microenvironment during Postnatal Development, Aging, and Inflammation', *Cell Reports*, 29(10), pp. 3313-3330.e4. Available at: https://doi.org/10.1016/j.celrep.2019.11.004.

Hérault, A. *et al.* (2017) 'Myeloid progenitor cluster formation drives emergency and leukaemic myelopoiesis', *Nature*, 544(7648), pp. 53–58. Available at: https://doi.org/10.1038/nature21693.

Himburg, H.A. *et al.* (2018) 'Distinct Bone Marrow Sources of Pleiotrophin Control Hematopoietic Stem Cell Maintenance and Regeneration', *Cell Stem Cell*, 23(3), pp. 370-381.e5. Available at: https://doi.org/10.1016/j.stem.2018.07.003.

Hinge, A. *et al.* (2020) 'Asymmetrically Segregated Mitochondria Provide Cellular Memory of Hematopoietic Stem Cell Replicative History and Drive HSC Attrition', *Cell Stem Cell*, 26(3), pp. 420-430.e6. Available at: https://doi.org/10.1016/j.stem.2020.01.016.

Hirche, C. *et al.* (2017) 'Systemic Virus Infections Differentially Modulate Cell Cycle State and Functionality of Long-Term Hematopoietic Stem Cells In Vivo', *Cell Reports*, 19(11), pp. 2345–2356. Available at: https://doi.org/10.1016/j.celrep.2017.05.063.

Ho, T.T. *et al.* (2017) 'Autophagy maintains the metabolism and function of young and old stem cells', *Nature*, 543(7644), pp. 205–210. Available at: https://doi.org/10.1038/nature21388.
Ho, Y.H. *et al.* (2019) 'Remodeling of Bone Marrow Hematopoietic Stem Cell Niches Promotes Myeloid Cell Expansion during Premature or Physiological Aging', *Cell Stem Cell*, 25(3), pp. 407-418.e6. Available at: https://doi.org/10.1016/j.stem.2019.06.007.

Hooper, A.T. *et al.* (2009a) 'Engraftment and Reconstitution of Hematopoiesis Is Dependent on VEGFR2-Mediated Regeneration of Sinusoidal Endothelial Cells', *Cell Stem Cell*, 4(3), pp. 263–274. Available at: https://doi.org/10.1016/j.stem.2009.01.006.

Hormaechea-Agulla, D. *et al.* (2021a) 'Chronic infection drives Dnmt3a-loss-of-function clonal hematopoiesis via IFNγ signaling', *Cell Stem Cell*, 28(8), pp. 1428-1442.e6. Available at: https://doi.org/10.1016/j.stem.2021.03.002.

Hormaechea-Agulla, D. *et al.* (2021b) 'Chronic infection drives Dnmt3a-loss-of-function clonal hematopoiesis via IFNγ signaling', *Cell Stem Cell*, 28(8), pp. 1428-1442.e6. Available at: https://doi.org/10.1016/j.stem.2021.03.002.

Hormaechea-Agulla, D., Le, D.T. and King, K.Y. (2020) 'Common Sources of Inflammation and Their Impact on Hematopoietic Stem Cell Biology', *Current Stem Cell Reports*, 6(3), pp. 96–107. Available at: https://doi.org/10.1007/s40778-020-00177-z.

Insinga, A. *et al.* (2013) 'DNA damage in stem cells activates p21, inhibits p53, and induces symmetric self-renewing divisions', *Proceedings of the National Academy of Sciences of the United States of America*, 110(10), pp. 3931–3936. Available at: https://doi.org/10.1073/pnas.1213394110.

Itkin, T. *et al.* (2016) 'Distinct bone marrow blood vessels differentially regulate haematopoiesis', *Nature*, 532(7599), pp. 323–328. Available at: https://doi.org/10.1038/nature17624.

Ito, K. *et al.* (2006) 'Reactive oxygen species act through p38 MAPK to limit the lifespan of hematopoietic stem cells', *Nature Medicine*, 12(4), pp. 446–451. Available at: https://doi.org/10.1038/nm1388.

Ito, Kyoko *et al.* (2016) 'Self-renewal of a purified Tie2+ hematopoietic stem cell population relies on mitochondrial clearance', *Science*, 354(6316), pp. 1156–1160. Available at: https://doi.org/10.1126/science.aaf5530.

Iwasaki, H. *et al.* (2010) 'Endothelial protein C receptor-expressing hematopoietic stem cells reside in the perisinusoidal niche in fetal liver', *Blood*, 116(4), pp. 544–553. Available at: https://doi.org/10.1182/blood-2009-08-240903.

Izzo, F. *et al.* (2020) 'DNA methylation disruption reshapes the hematopoietic differentiation landscape', *Nature Genetics*, 52(4), pp. 378–387. Available at: https://doi.org/10.1038/s41588-020-0595-4.

Jacobs, K. *et al.* (2022) 'Stress-triggered hematopoietic stem cell proliferation relies on PrimPol-mediated repriming', *Molecular Cell*, 82(21), pp. 4176-4188.e8. Available at: https://doi.org/10.1016/j.molcel.2022.09.009.

Jaiswal, S. and Ebert, B.L. (2019) 'Clonal hematopoiesis in human aging and disease', *Science*, 366(6465). Available at: https://doi.org/10.1126/science.aan4673.

Jan, M., Ebert, B.L. and Jaiswal, S. (2017) 'Clonal hematopoiesis', *Seminars in Hematology*, 54(1), pp. 43–50. Available at: https://doi.org/10.1053/j.seminhematol.2016.10.002.

Joice, R. *et al.* (2014) 'Plasmodium falciparum transmission stages accumulate in the human bone marrow', *Science Translational Medicine*, 6(244), pp. 1–9. Available at: https://doi.org/10.1126/scitranslmed.3008882.

Karlsson, G. *et al.* (2007) 'Smad4 is critical for self-renewal of hematopoietic stem cells', *Journal of Experimental Medicine*, 204(3), pp. 467–474. Available at: https://doi.org/10.1084/jem.20060465.

Kaufmann, K.B. *et al.* (2021) 'A latent subset of human hematopoietic stem cells resists regenerative stress to preserve stemness', *Nature Immunology*, 22(6), pp. 723–734. Available at: https://doi.org/10.1038/s41590-021-00925-1.

Kent, D.G. *et al.* (2009) 'Prospective isolation and molecular characterization of hematopoietic stem cells with durable self-renewal potential', *Blood*, 113(25), pp. 6342–6350. Available at: https://doi.org/10.1182/blood-2008-12-192054.

Kim, B.G. *et al.* (2021) 'Novel therapies emerging in oncology to target the TGF-β pathway', *Journal of Hematology and Oncology*, 14(1), pp. 1–20. Available at: https://doi.org/10.1186/s13045-021-01053-x.

King, K.Y. *et al.* (2011) 'Irgm1 protects hematopoietic stem cells by negative regulation of IFN signaling', *Blood*, 118(6), pp. 1525–1533. Available at: https://doi.org/10.1182/blood-2011-01-328682.

Kirova, D.G. *et al.* (2022) 'Article A ROS-dependent mechanism promotes CDK2 phosphorylation to drive progression through S phase A ROS-dependent mechanism promotes CDK2 phosphorylation to drive progression through S phase', pp. 1–16. Available at: https://doi.org/10.1016/j.devcel.2022.06.008.

Kleppe, M. *et al.* (2017) 'Jak1 Integrates Cytokine Sensing to Regulate Hematopoietic Stem Cell Function and Stress Hematopoiesis', *Cell Stem Cell*, 21(4), pp. 489-501.e7. Available at: https://doi.org/10.1016/j.stem.2017.08.011.

Kollek, M. *et al.* (2016) 'Bcl-2 proteins in development, health, and disease of the hematopoietic system', *FEBS Journal*, 283, pp. 2779–2810. Available at: https://doi.org/10.1111/febs.13683.

Kowalczyk, M.S. *et al.* (2015) 'Single-cell RNA-seq reveals changes in cell cycle and differentiation programs upon aging of hematopoietic stem cells', *Genome Research*, 25(12), pp. 1860–1872. Available at: https://doi.org/10.1101/gr.192237.115.

Kunisaki, Y. *et al.* (2013a) 'Arteriolar niches maintain haematopoietic stem cell quiescence', *Nature*, 502(7473), pp. 637–643. Available at: https://doi.org/10.1038/nature12612.

Kusumbe, A.P. *et al.* (2016) 'Age-dependent modulation of vascular niches for haematopoietic stem cells', *Nature*, 532(7599), pp. 380–384. Available at: https://doi.org/10.1038/nature17638.

Kwak, M. and Ghazizadeh, S. (2015) 'Analysis of histone H2BGFP retention in mouse submandibular gland reveals actively dividing stem cell populations', *Stem Cells and Development*, 24(5), pp. 565–574. Available at: https://doi.org/10.1089/scd.2014.0355.

Lamikanra, A.A. *et al.* (2007) 'Malarial anemia: Of mice and men', *Blood*, 110(1), pp. 18–28. Available at: https://doi.org/10.1182/blood-2006-09-018069.

Laurenti, E. *et al.* (2008) 'Hematopoietic Stem Cell Function and Survival Depend on c-Myc and N-Myc Activity', *Cell Stem Cell*, 3(6), pp. 611–624. Available at: https://doi.org/10.1016/j.stem.2008.09.005.

Laurenti, E. *et al.* (2015) 'CDK6 levels regulate quiescence exit in human hematopoietic stem cells', *Cell Stem Cell*, 16(3), pp. 302–313. Available at: https://doi.org/10.1016/j.stem.2015.01.017.

Laurenti, E. and Göttgens, B. (2018) 'From haematopoietic stem cells to complex differentiation landscapes', *Nature*, 553(7689), pp. 418–426. Available at: https://doi.org/10.1038/nature25022.

Lauridsen, F.K.B. *et al.* (2018) 'Differences in Cell Cycle Status Underlie Transcriptional Heterogeneity in the HSC Compartment', *Cell Reports*, 24(3), pp. 766–780. Available at: https://doi.org/10.1016/j.celrep.2018.06.057.

Lee, A.J. and Ashkar, A.A. (2018) 'The dual nature of type I and type II interferons', *Frontiers in Immunology*, 9(SEP), pp. 1–10. Available at: https://doi.org/10.3389/fimmu.2018.02061.

Lee, M.S.J. *et al.* (2017) 'Plasmodium products persist in the bone marrow and promote chronic bone loss', *Science Immunology*, 2(12). Available at: https://doi.org/10.1126/sciimmunol.aam8093.

Lee, R.S., Waters, A.P. and Brewer, J.M. (2018) 'A cryptic cycle in haematopoietic niches promotes initiation of malaria transmission and evasion of chemotherapy', *Nature Communications*, 9(1). Available at: https://doi.org/10.1038/s41467-018-04108-9.

Lee-Six, H. *et al.* (2018) 'Population dynamics of normal human blood inferred from somatic mutations', *Nature*, 561(7724), pp. 473–478. Available at: https://doi.org/10.1038/s41586-018-0497-0.

Li, B. *et al.* (2010) 'Endothelial cells mediate the regeneration of hematopoietic stem cells', *Stem Cell Research*, 4(1), pp. 17–24. Available at: https://doi.org/10.1016/j.scr.2009.08.001.

Li, J. *et al.* (2022) 'STAT1 is essential for HSC function and maintains MHCIIhi stem cells that resist myeloablation and neoplastic expansion', *Blood*, 140(14), pp. 1592–1606. Available at: https://doi.org/10.1182/blood.2021014009.

Li, W. *et al.* (2004) 'Hematopoietic stem cell repopulating ability can be maintained in vitro by some primary endothelial cells', *Experimental Hematology*, 32(12), pp. 1226–1237. Available at: https://doi.org/10.1016/j.exphem.2004.09.001.

Liang, R. *et al.* (2020) 'Restraining Lysosomal Activity Preserves Hematopoietic Stem Cell Quiescence and Potency', *Cell Stem Cell*, 26(3), pp. 359-376.e7. Available at: https://doi.org/10.1016/j.stem.2020.01.013.

Lin, D.S. and Trumpp, A. (2023) 'Differential expression of endothelial protein C receptor (EPCR) in hematopoietic stem and multipotent progenitor cells in young and old mice', *Cells and Development*, 174(January), p. 203843. Available at: https://doi.org/10.1016/j.cdev.2023.203843.

Liu, Yan *et al.* (2009) 'p53 Regulates Hematopoietic Stem Cell Quiescence', *Cell Stem Cell*, 4(1), pp. 37–48. Available at: https://doi.org/10.1016/j.stem.2008.11.006.

Lobo de Figueiredo-Pontes, L. *et al.* (2021) 'Improved hematopoietic stem cell transplantation upon inhibition of natural killer cell-derived interferon-gamma', *Stem Cell Reports*, 16(8), pp. 1999–2013. Available at: https://doi.org/10.1016/j.stemcr.2021.06.008.

Lu, Y. *et al.* (2022) 'Srebf1c preserves hematopoietic stem cell function and survival as a switch of mitochondrial metabolism', *Stem Cell Reports*, 17(3), pp. 599–615. Available at: https://doi.org/10.1016/j.stemcr.2022.01.011.

Luis, T.C. *et al.* (2023) 'Perivascular niche cells sense thrombocytopenia and activate hematopoietic stem cells in an IL-1 dependent manner', *Nature Communications*, 14(1). Available at: https://doi.org/10.1038/s41467-023-41691-y.

Luzio, J.P., Pryor, P.R. and Bright, N.A. (2007) 'Lysosomes: Fusion and function', *Nature Reviews Molecular Cell Biology*, 8(8), pp. 622–632. Available at: https://doi.org/10.1038/nrm2217.

Lv, Z. *et al.* (2021) 'Bis-sulfonyl-chalcone-BODIPY molecular probes for in vivo and in vitro imaging', *Journal of Molecular Structure*, 1234, p. 130201. Available at: https://doi.org/10.1016/j.molstruc.2021.130201.

Man, Y. *et al.* (2021) 'Hematopoietic Stem Cell Niche During Homeostasis, Malignancy, and Bone Marrow Transplantation', *Frontiers in Cell and Developmental Biology*, 9(January), pp. 1–11. Available at: https://doi.org/10.3389/fcell.2021.621214.

Maryanovich, M. *et al.* (2012) 'The ATM-BID pathway regulates quiescence and survival of haematopoietic stem cells', *Nature Cell Biology*, 14(5), pp. 535–541. Available at: https://doi.org/10.1038/ncb2468.

Matatall, K.A. *et al.* (2016a) 'Chronic Infection Depletes Hematopoietic Stem Cells through Stress-Induced Terminal Differentiation', *Cell Reports*, 17(10), pp. 2584–2595. Available at: https://doi.org/10.1016/j.celrep.2016.11.031.

Mbambiniotis Greek dictionary 2012

Méndez-Ferrer, S. *et al.* (2010a) 'Mesenchymal and haematopoietic stem cells form a unique bone marrow niche', *Nature*, 466(7308), pp. 829–834. Available at: https://doi.org/10.1038/nature09262.

Méndez-Ferrer, S. *et al.* (2020) 'Bone marrow niches in haematological malignancies', *Nature Reviews Cancer* [Preprint]. Available at: https://doi.org/10.1038/s41568-020-0245-2.

Morganti, C., Cabezas-Wallscheid, N. and Ito, K. (2022) 'Metabolic Regulation of Hematopoietic Stem Cells', *HemaSphere*, 6(7), p. E740. Available at: https://doi.org/10.1097/HS9.0000000000000740.

Mortensen, M. *et al.* (2011) 'The autophagy protein Atg7 is essential for hematopoietic stem cell maintenance', *Journal of Experimental Medicine*, 208(3), pp. 455–467. Available at: https://doi.org/10.1084/jem.20101145.

Mortensen, M. *et al.* (2022) 'Hematopoietic Stem Cell Metabolism during Development and Aging', *Cell Stem Cell*, 96(3), pp. 725-729.e4. Available at: https://doi.org/10.1016/j.devcel.2020.06.029.

Muller-Sieburg, C.E. *et al.* (2004) 'Myeloid-biased hematopoietic stem cells have extensive self-renewal capacity but generate diminished lymphoid progeny with impaired IL-7 responsiveness', *Blood*, 103(11), pp. 4111–4118. Available at: https://doi.org/10.1182/blood-2003-10-3448.

Mun, Y.V., Fazio, S. and Arrieta, C.N. (2021) *Remodeling of the Bone Marrow Stromal Microenvironment During Pathogenic Infections*, *Current Topics in Microbiology and Immunology*. Available at: https://doi.org/10.1007/978-3-030-86016-5_3.

Munz, C.M. *et al.* (2023) 'Regeneration after blood loss and acute inflammation proceeds without contribution of primitive HSCs', *Blood*, 141(20), pp. 2483–2492. Available at: https://doi.org/10.1182/blood.2022018996.

Murphy, M.P. (2009) 'How mitochondria produce reactive oxygen species', *Biochemical Journal*, 417(1), pp. 1–13. Available at: https://doi.org/10.1042/BJ20081386.

Naik, S. *et al.* (2018) 'Two to Tango: Dialog between Immunity and Stem Cells in Health and Disease', *Cell*, 175(4), pp. 908–920. Available at: https://doi.org/10.1016/j.cell.2018.08.071.

Nakagawa, M.M., Chen, H. and Rathinam, C.V. (2018) 'Constitutive activation of NF-κB pathway in hematopoietic stem cells causes loss of quiescence and deregulated transcription factor networks', *Frontiers in Cell and Developmental Biology*, 6(OCT), pp. 1–14. Available at: https://doi.org/10.3389/fcell.2018.00143.

Nakamura-Ishizu, A. *et al.* (2018) 'Thrombopoietin Metabolically Primes Hematopoietic Stem Cells to Megakaryocyte-Lineage Differentiation', *Cell Reports*, 25(7), pp. 1772-1785.e6. Available at: https://doi.org/10.1016/j.celrep.2018.10.059.

Nestorowa, S. *et al.* (2016) 'A single-cell resolution map of mouse hematopoietic stem and progenitor cell differentiation', *Blood*, 128(8), pp. e20–e31. Available at: https://doi.org/10.1182/blood-2016-05-716480.

Nguyen, T.H., Abidin, B.M. and Heinonen, K.M. (2022) 'Frizzled-6 promotes hematopoietic stem/progenitor cell mobilization and survival during LPS-induced emergency myelopoiesis', *Stem Cell Reports*, 17(10), pp. 2303–2317. Available at: https://doi.org/10.1016/j.stemcr.2022.08.004.

Nilsson, S.K. *et al.* (2005) 'Osteopontin, a key component of the hematopoietic stem cell niche and regulator of primitive hematopoietic progenitor cells', *Blood*, 106(4), pp. 1232–1239. Available at: https://doi.org/10.1182/blood-2004-11-4422.

Norddahl, G.L. *et al.* (2011) 'Accumulating mitochondrial DNA mutations drive premature hematopoietic aging phenotypes distinct from physiological stem cell aging', *Cell Stem Cell*, 8(5), pp. 499–510. Available at: https://doi.org/10.1016/j.stem.2011.03.009.

Nygren, J.M. and Bryder, D. (2008a) 'A novel assay to trace proliferation history in vivo reveals that enhanced divisional kinetics accompany loss of hematopoietic stem cell self-renewal', *PLoS ONE*, 3(11). Available at: https://doi.org/10.1371/journal.pone.0003710.

Oedekoven, C.A. *et al.* (2021) 'Hematopoietic stem cells retain functional potential and molecular identity in hibernation cultures', *Stem Cell Reports*, 16. Available at: https://doi.org/10.1016/j.stemcr.2021.04.002.

Omatsu, Y. *et al.* (2010) 'The Essential Functions of Adipo-osteogenic Progenitors as the Hematopoietic Stem and Progenitor Cell Niche', *Immunity*, 33(3), pp. 387–399. Available at: https://doi.org/10.1016/j.immuni.2010.08.017.

Orkin, S.H. and Zon, L.I. (2008) 'Hematopoiesis: An Evolving Paradigm for Stem Cell Biology', *Cell*, 132(4), pp. 631–644. Available at: https://doi.org/10.1016/j.cell.2008.01.025.

Ostrander, E.L. *et al.* (2020) 'Divergent Effects of Dnmt3a and Tet2 Mutations on Hematopoietic Progenitor Cell Fitness', *Stem Cell Reports*, 14(4), pp. 551–560. Available at: https://doi.org/10.1016/j.stemcr.2020.02.011.

Palikaras, K., Lionaki, E. and Tavernarakis, N. (2018) 'Mechanisms of mitophagy in cellular homeostasis, physiology and pathology', *Nature Cell Biology*, 20(9), pp. 1013–1022. Available at: https://doi.org/10.1038/s41556-018-0176-2.

Papa, L., Djedaini, M. and Hoffman, R. (2019) 'Mitochondrial role in stemness and differentiation of hematopoietic stem cells', *Stem Cells International*, 2019. Available at: https://doi.org/10.1155/2019/4067162.

Pascutti, M.F., Erkelens, M.N. and Nolte, M.A. (2016) 'Impact of viral infections on hematopoiesis: From beneficial to detrimental effects on bone marrow output', *Frontiers in Immunology*, 7(SEP), pp. 1–12. Available at: https://doi.org/10.3389/fimmu.2016.00364.

Passaro, D. *et al.* (2017) 'Increased Vascular Permeability in the Bone Marrow Microenvironment Contributes to Disease Progression and Drug Response in Acute Myeloid Leukemia', *Cancer Cell*, 32(3), pp. 324-341.e6. Available at: https://doi.org/10.1016/j.ccell.2017.08.001.

Pei W., *et.al.* (2017) 'Polylox barcoding reveals haematopoietic stem cell fates realized in vivo', Nature, 7668 (548), pp456-460

Picard, M. and Shirihai, O.S. (2022) 'Mitochondrial signal transduction', *Cell Metabolism*, 34(11), pp. 1620–1653. Available at: https://doi.org/10.1016/j.cmet.2022.10.008.

Pietras, E.M. *et al.* (2015) 'Functionally Distinct Subsets of Lineage-Biased Multipotent Progenitors Control Blood Production in Normal and Regenerative Conditions', *Cell Stem Cell*, 17(1), pp. 35–46. Available at: https://doi.org/10.1016/j.stem.2015.05.003.

Pietras, E.M. *et al.* (2016) 'Chronic interleukin-1 exposure drives haematopoietic stem cells towards precocious myeloid differentiation at the expense of self-renewal', *Nature Cell Biology*, 18(6), pp. 607–618. Available at: https://doi.org/10.1038/ncb3346.

Pineault, K.M. *et al.* (2019) 'Hox11 expressing regional skeletal stem cells are progenitors for osteoblasts, chondrocytes and adipocytes throughout life', *Nature Communications*, 10(1), pp. 1–15. Available at: https://doi.org/10.1038/s41467-019-11100-4.

Pinho, S. and Frenette, P.S. (2019a) 'Haematopoietic stem cell activity and interactions with the niche', *Nature Reviews Molecular Cell Biology*, 20(5), pp. 303–320. Available at: https://doi.org/10.1038/s41580-019-0103-9.

Pirillo, C. *et al.* (2022) 'Metalloproteinase inhibition reduces AML growth, prevents stem cell loss, and improves chemotherapy effectiveness', *Blood Advances*, 6(10), pp. 3126–3141. Available at: https://doi.org/10.1182/bloodadvances.2021004321.

Platanias, L.C. (2005) 'Mechanisms of type-I- and type-II-interferon-mediated signalling', *Nature Reviews Immunology*, 5(5), pp. 375–386. Available at: https://doi.org/10.1038/nri1604.

Prendergast, Á.M. *et al.* (2017) 'IFN α -mediated remodeling of endothelial cells in the bone marrow niche', *Haematologica*, 102(3), pp. 445–453. Available at: https://doi.org/10.3324/haematol.2016.151209.

Rabe, J.L. *et al.* (2020) 'CD34 and EPCR coordinately enrich functional murine hematopoietic stem cells under normal and inflammatory conditions', *Experimental Hematology*, 81, pp. 1-15.e6. Available at: https://doi.org/10.1016/j.exphem.2019.12.003.

Ramasamy, S.K. (2017) 'Structure and Functions of Blood Vessels and Vascular Niches in Bone', *Stem Cells International*, 2017(Figure 1). Available at: https://doi.org/10.1155/2017/5046953.

Rao, L.V.M., Esmon, C.T. and Pendurthi, U.R. (2014) 'Endothelial cell protein C receptor: A multiliganded and multifunctional receptor', *Blood*, 124(10), pp. 1553–1562. Available at: https://doi.org/10.1182/blood-2014-05-578328.

Reid, M.A., Dai, Z. and Locasale, J.W. (2017) 'The impact of cellular metabolism on chromatin dynamics and epigenetics', *Nature Cell Biology*, 19(11), pp. 1298–1306. Available at: https://doi.org/10.1038/ncb3629.

Rodriguez-Fraticelli, A.E. *et al.* (2018) 'Clonal analysis of lineage fate in native haematopoiesis', *Nature*, 553(7687), pp. 212–216. Available at: https://doi.org/10.1038/nature25168.

Rodriguez-Fraticelli, A.E. *et al.* (2020) 'Single-cell lineage tracing unveils a role for TCF15 in haematopoiesis', *Nature*, 583(7817), pp. 585–589. Available at: https://doi.org/10.1038/s41586-020-2503-6.

Sacchetti, B. *et al.* (2007) 'Self-Renewing Osteoprogenitors in Bone Marrow Sinusoids Can Organize a Hematopoietic Microenvironment', *Cell*, 131(2), pp. 324–336. Available at: https://doi.org/10.1016/j.cell.2007.08.025.

SanMiguel, J.M. *et al.* (2022) 'Cell origin–dependent cooperativity of mutant Dnmt3a and Npm1 in clonal hematopoiesis and myeloid malignancy', *Blood Advances*, 6(12), pp. 3666–3677. Available at: https://doi.org/10.1182/bloodadvances.2022006968.

Schofield, R. (1978) 'The relationship between the spleen colony-forming cell and the haemopoietic stem cell.', *Blood Cells*, 4(1–2), pp. 7–25.

Schröder, B. (2016) 'The multifaceted roles of the invariant chain CD74 - More than just a chaperone', *Biochimica et Biophysica Acta - Molecular Cell Research*, 1863(6), pp. 1269–1281. Available at: https://doi.org/10.1016/j.bbamcr.2016.03.026.

Sebert, M. *et al.* (2023) 'Clonal hematopoiesis driven by chromosome 1q/MDM4 trisomy defines a canonical route toward leukemia in Fanconi anemia', *Cell Stem Cell*, 30(2), pp. 153-170.e9. Available at: https://doi.org/10.1016/j.stem.2023.01.006.

Sender, R. and Milo, R. (2021) 'The distribution of cellular turnover in the human body', *Nature Medicine*, 27(1), pp. 45–48. Available at: https://doi.org/10.1038/s41591-020-01182-9.

Shi, K. *et al.* (2022) 'Bone marrow hematopoiesis drives multiple sclerosis progression', *Cell*, 185(13), pp. 2234-2247.e17. Available at: https://doi.org/10.1016/j.cell.2022.05.020.
Sies, H. and Jones, D.P. (2020) 'Reactive oxygen species (ROS) as pleiotropic physiological signalling agents', *Nature Reviews Molecular Cell Biology*, 21(7), pp. 363–383. Available at: https://doi.org/10.1038/s41580-020-0230-3.

Silva-Filho, J.L. *et al.* (2020) 'Plasmodium vivax in Hematopoietic Niches: Hidden and Dangerous', *Trends in Parasitology*, 36(5), pp. 447–458. Available at: https://doi.org/10.1016/j.pt.2020.03.002.

Sommerkamp, P. and Trumpp, A. (2016) 'Metabolic cues for hematopoietic stem cells', *Science*, 354(6316), pp. 1103–1104. Available at: https://doi.org/10.1126/science.aal3466.

Spangrude, G.J., Heimfeld, S. and Weissman, I.L. (1988) 'Hematopoietic Stem', *Science*, pp. 58–62.

Steensma, D.P. (2018) 'Clinical Implications of Clonal Hematopoiesis', *Mayo Clinic Proceedings*, 93(8), pp. 1122–1130. Available at: https://doi.org/10.1016/j.mayocp.2018.04.002.

Stergiou, I.E. and Kapsogeorgou, E.K. (2021) 'Autophagy and metabolism in normal and malignant hematopoiesis', *International Journal of Molecular Sciences*, 22(16). Available at: https://doi.org/10.3390/ijms22168540.

Sweatt,S.K, Gower, B.A, Chieh, A.Y, Liu, Y, Li, L. (2016) 'Deconstructing the Complexity of TGFβ Signaling in Hematopoietic Stem Cells: Quiescence and Beyond', *Physiology & behavior*, 176(1), pp. 139–148. Available at: https://doi.org/10.1007/s40778-016-0069-x.Deconstructing.

Takayama, N. *et al.* (2021) 'The Transition from Quiescent to Activated States in Human Hematopoietic Stem Cells Is Governed by Dynamic 3D Genome Reorganization', *Cell Stem Cell*, 28(3), pp. 488-501.e10. Available at: https://doi.org/10.1016/j.stem.2020.11.001.

Takihara, Y.J. *et al.* (2019) 'High mitochondrial mass is associated with reconstitution capacity and quiescence of hematopoietic stem cells', *Blood Advances*, 3(15), pp. 2323–2327. Available at: https://doi.org/10.1182/bloodadvances.2019032169.

Takizawa, H., Boettcher, S. and Manz, M.G. (2012) 'Demand-adapted regulation of early hematopoiesis in infection and inflammation', *Blood*, 119(13), pp. 2991–3002. Available at: https://doi.org/10.1182/blood-2011-12-380113.

Takubo, K. *et al.* (2010) 'Regulation of the HIF-1α level is essential for hematopoietic stem cells', *Cell Stem Cell*, 7(3), pp. 391–402. Available at: https://doi.org/10.1016/j.stem.2010.06.020.

Tikhonova, A.N. *et al.* (2019) 'The bone marrow microenvironment at single-cell resolution', *Nature*, 569(7755), pp. 222–228. Available at: https://doi.org/10.1038/s41586-019-1104-8.

Tovy, A. *et al.* (2020) 'Tissue-Biased Expansion of DNMT3A-Mutant Clones in a Mosaic Individual Is Associated with Conserved Epigenetic Erosion', *Cell Stem Cell*, 27(2), pp. 326-335.e4. Available at: https://doi.org/10.1016/j.stem.2020.06.018.

Umemoto, T. *et al.* (2018) 'Ca2+–mitochondria axis drives cell division in hematopoietic stem cells', *Journal of Experimental Medicine*, 215(8), pp. 2097–2113. Available at: https://doi.org/10.1084/jem.20180421.

Vainieri, M.L. *et al.* (2016) 'Systematic tracking of altered haematopoiesis during sporozoitemediated malaria development reveals multiple response points', *Open Biology*, 6(6). Available at: https://doi.org/10.1098/rsob.160038.

Vandoorne, K. *et al.* (2018) 'Imaging the vascular bone marrow niche during inflammatory stress', *Circulation Research*, 123(4), pp. 415–427. Available at: https://doi.org/10.1161/CIRCRESAHA.118.313302.

Vannini, N. *et al.* (2016) 'Specification of haematopoietic stem cell fate via modulation of mitochondrial activity', *Nature Communications*, 7, pp. 1–9. Available at: https://doi.org/10.1038/ncomms13125.

Venugopal, K. *et al.* (2020) 'Plasmodium asexual growth and sexual development in the haematopoietic niche of the host', *Nature Reviews Microbiology*, 18(3), pp. 177–189. Available at: https://doi.org/10.1038/s41579-019-0306-2.

Walter, D. *et al.* (2015) 'Exit from dormancy provokes DNA-damage-induced attrition in haematopoietic stem cells', *Nature*, 520(7548), pp. 549–552. Available at: https://doi.org/10.1038/nature14131.

Wang, X. *et al.* (2018) 'TGF-β1 Negatively Regulates the Number and Function of Hematopoietic Stem Cells', *Stem Cell Reports*, 11(1), pp. 274–287. Available at: https://doi.org/10.1016/j.stemcr.2018.05.017.

Wang, M. *et al.* (2023) 'Genotoxic aldehyde stress prematurely ages hematopoietic stem cells in a p53-driven manner', *Molecular Cell*, 83(14), pp. 2417-2433.e7. Available at: https://doi.org/10.1016/j.molcel.2023.05.035

Wei, Q. and Frenette, P.S. (2018) 'Niches for Hematopoietic Stem Cells and Their Progeny', *Immunity*, 48(4), pp. 632–648. Available at: https://doi.org/10.1016/j.immuni.2018.03.024.
White, N.J. *et al.* (2014) 'Malaria', *The Lancet*, 383(9918), pp. 723–735. Available at: https://doi.org/10.1016/S0140-6736(13)60024-0.

Wilkinson, A.C., Igarashi, K.J. and Nakauchi, H. (2020) 'Haematopoietic stem cell self-renewal in vivo and ex vivo', *Nature Reviews Genetics*, 21(9), pp. 541–554. Available at: https://doi.org/10.1038/s41576-020-0241-0.

Willemsen, J. *et al.* (2021) 'TNF leads to mtDNA release and cGAS/STING-dependent interferon responses that support inflammatory arthritis', *Cell Reports*, 37(6), p. 109977. Available at: https://doi.org/10.1016/j.celrep.2021.109977.

Wilson, A. *et al.* (2008a) 'Hematopoietic Stem Cells Reversibly Switch from Dormancy to Self-Renewal during Homeostasis and Repair', *Cell*, 135(6), pp. 1118–1129. Available at: https://doi.org/10.1016/j.cell.2008.10.048.

Wilson, N.K. *et al.* (2015a) 'Combined Single-Cell Functional and Gene Expression Analysis Resolves Heterogeneity within Stem Cell Populations', *Cell Stem Cell*, 16(6), pp. 712–724. Available at: https://doi.org/10.1016/j.stem.2015.04.004.

Winkler, I.G. *et al.* (2012) 'Vascular niche E-selectin regulates hematopoietic stem cell dormancy, self renewal and chemoresistance', *Nature Medicine*, 18(11), pp. 1651–1657. Available at: https://doi.org/10.1038/nm.2969.

Wong, H.S. *et al.* (2017) 'Production of superoxide and hydrogen peroxide from specific mitochondrial sites under different bioenergetic conditions', *Journal of Biological Chemistry*, 292(41), pp. 16804–16809. Available at: https://doi.org/10.1074/jbc.R117.789271.

Wu, X. *et al.* (2018) 'Intrinsic Immunity Shapes Viral Resistance of Stem Cells', *Cell*, 172(3), pp. 423-438.e25. Available at: https://doi.org/10.1016/j.cell.2017.11.018.

Xia, P. *et al.* (2018) 'A Circular RNA Protects Dormant Hematopoietic Stem Cells from DNA Sensor cGAS-Mediated Exhaustion', *Immunity*, 48(4), pp. 688-701.e7. Available at: https://doi.org/10.1016/j.immuni.2018.03.016.

Xu, C. *et al.* (2018) 'Stem cell factor is selectively secreted by arterial endothelial cells in bone marrow', *Nature Communications*, 9(1), pp. 1–13. Available at: https://doi.org/10.1038/s41467-018-04726-3.

Yamamoto, R. *et al.* (2013) 'XClonal analysis unveils self-renewing lineage-restricted progenitors generated directly from hematopoietic stem cells', *Cell*, 154(5), pp. 1112–1126. Available at: https://doi.org/10.1016/j.cell.2013.08.007.

Yamamoto, R. *et al.* (2018) 'Large-Scale Clonal Analysis Resolves Aging of the Mouse Hematopoietic Stem Cell Compartment', *Cell Stem Cell*, 22(4), pp. 600-607.e4. Available at: https://doi.org/10.1016/j.stem.2018.03.013.

Yamashita, M., Nitta, E. and Suda, T. (2015) 'Aspp1 Preserves Hematopoietic Stem Cell Pool Integrity and Prevents Malignant Transformation', *Cell Stem Cell*, 17(1), pp. 23–34. Available at: https://doi.org/10.1016/j.stem.2015.05.013.

Yamashita, M. and Passegué, E. (2019) 'TNF-α Coordinates Hematopoietic Stem Cell Survival and Myeloid Regeneration', *Cell Stem Cell*, 25(3), pp. 357-372.e7. Available at: https://doi.org/10.1016/j.stem.2019.05.019.

Yamashita, M. and Passegué, E. (2019c) 'TNF-α Coordinates Hematopoietic Stem Cell Survival and Myeloid Regeneration', *Cell Stem Cell*, 25(3), pp. 357-372.e7. Available at: https://doi.org/10.1016/j.stem.2019.05.019.

Yang, D. and de Haan, G. (2021) 'Inflammation and aging of hematopoietic stem cells in their niche', *Cells*, 10(8), pp. 1–13. Available at: https://doi.org/10.3390/cells10081849.

Yang, Y. *et al.* (2022) 'The histone lysine acetyltransferase HBO1 (KAT7) regulates hematopoietic stem cell quiescence and self-renewal', *Blood*, 139(6), pp. 845–858. Available at: https://doi.org/10.1182/blood.2021013954.

Young, A.L. *et al.* (2016) 'Clonal haematopoiesis harbouring AML-associated mutations is ubiquitous in healthy adults', *Nature Communications*, 7. Available at: https://doi.org/10.1038/ncomms12484.

Yu, V.W.C. *et al.* (2016) 'Epigenetic Memory Underlies Cell-Autonomous Heterogeneous Behavior of Hematopoietic Stem Cells', *Cell*, 167(5), pp. 1310-1322.e17. Available at: https://doi.org/10.1016/j.cell.2016.10.045

Zeng, A.G.X. *et al.* (2023) 'A hematopoietic stem cell subset that retains memory of prior inflammatory stress accumulates in aging and clonal hematopoiesis Abstract Hematopoietic stem cells (HSC) must persist through a lifetime of infections to ensure life-long blood production , bioRxiv'

Zhang, H. *et al.* (2016a) 'TGF-β inhibition rescues hematopoietic stem cell defects and bone marrow failure in Fanconi anemia', *Cell Stem Cell*, 18(5), pp. 668–681. Available at: https://doi.org/10.1016/j.stem.2016.03.002.

Zhang, H., Menzies, K.J. and Auwerx, J. (2018) 'The role of mitochondria in stem cell fate and aging', *Development (Cambridge)*, 145(8). Available at: https://doi.org/10.1242/dev.143420.

Zhang, Y. *et al.* (2018) 'Hematopoietic Hierarchy – An Updated Roadmap', *Trends in Cell Biology*, 28(12), pp. 976–986. Available at: https://doi.org/10.1016/j.tcb.2018.06.001.

Zhang, Y.W. *et al.* (2022) *Hyaluronic acid–GPRC5C signalling promotes dormancy in haematopoietic stem cells*, *Nature Cell Biology*. Springer US. Available at: https://doi.org/10.1038/s41556-022-00931-x.

Zhao, M. and Li, L. (2016) 'Dissecting the bone marrow HSC niches', *Cell Research*, 26(9), pp. 975–976. Available at: https://doi.org/10.1038/cr.2016.71.

Zheng, Z. *et al.* (2022) 'Uncovering the emergence of HSCs in the human fetal bone marrow by single-cell RNA-seq analysis', *Cell Stem Cell*, 29(11), pp. 1562-1579.e7. Available at: https://doi.org/10.1016/j.stem.2022.10.005.

Zhou, B.O. *et al.* (2014) 'Leptin-receptor-expressing mesenchymal stromal cells represent the main source of bone formed by adult bone marrow', *Cell Stem Cell*, 15(2), pp. 154–168. Available at: https://doi.org/10.1016/j.stem.2014.06.008.

Zhou, B.O., Ding, L. and Morrison, S.J. (2015) 'Hematopoietic stem and progenitor cells regulate the regeneration of their niche by secreting Angiopoietin-1', *eLife*, 2015(4), pp. 1–25. Available at: https://doi.org/10.7554/eLife.05521.

Appendix A

Single cell RNA sequencing data analysis methods

Kindly provided by Dr Qi Lu and Prof. Bertie Gottgens

Dataset processing

In total, there were 288 cells from three different plates. First, the data were mapped to the mm10 reference genome with 92 spike-ins developed by the External RNA Control Consortium (ERCC) using STAR. The raw expression matrix was then generated using featureCounts.

Quality control and normalization were performed using the in-house software smqpp (https://github.com/SharonWang/smqpp), which was constructed to filter out some low-quality cells in Smart-seq2 data. Briefly, based on several features after mapping, including the number of reads mapped to mitochondrial genes (nMito), the number of reads mapped to nuclear genes (nNuclear), the number of reads mapped to ERCC spike-ins (nERCC), the number of high-coverage genes (count per million greater than 10) (nHCGenes), the total number of mapped reads (nMapped), the total number of reads (nTotal), a cell failing one of these followed criteria will be removed (nMapped>0, nNuclear>$10^{5.2}$ (nMito+nNuclear):nTotal>0.2, nHCGenes>4000, nMito:nNuclear<0.2, nERCC:nMapped<0.4) . 113 cells were removed in this process. In addition, 4 cells without biotin information were removed from the subsequent analysis. Thus, a total 171 cells were retained. Furthermore, genes that were not expressed in any cell were deleted using the scanpy.pp.filter_genes function. As a result, a total of 28,386 genes were filtered. Finally, the expression matrix containing the raw count values for all 171 selected cells with 27,028 genes was normalized to a total count of 10000 in cell-wise and log-transformed using the smqpp function normalise_data.

Selection of highly variable genes

Highly variable genes (HVGs) were detected using the tech_var function in smqpp, which follows Brennecke's approach. Default parameters were used here and ERCC was not considered (meanForFit=10, useERCC=False).

UMAP Visualization

Uniform Manifold Approximation and Projection (UMAP) was used for visualization using the umap function in Scanpy. The normalized data containing all selected HVGs was first scaled using the scanpy.pp.scale function, and then the top 50 principal components were calculated using the scanpy.tl.pca function. Considering the variance ratio explained by each principal component and not involving too much noise, a neighborhood graph was computed using the first 15 components and the number of nearest neighbor cells was set to 11. Leiden clustering was performed at a resolution of 0.6, resulting in 3 clusters.

Cell-cycle analysis

Normalized and log-transformed data was scaled before calculating cell cycle scores. The three phases of the cell cycle (G1, S, and G2M) were estimated using the scanpy.tl.score_genes_cell_cycle function using 97 genes associated with cell cycle signature from Aviv Regev's lab.

Calculation of four measurement scores

All four measurement scores are calculated based on the expression values of a subset of genes defining a specific signature. The hscScore is calculated based on the expression values of the 103 MolO signature genes. The hematopoietic p53Score is calculated based on the expression values of 16 *Trp53* target genes. The Aging signature score was calculated based on the expression values of the top 20 of the 220 aging signature genes. The Repopulation signature score was calculated based on the expression values of 23 relevant Repopulation signature genes. In addition to calculating the hscScore using the hscScore model, the p53Score, Aging score and repopulation signature score were all generated using the score_genes function in Scanpy.

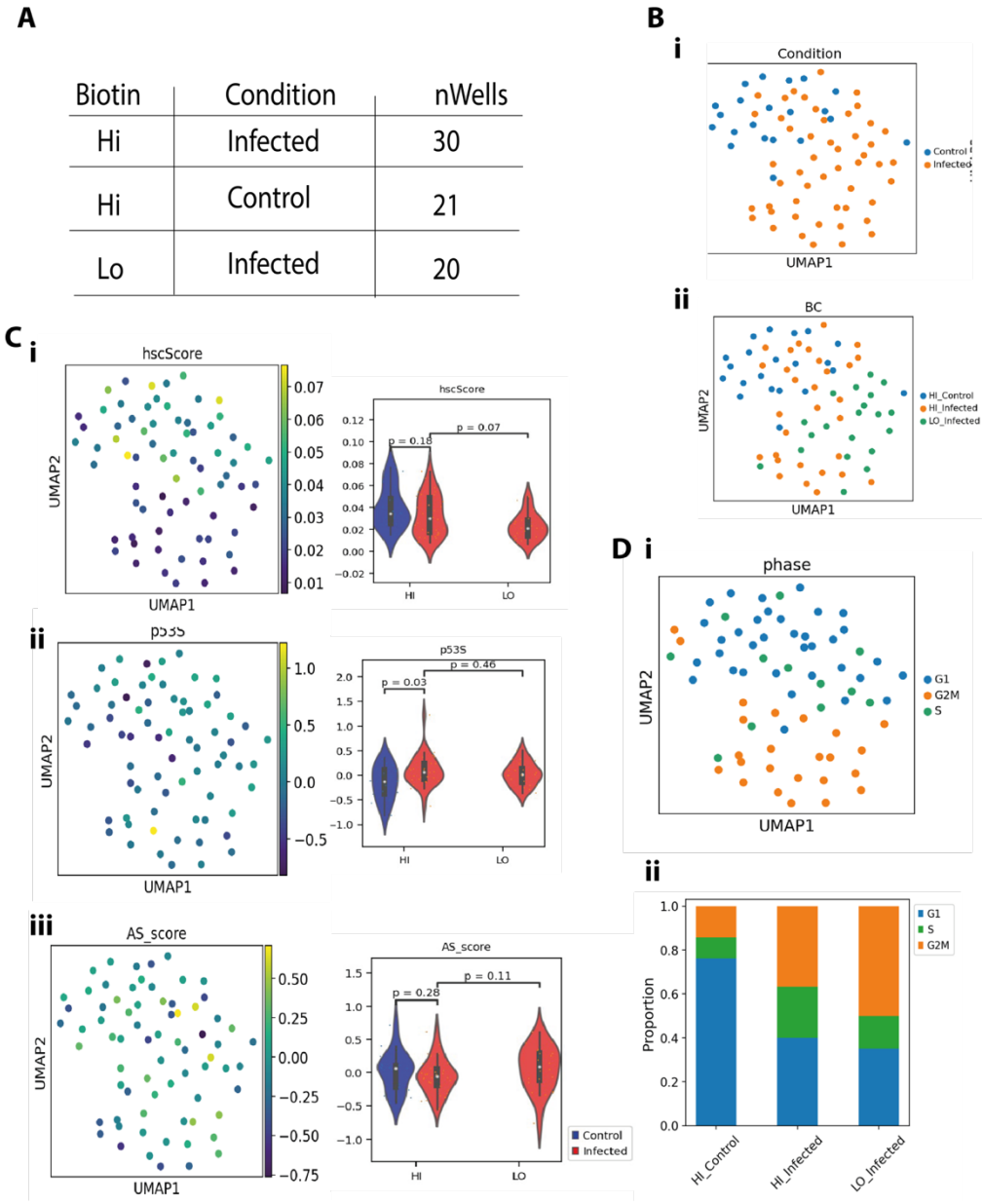
Differential gene expression analysis

Differential expression analysis between two categories was performed using rank_genes_groups function in scanpy. Differentially expressed genes (DEGs) were detected according to the thresholds set by adjusted p-value and logfoldchanges (adjusted p-value<0.05; absolute value of logfoldchange>1.5). Volcano plots were utilized to demonstrate the DEGs. Additionally, the DEGs in the two groups of cells were displayed comparatively using

split-violin plot. Significant DEGs were used for Gene Ontology enrichment analysis by Enrichr. All plotting was performed using matplotlib in Python.

Appendix B

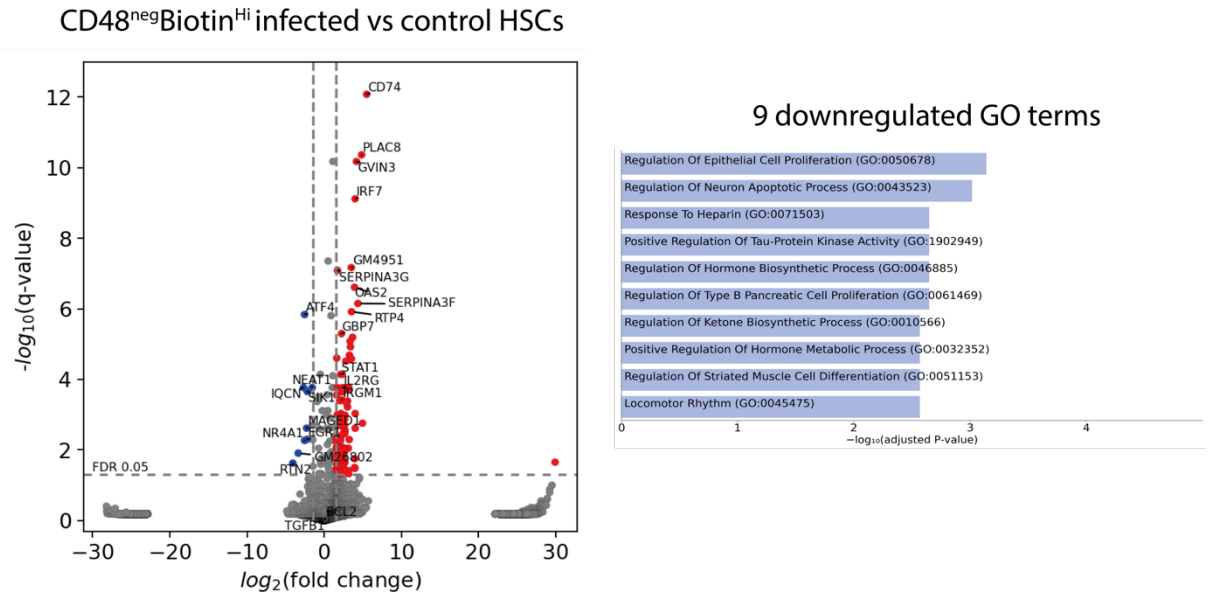
Bulk RNA sequencing analysis



Supplementary Figure 1 Minibulk RNA sequencing analysis. A) Number of wells per biotin subtype in both conditions. B) i) UMAP analysis per condition (control, infected) or ii) based on BiotinHi control/infected and BiotinLo infected. C) UMAP of BiotinHi/Lo infected and BiotinHi clustering based on i) hscScoring, ii) p53 and iii) ageing scoring. Violin plots comparing BiotinHi control/infected and BiotinLo infected cells based on i) hscScroing, ii)p53 and iii) ageing scoring. D) Cell cycle stages of biotin HSC subtypes per condition shown as i) UMAP clustering or ii) bar graphs. In UMAP and violin plots, each dot represents a cell. Statistical differences were determined with Mann-Whitney U test.

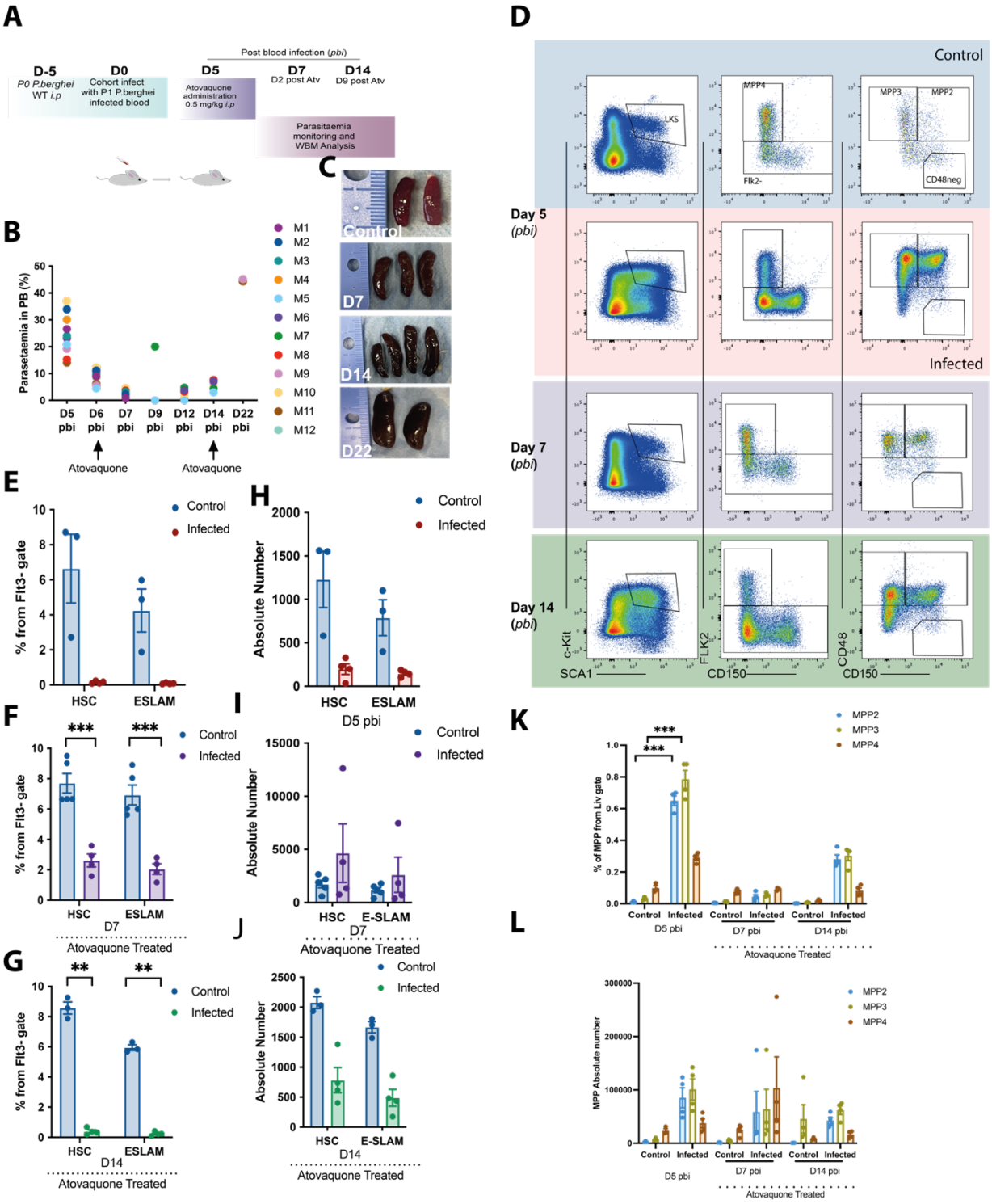
Appendix B

GO pathway gene enrichment terms downregulated in Biotin^{Hi} infected cells



Supplementary Figure 2 Upregulated genes in Biotin^{Hi} infected cells. Volcano plot (left) shows upregulated genes in CD48^{neg} Biotin^{Hi}HSCs shown in red and downregulated genes in blue. GO enrichment pathway analysis revealed 9 downregulated GO terms. Each dot represents a gene. Vertical lines represent the threshold of 1.5 for absolute logarithmic fold change and horizontal lines (FDR) represent the threshold of 0.05 for adjusted p-value. Statistical differences were determined using Student's *t*-test.

Appendix C



Supplementary Figure 3 HSC recover after atovaquone administration. A) Experimental methodology where animals at day 5 *pbi* were administered the anti-malaria drug atovaquone. B) Shows parasitaemia was monitored every day from day 5 until day 7 and then every 2 to 3 days until day 22. C) Splenomegaly in spleens of infected animals collected at days 7, 14 and 22. D) FACS plots showing SCA1 upregulation at day 5 *pbi* , recovery at day 7 but then again HSPC expansion at day 14. E-G) Proportion of HSCs and ESLAM at days 5, 7 and 14. H-J) Absolute number of HSCs and ESLAM at days 5,7 and 14. K) Proportion of MPP subsets five, seven and fourteen days *pbi.* L) Absolute number of MPPs post atovaquone treatment. Each dot represents one individual animal. Statistical differences were determined using Student's *t*-test. (*** represent P≤0.001, ** P≤0.01)